

UNIVERSITÄT
BAYREUTH

Functional Photonic Gradients in Colloidal Assemblies

Dissertation

to be awarded the degree of
Doctor of Natural Sciences (Dr. rer. nat.)

at the Faculty of Biology, Chemistry & Earth Sciences
University of Bayreuth

submitted by
Marius Schöttle
born in Burghausen

Bayreuth, 2023

The work described in this thesis was carried out from September 2019 to March 2023 at the Chair of Physical Chemistry 1 at the University of Bayreuth under the supervision of Prof. Dr. Markus Retsch.

This is a full reprint of the dissertation submitted to obtain the academic degree Doctor of Natural Sciences (Dr. rer. nat.) and approved by the Faculty of Biology, Chemistry & Earth Sciences at the University of Bayreuth.

Type of Dissertation: Cumulative Dissertation

Thesis submitted: 17.03.2023

Acceptance by the Exam Commission: 18.04.2023

Date of Scientific Colloquium: 15.09.2023

Acting Dean:

Prof. Dr. Benedikt Westermann

Doctoral Committee:

Prof. Dr. Markus Retsch	(1st Reviewer)
Prof. Dr. Anna Schenk	(2nd Reviewer)
Prof. Dr. Hans-Werner Schmidt	(Chairman)
Prof. Dr. Matteo Bianchini	

'What I believe' is a process rather than a finality. Finalities are for gods and governments, not for the human intellect.

EMMA GOLDMAN

Acknowledgements

Mein Dank gilt zuerst Prof. Dr. Markus Retsch für die Möglichkeit meine Doktorarbeit an seinem Lehrstuhl zu machen. Mir wurde alle Freiheit bei der Bearbeitung meiner Projekte gelassen, ich konnte mich aber immer auf seine Unterstützung verlassen.

Als zweites möchte ich dem gesamten Lehrstuhl PCI danken. Eine Promotion ist nicht immer einfach, aber zusammen dann meistens trotzdem Spaßig. Besonders möchte ich Thomas danken, für die vielen Stunden der unterschiedlichsten Diskussionen und die gemeinsamen Projekte, und Tobi, der es geschafft hat mich sowohl als Kollegen, als auch als Mitbewohner auszuhalten.

Der Dank an Paul und Seppl ist eh klar, unsere Kaffeepausen werden mir sehr fehlen. Fast täglich über die Hochs und Tiefs des wissenschaftlichen Arbeitens zu reden war essenziell fürs mental health. Allen anderen Freund*innen in Bayreuth natürlich auch, für die gemeinsame Zeit abseits der Uni. Lena, Kai, Kevin, Jul und allen Anderen die mich während der Promotion, aber auch während des Studiums begleitet haben. Genauso an die Friends in Burghausen.

Sandra. Du hast mich seit dem ersten Tag der Promotion begleitet und durchgehend unterstützt. Es ist bestimmt nicht immer leicht mit jemandem während dieser stressigen Zeit zusammen zu sein. Vielen Dank für wirklich alles. Ich freue mich sehr auf die nächsten Kapitel mit dir.

Als Letztes möchte ich meiner Familie danken. Tim und Sebastian, die ich mit in diese Kategorie zähle. Meinen Brüdern, auf die ich sehr stolz bin und die ich in Zukunft sehr viel öfter sehen möchte. Meinen Eltern, die jedes Jahr cooler werden und die mir unfassbaren Rückhalt geben. Ich bin mir sehr bewusst, dass es keine Selbstverständlichkeit ist, ohne finanzielle Sorgen aufzuwachsen und studieren zu können.

Publications and Contributions

This thesis is written as a cumulative dissertation. It is based on the following peer reviewed publications:

- [1] Marius Schöttle, Thomas Tran, Tanja Feller, and Markus Retsch, „Time-Temperature Integrating Optical Sensors Based on Gradient Colloidal Crystals“, *Advanced Materials*, **2021**, 33(40), 2101948.
- [2] Marius Schöttle, Tobias Lauster, Lukas J. Römling, Nicolas Vogel, and Markus Retsch, „A Continuous Gradient Colloidal Glass“, *Advanced Materials*, **2023**, 35(7), 2208745.
- [3] Marius Schöttle*, Thomas Tran,*, Harald Oberhofer, and Markus Retsch, „Machine Learning Enabled Image Analysis of Time-Temperature Sensing Colloidal Arrays“, *Advanced Science*, **2023**, 10(8), 2205512.
**These authors contributed equally to the work.*
- [4] Marius Schöttle, Maximilian Theis, Tobias Lauster, Stephan Hauschild, and Markus Retsch, „Microspectroscopy on Thin Films of Colloidal Mixture Gradients for Data-Driven Optimization of Optical Properties“, *Advanced Optical Materials*, **2023**, 16(11), 2300095.

This thesis does not include results from the following peer reviewed publications, book chapter and manuscripts:

- [5] Theresa Dörres,*, Malgorzata Bartkiewicz,*, Kai Herrmann,*, Marius Schöttle, Daniel Wagner, Zuyuan Wang, Olli Ikkala, Markus Retsch, George Fytas, and Josef Breu, „Nanoscale-Structured Hybrid Bragg Stacks With Orientation- and Composition-Dependent Mechanical and Thermal Transport Properties: Implications for Nacre Mimetics and Heat Management Applications“, *ACS Applied Nano Materials*, **2022**, 5(3), 4119–4129.
**These authors contributed equally to the work.*
- [6] Thomas Tran, Charly Kodisch, Marius Schöttle, Nelson W. Pech-May, and Markus Retsch, „Characterizing the Thermal Diffusivity of Single, Micrometer-Sized Fibers via High-Resolution Lock-in Thermography“, *The Journal of Physical Chemistry C*, **2022**, 126(32), 14003-14010.

- [7] Qimeng Song, Marius Schöttle, Pia Ruckdeschel, Fabian Nutz, and Markus Retsch, „Chapter 14: Heat Management by Colloidal Self-assembly“, *Functional materials from colloidal self-assembly*, **2022**, 493-538.
- [8] Alexander Berger, Marius Schöttle, Flora Lebeda, and Markus Retsch, „Structural and Conductivity Gradient Carbon Material From a Cellulose Precursor“, *Manuscript*.
- [9] Ina Klein, Thomas Tran, René Lars Reise, Maximilian Theis, Marius Schöttle, Sabine Rosenfeldt, Carl Schirmeister, Rolf Mühlhaupt, and Markus Retsch, „Anisotropic Thermal Conductivity of 3D Printed All-PE Composites“, *Manuscript*

The following conference presentations and miscellaneous scientific contributions were part of my PhD:

- [1] **Poster presentation:** „Time-Temperature Integrating Optical Sensors Based on Gradient Colloidal Crystals“, *Bayreuth Polymer Symposium*, **2021**, Bayreuth (DE), **Poster Award**
- [2] **Poster presentation:** „Gradient Colloidal Crystals via Infusion-Withdrawal Coating of Fluorescent Latex Particles“, *MRS Spring Meeting*, **2022**, Honolulu (USA), **Poster Presentation Award**
- [3] **Poster presentation:** „Time-Temperature Integrating Optical Sensors Based on Gradient Colloidal Crystals“, *MRS Spring Meeting*, **2022**, Honolulu (USA)
- [4] **Poster presentation:** „Macro- and Mesoscopic Gradients in Self-Assembled Colloidal Systems“, *36th European Colloid & Interface Society Conference*, **2022**, Chania (GRC)
- [5] **Art of Science:** Finalist and inclusion into the ECIS 2023 calendar
- [6] **Back cover:** „Time-Temperature Integrating Optical Sensors Based on Gradient Colloidal Crystals“, *Advanced Materials*, **2021**, 33(40)
- [7] **Frontispiece:** „A Continuous Gradient Colloidal Glass“, *Advanced Materials*, **2023**, 35(7)
- [8] **Press release:** „Artificial Opals Measure Temperature and Time: Researchers in Bayreuth Discover Novel Sensors“, *University of Bayreuth*, **27 September 2021**, Press release No. 134/2021

Abstract

This thesis comprises four projects that present new accomplishments in colloid-based materials. The common theme throughout all projects is the realization of superordinate gradients in colloidal crystals and glasses, which provide new ways of making use of the photonic properties. Spherical polymer particles were used as a model system, and the two main parameters altered on a single-particle level were the size and the thermal properties. Complexity in the form of defined gradients was introduced by controlling and adjusting the spatial distribution in mixed systems. This was enabled by a range of new synthesis and self-assembly procedures for size and composition gradients in photonic colloidal assemblies. The focus here lies on establishing new concepts, and while every project concludes with an application, I expect these to be applied in neighboring fields in the future as well.

The first project began with developing a novel coating procedure for lateral composition gradients in mixed colloidal crystals. This was achieved using a dual-syringe pump method, similar to dip-coating, and applying two particle types of the same size. The two particles differed regarding their thermal properties, which resulted in film formation kinetics that depended on the composition of the colloidal mixture. This aspect was studied first on discrete samples with defined mixtures and then transferred to gradient colloidal crystals. Since the film formation entailed a visible loss of structural coloration, this novel type of photonic crystal could be used as a time-temperature integrator with a very simple optical readout.

The second project was a follow-up and also applied mixed colloidal crystals as time-temperature integrators with a more detailed readout. The system's complexity was increased using four different particle types that could co-crystallize. Much faster and automated sample preparation was necessary here. This was made possible by a contact printing procedure that prepared several hundred identical samples comprising colloidal crystal arrays. The samples were characterized in-situ during the film formation with a smartphone camera to showcase the user-friendliness of this system. An artificial neural network could be developed that took pictures of a sample with an unknown thermal history as input and provided both time and temperature independently as output.

The third project also applied the dual syringe pump method for lateral gradients in colloidal assemblies. However, the objective here was not to prepare a sensor but to use the composition gradient as a screening platform. Several binary combinations of particles with different sizes were applied, and the optical properties were shown to

depend strongly on the diameter ratio and composition. Gradient samples, coupled with scanning microspectroscopy along the coating direction, provided large data sets. These described the optical properties of bidisperse mixtures over the entire composition range with a high resolution yet required only a few samples. An adjustable photonic stop band, as well as optimum light scattering, could, thereby, be distinguished.

The fourth project in this line of functional photonic gradients also aimed to tailor the optical properties. Here, the gradient was directly used to increase the reflectivity in the visible range. Instead of a lateral composition gradient, the objective was to prepare a thin, particulate film with a continuous particle-size gradient orthogonal to the surface. This required a novel semi-batch synthesis with gradual extraction and a subsequent semi-continuous filtration setup for the particle assembly. When examining the cross section, this revealed a photonic glass film with structural colors spanning the entire visible spectrum. In addition, light reflected from the top surface exhibited adjustable and optimized broadband reflectance.

All of these materials comprise densely packed particles with air in the interstitial spaces. This is an ideal starting point for a range of further projects that either directly make use of the gradient superstructure or apply the established procedures for other types of materials.

Zusammenfassung

Diese Arbeit umfasst vier Projekte, die neue Errungenschaften auf dem Gebiet der kolloidalen Materialien vorstellen. Das gemeinsame Thema aller Projekte ist die Realisierung von übergeordneten Gradienten in kolloidalen Kristallen und Gläsern, die neue Möglichkeiten zur Nutzung der photonischen Eigenschaften bieten. Als Modellsystem wurden sphärische Polymerpartikel verwendet, wobei die beiden wichtigsten Parameter, die auf Einzelpartikelebene verändert wurden, die Größe und die thermischen Eigenschaften sind. Komplexität in Form von definierten Gradienten wurde durch die Kontrolle und Anpassung der räumlichen Verteilung in gemischten Systemen eingeführt. Dies wurde durch eine Reihe neuer Synthese- und Selbstorganisationsverfahren für Größen- und Zusammensetzungsgradienten in photonischen kolloidalen Systemen ermöglicht. Der Schwerpunkt lag hier auf der Etablierung neuer Konzepte. Jedes Projekt präsentiert am Ende eine mögliche Anwendung, jedoch erwarte ich, dass diese Konzepte in Zukunft auch in benachbarten wissenschaftlichen Bereichen etabliert werden.

Das erste Projekt begann mit der Entwicklung eines neuartigen Beschichtungsverfahrens für laterale Zusammensetzungsgradienten in kolloidalen Mischkristallen. Dazu wurden zwei Partikeltypen gleicher Größe mit einer Methode basierend auf zwei Spritzenpumpen aufgetragen, ähnlich der Tauchbeschichtung. Die beiden Partikel unterschieden sich in ihren thermischen Eigenschaften, was zu einer Filmbildungskinetik führte, die von der Zusammensetzung der kolloidalen Mischung abhing. Dieser Aspekt wurde zunächst an diskreten Proben mit definierten Mischungen untersucht und dann auf kolloidale Gradientenkristalle übertragen. Da die Filmbildung mit einem sichtbaren Verlust der strukturellen Färbung einherging, konnte dieser photonische Kristall als Zeit-Temperatur-Integrator mit einer einfachen optischen Auslesung verwendet werden.

Das zweite Projekt ist ein Folgeprojekt und verwendet kolloidale Mischkristalle als Zeit-Temperatur-Integratoren mit einer detaillierteren Auslesung. Die Komplexität des Systems wurde durch die Verwendung von vier verschiedenen Partikeltypen erhöht, die kokristallisieren können. Hier war eine schnellere und automatisierte Herstellung nötig. Ermöglicht wurde dies durch ein Kontaktdruckverfahren, mit dem mehrere hundert identische Proben aus Matrixfeldern hergestellt wurden. Die Proben wurden während der Filmbildung mit einer Smartphone-Kamera in-situ charakterisiert, um die Benutzerfreundlichkeit dieses Systems zu demonstrieren. Ein künstliches neuronales Netz wurde entwickelt, das Bilder einer Probe mit einer unbekanntem thermischen Vorgeschichte als Input nahm und Zeit und Temperatur unabhängig voneinander lieferte.

Im dritten Projekt wurde ebenfalls die Beschichtungsmethode basierend auf zwei Spritzenpumpen für laterale Gradienten in kolloidalen Anordnungen angewandt. Das Ziel war hier jedoch nicht die Herstellung eines Sensors, sondern die Nutzung des Zusammensetzungsgradienten als Plattform für detaillierte Studien. Es wurden mehrere binäre Kombinationen von Partikeln unterschiedlicher Größe verwendet, und es zeigte sich, dass die optischen Eigenschaften stark vom Durchmesser Verhältnis und der Zusammensetzung abhängen. Gradientenproben, gekoppelt mit Mikrospektroskopie entlang der Beschichtungsrichtung, lieferten umfangreiche Datensätze. Diese beschrieben die optischen Eigenschaften von bidispersen Mischungen über den gesamten Zusammensetzungsbereich mit hoher Auflösung, wobei nur wenige Proben benötigt wurden. Dabei konnte ein einstellbares photonisches Stopband sowie optimale Lichtstreuung realisiert werden.

Das vierte Projekt in dieser Reihe funktioneller photonischer Gradienten zielt ebenfalls auf die Anpassung der optischen Eigenschaften ab. Hier wurde der Gradient direkt genutzt, um die Reflektivität im sichtbaren Bereich zu erhöhen. Anstelle eines lateralen Zusammensetzungsgradienten sollte ein dünner Film mit einem kontinuierlichen Partikelgrößengradienten orthogonal zur Oberfläche hergestellt werden. Dies erforderte eine neuartige Semi-Batch-Synthese mit schrittweiser Extraktion und eine anschließende semikontinuierliche Filtration für die Partikelanordnung. Bei der Untersuchung des Querschnitts zeigte sich ein photonisches Glas mit Strukturfarben, die das gesamte sichtbare Spektrum abdecken. Darüber hinaus wies das von der Oberfläche reflektierte Licht eine einstellbare und optimierte Breitbandreflektion auf.

Alle diese Materialien bestehen aus dicht gepackten Partikeln mit Luft in den Poren. Dies ist ein idealer Ausgangspunkt für eine Reihe weiterer Projekte, die entweder den Gradienten direkt nutzen oder die etablierten Verfahren für andere Materialtypen anwenden.

Contents

I	Fundamentals	1
1	Introduction	3
2	Theoretical Background	5
2.1	Synthesis and Assembly of Colloids	5
2.2	Optical Properties of Ordered Systems	14
2.3	Optical Properties of Disordered Systems	24
2.4	Responsive Photonic Materials as Sensors	30
2.5	Gradients in Functional Materials	34
3	Materials & Methods	39
3.1	Synthesis and Assembly Techniques	39
3.2	Optical Characterization	43
4	Thesis Overview	47
4.1	Synopsis	48
4.2	Individual Contributions to Joint Publications	63
5	References	65
II	Publications	79
6	Time–temperature integrating optical sensors based on gradient colloidal crystals	81
7	Machine learning enabled image analysis of time-temperature sensing colloidal arrays	109
8	Microspectroscopy on Thin Films of Colloidal Mixture Gradients for Data-Driven Optimization of Optical Properties	127
9	A Continuous Gradient Colloidal Glass	159

Part I

Fundamentals

When asked about my profession, I usually respond: "I'm a materials scientist." I illustrate this by explaining that I have the great privilege to go to work and essentially play with LEGO® bricks. At its core, this is precisely what my PhD was about. My building blocks were spherical polymer colloids, and my objective was to find creative ways to assemble these in structures that were previously not applicable and exhibited novel functionality.

The most apparent common theme of all my projects was the self-assembly of colloids with a superimposed gradient of a specific property. This required a significant degree of control, and I developed a range of modified synthesis procedures to ensure this. Controlling a colloidal system begins with the particle synthesis, where a narrow size distribution and electrostatic stabilization must be achieved. Then, a range of interactions must be considered when assembling the particles into ordered superstructures. Interesting interactions with visible light occur when these particles are in the sub-micron range. The gradients I introduced into colloidal systems made use of this in very different ways, ranging from autonomous temperature sensors, over optical screening platforms, to materials that showed superior and tailored optical properties.

Returning to the earlier analogy, one might say that I was in charge of fabricating my own building bricks, thinking of how these could interact and assemble, and, at times, also simply playing with them. Naturally, this does require knowledge of several important concepts. The following chapters will begin with a theoretical background of colloid science and photonic crystals, elucidating the range of possibilities in this field. Then, the synthesis and assembly procedures and the advanced optical techniques needed to characterize the gradients will be presented. An overview is shown thereafter, to present my projects and how they are connected. Finally, the corresponding publications are provided in the second part of the thesis.

This chapter introduces the fundamentals of the topics addressed in this thesis. It starts with the synthesis and self-assembly of colloids and elucidates the optical properties of ordered and disordered media. Subsequently, state-of-the-art responsive photonic materials and their use as sensors are provided. Finally, it concludes with an outline of the emerging field of gradient superstructures in photonic colloidal assemblies, which is brought into the context of the findings presented in this work.

2.1 Synthesis and Assembly of Colloids

The term 'colloid' was coined by Thomas Graham in the 1860s: "The colloidal is, in fact, a dynamical state of matter; the crystalloidal being the statical condition."¹ This dynamical nature already implied the usefulness and importance of colloidal systems we have observed in the past decades.² A colloid is generally defined as a mixed system where one component is dispersed in another. Examples found in nature are smoke (solid in gaseous), fog (liquid in gaseous), and milk (liquid in liquid). The definition also requires the size of the inclusions to be between several nm and 1 μm in at least one dimension.³ Consequently, such systems are dominated by interfaces, and properties can differ significantly from those of bulk materials.⁴

Inorganic colloidal particles

Colloid synthesis can be divided into 1) Top-down approaches, such as ball-milling of bulk materials, and 2) Bottom-up approaches, where particles are prepared from molecular precursors.⁵ The latter is of greater importance in this work, and some examples shall be presented. A widespread example is the synthesis of amorphous silica particles in aqueous suspension. Pioneered by Stöber et al.,⁶ the synthesis is based on controlled equilibrium reactions of hydrolysis and condensation of precursor orthosilicates. It results in particles between 50 - 2000 nm with a hydroxylated surface.^{7,8} Another important example are gold nanoparticles, their use dating back to the first stained glass windows. As established by Turkevich et al., synthesis proceeds via in-situ reduction of precursor complexes⁹, and the resulting nanoparticles exhibit characteristic coloration due to

localized surface plasmon resonance.¹⁰ Seeded growth methods can introduce further complexity in the form of anisotropy.¹¹ Lastly, besides these dielectric and metallic particles, semiconductor quantum dots can be discerned. Confinement effects influence the band structure and result in size-dependent absorption and emission of light.^{12,13}

A non-trivial aspect of colloid synthesis is the fabrication of monodisperse particles, i.e., a system with a narrow particle size distribution (PSD). As this is important for later assembly, the underlying mechanism will be elucidated. Particle formation can be separated into nucleation and subsequent particle growth. Classic nucleation theory begins with the case of a metastable, supersaturated solution. Homogeneous nucleation is initiated, but nuclei must first reach a critical radius before becoming thermodynamically stable.⁵ This can be explained by the two contributions to the Gibbs free energy change (ΔG) in equation 2.1:¹⁴

$$\Delta G = \frac{4}{3}r^3 \Delta g_v + 4\pi r^2 \sigma \quad (2.1)$$

Where r is the radius, Δg_v is the difference in energy per unit of volume (always negative), and σ is the surface tension. As the particle radius increases, the volume term ($\propto r^3$) begins to dominate the surface contribution ($\propto r^2$). When surpassing the critical radius, further addition of monomer units becomes energetically favorable, and particle growth and a concomitant decrease of the supersaturation ensues. According to the LaMer model,¹⁵ the formation of a narrow PSD is only possible by rapid nucleation, a fast drop of the supersaturation, and, consequently, particle growth proceeding without further nucleation. This model, however, was already criticized by Turkevich¹⁶, and more recent research suggests that simultaneous nucleation and growth processes are not necessarily detrimental to a narrow PSD. Smaller particles grow faster, and uniformity can still be obtained.^{17,18} Finally, it must also be taken into account that in real systems, heterogeneous nucleation by impurities such as dust plays a role and that after a completed synthesis, smaller particles may dissolve while large particles grow (Ostwald ripening).⁵

Polymer latex particles

The main building blocks of the structures presented in this work are submicron polymer particles. Aqueous suspensions of polymeric colloids, i.e., latexes, are ubiquitous and can be applied in paints, drug delivery, or as catalyst supports.¹⁹ In academic research, monodisperse polymer particles are often used as constituents of ordered structures, as they are readily available in large quantities.²⁰ The synthesis entails both a radical polymerization of monomers into polymer chains and the nucleation and growth aspects

mentioned in the previous section.²¹ Special care must, therefore, be taken to control this complex process. Polymer particles between 100 - 1000 nm and a narrow PSD can be prepared by the surfactant-free emulsion polymerization (SFEP) established by Ottewill.²² The components are an emulsion of monomer droplets in water, an ionic comonomer, and a water-soluble radical initiator.²³ In SFEP, homogeneous nucleation, rather than micellar or monomer-droplet nucleation, occurs and is the first stage of the reaction mechanism (Figure 2.1).²⁴

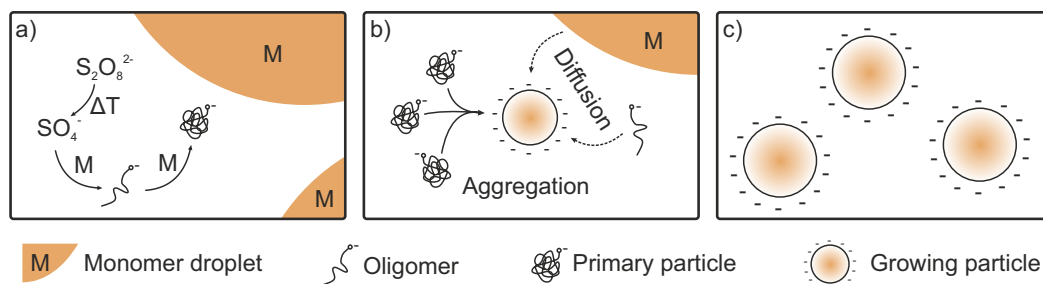


Figure 2.1.: Reaction mechanism of surfactant-free emulsion polymerization.

Upon homolysis of the initiator, the small amount of monomer dissolved in water reacts to form oligomers. Further propagation causes the chain to become insoluble and collapse into a primary particle. Only one charged moiety, attributed to the initiator molecule, is present at this stage. Therefore, the primary particles are colloiddally unstable, and agglomeration proceeds to form mature nuclei.^{25,26} Further adsorption of oligomers increases the charge density on the surface and, thereby, the stability of the dispersion. During the subsequent growth phase, monomer diffuses from the droplets, swells the growing particles, and polymerization primarily occurs on the interior. At approximately 40% conversion, the droplets are consumed, and in the last phase, the remaining monomer inside the particles is polymerized until the conversion plateaus (usually above 95%).²⁴ The electrostatically stabilized, monodisperse particles can then be used as-synthesized, or further growth can be initiated via a semi-batch process, mostly under monomer starved conditions.²⁷

Other approaches to polymer latex particles are, e.g., suspension polymerization, where an oil-soluble initiator is applied, and polymerization ensues inside the monomer droplets.²⁸ Alternatively, dispersion polymerization proceeds via precipitation from a homogeneous mixture.^{29,30} The latter is often used for the fabrication of particles greater than $1\ \mu\text{m}$ ³¹ and soft microgels.³²

Altering the composition of the polymer particles via copolymerization allows further control over material properties. The glass transition temperature (T_g), for example, can be adjusted between -50 and $125\ ^\circ\text{C}$ by changing the ratio of methyl methacrylate (MMA) and n-butyl acrylate (nBA) in a random copolymer.³³ Further alterations via

post-synthesis modification of particles can lead to more complex particle morphologies. One example is the formation of core-shell particles^{34,35}, which can be transformed into hollow spheres via calcination.^{36,37} Another is unidirectional stretching, which can change the aspect ratio and result in monodisperse ellipsoidal particles.^{38,39} Finally, swelling with apolar solvents and diffusion of amphiphilic copolymers or dyes into the particles provides pathways to steric stabilization⁴⁰ and fluorescent staining.^{41,42}

Interparticle interactions

Particles suspended in an aqueous medium experience a multitude of interactions. Precise adjustment is necessary to ensure both stable, agglomeration-free dispersions and controlled self-assembly of particles.⁴³ Beside external forces such as gravitation and Brownian motion^{44,45} (the interactions with the molecular motion of water), several interparticle interactions must be taken into account.⁴⁶ Van-der-Waals interactions, for example, are always attractive between identical surfaces. If two particles come into close contact, this will cause irreversible aggregation. This effect competes with the electrostatic double-layer force. Due to the high permittivity (ϵ) of water, most surfaces in an aqueous environment are charged. Electroneutrality is provided by an inner Stern layer of adsorbed ions and an outer diffuse (or Gouy-Chapman) layer. If two similarly charged surfaces approach each other, the respective diffuse layers overlap, and the consequential disjoining pressure causes repulsion. The interplay of these two contributions was famously investigated by B. Derjaguin, L. Landau, E. Verwey, and T. Overbeek.^{47,48} It is elucidated in the accordingly named DLVO theory which provides the interaction free energy $w(x)$ per unit area between two infinitely extended surfaces separated by a gap x :⁴⁹

$$w(x) = \underbrace{64c_0k_B T \lambda_D \left(\frac{e^{e\psi_0/(2k_B T)} - 1}{e^{e\psi_0/(2k_B T)} + 1} \right)^2 e^{-x/\lambda_D}}_{\text{Electrostatic double layer}} - \underbrace{\frac{A_H}{12\pi x^2}}_{\text{van-der-Waals}} \quad (2.2)$$

Where c_0 is the bulk concentration of salt, k_B is the Boltzmann constant, T is the temperature, ψ_0 is the surface potential and A_H is the Hamaker constant, specific for the respective surfaces and the medium between them. The Debye length (λ_D) is dependent on both the concentration of each type of ion (c_i) as well as the valance (Z_i):⁴⁹

$$\lambda_D = \left(\frac{e^2}{\epsilon \epsilon_0 k_B T} \sum_i c_i Z_i^2 \right)^{-\frac{1}{2}} \quad (2.3)$$

Where e is the elementary charge. However, the interaction energy between two bodies is not just dependent on the material properties and the distance. It is also influenced by the shape of the particles. In this work, interactions between identical spheres are of interest. The Derjaguin approximation⁵⁰ allows a simple derivation of the energy (W) between two spheres with the same radius (R) from the energy per unit area of infinitely extended planes. ($w(x)$). This is dependent on the distance (D) between the spheres. An assumption that must be true here is that the interaction range is much smaller than R and, therefore, the interaction is dominated by the caps of the spheres.⁴⁹

$$W(D) = \pi R \int_D^{\infty} w(x) dx \quad (2.4)$$

Applying the Derjaguin approximation 2.4 to the DLVO equation 2.2 provides the interaction free energy for spheres in an aqueous solution of electrolytes. This is a significant relationship when examining the stability of dispersed colloids and has been verified by experimental force measurements.⁵¹ The derivation assumes that at large distances the interaction energy $W(\infty)$ is zero:

$$W(D) = 64c_0k_B T \lambda_D^2 \pi R \left(\frac{e^{e\psi_0/(2k_B T)} - 1}{e^{e\psi_0/(2k_B T)} + 1} \right)^2 e^{-D/\lambda_D} - \frac{A_H R}{12D} \quad (2.5)$$

By applying equation 2.5 the stability of aqueous suspensions can be predicted at different ionic strengths. For a typical suspension of polymer latex particles, one can assume $A_H = 1.0 \times 10^{-20}$ J and $\psi_0 = 50$ mV.⁵² In Figure 2.2a the interaction potential, calculated via equation 2.5 is shown for particles with a diameter of 250 nm, for various concentrations of a monovalent salt such as NaCl.

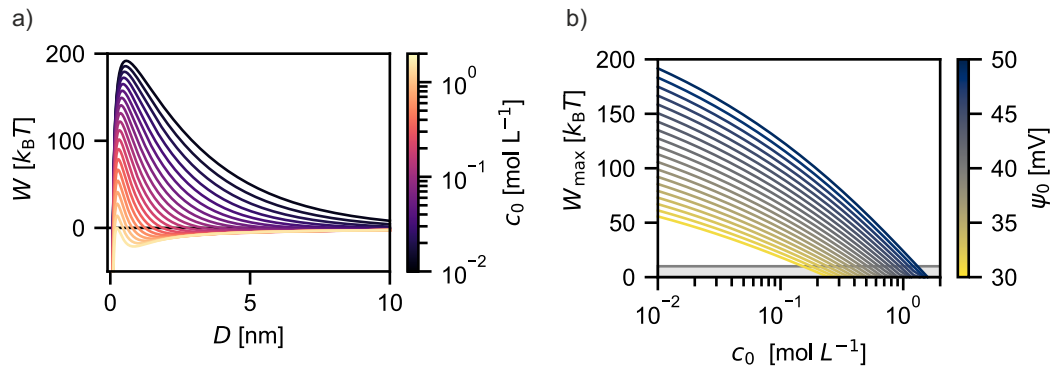


Figure 2.2.: Visualization of the DLVO theory. a) Interaction potential in units of $k_B T$ for different salt concentrations. b) Maximum of the energy barrier with respect to the salt concentration and surface potential. The shaded area is where aggregation occurs ($W > 10 k_B T$.)

As a simplification, the surface potential is assumed to be independent of the ionic background. With an increasing amount of ions in the solution, the energy barrier caused by electrostatic repulsion becomes smaller. As a rule of thumb, the dispersion becomes colloidally unstable when the maximum potential is lower than $10 k_B T$, and particles will irreversibly aggregate.⁴⁹ The importance of the ionic comonomer, which introduces charged moieties on the surface of the polymer particles, becomes apparent in Figure 2.2b. The maximum of the interaction potential is shown with respect to both the salt concentration as well as the surface potential. The grey shaded area shows the aggregation regime, which is reached at lower ionic strengths when charge concentration on the particle surface is reduced. When transitioning from a monovalent salt to ions of a higher valence, this induces a much more significant reduction of the Debye length (see equation 2.3).

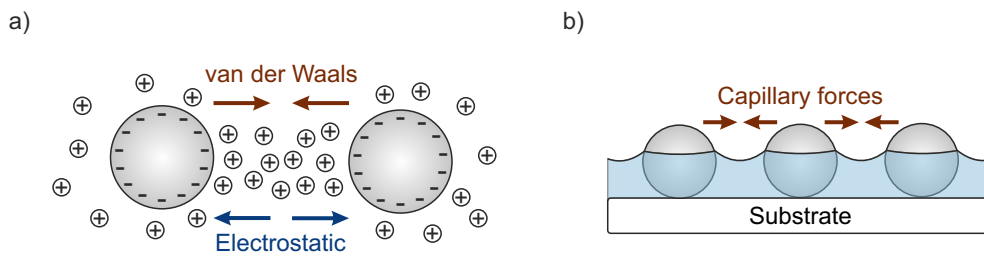


Figure 2.3.: Interparticle interactions relevant during the self-assembly of colloids a) Schematic of two overlapping electric double layers. b) Immersion capillary force between particles on a solid support.

Besides van-der-Waals forces and the electrostatic double layer interaction (Figure 2.3a), other interparticle forces must be considered. The addition of polymeric substances can introduce interactions such as steric stabilization⁵³ (especially relevant in apolar solvents) as well as flocculation via bridging⁵⁴ or depletion forces.⁵⁵ Another non-DLVO interaction that becomes important when particles are present at an air-liquid interface is the occurrence of capillary forces.⁵⁶ These are the basis of several assembly techniques for microparticles.⁵⁷ Particles on a solid support, partially immersed in a liquid film, are subjected to immersion capillary forces (Figure 2.3b). Identical particles with good wetting properties are attracted and approach each other upon evaporation of the liquid. The force can be quantified with respect to the respective densities (ρ) of the liquid (L) and the particles (P) as well as the contact angle (θ) between the particle surface and the liquid:⁵⁸

$$F(D) = -\frac{\gamma_L R^6 \pi}{18 \kappa_c (D + 2R)} \left(2 - 4 \frac{\rho_P}{\rho_L} + 3 \cos \theta - \cos^3 \theta \right)^2 \quad (2.6)$$

Where κ_c is the capillary constant and γ_L the surface tension (2.7 mN m⁻¹ and 72 mN m⁻¹, respectively, for water). If the interplay of electrostatic stabilization and attraction via

capillary action is optimal, monodisperse particles tend to self-assemble into densely packed, highly ordered structures.⁵⁹ Due to distinct parallels of this process to crystallization on a molecular level, the resulting periodic structures are termed colloidal crystals.⁶⁰ Most processes favor a densely packed structure with a filling fraction of 0.74 and either a face-centered cubic (fcc) structure or a random mixture of cubic and hexagonal closed packing.⁶¹ The thin films examined in this work mostly exhibit an fcc structure kinetically promoted via viscous drag during the assembly.⁶² Different techniques exist to produce colloidal crystals from aqueous suspensions, and the most relevant will be presented in the following.

Self-assembly of colloidal crystals

Colloidal crystals (CCs) exist as either 2D hexagonal monolayers or 3D ordered structures. Various interface-mediated methods exist to fabricate monolayers,^{63–65} but the focus of this work will lie on 3D colloidal assemblies.

The simplest and fastest way to assemble particles from a suspension is drop-casting on a flat surface and subsequent water evaporation. However, evaporation usually proceeds faster at the droplet's edges and entails radial mass flow from the center outwards, the so-called coffee-stain effect. Several techniques can overcome this. First, adding a second solvent to the mixture induces gradients in the surface tension and, thereby, Marangoni flow, which counteracts the outwards transport.⁶⁶ Alternatively, optimizing external parameters such as temperature and relative humidity has been shown to induce a milk-skin-like layer of colloids on the air/water interface.⁶⁷ This effectively seals the drop and ensures a uniform coating. Lastly, drop-casting on superhydrophobic surfaces circumvents pinning during the drying procedure, allowing for a receding contact line and, thereby, uniform and crack-free assembly.⁶⁸

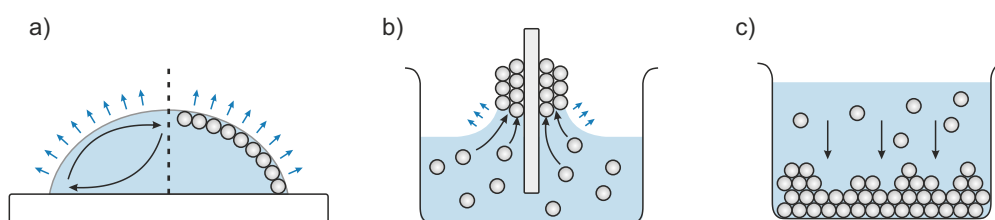


Figure 2.4.: Self-assembly methods for the fabrication of colloidal crystals. a) Drop-casting. b) Vertical deposition. c) Sedimentation/Centrifugation.

A widely used method for large-area and uniform coating is vertical deposition. A substrate is immersed in the suspension, and either by pulling out the substrate or letting the water evaporate, the contact line moves along the surface.⁴⁶ While some inhomogeneities, such as thickness variations along the coating direction, can occur due

to meniscus pinning,⁶⁹ in general, this presents a controlled and simple process to thin films of CCs.^{70,71} Vertical deposition is also often used to fabricate composite CCs via the co-assembly of particles and inorganic precursors,⁷² where the voids between particles are filled with compounds such as silica or titania. Subsequent calcination provides a route to inverse opals, an entire field of research in its own right.^{73,74}

If left still, suspended particles will sediment due to gravitation and assemble at the bottom of the container.^{75,76} As the differences in density are rather small between polymers and water, this process is often sped up by centrifugation.⁷⁷ Since the formation occurs in water, the resulting structure can be retained inside a hydrogel.⁷⁸

Further complexity can be added to CCs by an additional level of hierarchy.⁴⁶ A straightforward approach is coating a substrate that is not homogeneous but exhibits a pattern with a periodicity greater than the particle size. Topographically or chemically patterned substrates can both be applied. Examples of the former are the assembly of particles in vertical trenches⁷⁹, a sinusoidal topography⁸⁰, or more complex patterns that control the nucleation and degree of disorder⁸¹. Chemical patterning, on the other hand, forces selective particle assembly on hydrophilic sections of an inhomogeneous substrate^{82,83}. Patterns on a larger scale can be fabricated as arrays of small crystalline spots. These can be fabricated via transfer printing⁸⁴ or inkjet printing.⁸⁵ The latter resembles repeated drop-casting of minute suspension volumes into a defined superstructure that can have either a functional or an artistic purpose.^{86,87} A last, rather different example is the assembly of several particles into supraparticles. Slow diffusion of water from suspension droplets in an oil-in-water emulsion results in a superordinate spherical or polyhedron shape via the assembly of particles.⁸⁸ These supraparticles are interesting model systems^{89,90} and can even be assembled into ordered structures themselves.⁹¹

Self-assembly of colloidal glasses

Monodisperse particles tend to spontaneously form densely packed, periodic structures when assembled from a suspension. While it may seem counter-intuitive, it is, therefore, a more significant challenge to fabricate fully disordered colloidal assemblies from suspensions with a narrow PSD. Since the monodisperse nature of the particles is of great importance later for the optical properties of the ensemble, some fabrication methods will be illustrated here. Generally, two extreme cases can be discerned: 1) ordered colloidal crystals and 2) disordered colloidal glasses (CGs). Between the two, many unwanted cases exist, such as microcrystalline domains in an amorphous matrix or a crystalline overlayer with a disordered, underlying structure.⁹² To obtain a homogeneous CG, dense packing must be entirely prevented. The filling fraction of an amorphous case is naturally lower than in crystalline assemblies. An empirical determination of

the volume fraction of spheres in a random closed packing (rcp) provided the widely accepted value of 0.64.⁹³ However, due to the ill-defined nature of disordered assemblies, a multitude of structures can be realized, with different degrees of disorder and filling fractions.⁹⁴

One of the first approaches to producing monodisperse CGs was adding excess electrolytes to the solution, thereby overcoming the electrostatic repulsion between particles. This decreases the kinetic stabilization observed in the DLVO theory for various ionic strengths in Figure 2.2. When enough salt is added and this potential barrier $W(x)$ is reduced below $10k_B T$, Brownian motion causes collisions between particles. At small distances, attractive Van-der-Waals interactions dominate, and the system falls into the primary energy minimum of the DLVO equation. Irreversible aggregation into random clusters ensues. The CG begins to form, and large samples can be formed via the evaporation of water. Interestingly, the resulting structure can be tailored by changing the amount of salt. A greater ionic background reduces the filling fraction, which can be adjusted between 0.55 and 0.64.⁹² The flocculation can also be initiated by adding polyelectrolytes, which additionally provide mechanical stabilization.⁹⁵ Furthermore, this allows layer-by-layer assembly of thin CG-films on flat substrates.⁹⁶

In many systems, adding a (poly-)electrolyte might be unwanted. An alternative approach to CGs is to rely on interparticle friction and jamming in a metastable state. This can, for example, be achieved via the filtration of an aqueous suspension. The fast assembly process can ensure the jamming of particles in the filter cake.⁹⁷ Clogging and accumulation at pore entrances thereby promote the formation of irregular structures.⁹⁸ Jamming may also be achieved by processing dry powders of monodisperse particles⁹⁹ or highly concentrated pastes. The latter even allows the realization of intricate superstructures via 3D printing.¹⁰⁰ Lastly, jammed particle assemblies can also be realized by self-assembly in confinement, which does not allow for rearrangements necessary to provide a crystalline order.¹⁰¹

The assembly of bidisperse colloidal mixtures is an approach that compromises the monodisperse nature yet allows simple sample preparation. While some specific diameter ratios and compositions allow co-crystallization,^{102,103} the mixture of two particles with different sizes (or shapes) will mostly result in the isotropic case of a CG.^{104,105} The binary mixture can even provide further functionality, as one particle type might act as a broadband absorber and the other as the primary source of light scattering. The ensemble can thereby exhibit optical properties not applicable with either of the single components.¹⁰⁶ Other assembly procedures for CGs include electrophoretic deposition¹⁰⁷, spray-coating combined with fast evaporation¹⁰⁸ and an increase of the surface roughness of particles.¹⁰⁹

2.2 Optical Properties of Ordered Systems

The previous section showed how colloids are synthesized and assembled into specific superstructures. Now the focus will lie on the light-matter interactions of these materials. This section will introduce relevant aspects in ordered systems, i.e., homogeneous bulk materials and periodic photonic crystals.

Homogeneous materials

Light is known to behave both as a particle (photon) as well as a wave. The former is relevant in processes such as absorption, but the wave nature is better suited to explain the interactions in the cases presented here. Therefore, the wave function dependent on the time (t) and the position (\vec{r}) is defined:¹¹⁰

$$\Psi(\vec{r}, t) = A_0 \cos(2\pi \nu t - \vec{k}\vec{r} + \phi) \quad (2.7)$$

Where A_0 is the amplitude, ν the frequency, and ϕ the phase shift. The vector \vec{k} describes the orientation of the wave, and the magnitude is defined by $k = 2\pi/\lambda$, where λ is the wavelength. Mainly, phenomena occurring in the visible range will be examined here, which means λ ranges between 380-750 nm.¹¹¹

When a beam of light hits an interface between air and a solid, various interactions can play a role (Figure 2.5a). The light can be reflected (R), absorbed (A), scattered at inhomogeneities (S), or simply transmitted (T). Due to energy conservation, the sum of all separate intensities must equal the incident intensity (I_0).¹¹² For now, reflection and transmission are the most relevant. The scattering of light in disordered systems is the focus of the next section.

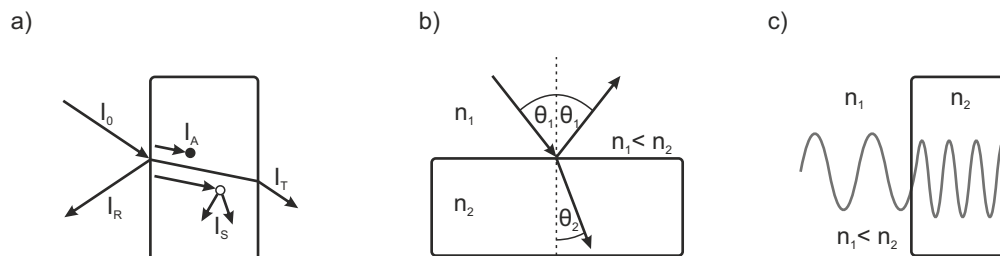


Figure 2.5.: Interaction of light with bulk materials. a) All possible interactions of light and bulk matter. b) Refraction and reflection at an interface of two materials. c) Shortening of the wavelength when light passes through a material with a high refractive index.

When examining the transmitted light, it becomes apparent that the propagation direction changes inside the material (Figure 2.5b). The angles of the incident ray (θ_1) and the refracted ray (θ_2) to the surface normal can be correlated with the respective refractive indices (n_i) by Snell's law:¹¹²

$$\frac{\sin \theta_1}{\sin \theta_2} = \frac{n_2}{n_1} \quad (2.8)$$

The refractive index also has an influence on the wavelength of light inside the material (Figure 2.5c). With an abrupt increase in the refractive index, both the wavelength and the speed of light inside the medium decrease. The frequency, however, must remain constant due to energy conservation.¹¹²

Reducing at least one dimension of the material to a size that roughly corresponds to the wavelength of the incident light results in more interesting interactions. One illustrative example is the structural color of thin films that do not rely on selective absorption but rather interference of parallel waves (Figure 2.6a).¹¹²

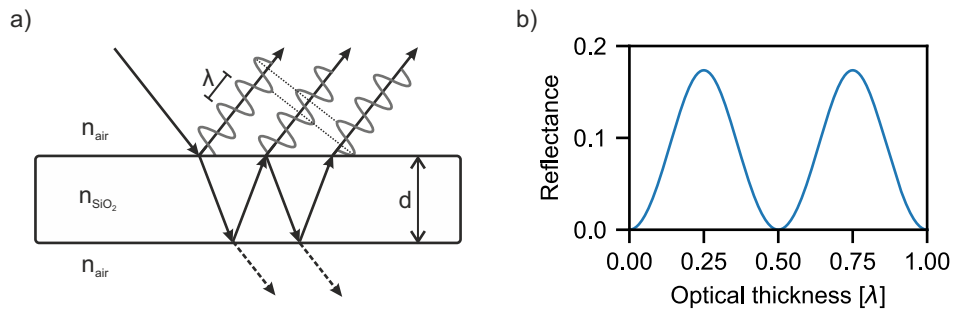


Figure 2.6.: a) Interference of light caused by a thin film of silica. b) Reflectance of the film at different thicknesses given in units of the wavelength λ .

As a monochromatic light beam hits the interface between air and the thin film, the beam is reflected and refracted. This repeatedly happens at both interfaces and causes parallel waves to experience a phase shift. Interference of these waves can be constructive if they are in phase or result in cancellation if the phase shift is a multiple of π .¹¹³ For a fixed wavelength, the reflectivity is dependent on the angle and the optical thickness ($[d]_i = n_i \cdot d_i$) of the film. For normal incidence the reflectance (R) is given by:¹¹²

$$R = \frac{1 - \cos\left(\frac{2\pi n_i d_i}{\lambda}\right)}{1 + \cos\left(\frac{2\pi n_i d_i}{\lambda}\right)} \quad (2.9)$$

In Figure 2.6b, this relationship is plotted, and it becomes apparent that constructive interference of the reflected light occurs when the optical thickness is $\lambda/4$, while transmittance dominates at multiples of $\lambda/2$. If the thickness is fixed and the film is illuminated

with white light, some wavelengths experience strong reflection while others do not, and the film appears colorful. This, for example, explains the color of an oil film on water and the iridescence of pigeon feathers.¹¹⁴ Such effects can significantly be enhanced in periodic multilayers, which will be discussed in the next section.

1D photonic crystals

A multilayer structure comprising multiple bilayers of two materials with different refractive indices is examined (Figure 2.7a). Both types of layers fulfill the $\lambda/4$ condition for the same wavelength. In this example, the multilayer consists of alternating layers of amorphous silica ($n_{\text{SiO}_2} = 1.5$)¹¹⁵ and amorphous titania ($n_{\text{TiO}_2} = 2.5$).¹¹⁶

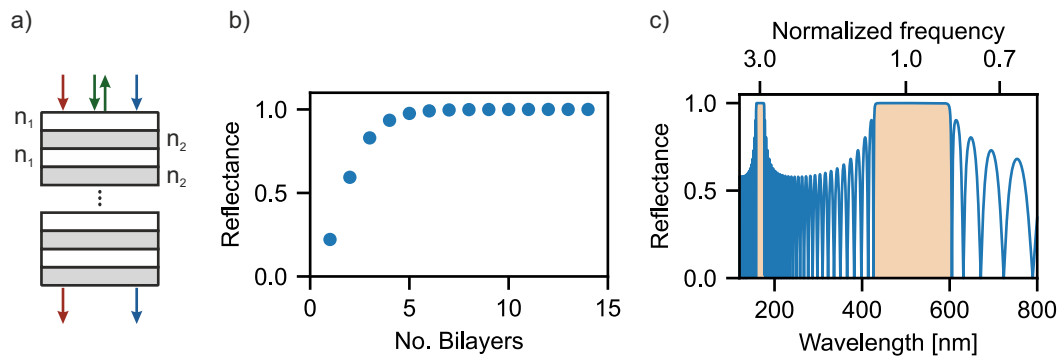


Figure 2.7.: a) Schematic of a quarter wave stack. b) Reflectance of the wavelength corresponding to the $\lambda/4$ condition as a function of the number of bilayers. c) Calculated reflectance spectrum for a stack comprising silica and titania with a maximum reflectance set at 500 nm.

Multiple reflections and an accumulation of the interference phenomena provide a much higher reflectance than the single thin film. The maximum reflectance of such a quarter wave stack increases with the number of bilayers (N):¹¹²

$$R = \left(\frac{1 - (n_1/n_2)^{2N}}{1 + (n_1/n_2)^{2N}} \right)^2 \quad (2.10)$$

The reflectance quickly reaches a value close to 100% at about five bilayers (Figure 2.7b), which elucidates why this type of structure is also called a dielectric mirror.¹¹⁷ Naturally, the next question to arise is how the reflectance behaves over a broad spectral range when most wavelengths do not fulfill the $\lambda/4$ condition. One possible approach to this problem stems from ray optics. It is called the transfer matrix method, and allows the derivation of the optical properties of a system comprising a series of multiple components.^{118–120} The calculated spectrum in Figure 2.7c shows how the multilayer structure acts as a perfect mirror for a wavelength band around the value for which the $\lambda/4$ condition

applies (here: 500 nm). The width of this band correlates with the refractive index contrast between the two materials.¹²¹ Additionally, higher order peaks can be observed at $(2n + 1)\nu_{max}$.

This dielectric mirror, also known as a 1D photonic crystal (1D-PC), is generally characterized by a periodic variation of the refractive index along one axis. This term originated towards the end of the 20th century when a novel way of explaining the optical properties of such materials evolved.^{122,123} The theory treats the propagation of electromagnetic waves through a periodic structure similar to that of electrons in a crystalline semiconductor.^{124,125} An analogous band structure can be derived, which has significant advantages, such as an intuitive illustration of the photonic properties of materials with periodicity in two or three dimensions. For the 1D case, a heuristic illustration is shown in Figure 2.8a.¹²⁶

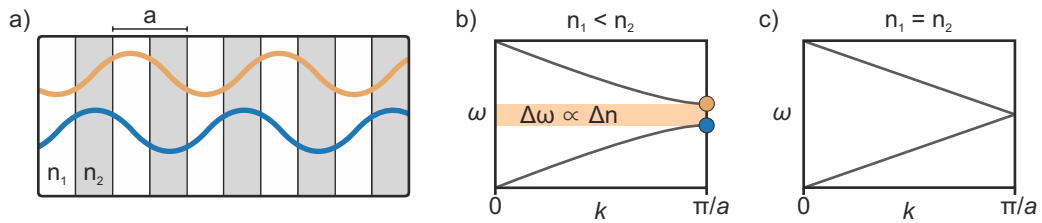


Figure 2.8.: a) 1D photonic crystal with the modes corresponding to the upper and lower bound of the band gap as shown in Ref. [126]. b) Dispersion relation showing the band structure of the photonic crystal. c) Dispersion relation of an arbitrary homogeneous material.

Waves with a wavelength much greater than the thickness of one bilayer (a) are not significantly affected. However, as the wavelength gets smaller (k increases), a critical point is reached when $\lambda = 2a$. Two possibilities exist, and the extrema of the electric field vector can either lie in the domains with a high or a low refractive index. The two modes experience different localization of the energy density.¹²⁶ Since the wavelength of the two is the same, the frequency must be different, and the states become non-degenerate. The dispersion relation exhibits a gap between the two states and comprises frequencies not sustainable in the 1D-PC (Figure 2.8b). This results from the condition that such states must be orthogonal to each other.¹²⁷ The band gap corresponds to the broad, cut-off peak in the reflectance spectrum in Figure 2.7c as it represents a different way to explain the same physical effect. Concomitantly, the width of the band gap is also proportional to the refractive index contrast (Δn). For comparison, a homogeneous medium exhibits a linear dispersion, also known as the light line, and no band gap (Figure 2.8c).¹²⁶ Since no actual periodicity exists, an arbitrary value of a is assigned. The folding at $k = \frac{\pi}{a}$ in both dispersion relations occurs due to symmetry and the definition of a Brillouin zone in which all \vec{k} are defined. This will be elucidated in the next section on 2D-PCs, as these allow intuitive illustrations of the principles involved.

2D photonic crystals

2D-PCs are materials with periodicity along two axes and homogeneity along the third. A classic example is infinitely extended cylinders assembled in a repetitive pattern. Here, the derivation of the band structure from the specific spatial distribution of the refractive index in such a heterogeneous material will be discussed. Prior to this, and as the name 'photonic crystal' suggests, we must first recognize some mathematical tools from crystallography. Geometrically, the only difference from molecular or ionic crystals is the length scale, and many of the same concepts apply here as well.

Three-dimensional crystal structures can be described by seven types of lattice systems that describe the shape of the unit cell. Adding specific locations of lattice points in this unit cell provides the 14 Bravais lattices, which comprise all possible types of periodic 3D patterns. By decorating this unit cell with constituents exhibiting their own specific point symmetry, 230 space groups can be defined. Since this work focuses on isotropic shapes (cylinders in 2D and spheres in 3D), only the Bravais lattices are relevant. In two dimensions, their number is reduced to 5.¹²⁸ In Figure 2.9, a rectangular lattice with the unit cell spanned by the translation vectors \vec{a} and \vec{b} is shown. Note that many cases exist where the primitive unit cell does not correspond to the conventional unit cell. The latter can incorporate more than one lattice position and is often chosen for visualization as it best reflects the symmetry of the lattice, albeit containing redundant information.¹²⁹

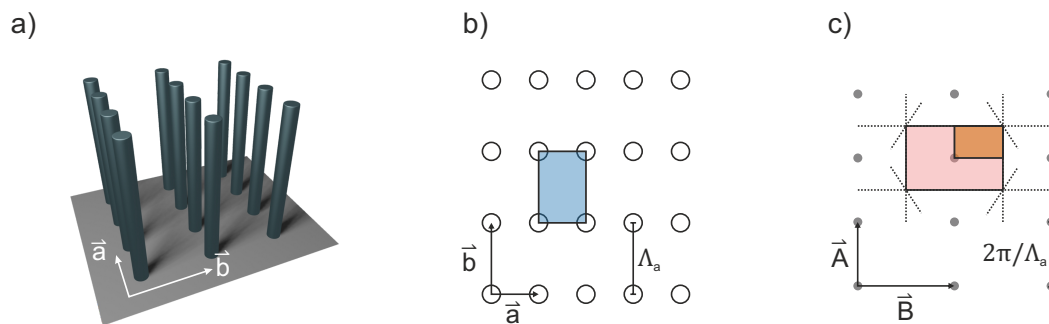


Figure 2.9.: a) Three dimensional and b) two-dimensional representation of a rectangular pattern of infinitely extended cylinders with the unit cell shown in blue. c) Reciprocal lattice with the full and irreducible Brillouin zone shown in red and orange, respectively.

Another way of describing this pattern is by means of the reciprocal lattice. This will prove very practical when examining the interaction of waves with periodic media. Similar to the lattice in real space, it is also defined by two vectors \vec{A} and \vec{B} , where \vec{A} is defined as perpendicular to \vec{b} (or to $\vec{b} \times \vec{c}$ in 3D) and a magnitude inversely proportional to the spacing of lattice planes Λ .¹²⁸ In reciprocal space, the primitive unit cell in the form of the Brillouin zone (BZ) is usually chosen. This is equivalent to the Wigner-Seitz cell in real space and is constructed via Voronoi tessellation. All areas are incorporated closer to one specific lattice point than any other point (Figure 2.9c).¹³⁰ The BZ of the

rectangular case shows mirror symmetry along the vertical and horizontal axes, which implies some redundancy. Further reduction is possible in the form of the irreducible Brillouin zone (iBZ). This is the smallest possible part of the BZ that still fully describes the entire lattice.¹³¹ Now that we have an efficient way of describing the periodic variation of the refractive index, we can begin to think about how such a structure might interact with an electromagnetic wave. From the observations made in the previous section, it already stands to reason that interesting effects will occur when the lattice periodicity and the wavelength of incident light are on a similar length scale.

An incident plane wave propagating through a periodic array of cylinders with a high refractive index will be affected by this structure. Since the speed of light in the cylinders is lower than in between, perturbations occur. This results in the amplitude of the plane wave taking on the symmetry and periodicity of the structure. This relation closely resembles that of electrons affected by the periodic potential in a crystal lattice. Similar to the analogy, Bloch's Theorem can be applied here. The overall field can thereby be defined as the product of the plane wave with an envelope function that contains the information of the periodic lattice:¹³²

$$\underbrace{H(\vec{r})}_{\text{Overall field}} = \underbrace{\vec{A}_k(\vec{r})}_{\text{Envelope}} \cdot \underbrace{e^{i\vec{k}\vec{r}}}_{\text{Plane wave}} \quad (2.11)$$

Generally, when examining phenomena regarding macroscopic electromagnetism, one will be confronted with Maxwell's equations. This will be touched upon briefly since one significant relation is essential here: that of the Eigenvalue problem.¹³³ Some assumptions and simplifications must be made. For example, the material is assumed to be transparent, and the dispersion, i.e., the frequency dependence of the refractive index, is neglected. For these assumptions, the permittivity ($\epsilon(\vec{r})$) of an ideal dielectric medium is related to the refractive index by $n_i(\vec{r}) \approx \sqrt{\epsilon_i(\vec{r})}$. Maxwell's Curl equations can then be applied to yield the following wave equation:¹²⁶

$$\nabla \times \left(\frac{1}{\epsilon(\vec{r})} \nabla \times \vec{H}(\vec{r}) \right) = \left(\frac{\omega}{c} \right)^2 \vec{H}(\vec{r}) \quad (2.12)$$

Where the circular frequency ω is equal to $2\pi\nu$ and ∇ is the Nabla operator, the cross product of which denotes the curl (or rotation) of a vector field. Inserting equation 2.11 into equation 2.12 provides a so-called Eigenvalue problem. This means that for a given structure $\epsilon(\vec{r})$ and a Bloch-vector \vec{k} , there exist infinite yet discrete solutions (frequencies). These so-called Bloch modes describe the electromagnetic waves that are sustained in the structure.¹³³ For a full analysis of the 2D structure, computation of all vectors defined by the area in the iBZ would have to be performed. However, computation

time is generally reduced by simply examining vectors at the edges of the iBZ. In highly symmetric cases, this is adequate since this incorporates the states where local maxima and minima of the photonic bands occur.¹³⁴ The corners of the iBZ are labeled with uppercase letters following a specific nomenclature¹²⁹, and solutions to the Eigenvalue problem are calculated for equidistant vectors \vec{k} between these points. The Eigenvalues, in succession, are referenced by their order (n) which allows the combination of solutions for different \vec{k} to the aforementioned photonic bands.¹²⁶

Thankfully, efficient tools have been developed for deriving these band structures, among others, by the group of J.D. Joannopoulos, who belongs to the pioneers of this area. Useful, open-source packages for the programming language Python3 exist and can be applied to analyze arbitrary structures.¹³⁵ For the intents and purposes of this introduction, the software can be seen as a black box for solving the Eigenvalue problems given by the combination of Maxwell's equations and the Bloch theorem. In short, the Finite Difference Frequency Domain (FDFD) method is applied, which provides numerical solutions for the Eigenvalues, which in combination make up the photonic band diagram.¹²⁶ Here, this will be applied to a hexagonal structure of infinitely extended rods (Figure 2.10a). The rods are air ($\epsilon \approx 1$), and the surrounding medium is titania ($\epsilon \approx 6$). The radius of the rods is set to $0.4a$, where a is the periodicity of the lattice. Note that this lack of specification of the length scale can be maintained throughout the entire derivation. Therefore, the interaction of sub-micron structures with visible light as well as millimeter structures with microwaves, can be described with the same band diagram (assuming a constant refractive index). The first ten bands are calculated and combined in the band diagram shown in Figure 2.10c.

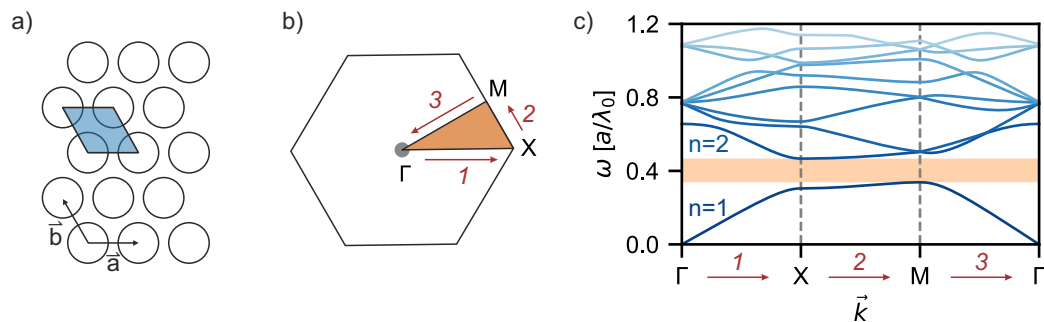


Figure 2.10.: a) A hexagonal lattice of air cylinders in a matrix of amorphous titania. b) The corresponding (irreducible) Brillouin zone with annotations showing the labels at the corners. The red arrows along the edge of the iBZ indicate in which succession the Eigenvalues are calculated c) Band diagram calculated with the MPB package provided for Python.^{135,136} The red arrows correspond to those in (b).

The most important feature of the band diagram can be observed between the first and second-order bands. Here, a photonic band gap (PBG) exists over the entire range, which denotes frequencies of waves that cannot propagate through the material in any

direction. These are consequently reflected, which can result in bright structural colors. It should be noted here that the band structure is only shown for one polarization (the TE mode). For a true photonic band gap, the TM mode must also be considered. Different design rules apply to the two modes, and photonic bandgap engineering must find a compromise between them.¹²⁶

Since the design of a structure also necessitates its realization, the self-assembly of monodisperse particles into periodic superstructures is of great value for this research area. Consequently, many of the photonic crystals that can easily be fabricated are periodic in three dimensions. This class of PCs will be discussed in the next section.

3D photonic crystals

While 2D-PCs are useful for visualizing the origin of photonic band gaps, the three-dimensional version plays a more prominent role in materials science. These 3D-PCs can be fabricated in a variety of ways. Standard examples are liquid crystals^{137,138}, microphase separated block copolymers^{139,140} and self-assembled colloidal crystals¹⁴¹. The simplest fabrication is provided by the CCs (also: 'synthetic opals'), which will play a significant role in this work. In 3D-PCs, Bloch modes exist in all three dimensions, and if the periodicity is in the sub-micron range, the material can exhibit bright structural colors.^{142,143}

As mentioned in section 2.1, monodisperse colloids tend to assemble in the form of stacked, hexagonal layers. Depending on the fabrication technique, these can be in a random sequence (e.g., ABACBA) or, as is the case for vertical deposition, in an fcc structure (ABCABC).¹⁴⁴ Both cases have in common that the substrate dictates the stacking direction (Figure 2.11a).

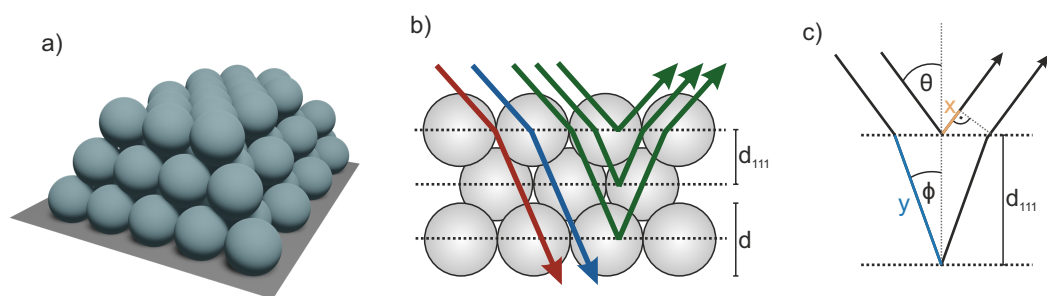


Figure 2.11.: Visualization of the fcc structure in colloidal crystals. a) 3D representation of densely packed spheres. b) and c) Cross section showing the approach of the Bragg-Snell equation for constructive interference of distinct wavelengths.

When examining a cross section (Figure 2.11b), it becomes apparent that these CCs can be seen as periodic, dielectric layers, not unlike the 1D-PC shown in Figure 2.7a.

Depending on the incident angle, different frequencies are forbidden inside the structure. This causes reflection of the corresponding waves and iridescent (angle-dependent) structural coloration (Figure 2.11b).¹⁴⁵ Due to the predetermined stacking geometry, a simple formula can be derived for the wavelength at which constructive interference occurs. Here, the surrounding medium is assumed to be air ($n = 1$). The colloidal crystal is assigned an effective refractive index (n_{eff}) given by the weighted average of the indices of colloids and the interstitial medium,¹⁴⁶ and the (111)-interplanar distance is provided by the height of a tetrahedron, i.e., $d_{111} = \sqrt{\frac{2}{3}}d$. The difference in the optical length ($[d] = nd$) that the two beams in Figure 2.11c traverse has to be a multiple (m) of the wavelength for constructive interference to occur:

$$m\lambda = 2n_{\text{eff}}y - 2x \quad (2.13)$$

Simple trigonometry provides the two lengths x and y :

$$y = \frac{d_{111}}{\cos \phi} \quad x = y \sin \theta \sin \phi = \frac{d_{111} \sin \theta \sin \phi}{\cos \phi} \quad (2.14)$$

Inserting equations 2.14 into equation 2.13:

$$m\lambda = 2d_{111} \left(\frac{n_{\text{eff}} - \sin \theta \sin \phi}{\cos \phi} \right) \quad (2.15)$$

Taking into account the relation of sine and cosine ($\cos = \sqrt{1 - \sin^2}$) as well as Snell's law (equation 2.8: $\sin \phi = \sin \theta / n_{\text{eff}}$):

$$m\lambda = 2d_{111} \left(\frac{n_{\text{eff}} - \frac{\sin^2 \theta}{n_{\text{eff}}}}{\sqrt{1 - \frac{\sin^2 \theta}{n_{\text{eff}}^2}}} \right) = 2d_{111} \left(\frac{n_{\text{eff}}^2 - \sin^2 \theta}{\sqrt{n_{\text{eff}}^2 - \sin^2 \theta}} \right) \quad (2.16)$$

Finally, the Bragg-Snell equation is obtained:

$$m\lambda = 2d_{111} \sqrt{n_{\text{eff}}^2 - \sin^2 \theta} \quad (2.17)$$

These equations explain both the blue shift when observing CCs at increasing angles θ , as well as the red shift when a solvent enters the porous structure and replaces air.^{147,148} This responsive behavior will become important in section 2.4, where sensing applications of responsive photonic materials is discussed. Many other applications also exist for photonic colloidal crystals, such as waveguides with acute angles^{149,150} or dispersion

engineering, where materials are designed that exhibit properties such as negative refraction or self-collimation.^{151,152}

As the name suggests, these synthetic opals were predated by naturally occurring opals. These gemstones consist of monodisperse silica particles in a periodic superstructure and therefore exhibit the same interference phenomena and structural coloration. In fact, examples of all types of PCs can be found in nature. This includes multilayer, 1D-PCs in nacre^{153,154}, 2D-PCs in the tail feathers of male peacocks,¹⁵⁵ as well as the mentioned natural opals.¹⁵⁶ Images showing the iridescence of these three examples are shown in Figure 2.12.

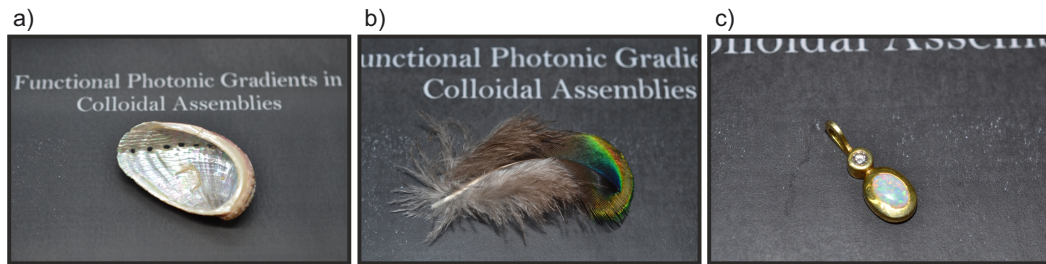


Figure 2.12.: Photonic crystals found in nature. a) 1D-PC in the form of Nacre. b) 2D-PCs in the tail feathers of male peacocks. c) 3D-PCs comprising monodisperse silica spheres. Copyright is my own.

The fact that these colors are angle-dependent suggests that a given wavelength is reflected at a certain angle of incidence but can pass through the structure at another. This would correspond to a gap in the band structure that is not continuous over the entire iBZ. The fcc structure indeed does not possess a so-called full photonic band gap (FPBG).^{126,157} The peaks observed in the reflectance spectrum of CCs are, therefore, usually called stop bands rather than band gaps. To achieve an actual FPBG, a more intricate design is necessary. Some improvement can be made when converting CCs into inverse opals via templating.¹⁵⁸ Other approaches that presented robust FPBGs were presented in the form of a diamond lattice¹⁵⁹ and the Yablonovite structure.¹⁶⁰ One of the aspects that promote the formation of an FPBG is a structure with a high degree of symmetry. The closer the BZ of a lattice resembles an isotropic sphere, the less angle dependency will be observed.¹³² Simulations of photonic, quasiperiodic systems, for example, exhibit smooth bands that facilitate band gap formation over the entire width of the band diagram.¹⁶¹ The next step in this reasoning would be to examine the potential photonic properties of fully amorphous (disordered) structures. Consequently, the optical properties of such materials will be the focus of the following section.

2.3 Optical Properties of Disordered Systems

Up to this point, the optical properties of homogeneous materials and heterogeneous ordered superstructures were examined. However, examples where this periodicity is not given also play a prominent role in nature and materials science. For example, particle suspensions, roughened glass surfaces, and aerogels mostly appear milky white or blueish due to light scattering.¹⁶² Contrary to what might be the intuitive impression, the disorder does not mean loss of control. Precise tailoring of specific parameters in an amorphous particle assembly allows the optimization of specific optical properties. The fundamental aspects of this type of light-matter interaction will be discussed here.

Single-particle scattering

Scattering of light, e.g., at a roughened interface, is not specular as it is for the reflection from a flat mirror. Light scattering instead causes a redistribution of electromagnetic waves in (at first) seemingly arbitrary directions. On a single particle level, this angular distribution depends on the respective particle diameter. Here, spheres are assumed to consist of an ideal dielectric (lossless) material without resonances (such as electronic transitions) in the examined frequency range. Only the real part of the refractive index must, therefore, be considered.^{163,164}

We will begin with particles with a diameter (d) much smaller than the wavelength of incident radiation. For example, the interaction of 20 nm particles with visible light. The charges in this particle will be affected by the oscillating electric field, and due to the small diameter, this field can be assumed to be homogeneous over the entire particle. This 'electrostatic approximation' entails the induction of a simple dipole in the particle. The dipole results from polarization via the acceleration of electrons away from the nuclei, which, in turn, causes emission of electromagnetic radiation. Since the dipole oscillates at the same frequency as the incoming wave, the emitted radiation matches the wavelength of the scattered light, and the process is elastic.^{165,166} This phenomenon is called Rayleigh scattering, and the scattering intensity (I_S) can be quantified with respect to the distance (R) from the particle and the scattering angle (θ):¹¹²

$$I_S = I_0 \left(\frac{\pi^4}{8R^2} \right) \left(\frac{(n_1/n_2)^2 - 1}{(n_1/n_2)^2 + 2} \right)^2 (1 - \cos^2 \theta) \left(\frac{1}{\lambda^4} \right) d^6 \quad (2.18)$$

The intensity profile of the emission caused by an oscillating dipole has the shape of a torus (Figure 2.13a), which for unpolarized light results in the $(1 - \cos^2 \theta)$ dependency.¹⁶⁷ The overall scattering intensity is affected by the ratio of the refractive indices of the

particles (n_1) and the medium (n_2), which explains why particles in air scatter light more efficiently than, e.g., in water. Furthermore, shorter wavelengths (e.g., blue light) are affected stronger than longer wavelengths (e.g., red light). This is one of the most notable characteristics, as Rayleigh scattering off molecules in the atmosphere gives the sky its blue and sunset its red color.¹⁶⁸ Finally, increasing the particle diameter also results in much more efficient scattering. A suspension of nanoparticles that previously appears transparent, can, therefore, suddenly turn opaque if aggregation occurs. This monotonous size dependence, however, is only valid up to a certain point.

When the particle diameter reaches the range of the wavelength, the Rayleigh theory is at its limit and cannot describe the light-matter interaction anymore.¹⁶⁹ At this point, the system must be explained by solving Maxwell's equations, which was done analytically for spheres by Gustav Mie in 1908.¹⁷⁰ The aptly named phenomenon 'Mie scattering' of spheres is generally characterized by an enhanced contribution of forward scattering and a more complex angle dependence (Figure 2.13b). Especially when the diameter becomes larger than the wavelength, excitation of more complex modes results in side lobes¹⁷¹ (Figure 2.13c).

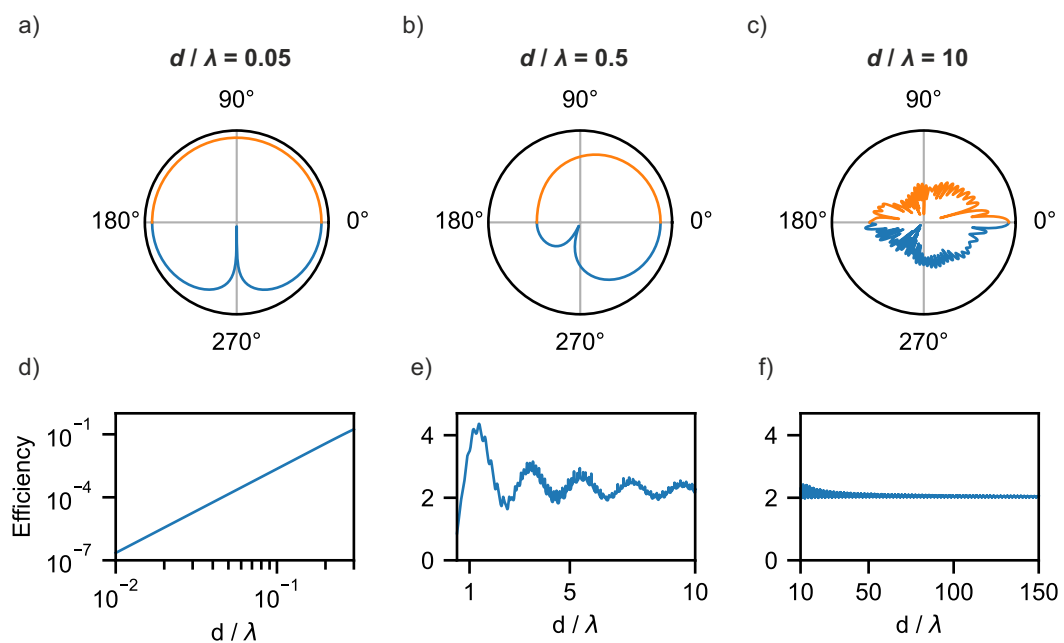


Figure 2.13.: a)-c) Scattering profiles in different size ranges calculated with the miepython package for python3.^{172,173} Light enters from the left of the graphs and 0° corresponds to forward scattering. The data is normalized and plotted on a logarithmic scale to highlight details in the angle dependence. Blue profiles correspond to light polarized parallel to the plane of the graph, and orange profiles to perpendicular polarization. a) Rayleigh scattering regime where $d \ll \lambda$. b) Mie scattering where $d \approx \lambda$. c) Mie scattering where $d > \lambda$. In subfigures d)-f) the scattering efficiency normalized with respect to the particle cross section is shown. d) Rayleigh regime. e) Mie regime. f) Geometric optics regime.

When the particle size becomes even larger and surpasses the wavelength by magnitudes, the interactions can be described via ray optics as multiple events of reflection and refraction. This is sometimes also called 'geometric optics'.¹⁷⁴

The three regimes exhibit pronounced differences regarding the particle size dependence of the scattering efficiency. Rayleigh scattering efficiency, for example, increases monotonously with an increasing particle diameter (Figure 2.13d). This coincides with the implications of equation 2.18. Mie scattering, on the other hand, shows discrete maxima and minima of the scattering efficiency at specific diameters (Figure 2.13e). The fine structure (ripple) is caused by additional, more complex resonances.¹⁷⁵ As the size increases further, the primary oscillations become smaller, and the scattering efficiency converges. In this regime of geometric optics, the scattering efficiency remains constant (Figure 2.13f).

The analytical approach of the Mie theory, applied for the simulations of the profiles in Figure 2.13, is only valid for spherical particles. More complex systems require numerical solutions but can provide more elaborate control of the scattering properties.

Efficient scattering in particulate thin-films

The previous theoretical concepts were on a single-particle level and assumed an isotropic geometry. However, in real systems, both the single-particle properties (refractive index, size, and shape) as well as the characteristics of the ensemble (alignment, filling fraction, and distribution) play an important role. This provides many further possibilities for influencing the optical properties of materials. An important example is the fabrication of thin films exhibiting a pronounced white appearance due to multiple scattering events.¹⁷⁶ In many applications, ranging from paint to coatings in photovoltaics,¹⁷⁷ particles with a high refractive index are applied. These mainly comprise titania colloids that are efficient scatterers but entail both environmentally problematic fabrication and health hazards.^{178,179} Using naturally occurring low refractive index materials requires a different approach: precise engineering of the particle morphology and superstructure.

Inspiration can be found in nature, most famously in the scales of the white beetle (*Cyphochilus*) that are strikingly white, while only about 5 μm thick.^{180,181} The scales consist of a heterogeneous network of air and chitin, a biopolymer with a low refractive index of 1.56.¹⁸¹ The efficient scattering is attributed to an anisotropic structure, dimensions in the range of visible wavelengths, and an optimized filling fraction of about 45%.¹⁸² Thereby, efficient scattering and a high reflectance are possible even with a thin film, minimizing the weight the insect must carry but providing good heat management even under direct sunlight.¹⁸³ Many biomimetic structures have been presented

that make use of these insights. These often apply biologically derived cellulose in all its variations, ranging from cellulose nanocrystals¹⁸⁴ to delignified wood.¹⁸⁵ It was shown that a porous structure, with scattering centers mainly in the sub-micron range¹⁸⁶ and anisotropic particles oriented perpendicular to the light beam,¹⁸⁷ show the best scattering properties. The effect of anisotropy was examined more directly by comparing spherical and rod-shaped silica particles.¹⁸⁸ The results corroborated numerical predictions,¹⁸⁹ showing more efficient scattering by the anisotropic rods. Furthermore, these could be assembled as supraparticles that showed potential for use as white pigments and might replace titania particles in paint.

Similar to how the *Cyphochilus* beetle evolved to have good thermal management, artificial thin films can provide a solution to excessive energy use caused by space cooling in urban areas. Strong scattering of visible light can result in pronounced back reflection of sunlight, which minimizes absorption of photons and unwanted heating. In combination with a high emissivity in the infrared range, the temperature of an object can be lowered via passive radiative cooling. This is especially efficient if the emissivity is high between 8-15 μm where the atmosphere is transparent. The object that is to be cooled can thereby release energy into outer space.¹⁹⁰ Such coatings have even been developed with an environmentally benign cellulose derivative, which could make large-scale coatings on houses more applicable.¹⁹¹ Large cities in particular could profit from this approach.

The scattering properties of such heterogeneous materials are characterized mainly by two parameters: 1) The transport mean free path, which is the length beyond which light propagation is randomized, and is the key characteristic of diffusive transport.^{188,192} It can be measured by diffuse transmittance measurements of several samples thick enough to exclude ballistic light transport.¹⁸⁴ 2) Optical haze, the fraction of transmitted light that changes direction upon passing through the sample, and is an important property for diffusers in optoelectronic devices.^{193,194} Both properties can be tailored with an optimized polydispersity. Cellulose nanofibrils exhibiting an asymmetric distribution of diameters were assembled via filtration.¹⁹⁵ The lack of uniformity in the sample provided anomalous diffusion, which could further improve the scattering properties. In a related approach, binary mixtures of large and small spherical polymer particles were applied to adjust the optical haze of monolayers.¹⁹⁶ This is influenced by the degree of short-range and long-range order that results from the self-assembly process, as well as Mie-scattering of the individual components.¹⁹⁷ The complimentary system to this bidisperse case would be monodisperse particles assembled in an amorphous structure without long-range periodicity. As this class of materials also has unique and interesting optical properties, it will be discussed in the next section.

Photonic glasses

The optical appearance of the previously discussed, disordered systems was mainly white (due to multiple scattering) or blueish (caused by Rayleigh scattering and the λ^{-4} dependence). Other colors in the visible range were only shown for periodic photonic crystals. However, structural coloration is possible even in disordered systems if some uniformity is ensured.¹⁹⁸ If a structure is made up of monodisperse spheres and crystallization is successfully avoided by one of the approaches shown at the end of section 2.1, the system can exhibit a discrete color other than blue. As a counterpart to photonic crystals, these materials were defined by García et al. as 'photonic glasses' (PGs).^{92,199}

While the optical properties of periodic systems are subject to ballistic light transport (Figure 2.14a), propagation through photonic glasses proceeds in a randomized manner. The process can therefore be described as dispersive light diffusion.^{200,201} The structural coloration (Figure 2.14b) is attributed to several different effects. Particles in the size range of the incident wavelength exhibit Mie-resonances, i.e., maxima of the scattering cross section, at specific ratios of size and wavelength.¹⁷⁶ These were already observed in the single particle calculations in Figure 2.13b. When the separate spheres are brought into contact, near-field effects influence these Mie-modes.^{202,203} Evanescent wave-coupling leads to a depletion of the density of states which prohibits certain frequencies in the structure.²⁰⁴ Furthermore, even though no long-range periodicity is present, a certain short-range order persists. This entails a characteristic separation length of the individual scatterers. Scattered waves can, therefore, experience phase correlation. Constructive interference of specific wavelengths and structural coloration is the result of this coherent scattering process.²⁰⁰

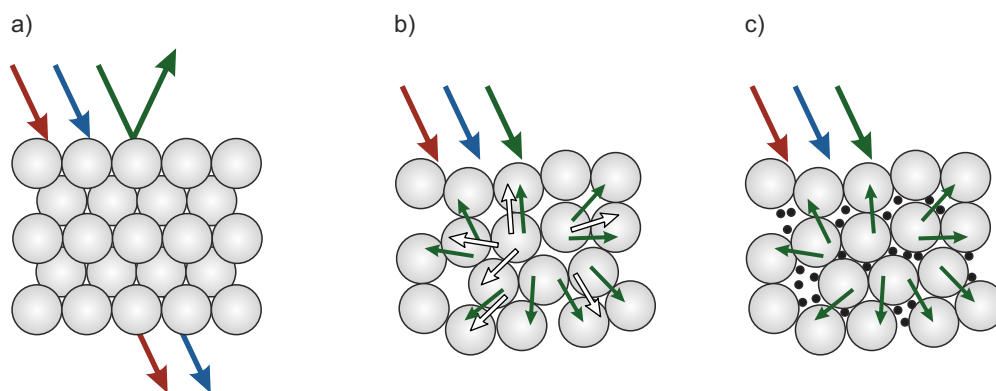


Figure 2.14.: Interaction of visible light with photonic crystals and glasses as shown in Ref [200]. a) Specular reflection of a specific wavelength from a photonic crystal. b) Coherent scattering in a photonic glass, masked by diffuse scattering of all wavelengths. c) Saturation improvement in a photonic glass via the addition of a broadband absorber.

The structural colors of PGs are often masked by random scattering. Especially pronounced in thick films,²⁰⁵ this causes an overall white appearance. To counteract this, a broadband absorber can be added to the assembly. At the correct amount, this increases the ratio of the reflection of the peak and the baseline, thereby enhancing the contrast.²⁰⁰ This can be observed, for example, in the structural colors of some birds, where melanin is incorporated into the structural motifs and acts as the broadband absorber.^{206,207} In contrast, albino specimens that do not produce melanin do not show any perceivable colors, even though their feathers exhibit the same nanostructure.²⁰⁰ In synthetic PGs, the contrast can be improved in several ways. For example, physical vapor deposition of carbon on the surface of an already assembled colloidal glass can increase the saturation post-fabrication.²⁰⁸ This effect can also be achieved by modifying particles with a layer of polydopamine, thereby directly mimicking the natural melanin equivalent,²⁰⁹ or by co-deposition of microparticles with smaller, absorbing particles.²¹⁰ Another way to improve the color purity is by changing the particle morphology. Hollow sphere structures have been shown to influence Mie-scattering and provide pronounced structural coloration.³⁶

An obvious application of these photonic glasses is the coloration of surfaces. In this, they possess significant advantages. In contrast to photonic crystals, the structural colors are non-iridescent. In most applications, this angle independence of the color is preferred.²¹¹ Furthermore, colloidal glasses can be fabricated on a large scale and are less prone to defects, in contrast to their crystalline counterpart.²¹² If assembled in confinement, PGs can even be fabricated as supraparticles and thereby directly applied as photonic pigments.¹⁰¹ Compared to classic, absorption-based pigments, PGs have the advantage that the color does not fade over time, and the materials themselves are non-toxic and environmentally benign dielectrics such as polystyrene or silica. Due to the lack of absorption, PGs can also be applied in photovoltaic coatings, making solar cells colorful and, thereby, more visually appealing to improve the acceptance of their installation.¹⁰⁸ Beside the coloration approach, these structures can also provide broadband reflectance, enabling their use as spectral filters,²¹³ reflective coatings (e.g., for radiative cooling)²¹⁴ or thermal barrier coatings.²¹² The latter requires reflectivity in the mid-IR range. In contrast to light absorption by pigments, photonic properties can easily be tuned by changing the characteristic length scale. In the case of colloidal glasses, this simply means applying micrometer-sized rather than sub-micron particles.

Photonic systems, in general, have another large area of applications. Due to their often responsive optical properties, PCs and PGs can be used as suitable sensing materials. The state of the art of this research field will be discussed in the next section.

2.4 Responsive Photonic Materials as Sensors

Up to this point, the photonic properties of ordered and disordered media have been considered constant. Besides the blue shift of the stop band position caused by a change of the angle between the light source, sample, and observer, no dynamic variation of the color has been discussed. Photonic materials, PCs, in particular, do, however, provide some distinct responsive properties. Due to their visible structural colors and the possibility for these to change by means of an external trigger, numerous types of photonic sensors have been developed.²¹⁵ Materials such as 1D-PCs,²¹⁶ microphase separated block copolymers,²¹⁷ CCs,²¹⁸ inverse opals, and hydrogel immobilized CCs²¹⁹ belong to the most important examples. These can rely on various mechanisms, mainly affecting one of the parameters in equation 2.17. A simple example is a periodic multilayer structure with one component capable of swelling in a specific medium. When the corresponding solvent is present, this can dramatically change the stacking constant and, thereby, the color. Further possibilities are infiltration of CCs and change of the effective refractive index, mechanical change of the periodicity, defect-induced loss of order, and dry-sintering of particles (Figure 2.15).²²⁰ This can be made use of in the form of sensors that respond to either chemical or physical triggers. Further complexity and, therefore, functionality can then be provided in the form of a readout with advanced computational techniques and by preparing arrays of photonic sensors that allow combinatorial data analysis.

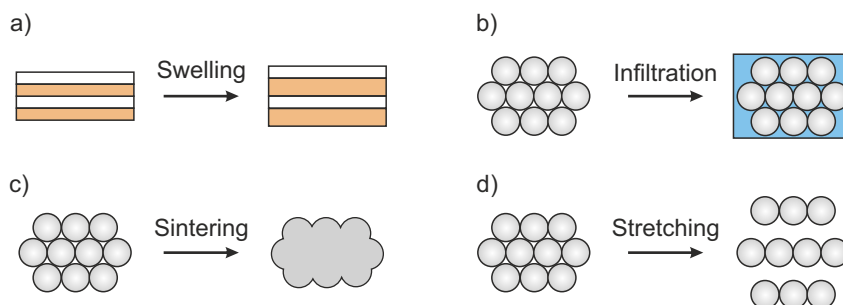


Figure 2.15.: Mechanisms underlying the responsive properties and change in coloration of photonic crystals when affected by an external trigger.

Sensing of chemical triggers

One of the most basic yet also equally important environmental parameters that must be tracked in various applications is relative humidity (RH). Photonic sensors that provide autonomous sensing of this parameter mostly rely on water condensation on the inner interfaces of an open porous network. This changes the effective refractive index and causes a perceivable and measurable red shift of the structural color. Refractive index

matching of the solid structure and water in the interstitial gaps would also reduce the saturation and, thereby, the visibility of colors. Therefore, a high refractive index material such as titania is often applied. When prepared as a porous PC, this was shown to provide a sensitive response to a change in the RH.²²¹ Naturally, this is affected by a slight hysteresis which is apparent when comparing rising and sinking RH. Disordered colloidal glasses have also been shown to provide similar sensing capability, with a swift response due to the nanoporous nature.²²² A similar approach can allow sensing of organic solvents that induce swelling²²³ or penetrate a porous structure. The latter was also improved by dynamic analysis of the infiltration process, which increased the available information.²²⁴

Another basic necessity in aqueous systems is colorimetric sensing of the pH value. This can be achieved in photonic multilayers by protonation of, e.g., pyridine groups, which induces conformational changes in polymer chains and influences the periodicity.²²⁵ A similar effect can be observed in photonic hydrogels that reversibly swell when the pH value increases.²²⁶ Inorganic ions can be sensed in a similar manner. Both cations²²⁷ and anions²²⁸ have been tracked this way. Finally, biological functionalization has been used to allow the detection of more complex analytes, such as specific microbes.²²⁹

Sensing of physical triggers

A very intuitive type of physical sensing is the response to mechanical deformation. Just as chameleons actively change color by varying the spacing of photonic crystals in their skin,²³⁰ this response can be utilized for mechanochromic sensing. This means that photonic sensors can change color either upon compression²³¹ or stretching.²³² A different type of force, in the form of a response to a magnetic field, can also change the color of periodic assemblies of, e.g., iron oxide particles.²³³

The most important type of sensing application for this thesis is the recording of thermal events. Polymeric PCs are an ideal system for this case, as the thermal properties of polymers (e.g., glass transition temperature) can chemically be tuned over a broad temperature range. Autonomous temperature tracking is essential for transporting medical products to remote areas and detecting food spoilage. Several different types of sensors exist and will be defined here. In the most strict sense, a temperature sensor is a material that changes its color fully reversibly. For a given photonic system, this means that a change in the periodicity only persists while the temperature remains elevated. Afterward, it returns to its original state. While this is advantageous in direct temperature monitoring, other applications require irreversible recording of the thermal history. Two types exist: 1) Indicators that spontaneously switch states when a specific temperature is reached. 2) Integrators that gradually change their periodicity and color.

The latter provides information regarding both temperature as well as the duration of the heating event, which is an important pair of parameters (Figure 2.16).²³⁴ A polymer often used in thermoresponsive systems is poly(N-isopropyl acrylamide), which, when heated in water above a critical temperature, collapses. In 1D-PCs, this changes the periodicity and results in a blue-shift,²³⁵ and in doped CCs, it causes defects and loss of structural color.²³⁶ Both are fully reversible. There also exist intermediate examples, where up to a specific temperature, a reversible process occurs (e.g., water evaporation); beyond this, the structure irreversibly changes.²³⁷

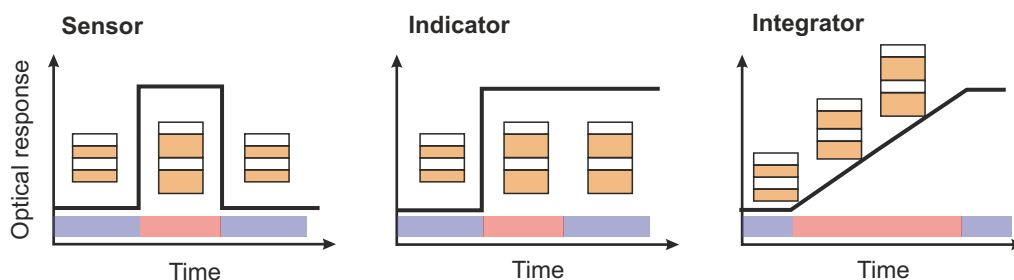


Figure 2.16.: The three different response types in photonic thermal tracking devices as shown in Ref [234]. The plots schematically show the sensor's response during the indicated low (blue) and high (red) temperature events.

More often, pure time-temperature integrators are prepared. Good examples are changes in the photonic properties of liquid crystals,²³⁸ and the deformation of polymeric inverse opals. An example presented by Lee et al.²³⁹ was an important inspiration for some projects in this thesis. In-situ UV-Vis spectroscopy of inverse opals with different glass transition temperatures provided time-dependent characterization of the irreversible blue shift of the stop band. A semi-analytical approach was applied that took into account the creep deformation kinetics in polymers and temperature time equivalence as per the Williams-Landel-Ferry theory.²⁴⁰ The method thereby allowed independent determination of time and temperature.

Advanced data acquisition and handling

A rapid increase in computational power has brought new and advanced ways of managing and interpreting data. Machine learning, in particular, can derive information from, e.g., images without necessarily requiring guidance or further information regarding the underlying system. In this manner, machine learning can enable the readout of sensors, independent of whether a physical model exists to describe the process.²⁴¹ This allows using non-conventional characterization methods, most prominently digital cameras. For example, a smartphone camera has been used to measure the switchable luminescence in metal-organic frameworks. Sensing both water content and the temperature was,

thereby, possible.²⁴² A similar approach using lanthanide complexes as sensors for physiological temperatures has also been shown.^{243,244} Deep learning algorithms have been applied for analyzing excitation spectra of carbon dots in different environments, which made a prediction of the ethanol content possible.²⁴⁵ The same material was also used for biomolecular sensing. A machine learning model could correlate different absorbed proteins to the sensors' fluorescent response.²⁴⁶ Temperature monitoring via such a model has also been realized.²⁴⁷ For example, the luminescence signal of quantum dots provided temperature sensing in microfluidic channels with a high thermal resolution.²⁴⁸ Such thermometry methods could be further improved with specific arrangements of the sensing materials, i.e., in the form of QR-codes.²⁴⁹

Patterning of photonic colloidal crystals and inverse opals is a long-standing research field. Specifically, local tuning of the wettability by surface functionalization (e.g., with hydrophobic silanes) can lead to selective infiltration, which depends on the pore geometry and contact angle.²⁵⁰ This can be made use of in sensor arrays or anti-counterfeiting applications.²⁵¹ For example, a 4×4 array of mesoporous supraparticles, with different local wetting properties, has been used to realize an 'optical nose'.²⁵² Combinatorial evaluation of a set of colors was shown to be distinct for several different organic solvent vapors. In a similar geometry, a combination of photonic properties and concomitant fluorescence enhancement enabled high-performance sensing of metal ions.²⁵³

A less random and often more effective way of providing spatial selectivity in sensors is in the form of a gradient. For example, biomimetic polarity gradients in photonic sensors have been used for multivariable vapor sensing.²⁵⁴ Additionally, a sensor based on a macroscopic stepwise gradient of the infiltration properties allowed facile readout in an ethanol sensor.²⁵⁵ In general, gradients in functional (photonic) materials are an emerging topic. These can provide a range of properties that include but are not limited to sensing applications. The next section will, therefore, provide a state of the art of research on such materials.

2.5 Gradients in Functional Materials

Besides the use in sensors with a local readout, gradients of physical properties along a specific axis are an important aspect of materials science and biological systems. For example, marine mussels attach to rocks with byssi that exhibit a gradient of the elastic modulus. This significantly enhances the strength of attachment and has inspired researchers to implement such gradients in synthetic materials.²⁵⁶

Structural and chemical gradients

Gradients of the mechanical properties can also be relevant in medical aspects, such as interfaces between tendons and bones. Here, CC-templates have been used to prepare polymeric inverse opals with a gradually increasing inorganic filler content, realized via sedimentation (Figure 2.17a).²⁵⁷ Gradients of the pore size, on the other hand, have been prepared in self-assembled materials with subsequent carbonization (Figure 2.17b).²⁵⁸ Such structures were shown to be efficient anodes in electrochemical setups, as the gradient optimizes gas transport through the substrate.²⁵⁹

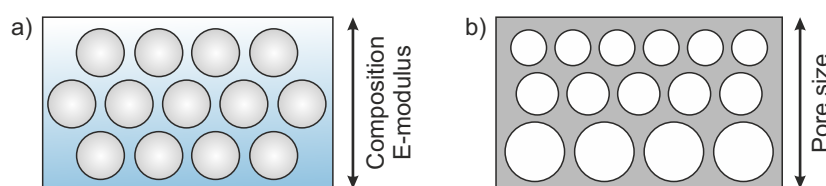


Figure 2.17.: a) Mechanical gradient in an inverse opal. b) Pore size gradient.

An approach that provided significant inspiration to two projects in this thesis was shown for the fabrication of polarity gradients on solid surfaces.²⁶⁰ Here, a dual syringe pump method (Infusion-withdrawal coating) generated gradient interfaces either by adjusting sol-gel chemistry,²⁶¹ or surface functionalization.²⁶² This can, for example, result in self-propelling water droplets along the gradient.²⁶³

Optical properties of gradients

Several examples of photonic crystals with a lateral gradient of optical properties exist. For example, vertical deposition was shown to create thickness gradients when the concentration of the coating suspension gradually increased during the assembly.²⁶⁴ Similarly, the periodicity and the thickness of 1D-PCs could be tuned by preparing films with repetitive vertical deposition by applying a continuous acceleration of the coating speed.²⁶⁵ A different way of preparing such lateral gradients of the structural color is by

taking advantage of a substrate with gradient elasticity. This resulted in responsive PCs that exhibited gradient colors upon stretching.²⁶⁶ In another approach, gradient metallic wrinkles with optical interference were prepared via stretching and relaxation.²⁶⁷

Interesting optical effects can be obtained when examining vertical rather than lateral gradients. Gradients of the porosity, normal to the surface of thin films, can affect the reflectivity. This can be tuned in both extremes, one being anti-reflective coatings prepared via a gradual change of the effective refractive index.²⁶⁸ Gradient photonic crystals, specifically step-gradients comprising multiple heterostructures, have also been used to increase the reflectivity as high as possible over a broad spectral range. This has been accomplished by preparing stacked colloidal crystals with three²⁶⁹ and five²⁷⁰ different particle sizes on top of each other (Figure 2.18). The combination of several stop bands resulted in an effective broadening of the reflected wavelength range, similar to effects observed for multiple excitation peaks in multilayer quantum dot films.²⁷¹

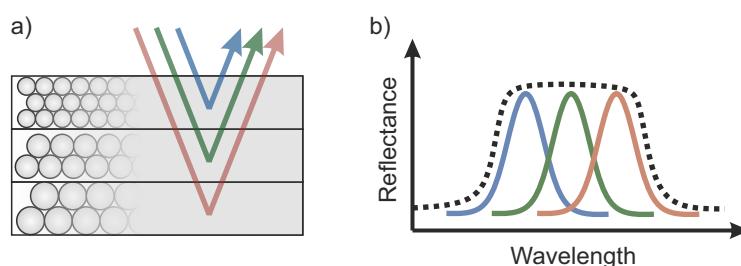


Figure 2.18.: a) Multilayer structure of several photonic colloidal crystals. b) Schematic of the overall reflectance (black) resulting from the combination of multiple photonic stop bands.

Interestingly, simulations have predicted that the reflectivity of colloidal films is highest when a continuous size gradient exists perpendicular to the surface.²⁷² While this is considered advantageous for solar reflection in passive cooling applications, a fully continuous and controlled gradient has not yet been developed in this size range. More complex gradients in structures such as the woodpile lattice have been presented, but these were on a millimeter scale and exhibited band gaps in the microwave range.²⁷³

Other, more peculiar, optical properties in gradient materials will also be discussed. Angular selectivity has, for example, been achieved by taking advantage of the angle-dependent band structure in 1D-PCs. By engineering a gradient of the stacking periodicity, radiation in a broad spectral range was selectively reflected at a specific angle.²⁷⁴ Alternatively, 3D-graded PCs have been predicted to provide tailored guiding of light, e.g., for wavelength demultiplexing.²⁷⁵ Integration of such graded materials into devices has been achieved in the form of chirped photonic crystal fibers. These were prepared by fiber drawing from pre-assembled glass tubes.²⁷⁶ Gradient index optics have been applied in lenses that can concentrate sunlight from all angles onto photovoltaic devices. This eliminates the need for tracking the position of the sun.²⁷⁷

Combinatorial materials science

Besides providing novel structural and optical properties, multicomponent gradients can be of interest in screening applications. Materials scientists in various fields have increased the complexity of their respective systems by incorporating many different elements and compounds into, e.g., alloys and composites. While this can allow precise tailoring of the materials' properties, it significantly increases the effort of the screening process. Since computational power and automated characterization techniques have evolved tremendously in the past decades, the bottleneck here is sample preparation. Composition gradients, comprising all possible combinations of a binary system, can expedite this process. Provided local measurements are possible, entire libraries can be obtained from a few samples when measuring along the gradient. This has been done extensively for systems that can be prepared via physical deposition techniques.²⁷⁸ Few examples exist in the field of colloidal assembly, with the most relevant being lateral gradients in plasmonic arrays.²⁷⁹ This can give insight into the size and shape-dependent sensing efficiency of gold nanoparticles without the need for a time-consuming iterative process.²⁸⁰

Fabrication of colloidal gradients

The most important aspect of this thesis, and the common theme of all projects, is the fabrication of gradients in photonic colloidal assemblies. This topic has continuously increased in significance over the past decade. Nevertheless, only a few different types of fabrication methods have been presented so far. Some top-down techniques for particle or pore size gradients exist, such as electrochemical etching of silicon²⁸¹ or plasma etching of polymer colloidal crystals.²⁸² These are, however, difficult to control, and the fabrication of tailored gradient profiles (linear, convex, concave) is not possible in this manner. A bottom-up approach to a particle size gradient was shown to be mediated by microfluidic particle synthesis.²⁸³ However, this resulted in particles in the range of several tens of microns and was not targeted to noticeably interact with visible light.

A method for preparing composition gradients from nano- and microparticle suspensions is ultracentrifugation. This can either result in a concentration gradient of one particle type in a gel,²⁸⁴ or a composition gradient in a binary system.²⁸⁵ Bidisperse suspensions show segregation also upon drying,²⁸⁶ but control over the spatial distribution of the two particle types is only possible via adjustment of the gravitational field. Strong separation conditions resulted in a bilayer structure with large close-packed particles at the bottom and smaller particles on top. On the other hand, weak separation can result in a mixed, disordered state with a continuously increasing amount of large particles towards the

bottom of the sample (Figure 2.19a).²⁸⁷ Due to the three-dimensional geometry of the centrifuged pellets, these were not explicitly characterized regarding the optical properties. It was, however, shown that functionally graded carbon monoliths could be prepared,²⁸⁸ and that these could be adjusted even further with chemical gradients.²⁸⁹

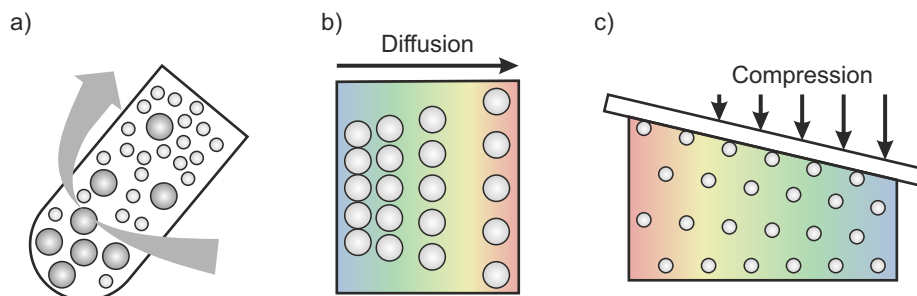


Figure 2.19.: Fabrication methods for colloidal gradients. a) (Ultra-)centrifugation of a bidisperse suspension. b) Concentration gradient induced by diffusion. c) Compression of a hydrogel immobilized colloidal crystal with spatial force variation.

Besides size and composition gradients, the possibility of a gradual change in the interparticle distance exists. This, naturally, requires particles that are not close-packed and in an aqueous suspension or immobilized in a hydrogel. Diffusion of colloids in a concentration gradient was shown to provide such a material.²⁹⁰ Due to the repulsive electrostatic interactions between particles, crystalline arrays are formed spontaneously with a lattice constant that is dependent on the particle concentration. Diffusion results in a concentration gradient, which can be observed as a gradual change of the structural color (Figure 2.19b).²⁹¹ Another possible approach is the deformation of pre-assembled colloidal crystals.²⁹² This can be achieved by exposing superparamagnetic particles to a non-homogeneous magnetic field. The periodicity of the photonic crystal depends on the magnetic field strength, which results in a positional dependence of the reflected wavelength. Lastly, such a graded PC can be prepared by an applied compression gradient (Figure 2.19c). Particles that were previously non-close packed with a maximum separation were brought closer together.²⁹³ Structural colors covering the entire visible spectrum were obtained, which enabled the use as a diffraction grating in a miniaturized spectrometer.²⁹⁴

From these examples, it becomes apparent that two types of colloidal gradients are missing: 1) composition gradients in binary colloidal assemblies in a thin-film geometry that allows optical characterization, such as transmission UV-Vis spectroscopy. 2) A continuous gradient of the particle size, prepared via bottom-up assembly with control regarding the gradient profile. The realization of these two types of colloidal assemblies and the characterization of the respective optical properties are at the heart of the projects presented in this thesis.

3.1 Synthesis and Assembly Techniques

This section presents the conventional fabrication methods used in this work, as well as the novel variations that I developed. Particle synthesis procedures, post-synthesis staining, and various self-assembly techniques will be discussed.

Particle synthesis and modification

All projects in this thesis included the self-assembly of polymer microparticles, specifically: poly(methyl methacrylate) and random copolymers of n-butyl acrylate and methyl methacrylate. The latter was applied when the glass transition temperature needed to be adjusted. Surfactant-free emulsion polymerization (SFEP) of the copolymer is conducted analogously to the homopolymer particles. A representative synthesis of monodisperse particles proceeds with 10-20 mL monomer and 240 mL water (MilliQ quality), stirred in a three-necked flask and heated to 80 °C under a stream of nitrogen. After equilibration for 60 min, 10 mg of sodium styrene sulfonate (ionic comonomer) is dissolved in 5 mL water and added to the mixture. After 5 min, 100 mg potassium persulfate (initiator), also dissolved in 5 mL water, is quickly added as well. The reaction is left to run overnight, terminated with ambient oxygen, and filtered to remove the coagulated polymer. The final particle size can easily be varied by changing the monomer volume.

I developed a variation to SFEP (Figure 3.1a), which provides a continuous size gradient of monodisperse particles: controlled extraction emulsion procedure (CrEEP). Seed particles are prepared analogously to standard SFEP and left to react for 30 min. After the seed synthesis, a second part of the procedure begins. A silicon tube with a length of 2 m and an inner diameter of 2 mm is inserted into the flask and dipped into the reaction mixture. The tube is attached to a syringe, and both had previously been filled with water. The pump slowly pulls a volume of 5 mL suspension into the tube over the course of 60 min. A second syringe, filled with air and attached to a perfusor tube, is set into another syringe pump. A cannula with a bent tip is attached to the perfusor and inserted into the opening of the silicone tube. Periodic pumping of 16 μ L air, every 30 s induces evenly spaced air bubbles as separators into the tube. Simultaneously to the

extraction, a third syringe slowly adds further monomer to the reaction vessel. Due to excess initiator in the solution, the reaction proceeds further, and particles slowly grow under monomer starved conditions during the 60 min the reaction is left to proceed. Finally, more than 100 evenly spaced fractions are stored in the tube. While every fraction itself is monodisperse, the particle size gradually increases along the length of the tube. Assembly of these particles via filtration is shown later.

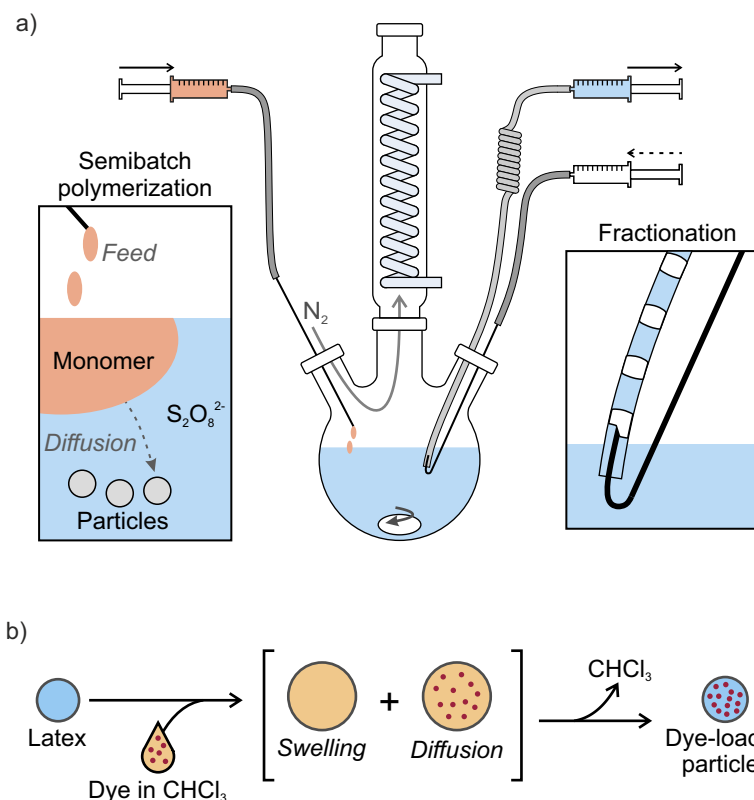


Figure 3.1.: a) Continuous extraction emulsion process for size gradients of monodisperse polymer particles. b) Post-synthesis fluorescent staining of polymer particles. *Reproduced from [295] under terms of the Creative Commons license.*

For some experiments, it was necessary to include fluorescent tracer particles. Ideally, these should have the same diameter as the other particles so that the periodic structure can be formed without unnecessary defects. An ideal way of achieving this is by taking aliquots of the pristine particles and staining them (Figure 3.1b). I did this by dissolving hydrophobic fluorescent dyes in chloroform and adding the solution to a heavily stirred, aqueous particle suspension. The resulting emulsion is stirred with a closed lid for 24 h, during which the solvent and the dye diffuse into the apolar polymer, swelling the particles. Then, the suspensions are left to stir with an open lid for 72 h. During this time, the volatile solvent evaporates, leaving the dye dissolved in the polymer. The particles show fluorescence when illuminated with UV light but otherwise remain unchanged. Self-assembly into colloidal crystals proceeds just as it does for the pristine particles.

Self-assembly into colloidal crystals and glasses

After synthesizing monodisperse particles, the next step is their self-assembly into photonic colloidal ensembles. In my projects, vertical deposition was one of the most important fabrication techniques for colloidal crystals. For standard (i.e., non-gradient) samples, this could be achieved by simply dipping a plasma-cleaned glass substrate into a 1 wt% particle suspension and slowly pulling it out. This was done in a climate chamber at 20 °C and 75 % relative humidity, with vibration isolation, and an extraction speed of $0.25 \mu\text{m s}^{-1}$. This results in a colloidal crystal with a thickness of a few microns forming on both sides of the substrate.

I developed a variation of this approach, which provides a route to gradient colloidal assemblies (Figure 3.2a). Two particle suspensions are applied, and the resulting sample exhibits a lateral gradient of the composition of the two particle types. Gradient fabrication via infusion-withdrawal coating (IWC) was done analogously to dip-coating, except for the addition of two syringe pumps. The substrate is dipped into a suspension of one particle type (1.0 wt%), and two cannulas attached to syringes are inserted. One syringe pump extracts the suspension at 0.60 mL h^{-1} , the other infuses a suspension of a second particle type with 0.79 wt% at 0.76 mL h^{-1} . The difference between the infusion and withdrawal speed is adjusted to account for the evaporation of water. Thereby, both the water level, as well as the particle concentration remain constant as the substrate is pulled upwards. Another possible way to conduct IWC is without actively pulling the substrate out of the suspension. If the extraction proceeds faster than the infusion, the water level is slowly and gradually lowered. If the ratio of the two pumping rates is exactly two, this results in a linear gradient.

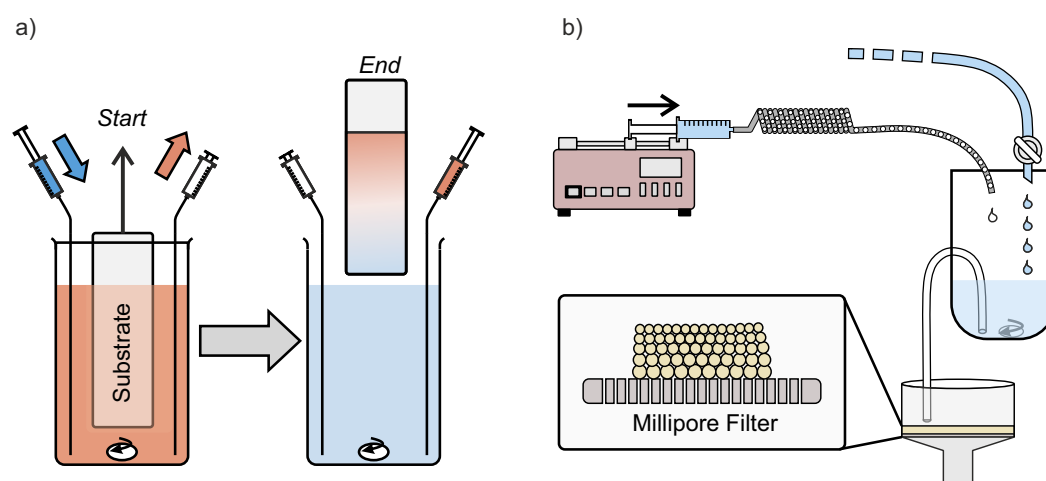


Figure 3.2.: a) Infusion-withdrawal coating setup for gradient colloidal assemblies. b) Semi-continuous filtration setup, utilizing the gradual size distribution obtained during CrEEP and fabricating a gradient colloidal glass. *Reproduced from [296] under terms of the Creative Commons license.*

A faster assembly method that was used both for rapid characterization of the particle quality, as well as for array printing of sensors is drop-casting. This is advantageous since it provides CCs in a matter of seconds, and the structural coloration (or lack thereof) directly indicates whether the suspension is monodisperse and which size the particles have. If done at room temperature, a pronounced coffee stain effect significantly impairs the optical appearance, rendering the structural colors almost invisible. I found that heating the substrate to 70-80 °C changes the dynamics of the assembly process, providing homogeneous colloidal crystals.

Finally, an assembly method using the gradient size distribution provided by the CrEEP had to be developed. I achieved this by employing a semi-continuous filtration setup (Figure 3.2b). The tube, filled with the fractions and connected to the same syringe, is inserted into an intermediate mixing container. The fractions are slowly pushed out of the tube at 0.4 mL h^{-1} . Simultaneously, water drips into the same container at a much greater rate of 60 mL h^{-1} to dilute the fractions. Due to a siphon-type mechanism, the container is periodically emptied into a vacuum filtration setup equipped with a hydrophilized polytetrafluoroethylene filter with a pore size of 200 nm. The timing is adjusted so that only one fraction is diluted at once, and the filtration assembly proceeds autonomously overnight. Between each emptying of the mixing container, the water passes through the filter completely, but the filter cake does not dry, leaving an aqueous paste. In the end, a colloidal glass with a thickness of approximately 100 μm is obtained, with a continuous particle size gradient from top to bottom.

3.2 Optical Characterization

The colloidal assemblies I prepared in my projects required specific optical characterization techniques. Analyzing gradients naturally necessitates local measurements that can be conducted while scanning across the sample. The two most important techniques will be discussed here.

Laser Scanning Confocal Microscopy

The most relevant imaging method in most projects presented in this thesis was laser scanning confocal microscopy (LSCM).²⁹⁷ The problem with conventional optical microscopy is that samples that are not flat, but exhibit an irregular topography or are tilted, cannot easily be measured. Parts of the surface will not be in the focus plane and, therefore, appear blurry. With LSCM, the use of two separate optical paths solves this problem (Figure 3.3a,b). The first path, color optics, is comparable to conventional microscopy. A white LED acts as a light source, and the beam is focused onto the sample with an objective. The reflected light is captured with the same objective and redirected to a CMOS image sensor which acquires the colored image.

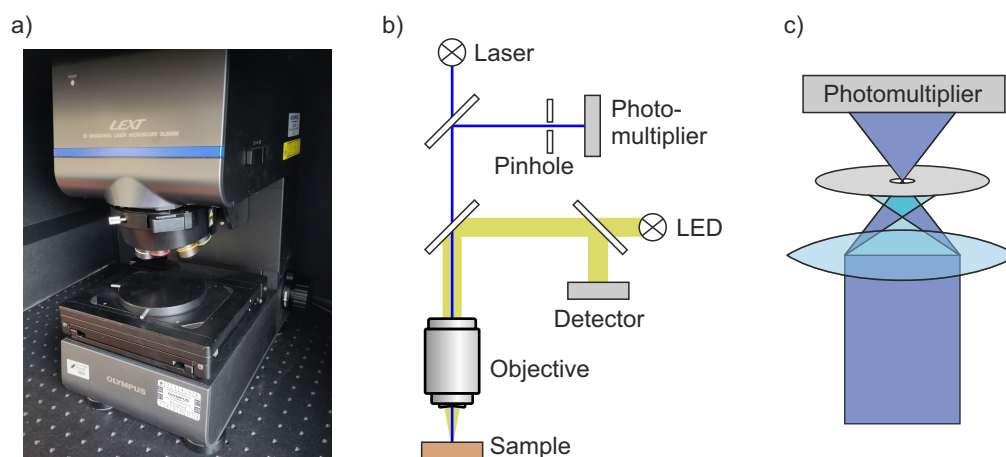


Figure 3.3.: a) Photograph of the microscope (Olympus LEXT OLS4000). b) Optical paths involved in the laser scanning microscopy setup. c) Function of the pinhole that reduces the depth of field in confocal microscopy.

Additionally, topographic information is obtained via a second optical path. The light source is a laser emitting light at 405 nm. This significantly improves the lateral resolution compared to light of longer wavelengths. A micro-electromechanical system scans the laser point across the sample, providing local information. Before a photomultiplier detects the reflected light, it passes through a pinhole (Figure 3.3c). This confocal technique eliminates blur and provides precise height information by ensuring a shallow

depth of field. In this specific setup, two detectors with pinholes of different diameters are built in, and the optical channel can dynamically be switched, depending on the lens type and acquisition method.

A standard workflow to characterize a sample with non-negligible topography is shown in Figure 3.4. Multiple images are obtained by shifting the focus plane (Figure 3.4a). Lateral scans with the laser optics are conducted, which results in a greyscale intensity image at each z-position. For a single pixel, the system estimates a light-intensity variation curve (Figure 3.4b). When this is done for all pixels, the combination of all peak positions corresponds to the height image (Figure 3.4c). Optical microscopy scans through the z-axis proceed at the same focal positions. Therefore, each pixel can be assigned the color of the image where this position is in focus. A color image is provided that is not impaired by individual regions being out of focus (compare Figures 3.4d and 3.4e).

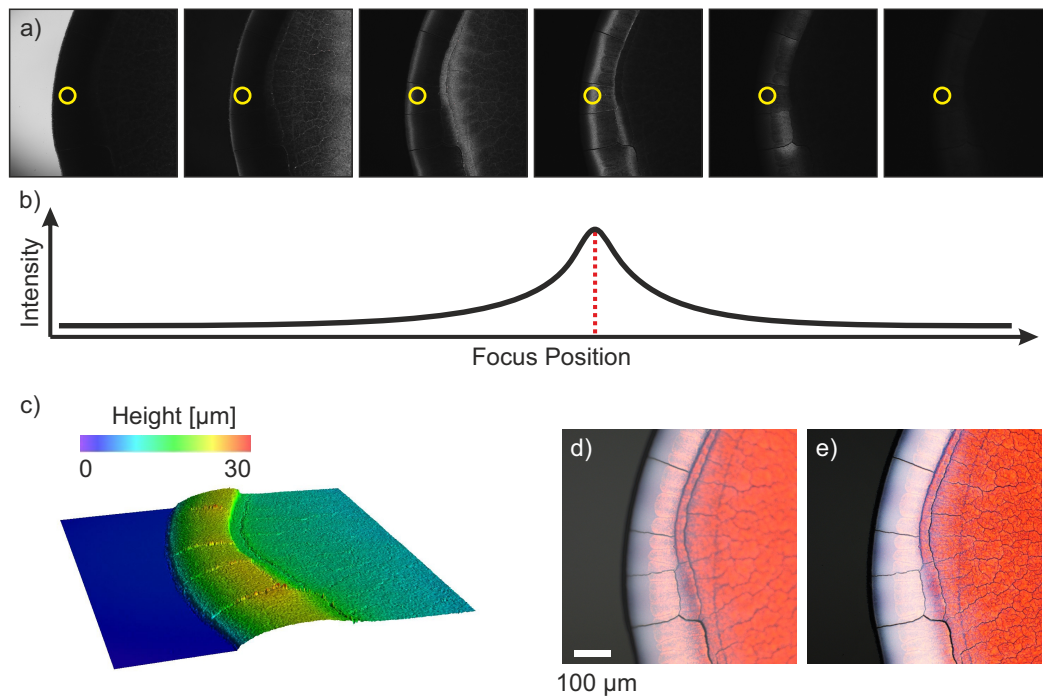


Figure 3.4.: a) Intensity images obtained at various focal positions. b) Light-intensity variation curve of the spot marked by the yellow circle. c) Height image. d) Standard optical image with parts out of focus. e) Extended optical image with all parts in focus.

Further advantages of LSCM are that it is fast, non-invasive, and does not require special sample preparation (especially compared to electron microscopy). Line scans and height determination analogous to profilometry are possible without the inherent drawbacks such as surface damaging or positioning difficulties. Mapping several images can further provide measurements over an area of several cm² with sub-micron height resolution.

Microspectroscopy

Complementary to the imaging method, a quantitative spectroscopic characterization was also necessary. Standard spectroscopic methods are, however, ordinarily not specialized for local measurements. Most spot sizes in such experiments are on the scale of several millimeters and would not allow a detailed characterization of gradients. I, therefore, applied an inverted optical microscope (Olympus IX71), which can direct light through a specific point on a sample and transport the transmitted light to a spectrometer (Figure 3.5a). A halogen lamp provides broadband illumination, and the condenser focuses the light onto the sample. The transmitted light is collected by the objective and can then either be directed to a camera for imaging or to an adapter for fiber optics via an adjustable mirror. The fiber optics cable transports light to the input port of a spectrometer (Ocean Optics USB4000).²⁹⁸ In this device, light is focused onto a diffraction grating, which splits it into its respective wavelengths. Then, light is directed onto a detector comprising an array of pixels, each of which detects photons in a finite wavelength range (approximately 1 nm resolution). The significant advantage provided by this device is that all wavelengths are measured at once. Spectra can be obtained in a matter of milliseconds, which allows in-situ experiments. This was important for two types of measurements: 1) Time-dependent determination of the optical response while samples were held at elevated temperatures with a heating stage exhibiting transmission capability (Instec HCS622HV). 2) Position-dependent measurements conducted by moving the sample normal to the light path with a motorized stage and simultaneously measuring several thousand spectra along the length of it.

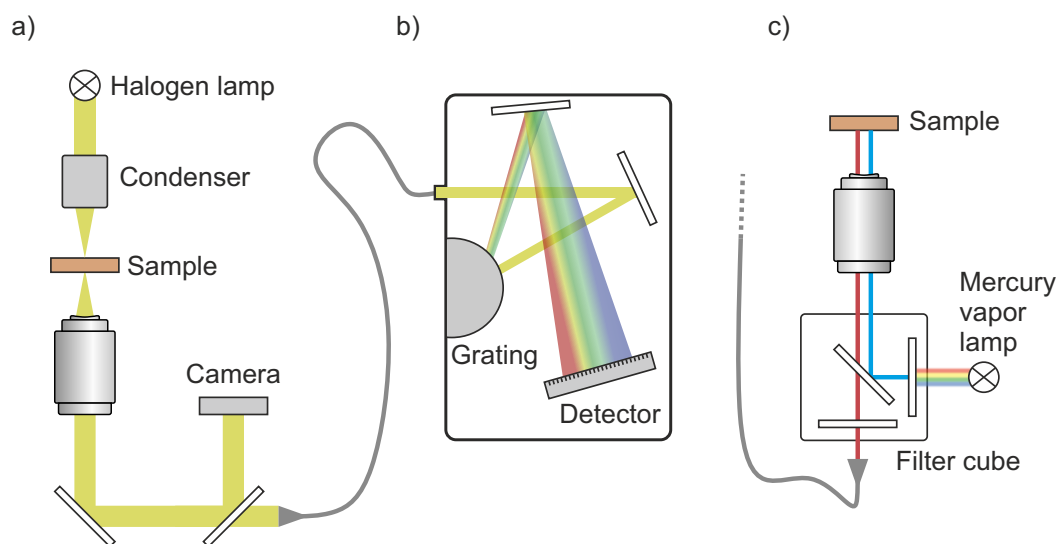


Figure 3.5.: a) UV-Vis microspectroscopy setup with mechanical mirror switching between camera and spectrometer. b) USB spectrometer coupled to the microscope via fiber optics. c) Fluorescence microscopy setup with a filter cube.

The microscope also provides fluorescence capability in reflection geometry with a mercury gas lamp positioned at a second port (Figure 3.5c). The light passes through several elements of a filter cube. An excitation filter lets a small wavelength band pass (e.g., 530-560 nm), which is directed to the sample via a dichroic mirror and the objective. The sample absorbs the photons and emits radiation of a longer wavelength. This fluorescence light passes through the objective and then an emission filter, which lets a different wavelength band pass (e.g., 570-640 nm). Fluorescence can also be used for imaging methods such as particle tracking and spectroscopy with the same fiber optics setup shown in Figure 3.5b.

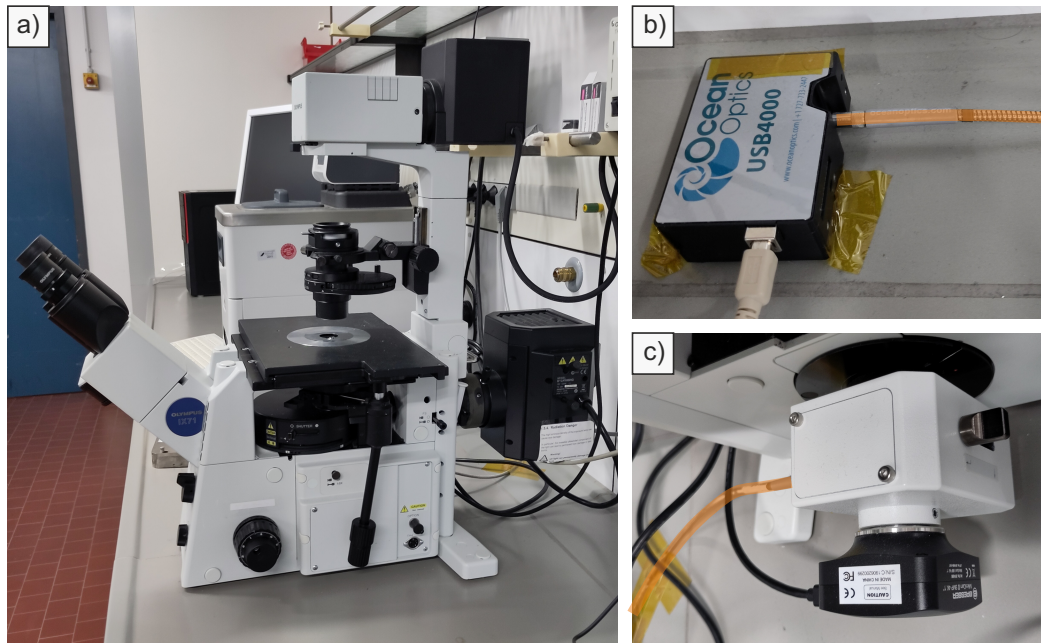


Figure 3.6.: a) The microscope used for microspectroscopy in all projects. b) Microspectrometer with the fiber optics cable highlighted in orange. c) Port and mechanical mirror switching between camera and fiber optics.

As the overall theme of this thesis is the fabrication and characterization of photonic materials, these two techniques are at the heart of all projects that will be discussed in the next section. The qualitative imaging and quantitative spectroscopic methods provided insights into the optical properties of novel gradient materials and allowed the readout of sensors and fluorescent tracers.

The four projects making up the contents of this thesis present three different opportunities for gradient colloidal assemblies: autonomous sensing, efficient screening, and novel optical properties. In the first project, **Thermal Recorder I**, gradient colloidal crystals are prepared from binary particle mixtures and applied as time-temperature integrators. This is followed up in **Thermal Recorder II**, where additional complexity allows readout with a smartphone camera, which requires many samples for data-driven analysis. The third project, **Order to Disorder**, also plays into the complementary nature of computational methods and materials science. A composition gradient and local optical characterization allow efficient screening of bidisperse mixtures with only a few samples. Finally, a novel synthesis method is developed in the last project, **Size Gradient**. The fabricated continuous gradient colloidal glass also has tailored optical properties in the form of homogeneous broadband reflectance.

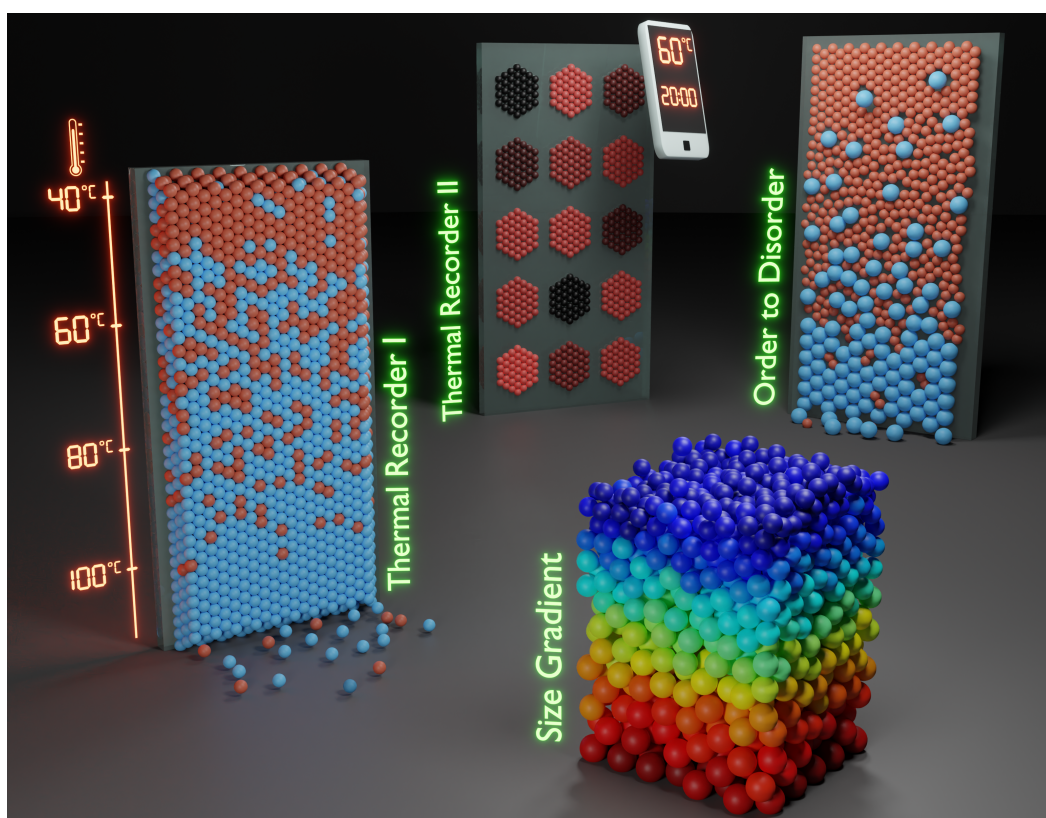


Figure 4.1.: Graphical Abstract.

4.1 Synopsis

Colloidal crystals (CCs), assembled via vertical deposition, are usually obtained as films with a thickness of a few microns. The lateral dimensions mainly lie between a few millimeters to centimeters. In the first project of my thesis, I aimed to fabricate a CC with a gradual change of a binary particle composition along one lateral axis (compare 'Thermal recorder I' in Figure 4.1). Two particle types that exhibit different thermal properties but are identical regarding size and surface chemistry were applied. This allowed co-crystallization and ensured consistent periodicity throughout the entire sample. In the first part, I examined the composition-dependent film formation kinetics of binary CCs prepared via standard vertical deposition. Then, in the second part, I established a modified assembly method that produces gradient CCs. These were applied as low-tech solutions for autonomous time-temperature integrators with an extremely simple readout.

The two particle types were produced with a consistent hydrodynamic diameter of 250 nm but, due to different comonomer ratios, distinct glass transition temperatures (T_g) of 49 °C and 94 °C, respectively. Upon (co-)crystallization, CCs with bright structural colors were formed and UV-Vis microspectra revealed a photonic stop band at 510 nm for all compositions. Exposing these polymer CCs to temperatures between the T_g s of the two components resulted in dry sintering (film formation) and a loss of the refractive index contrast as well as the periodicity (Figure 4.2a). Although a slight blue shift of the stop band (approximately 10 nm) could be observed, the decrease of the peak intensity offered a much more sensitive signal. Therefore, it was the key parameter throughout this project (Figure 4.2b).

This spectroscopic characterization allowed a fast, in-situ analysis in the form of the time-dependent decrease of the normalized stop band intensity. Several samples, with a range of compositions, were prepared via vertical deposition coating of glass substrates from (mixed) particle suspensions. In-situ measurements were conducted at various temperatures between 50 and 90 °C, which showed that the film formation kinetics were distinct for each composition. Interestingly, for the binary cases, this was not a simple superposition of the profiles observed for the pure phases. This was attributed to a complex, multi-step process where low- T_g particles form contact areas and coalesce before slowly entering the voids in domains dominated by high- T_g particles. The viscous flow would thereby cause further loss of the refractive index contrast. This formation of small domains comprising only high- or low- T_g particles, respectively, is not caused by segregation but simply a stochastic effect. Comparison of the pair distribution functions of scanning electron microscopy (SEM) images (Figure 4.2c) as well as of 2D simulations proved an entirely random arrangement of the two particle types.

A 3D representation of all in-situ experiments performed at one temperature allows visualization of the entire parameter space (Figure 4.2e). In 2D, this could either be shown as the original, time-dependent degradation (Figure 4.2d) or transformed into a composition-dependent plot (Figure 4.2f). The latter presents the intensity profile at given points in time on a theoretical sample exhibiting a linear composition gradient. Between 40-60 %, the change was most pronounced, which was attributed to the inversion of the majority phase. Nevertheless, this was not a discrete jump, and the transition remains gradual.

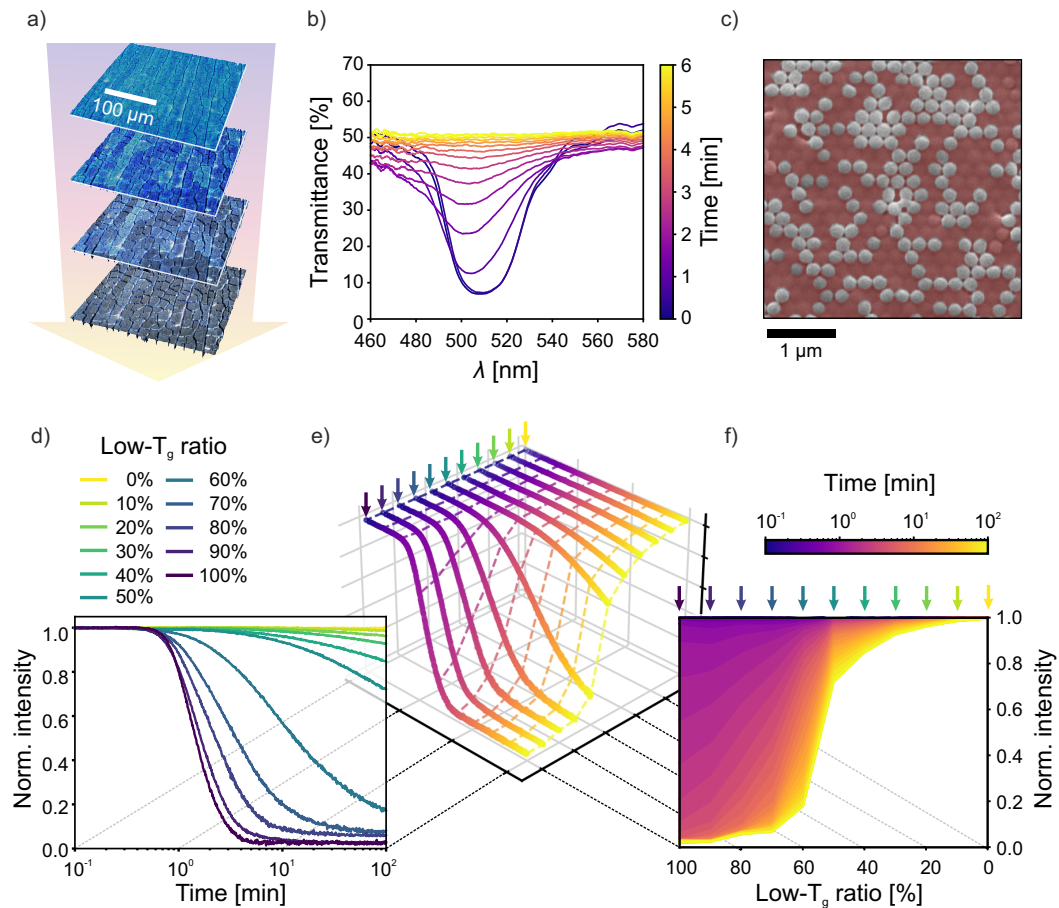


Figure 4.2.: Characterization of the time-dependent degradation of structural coloration on discrete (non-gradient) substrates at 60 °C. a) Microscopy images showing the transition from blue to colorless. b) In-situ UV-Vis microspectra obtained during the dry-sintering. c) Ex-situ scanning electron microscopy image of a sample consisting of 50 % high- T_g particles. d-f) Full in-situ characterization of the normalized stop band intensity. *Reproduced from [295] under terms of the Creative Commons license.*

The next step was developing a modified coating method to produce gradient CCs. This was inspired by the infusion-withdrawal coating (IWC) approach established for wettability gradients which involves a dual syringe pump setup (Figure 4.3a). A glass substrate is suspended in a particle suspension. One syringe pump infuses a different suspension,

while the second pump extracts the liquid at twice the rate of infusion. Thereby, the composition in the cell is slowly changed while the water level is simultaneously lowered, mimicking the process of vertical deposition coating. The time-dependent change in composition is translated into a position dependence on the substrate along the coating direction. As a proof-of-principle of the coating method, CCs were prepared with a gradual addition of fluorescent tracer particles. These commercial colloids, with a diameter of 100 nm were added between 0-1 wt%. Theoretically, they are small enough to occupy octahedral vacancies spanned by the larger particles and, therefore, do not affect the crystalline order. Fluorescence- and UV-Vis microspectroscopy were performed at several positions along the sample. Normalizing the fluorescence intensity with the stop band maximum provided a thickness-independent calibration and allowed mapping of the exact composition to each position. While this calibration method was sufficient for this work, it has limited use on, e.g. non-crystalline samples. An adjusted version will, therefore, also be shown in a later project. In general, the CCs showed a homogeneous structural color in stitched microscopy images, a consistent stop band, and a linear composition gradient along the coating direction.

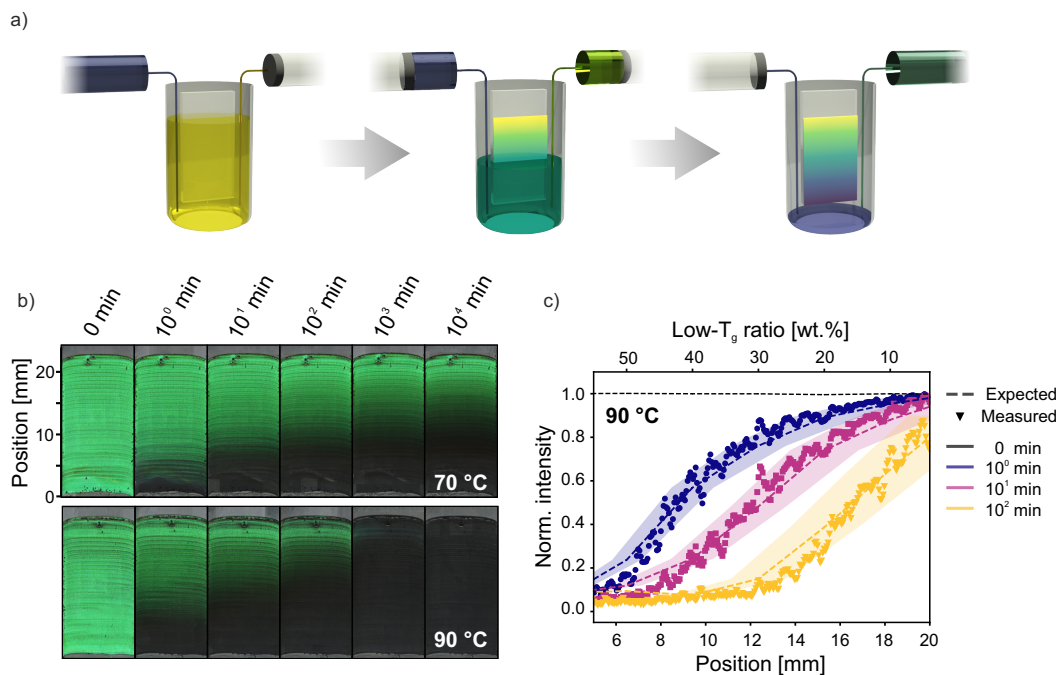


Figure 4.3.: Gradient colloidal crystals. a) Infusion-withdrawal coating setup showing the beginning, middle, and end of the dual syringe pump process. b) Gradient colloidal crystals acting as time-temperature integrators, exposed to two different temperatures and characterized ex-situ via optical microscopy. c) Stopband intensity profiles of the samples in (b). The dotted lines are predicted profiles from the in-situ measurements, such as those in Figure 4.2f, with a 10% margin of error. *Reproduced from [295] under terms of the Creative Commons license*

The two presented concepts could then be brought together in the form of CCs with a continuous composition gradient of high and low- T_g particles. These gradient samples

were subjected to isothermal heating events and characterized ex-situ with optical microscopy and microspectroscopy. While the increased temperature persists, the degraded (colorless) area spreads from the bottom to the top of the sample, following the gradient from mainly low- to mainly high- T_g particles. Naturally, this proceeds faster for a higher temperature, i.e., for 90 °C compared to 70 °C (Figure 4.3b). Several hundred microspectra were obtained along the gradients to quantify this observation in the form of the normalized stop band intensity (Figure 4.3c). Due to the calibration and the correlation of position and composition, this could be compared to expected profiles obtained from the in-situ measurements of non-gradient samples such as those in Figure 4.2f. The overlap of the two data sets is very good and corroborates that this type of material can be used for advanced temperature sensing techniques. An interesting aspect of this application is the logarithmic time dependence of the degradation. This entails that time steps between 1-10 min, as well as between 100-1000 min can be distinguished, using a single sample. Good reproducibility of the gradient CCs' response to isothermal events could be shown. The precision was determined to be 5-10 °C and 1-2 steps between each order of magnitude for the duration. However, it was not yet possible to independently determine time and temperature; this topic will be addressed later.

The sensor shows a rather intuitive response, effectively mimicking the icon representing the battery charge in smartphones. Therefore, the material might be applied in various ways. Potential examples are safety evaluation during the storage of perishable food or medicine, and battery management. For example, when the colorless region of a sensor passes a certain threshold, this could mean that the monitored battery has either been used for a long time at a moderate temperature or has experienced short exposure to an excessive temperature. Both would require renewal and could be judged by non-specialists without expensive devices for tracking and readout. I showed that such an analysis could readily be quantified via simple image analysis. Green-channel separation and grey scale evaluation of the samples in Figure 4.3b provided similar profiles compared to the spectroscopic analysis. This led me to believe that this type of sensor could be read out in more detail with a standard smartphone camera, coupled with a more complex evaluation procedure. Therefore, I decided to approach a computer-savvy colleague of mine and use this possibility in a follow-up project.

Changing the comonomer ratios of the polymer particles makes it easy to vary the film formation temperature of the colloidal assembly. It is, naturally, also possible to use mixtures of more than two particles, thereby further increasing the complexity of the system. While the last project provided sensors with an intuitive optical readout, the following approach yields more complex but comprehensive results. The sample geometry here was not a continuous gradient but a pattern of spots with discrete compositions

examined via photography. Combined with an artificial neural network, this allowed independent determination of time and temperature.

Four different particle types were synthesized with MMA/nBA ratios of 85:15, 90:10, 95:5, and 100:0, respectively. All of these had a consistent hydrodynamic diameter of 320 ± 5 nm. Differential scanning calorimetry showed that T_g s were evenly spaced between 85-125 °C (Figure 4.4a) and UV-Vis spectroscopy of self-assembled CCs provided the position of the stop bands in a narrow range at 635 ± 3 nm (Figure 4.4b). Co-crystallization of all possible mixtures was, therefore, possible. A prerequisite for machine learning-enabled analysis is a large amount of data. To comply with this, developing a fast and reproducible sample preparation technique was necessary. This was realized in the form of an array printing setup. A hydrophilic pin was first dipped into a (mixed) particle suspension and subsequently brought into contact with a heated glass substrate (Figure 4.4c). After washing, the process repeated with the following suspension at a different position. This allowed facile automation with a 3D-motorized stage and provided site-selectivity. Another advantage was that almost none of the suspension was wasted, and a standard laboratory scale synthesis (250 mL) was sufficient to produce several hundred samples.

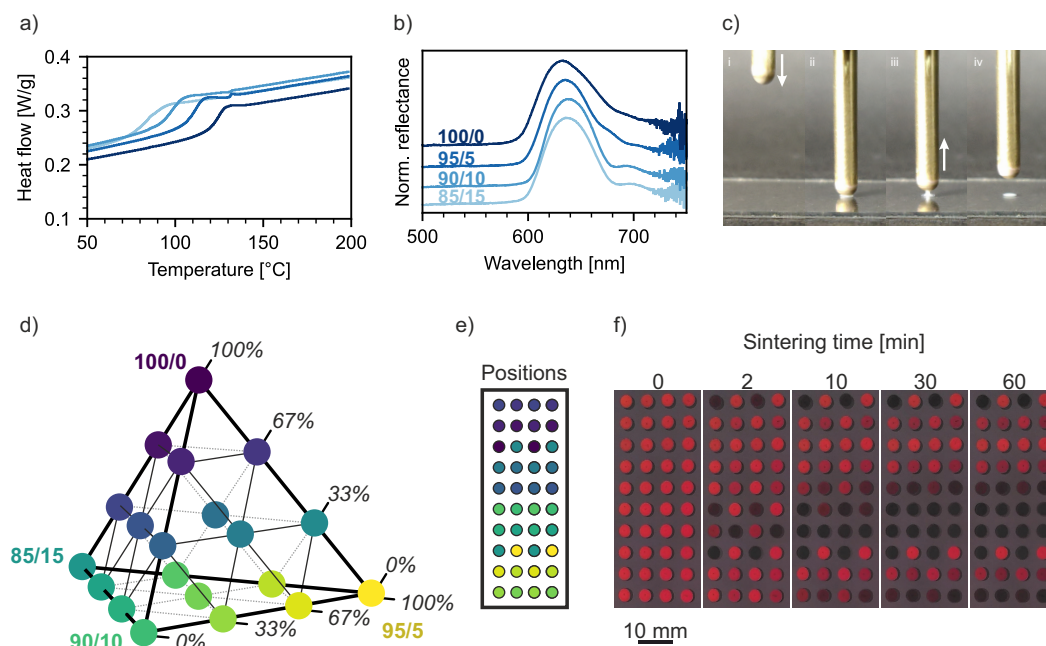


Figure 4.4.: a) DSC heating curves of the four polymer particles. b) UV-Vis reflectance spectra of self-assembled colloidal crystals. c) Snapshots of the contact printing procedure. d) Quaternary phase diagram showing all particle combinations applied in this project. e) Positions of the mixtures on the substrates. f) Exemplary photographs taken while heating a sample at a set temperature of 120 °C. *Reproduced from [299] under terms of the Creative Commons license.*

The substrate had to be heated during the assembly to ensure uniform coating. A pronounced coffee stain effect was observed if the substrate was coated at room temperature

and no discernible color was visible. Heating and the consequent milk-skin overlayer ensured the homogeneous color of the CC spots and also, due to nearly instantaneous evaporation and pinning at the edges, a consistent circular shape. Twenty different particle combinations were applied, spanning the quaternary phase diagram shown in Figure 4.4d. Two spots were fabricated with each mixture at defined positions on the substrate to introduce some redundancy and increase the accuracy (Figure 4.4e). The pristine spots (before heating and degradation) were all identical in shape and color.

When exposing these samples to elevated temperatures, some spots immediately lose their color, and others do not change. Many also show various degrees of discoloration, dependent on the dry-sintering duration. It should be pointed out that compositions exist where one particle type experiences fast deformation and another does so as well, but slower. This increases the system's complexity far beyond that of the first project. Characterization procedures for this process can be classified as one of two types: 1) In-situ methods that can only measure one spot at a time; 2) Ex-situ methods that examine the entire substrate but provide limited temporal resolution. In-situ measurements were performed via UV-Vis spectroscopy, and similar composition-dependent kinetics of the stop band degradation compared to the gradient samples could be observed. However, acquiring data for all 40 spots at once was far from practical. Ex-situ microscopy also failed to characterize the system fully and only allowed a qualitative examination of the loss of structural color. We, therefore, decided to switch to a non-conventional type of data acquisition: digital photography with a smartphone camera. This had two distinct advantages. First, it allowed in-situ characterization but provided information for all spots on the substrates at once. Consequently, it can be considered a holistic solution for the readout of our sensors. Secondly, optimizing the sensor for an evaluation with a commercial smartphone provides a user-friendly approach, as it does not rely on specialized laboratory-type equipment such as a spectrometer. The final setup was a black hot plate with a defined position for the substrate and a fixed mount for both a lamp and the smartphone. This ensured constant lighting conditions (distance, angle, and brightness). Figure 4.4f shows snapshots taken with the setup during isothermal heating of a substrate.

The difficulty in fabricating a time-temperature integrator capable of independently providing both parameters is realizing a system complex enough to over-determine the parameter space but simple enough to allow reasonably facile evaluation. Measuring the optical response of the mixed particle systems with a digital camera does not provide data directly related to physical properties and processes. Machine learning is an ideal candidate where such an analytical approach fails, as there is no need for refined physical models. A prerequisite for machine learning is a large amount of data. Since we developed a fast and reproducible coating method and could measure several hundred

substrates with a high temporal resolution, this was readily available. The data was pre-processed by acquiring the brightest red values on each spot (Figure 4.5a). Additionally, this reduced the risk of overfitting by incorporating unwanted information, such as specific defects. The time dependence of the red values exhibited a similar trend as the stop band intensity, which led us to believe that the same (or more) information was hidden in the data. Measurements proceeded between 100-140 °C with intervals of 5 °C and photographs were obtained every 5 s over the course of 120 min. Ten samples were measured at each temperature, eight for training and two for validation. My colleague then set up an artificial neural network to decipher the matrices of red values. Two networks, with ten hidden layers each, were trained and then were able to provide a time and temperature pair for any given (unknown) photograph. Both time and temperature prediction worked very well (Figure 4.5b,c), with most of the deviations greater than 10 min being at the edges of the temperature range. As the particles' T_g can easily be adjusted, the temperature range is not fixed and can easily be tailored to specific needs. Validation data existed over the full parameter space, and absolute errors could be obtained for each time and temperature combination. Additionally, we showed that if the sensor was subjected to a series of heating processes, it mainly reacted to the highest temperature, reliably providing the duration of this event.

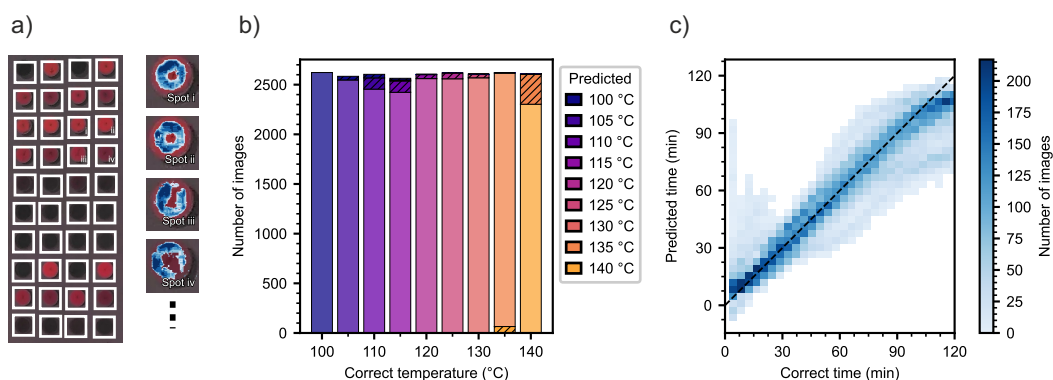


Figure 4.5.: a) Pre-processing of the photographs obtained during isothermal heating. b) Validation results for the temperature evaluation. Shaded areas correspond to incorrect assignment of the temperature. c) Validation results for the time evaluation. The closer points lie to the diagonal, the smaller the error. *Reproduced from [299] under terms of the Creative Commons license*

We expect this type of sensor could be optimized for commercial use and analyzed with a smartphone with the evaluation model installed as an application. This would pave the way to cheap and user-friendly multiparameter sensors. In general, the project showed the relevance of advanced computational data analysis and the synergy between artificial intelligence and materials science. Since training such a network requires vast amounts of data and, therefore, measurements on a large number of physical samples, efficient fabrication techniques are becoming more critical. While the time-temperature

integrators were prepared via automated sample preparation, the following project will introduce gradient colloidal assemblies as advanced screening platforms for the optical properties of colloidal assemblies. The IWC setup, combined with local spectroscopic measurements along the samples, has great potential in generating large data sets from only a few samples, thereby significantly reducing the preparation effort.

Binary mixtures of particles with different sizes provide a simple way of varying the superstructure by means of composition. Together with the single-particle scattering, this determines the optical properties of the ensemble. Materials with defined haze or transmittance can easily be prepared if the system is well characterized. In this work, I prepared colloidal crystals and glasses from particle mixtures with different size-ratios (R_S) of 0.7, 0.8, and 0.9 as well as monodisperse suspensions ($R_S = 1.0$). Samples prepared via vertical deposition from bidisperse suspensions with $R_S = 0.9$ showed co-crystallization and a stop band position dependent on the composition. Mixtures with R_S of 0.8 and 0.7 resulted in disordered structures, and the light scattering efficiency varied depending on the composition. However, the finite and few examined compositions did not allow a satisfactory characterization of the entire composition range. Since it would be a considerable effort to realize this with discrete samples, I addressed this problem with gradient colloidal assemblies (Figure 4.6). A thin film with a gradual composition change along one lateral axis could, theoretically, contain all possible compositions of a binary system. I used IWC to fabricate these gradients for all size ratios. Local optical characterization along these samples could provide large data sets from a few samples.

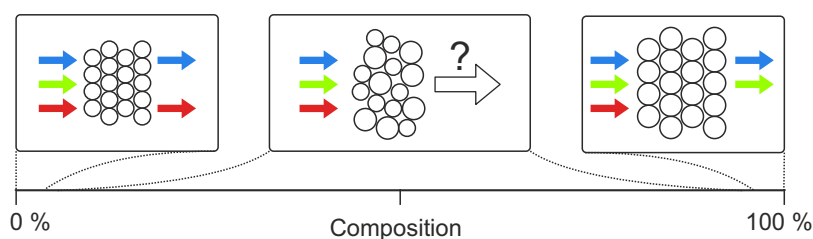


Figure 4.6.: Schematic showing the objective of this project. Composition gradients from binary colloidal mixtures are prepared, and local optical characterization provides information over the entire composition range. *Reproduced from [300] under terms of the Creative Commons license.*

For this project, it was necessary to precisely correlate the position along the gradient with the corresponding composition. Since parts of some samples were not crystalline and did not exhibit a photonic stop band, the calibration developed in the first project was not applicable. A similar but refined approach was established, where particles were labeled via post-synthesis fluorescent staining. Aliquots of the polymer particle suspensions were taken and stained with a blue or red fluorescent dye via a swelling-deswelling mechanism. Defined concentrations of the blue tracers were added to one suspension and red tracers to the other in the gradient fabrication. I was able to show that the ratio of blue and red fluorescence signals, measured locally via microspectroscopy,

could be used to accurately determine the respective composition (Figure 4.7). While the separate signals of blue and red fluorescence showed strong fluctuations due to thickness variations along the sample (Figure 4.7a-c), the ratio of the two provided a smooth and thickness-independent calibration curve (Figure 4.7d). Since the tracer particles were identical in shape and size to the pristine particles, the addition did not influence the assembly process and the resulting superstructure. Furthermore, the calibration technique is non-invasive and entirely orthogonal to UV-Vis microspectroscopy. As fluorescence was measured in reflection and UV-Vis in transmission geometry, both can be measured with the same microscope (see chapter 3 for details). This allowed mapping the composition to the position and the corresponding transmittance spectrum.

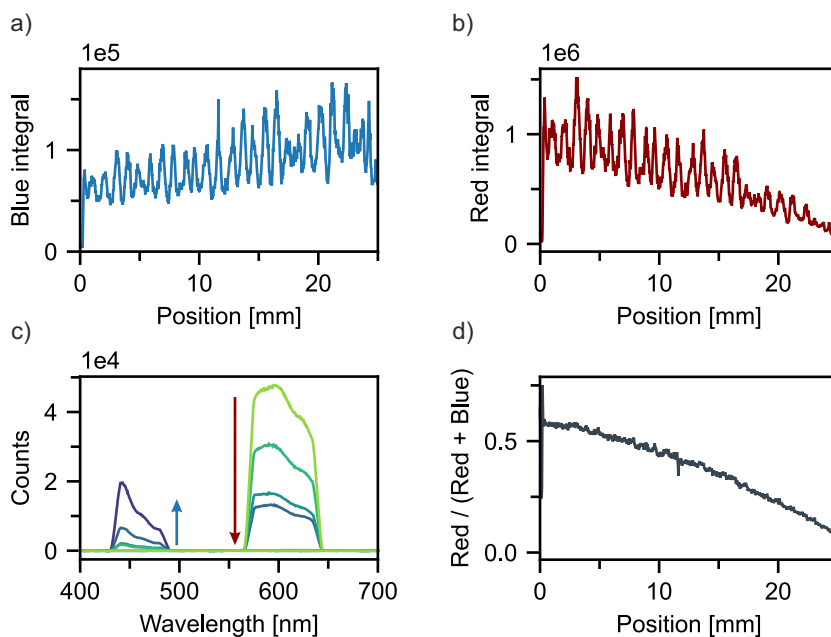


Figure 4.7.: Fluorescence calibration of a gradient colloidal assembly. a),b) Integrals of the blue and red fluorescence, respectively, along the gradient. c) Exemplary spectra showing how the blue fluorescence signal increases while the red signal simultaneously decreases. d) Normalized ratio of the red and blue integral, providing a thickness-independent determination of the composition at each position along the gradient. *Reproduced from [300] under terms of the Creative Commons license.*

The optical properties of the gradients were examined by acquiring several thousand transmission UV-Vis microspectra while scanning along the gradient. For a better interpretation, the mean transmittance (\bar{T}) between 450-700 nm was calculated and plotted with respect to the position. On homogeneous CCs, it became apparent that this was dramatically superimposed by strong fluctuations with an amplitude of 25 % and a spatial frequency of about $\frac{1}{30} \mu\text{m}^{-1}$. Closer examination showed that this was caused by light scattering at cracks in the films, which originated in the drying process. Furthermore, the magnitude of this effect depended on the degree of crystallinity. This presented a problem, as the influence of the particle composition on the mean transmittance was overlaid

by the wavelength-independent scattering at the domain boundaries. I approached this problem by applying a Savitzky-Golay algorithm, which filtered the data to exclude all oscillations exhibiting a high spatial frequency. As a result, the remaining spectra (several hundred along each sample) were much easier to compare due to a consistent baseline throughout each data set. A streamlined analysis of microspectra measured along the gradients was thereby made possible.

I started with analyzing binary mixtures with $R_S = 0.9$. Gradients, transitioning from mainly small to mainly large particles, showed a gradual red shift of the stop band. Co-crystallization, therefore, occurred over the entire composition range. Due to the fluorescent tracer particles, it was possible to relate the stop band position to the respective particle composition. This system was shown to provide thin films with structural coloration anywhere between 560-600 nm simply by choosing the correct mixture of the two suspensions. Going on to gradients with size ratios of 0.8 and 0.7, samples showed disorder over most of the composition range. An increasing amount of large particles brought a shoulder in the transmittance spectrum (Figure 4.8a,b). This was attributed to the transition from a diffusely scattering material to a photonic glass, dominated by the scattering properties of the monodisperse, large particles. Further to the edge of the composition range, the transition from a disordered amorphous assembly to order and crystallinity was observed. This entailed a gradual change from omnidirectional scattering to constructive interference of ballistic photons. The baseline moved to higher transmittance values, and a sharp stop band evolved. For the mean transmittance, this meant a minimum at a specific composition. This was found near the edge of the composition range, where a maximum of large particles was present with enough small particles in the mixture to induce disorder (Figure 4.8c). For $R_S = 0.8$, the optimum of the scattering efficiency was found at approximately 90 wt% large particles. A greater difference in the particle size ($R_S = 0.7$) inhibited crystallization at even lower percentages of small particles.

Another approach corroborated this optimum of the scattering efficiency. Transmittance spectra are, naturally, influenced quite strongly by the sample thickness. However, this parameter was not constant along the length of the gradients. Meniscus pinning during vertical deposition induced oscillations of the sample thickness. Additionally, the transition from mono- to bidisperse suspension influenced the assembly process, which induced an overall drift of the sample thickness in some cases. Therefore, verifying the previous results with an independent set of experiments was essential. Patterned substrates were applied to force the colloids to assemble with a defined thickness. Particles (co-)assembled in the ridges of the hydrophilized substrates, and the thickness of the assembly was determined by the ridge height and the meniscus (Figure 4.8d). Discrete compositions were coated via vertical deposition, and microspectroscopy was

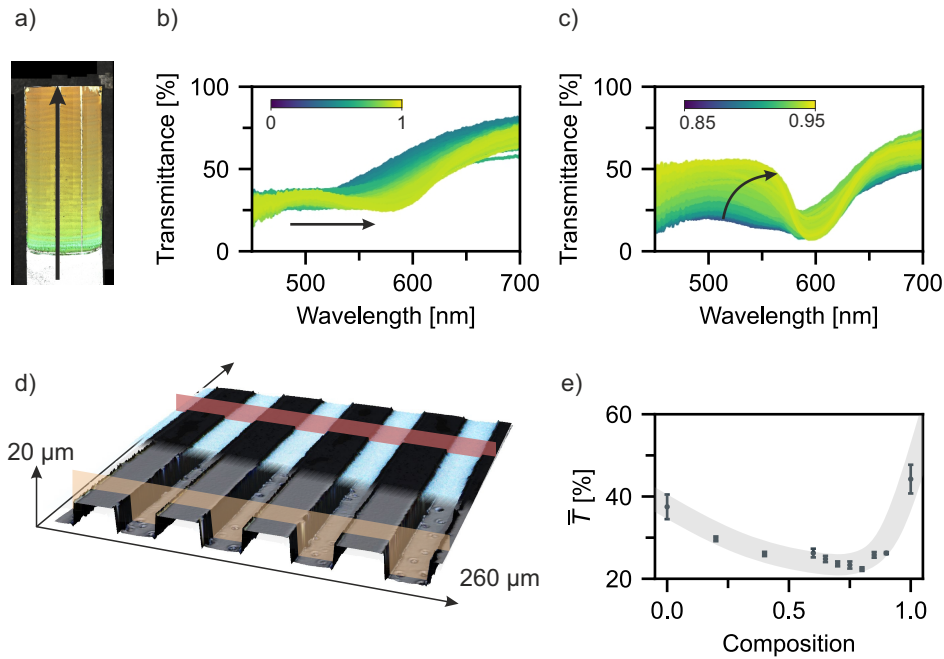


Figure 4.8.: a) Stitched microscopy image of a gradient with a size ratio of 0.8. b),c) Filtered UV-Vis microspectra along the gradient shown in (a). d) Overlaid 3D reconstructions of a topographically structured template, with and without particles assembled in the trenches. e) Mean transmittance of several particle compositions with a size ratio of 0.8, measured inside the trenches to obtain optical data from samples with a defined thickness. *Reproduced from [300] under terms of the Creative Commons license.*

performed at the center of the ridges. Normalized transmittance values were obtained for the different ensembles while maintaining complete control over the thickness. While it did not provide the amount of information the gradients did, this approach was complementary because it corroborated the previous results. The combination of the two sets of experiments manifested that the optimum scattering efficiency is given at the composition where the amount of small particles is just high enough to prevent crystallization.

The IWC approach is an efficient screening platform for the optical properties of binary colloidal systems. In the future, this could provide insights into more complex systems, such as the effect of adding anisotropic particles to colloidal mixtures. Properties such as solar reflectance might be improved even further this way and provide better passive cooling. Besides an optimized particle mixture, I believed it should be possible to tailor the optical properties by going one level of hierarchy higher. A gradient along the z-direction (normal to the substrate) might also provide novel functionality. This, of course, required a very different set of synthesis and assembly methods. I looked into this possibility in the last project and developed a novel synthesis procedure. The resulting gradient superstructure indeed provided enhanced broadband reflectance compared to reference samples.

In this project, I aimed for a very different type of gradient. Instead of a change in composition, a gradual increase in the particle size should be prepared. Therefore, it was not sufficient to synthesize two suspensions and change the respective mixing ratio. Every particle size inside the range of the gradient needed to be prepared. The definition set here for a fully continuous gradient was that the step size should 1) be so small that it could not be analytically resolved and 2) be irrelevant compared to the natural particle size distribution. This was not practical or even possible with a set of discrete batch particle syntheses. The idea of this work was rather to prepare seed particles and gradually increase the size via a semi-batch approach and slow monomer addition. Through a set of modified synthesis and assembly methods, this would later be transformed into a continuous size gradient.

The most intuitive way of characterizing a photonic gradient is by means of an imaging method. This meant that the gradient of the structural coloration should range between blue and red, i.e., over the visible spectrum. Therefore, the particle size range needed to be roughly adjusted between 200-300 nm. I developed a modified variation of surfactant-free emulsion polymerization to achieve this. Poly(methyl methacrylate) particles with a hydrodynamic diameter of 220 nm were synthesized with an excess initiator. Shortly after completion of the reaction and without letting oxygen enter the flask, further monomer was slowly added via a syringe pump. Since the reactive conditions inside the system persisted, this resulted in controlled particle growth under monomer-starved conditions. Simultaneously, part of the suspension was extracted into a long, thin tube previously inserted into the aqueous mixture. Pulling the suspension into this tube translated the time-dependent growth into a positional dependence along the length of it. While this proceeded slowly enough to ensure laminar flow, it was insufficient to entirely prevent mixing inside the tube due to a flow rate near zero at the interface. This problem was overcome by periodically introducing evenly spaced air bubbles as separators in the tube (Figure 4.9a). The surface tension forced the separated fractions to remain intact, preventing mixing entirely. We called this a 'controlled extraction emulsion process' (CrEEP). After the synthesis, more than 100 fractions were saved in the tube with the particle size gradually increasing from 220 to 310 nm. The consequent sub-nm step size between neighboring fractions satisfies the earlier definition of a fully continuous size gradient. This change in diameter was linear, as determined via dynamic light scattering (Figure 4.9b). A representative number of evenly spaced fractions was separately left to self-assemble and form CCs. Iridescent colors, ranging the entire visible spectrum, could be observed and, together with SEM images, proved that the monodisperse nature was maintained through the fractionation (Figure 4.9c). This meant that the prerequisites for a gradient photonic assembly were fulfilled, and an appropriate assembly method needed to be developed to make use of the stored fractions.

I achieved this through semi-continuous filtration (Figure 4.9d). The fractions were pushed out of the tube, one by one, into a preliminary mixing container. The suspension was diluted with water and periodically emptied into a vacuum filtration setup. This proceeded automatically using a siphon-type mechanism. The largest particles were deposited first; overnight, all subsequent fractions were filtered on top. Due to the filtration, the particles did not form CCs but remained disordered. Samples produced in this manner were films with a diameter of several cm and a thickness of approximately 100 μm . Normal to the surface (z-direction), a continuous particle size gradient was observed via SEM. No discrete steps could analytically be resolved. By careful optimization of the gas permeability of the tube and the extraction speed, the volume of the fractions could dynamically be adjusted during the CrEEP. The first fractions were the largest, after which the volume gradually decreased. This counteracted the increasing polymer weight percentage and ensured a linear gradient in the later assembly. While the size did change along the gradient, particles at any given z-position were monodisperse. Therefore, the prerequisite for a photonic glass was fulfilled, and structural coloration could be observed on cross sections under an optical microscope (Figure 4.9e).

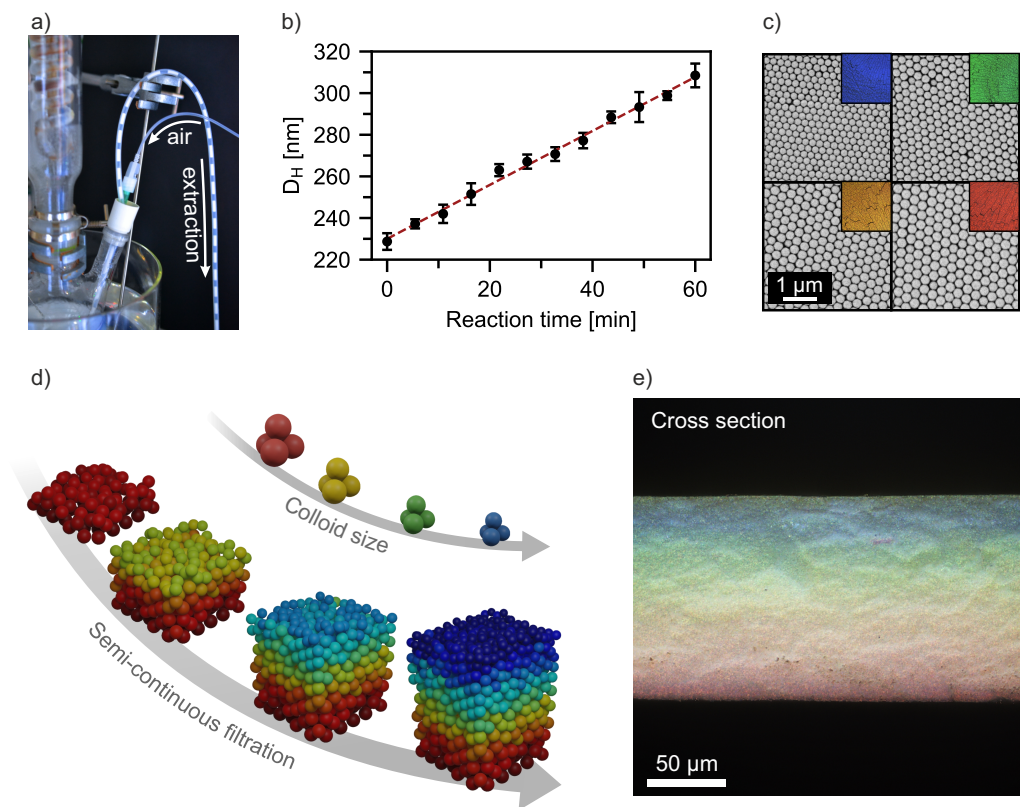


Figure 4.9.: a) Snapshot of the synthesis. b) Hydrodynamic particle diameter as a function of the reaction time. c) Electron and optical microscopy of CCs prepared via self-assembly of selected fractions. d) Visualization of the semi-continuous filtration assembly. e) cross section of a gradient colloidal glass, showing the continuous range of structural colors. *Reproduced from [296] under terms of the Creative Commons license.*

Due to the size gradient, this cross section distinctly resembled a rainbow. A continuous color change was observed from blue over green and yellow to red. The impression was amplified by increasing the saturation with a carbon nanolayer deposited on top to reduce the effect of diffuse scattering. This material presents a type of structure that was previously not accessible: a close-packed colloidal assembly with a continuous size gradient. Both local and bulk optical characterization was then performed to illustrate the photonic properties and possible applications.

UV-Vis reflectance microspectra were obtained at equidistant positions along the cross section. Here, the carbon layer proved especially important in reducing the influence of scattering at shorter wavelengths. The reflectance peaks shifted from about 650 nm to below 500 nm when moving from the bottom to the top of the gradient, corroborating the visual impression. The angle independence of the structural colors, which is expected for a photonic glass, was also elucidated. 3D reconstructions, combined with optical microscopy images, exhibited an identical color range of the gradient, irrespective of the angle of incidence. The non-iridescent coloration is an important property, e.g., for optical filters. In many applications, a specific wavelength range should be reflected at all angles. For example, in passive cooling applications, sunlight has to be reflected from the surface at all times of day, i.e., at all solar altitudes.

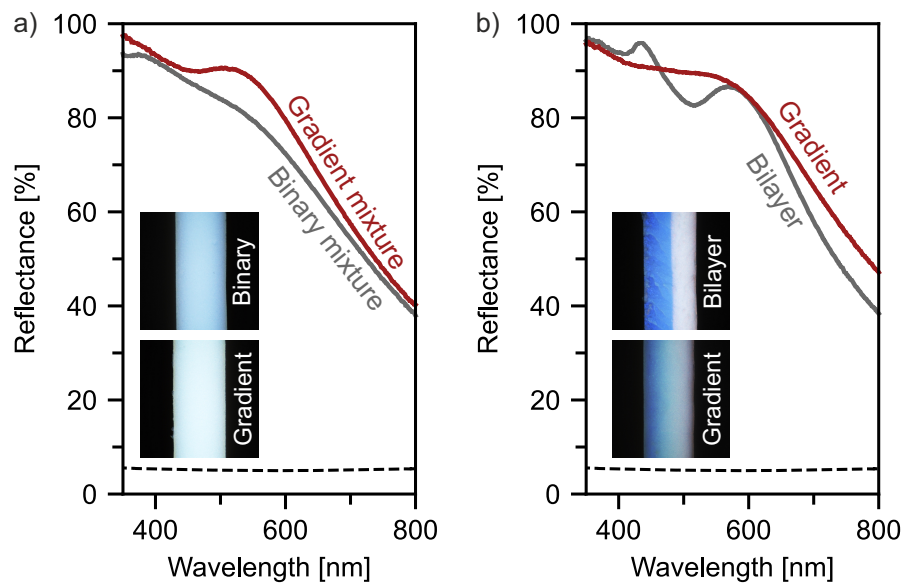


Figure 4.10.: Diffuse reflectance spectra from the top surface of the colloidal assemblies. a) Spectra and cross sections of a binary mixture of large and small particles and an assembly prepared by mixing and subsequent filtration of all fractions obtained via CrEEP. b) Spectra and cross sections of a bilayer of large and small particles and the gradient colloidal glass. *Reproduced from [296] under terms of the Creative Commons license.*

The diffuse reflectance from the sample's surface was measured to showcase the potential of the photonic gradient. A set of other colloidal films was also prepared via filtration to

provide reference materials. Small and large particles were used for the fabrication of reference samples. When assembled separately, the colloidal glasses showed discrete peaks in the blue and red wavelength range, respectively. A binary mixture of the two particle types was then compared to a mixed gradient assembly. The latter was prepared by mixing all fractions obtained via CrEEP and subsequent filtration. Compared to the bidisperse case, the gradient mixture showed a higher overall reflectance and a broad peak in the middle of the visible spectrum. I investigated this by comparing 2D simulations of corresponding systems and showing a higher degree of local order in the case of the mixed gradient. This explained the occurrence of coherent scattering and a local peak of the reflectance in the actual sample. Lastly, a bilayer of large and small particles was compared to the previously discussed gradient superstructure. To minimize effects caused by diffuse scattering, samples were oriented so that the light beam first hit the top surface (smallest particles). Two distinct peaks were observed for the bilayer, while the gradient showed a plateau over the visible range. Since the plateau roughly spans the wavelength range between the peaks of small and large particles, this is the behavior that was expected and aimed for. This is advantageous regarding broadband reflectance, as the reflectance is monotonous, and no local minima or maxima exist in the gradient spectrum. I further showed that the range of this plateau could be tuned. A modified CrEEP and subsequent self-assembly provided a gradient with the particle size ranging from 220-450 nm. The plateau in the diffuse reflectance spectrum consequently extended into the near-IR, proving the customizability of the approach. Furthermore, the spectra of the gradient and the mixed gradient were directly compared. Great care was taken to ensure that the total particle size distribution in both samples was identical, and they only differed in the allocation, i.e., the superstructure. It was shown that the gradient provided a higher reflectivity over the entire visible range, proving the advantage of maintaining this amount of control over the synthesis and assembly process. In conclusion, this provided a material class that shows tailorable broadband reflection with no angle dependence.

I believe that these projects merely opened the door to a novel aspect of colloidal self-assembly. Infusion-withdrawal coating has great potential in advancing sensing and screening procedures. Adding more complex particles, such as rods and platelets, will generate a much more detailed understanding of light scattering properties in mixed assemblies. The size gradient, on the other hand, can directly be converted into an inverse structure, which might provide novel mechanical or mass transport properties in membranes. The mixture of all fractions after CrEEP is also an exciting system, which could be examined in more detail when assembled at an interface as a monolayer. In conclusion, the field of functional photonic gradients in colloidal assemblies is ready to be explored!

4.2 Individual Contributions to Joint Publications

The results presented in this work were prepared in cooperation with other colleagues. The individual contributions of all authors are designated below.

Chapter 6: Time-Temperature Integrating Optical Sensors Based on Gradient Colloidal Crystals

Marius Schöttle, Thomas Tran, Tanja Feller, and Markus Retsch

We published this article in *Advanced Materials*, **2021**, 33(40), 2101948.

I led the conceptualization, investigation, formal analysis, and data curation. This included sample creation and both microscopic and spectroscopic analysis. I also wrote the original draft and designed an image that was chosen as the back cover of the journal issue. Thomas Tran supported the investigation and formal analysis by creating software solutions for analyzing the time-dependent optical data. Tanja Feller was involved in the investigation by doing SEM measurements. Markus Retsch supervised the project and reviewed and edited the manuscript.

Chapter 7: Machine Learning Enabled Image Analysis of Time-Temperature Integrating Colloidal Arrays

Marius Schöttle, Thomas Tran, Harald Oberhofer, and Markus Retsch

We published this article in *Advanced Science*, **2023**, 10(8), 2205512.

Thomas Tran and I were responsible for the conceptualization, investigation, formal analysis, and data curation. I focused on chemical synthesis, sample fabrication, and conventional analysis, i.e., UV-Vis spectroscopy, SEM, and DSC measurements. Thomas Tran managed the image processing and wrote the software for the machine learning model. Thomas Tran and I wrote the original draft and visualized the data together. Harald Oberhofer and Markus Retsch supervised the project and reviewed and edited the manuscript.

Chapter 8: Microspectroscopy on Thin Films of Colloidal Mixture Gradients for Data-Driven Optimization of Optical Properties

Marius Schöttle, Maximilian Theis, Tobias Lauster, Stephan Hauschild, and Markus Retsch

We published this article in *Advanced Optical Materials*, **2023**, *11*(16), 2300095.

I led the conceptualization, investigation, formal analysis, and data curation. This included all synthesis procedures, particle assembly, and the development of the characterization methods as well as the programming of automated scripts for the data analysis. I also wrote the original manuscript. Maximilian Theis conducted preliminary fluorescence measurements. Tobias Lauster was involved in the original optimization of the patterned substrates and edited the manuscript. Stefan Hauschild provided the master wafers prepared via photolithography. Markus Retsch supervised the project and reviewed and edited the manuscript.

Chapter 9: A Continuous Gradient Colloidal Glass

Marius Schöttle, Tobias Lauster, Lukas J. Römling, Nicolas Vogel, and Markus Retsch

We published this article in *Advanced Materials*, **2023**, *35*(7), 2208745.

I led the conceptualization, investigation, formal analysis, and data curation. This included the development of a new type of synthesis procedure as well as the self-assembly processes. I conducted optical and electron microscopy, local spectroscopy, and structural characterization. I wrote all scripts for data analysis and the 2D simulations, visualized the data, and wrote the original manuscript. I also designed an image that was chosen as the frontispiece in the journal issue. Tobias Lauster conducted the diffuse reflectance measurements, was involved in the discussion of the optical measurements and edited the manuscript. Lukas J. Römling assisted with the local spectroscopy along the gradient. Nicolas Vogel and Markus Retsch supervised the project and reviewed and edited the manuscript.

- (1) Graham, T. *Philosophical Transactions of the Royal Society of London* **1997**, *151*, 183–224.
- (2) *Colloid Chemistry I*; Topics in Current Chemistry, 2003.
- (3) Xia, Y.; Gates, B.; Yin, Y.; Lu, Y. *Advanced Materials* **2000**, *12*, 693–713.
- (4) Evans, D.; Wennerström, H.; Wennerström, H., et al., *The Colloidal Domain: Where Physics, Chemistry, Biology, and Technology Meet*; Wiley: 1999.
- (5) De Mello Donegá, C., *Nanoparticles*, 2014.
- (6) Stöber, W.; Fink, A.; Bohn, E. *Journal of Colloid and Interface Science* **1968**, *26*, 62–69.
- (7) Bogush, G. H.; Tracy, M. A.; Zukoski, C. F. *Journal of Non-Crystalline Solids* **1988**, *104*, 95–106.
- (8) Bergna, E. H., *Colloid Chemistry of Silica - An Overview*, 1994.
- (9) Turkevich, J.; Stevenson, P. C.; Hillier, J. *The Journal of Physical Chemistry* **1953**, *57*, 670–673.
- (10) Pastoriza-Santos, I.; Kinnear, C.; Pérez-Juste, J.; Mulvaney, P.; Liz-Marzán, L. M. *Nature Reviews Materials* **2018**, *3*, 375–391.
- (11) Sau, T. K.; Rogach, A. L. *Advanced Materials* **2010**, *22*, 1781–1804.
- (12) Lim, S. Y.; Shen, W.; Gao, Z. *Chemical Society Reviews* **2015**, *44*, 362–381.
- (13) Garcia de Arquer, F. P.; Talapin, D. V.; Klimov, V. I., et al. *Science* **2021**, *373*, eaaz8541.
- (14) Abraham, F. F.; Zetlemoyer, A. C. *Physics Today* **1974**, *27*, 52–53.
- (15) LaMer, V. K.; Dinegar, R. H. *Journal of the American Chemical Society* **1950**, *72*, 4847–4854.
- (16) Turkevich, J.; Stevenson, P. C.; Hillier, J. *Discussions of the Faraday Society* **1951**, *11*, 55–75.
- (17) Whitehead, C. B.; Özkar, S.; Finke, R. G. *Chemistry of Materials* **2019**, *31*, 7116–7132.
- (18) Handwerk, D. R.; Shipman, P. D.; Whitehead, C. B.; Ozkar, S.; Finke, R. G. *Journal of the American Chemical Society* **2019**, *141*, 15827–15839.
- (19) Ai, Z.; Deng, R.; Zhou, Q.; Liao, S.; Zhang, H. *Advances in colloid and interface science* **2010**, *159*, 45–59.
- (20) Egen, M.; Zentel, R. *Macromolecular Chemistry and Physics* **2004**, *205*, 1479–1488.
- (21) Fitch, R., *Polymer Colloids*, 1997.

- (22) Goodwin, J. W.; Hearn, J.; Ho, C. C.; Ottewill, R. H. *Colloid & Polymer Science* **1974**, *252*, 464–471.
- (23) Tanrisever, T.; Okay, O.; Snmezoglu, I. C. *Journal of Applied Polymer Science* **1996**, *61*, 485–493.
- (24) Lovell, P. A.; Schork, F. J. *Biomacromolecules* **2020**, *21*, 4396–4441.
- (25) Telford, A. M.; Pham, B. T. T.; Neto, C.; Hawkett, B. S. *Journal of Polymer Science Part A: Polymer Chemistry* **2013**, *51*, 3997–4002.
- (26) Dobrowolska, M. E.; van Esch, J. H.; Koper, G. J. *Langmuir* **2013**, *29*, 11724–11729.
- (27) Li, J. Q.; Salovey, R. *Journal of Polymer Science Part A: Polymer Chemistry* **2000**, *38*, 3181–3187.
- (28) Yuan, H. G.; Kalfas, G.; Ray, W. H. *Journal of Macromolecular Science, Part C: Polymer Reviews* **1991**, *31*, 215–299.
- (29) Tseng, C. M.; Lu, Y. Y.; El-Aasser, M. S.; Vanderhoff, J. W. *Journal of Polymer Science Part A: Polymer Chemistry* **1986**, *24*, 2995–3007.
- (30) Peng, B.; van der Wee, E.; Imhof, A.; van Blaaderen, A. *Langmuir* **2012**, *28*, 6776–6785.
- (31) Lee, J.; Ha, J. U.; Choe, S.; Lee, C. S.; Shim, S. E. *Journal of Colloid and Interface Science* **2006**, *298*, 663–671.
- (32) Karg, M.; Pich, A.; Hellweg, T., et al. *Langmuir* **2019**, *35*, 6231–6255.
- (33) Grunlan, J. C.; Ma, Y.; Grunlan, M. A.; Gerberich, W. W.; Francis, L. F. *Polymer* **2001**, *42*, 6913–6921.
- (34) Ruckdeschel, P.; Retsch, M. *Advanced Materials Interfaces* **2017**, *4*, 1700963.
- (35) Kang, E.; Graczykowski, B.; Jonas, U., et al. *Macromolecules* **2019**, *52*, 5399–5406.
- (36) Retsch, M.; Schmelzeisen, M.; Butt, H. J.; Thomas, E. L. *Nano Letters* **2011**, *11*, 1389–1394.
- (37) Ruckdeschel, P.; Philipp, A.; Retsch, M. *Advanced Functional Materials* **2017**, *27*, 1702256.
- (38) Ho, C. C.; Keller, A.; Odell, J. A.; Ottewill, R. H. *Colloid & Polymer Science* **1993**, *271*, 469–479.
- (39) Ho, C. C.; Ottewill, R. H.; Keller, A.; Odell, J. A. *Polymer International* **1993**, *30*, 207–211.
- (40) Kim, A. J.; Manoharan, V. N.; Crocker, J. C. *Journal of the American Chemical Society* **2005**, *127*, 1592–1593.
- (41) Lee, J. H.; Gomez, I. J.; Sitterle, V. B.; Meredith, J. C. *Journal of Colloid and Interface Science* **2011**, *363*, 137–144.
- (42) Behnke, T.; Würth, C.; Laux, E.-M.; Hoffmann, K.; Resch-Genger, U. *Dyes and Pigments* **2012**, *94*, 247–257.
- (43) Israelachvili, J. N., *Intermolecular and Surface Forces*, 2011.

- (44) Einstein, A. *Annalen der Physik* **1905**, 322, 549–560.
- (45) Von Smoluchowski, M. *Annalen der Physik* **1906**, 326, 756–780.
- (46) Vogel, N.; Retsch, M.; Fustin, C. A.; Del Campo, A.; Jonas, U. *Chemical Reviews* **2015**, 115, 6265–6311.
- (47) Derjaguin, B.; Landau, L. *Acta Physicochim. URSS* **1941**, 14, 635–649.
- (48) Verwey, E.; Overbeek, J. T. G.; Nes, K. v., *Theory of the stability of lyophobic colloids: the interaction of sol particles having an electric double layer*; Elsevier: New York, 1948.
- (49) Butt, H.-J.; Graf, K.; Kappl, M., *Physics and Chemistry of Interfaces*, 2003.
- (50) Derjaguin, B. *Kolloid Zeitschrift* **1934**, 69, 155–164.
- (51) Rentsch, S.; Pericet-Camara, R.; Papastavrou, G.; Borkovec, M. *Physical Chemistry Chemical Physics* **2006**, 8, 2531–2538.
- (52) Furusawa, K.; Anzai, C. *Colloids and Surfaces* **1992**, 63, 103–111.
- (53) Romero-Cano, M. S.; Martín-Rodríguez, A.; de las Nieves, F. J. *Langmuir* **2001**, 17, 3505–3511.
- (54) Dickinson, E.; Eriksson, L. *Advances in Colloid and Interface Science* **1991**, 34, 1–29.
- (55) Jenkins, P.; Snowden, M. *Advances in Colloid and Interface Science* **1996**, 68, 57–96.
- (56) Kralchevsky, P. A.; Nagayama, K. *Advances in Colloid and Interface Science* **2000**, 85, 145–192.
- (57) Kralchevsky, P. A.; Nagayama, K. *Langmuir* **2002**, 10, 23–36.
- (58) Butt, H.-J.; Kappl, M., *Surface and Interfacial Forces*, 2010.
- (59) Li, Q.; Jonas, U.; Zhao, X. S.; Kappl, M. *Asia-Pacific Journal of Chemical Engineering* **2008**, 3, 255–268.
- (60) Okubo, T. In *Encyclopedia of Biocolloid and Biointerface Science*, 2016, pp 355–379.
- (61) Zhu, J.; Li, M.; Rogers, R., et al. *Nature* **1997**, 387, 883–885.
- (62) Norris, D. J.; Arlinghaus, E. G.; Meng, L.; Heiny, R.; Scriven, L. E. *Advanced Materials* **2004**, 16, 1393–1399.
- (63) Burmeister, F.; Schäfle, C.; Matthes, T., et al. *Langmuir* **1997**, 13, 2983–2987.
- (64) Retsch, M.; Zhou, Z.; Rivera, S., et al. *Macromolecular Chemistry and Physics* **2009**, 210, 230–241.
- (65) Vogel, N.; Goerres, S.; Landfester, K.; Weiss, C. K. *Macromolecular Chemistry and Physics* **2011**, 212, 1719–1734.
- (66) Majumder, M.; Rendall, C. S.; Eukel, J. A., et al. *The Journal of Physical Chemistry B* **2012**, 116, 6536–6542.
- (67) Zhang, J.; Zhu, Z.; Yu, Z., et al. *Materials Horizons* **2019**, 6, 90–96.

- (68) Huang, Y.; Zhou, J.; Su, B., et al. *Journal of the American Chemical Society* **2012**, *134*, 17053–17058.
- (69) Lozano, G.; Miguez, H. *Langmuir* **2007**, *23*, 9933–9938.
- (70) Jiang, P.; Bertone, J. F.; Hwang, K. S.; Colvin, V. L. *Chemistry of Materials* **1999**, *11*, 2132–2140.
- (71) Kang, H.; Lee, J. S.; Chang, W. S.; Kim, S. H. *Advanced Materials* **2015**, *27*, 1282–1287.
- (72) Stein, A.; Li, F.; Denny, N. R. *Chemistry of Materials* **2007**, *20*, 649–666.
- (73) Hatton, B.; Mishchenko, L.; Davis, S.; Sandhage, K. H.; Aizenberg, J. *Proceedings of the National Academy of Sciences of the United States of America* **2010**, *107*, 10354–10359.
- (74) Phillips, K. R.; Shirman, T.; Shirman, E., et al. *Advanced Materials* **2018**, *30*, e1706329.
- (75) Vos, W. L.; Megens, M.; van Kats, C. M.; Bösecke, P. *Langmuir* **1997**, *13*, 6004–6008.
- (76) Wijnhoven, J. E. G. J.; Vos, W. L. *Science* **1998**, *281*, 802–804.
- (77) Xu, X.; Colfen, H. *Nanomaterials* **2021**, *11*, 333.
- (78) Ma, C.; Jiang, Y.; Yang, X., et al. *ACS Applied Materials & Interfaces* **2013**, *5*, 1990–1996.
- (79) Li, J.; Luan, S.; Huang, W.; Han, Y. *Colloids and Surfaces A: Physicochemical and Engineering Aspects* **2007**, *295*, 107–112.
- (80) Schweikart, A.; Fortini, A.; Wittemann, A.; Schmidt, M.; Fery, A. *Soft Matter* **2010**, *6*, 5860–5863.
- (81) Mishchenko, L.; Hatton, B.; Kolle, M.; Aizenberg, J. *Small* **2012**, *8*, 1904–1911.
- (82) Fustin, C. A.; Glasser, G.; Spiess, H. W.; Jonas, U. *Advanced Materials* **2003**, *15*, 1025–1028.
- (83) Brozell, A. M.; Muha, M. A.; Parikh, A. N. *Langmuir* **2005**, *21*, 11588–11591.
- (84) Li, X.; Chen, L.; Ma, Y., et al. *Advanced Functional Materials* **2022**, *32*, 2205462.
- (85) Park, J.; Moon, J.; Shin, H.; Wang, D.; Park, M. *Journal of Colloid and Interface Science* **2006**, *298*, 713–719.
- (86) Wang, J.; Wang, L.; Song, Y.; Jiang, L. *Journal of Materials Chemistry C* **2013**, *1*, 6048–6058.
- (87) Wu, L.; Dong, Z.; Kuang, M., et al. *Advanced Functional Materials* **2015**, *25*, 2237–2242.
- (88) Wintzheimer, S.; Granath, T.; Oppmann, M., et al. *ACS Nano* **2018**, *12*, 5093–5120.
- (89) Wang, Y.; Wise, A. K.; Tan, J., et al. *Small* **2014**, *10*, 4244–4248.
- (90) Wang, J.; Schwenger, J.; Strobel, A., et al. *Science Advances* **2021**, *7*, eabj0954.
- (91) Wang, J.; Mbah, C. F.; Przybilla, T., et al. *Nature Communications* **2018**, *9*, 5259.

- (92) Garcia, P. D.; Sapienza, R.; Lopez, C. *Advanced Materials* **2010**, *22*, 12–19.
- (93) Scott, G. D.; Kilgour, D. M. *Journal of Physics D: Applied Physics* **1969**, *2*, 863–866.
- (94) Torquato, S.; Truskett, T. M.; Debenedetti, P. G. *Physical Review Letters* **2000**, *84*, 2064–2067.
- (95) Shen, H.; Liang, Q.; Song, L., et al. *Journal of Materials Science* **2019**, *55*, 2353–2364.
- (96) Iwata, M.; Teshima, M.; Seki, T.; Yoshioka, S.; Takeoka, Y. *Advanced Materials* **2017**, *29*, 1605050.
- (97) Highley, C. B.; Song, K. H.; Daly, A. C.; Burdick, J. A. *Advanced Science* **2019**, *6*, 1801076.
- (98) Wyss, H. M.; Blair, D. L.; Morris, J. F.; Stone, H. A.; Weitz, D. A. *Physical review E: Statistical, nonlinear, and soft matter physics* **2006**, *74*, 061402.
- (99) Naoi, Y.; Seki, T.; Ohnuki, R.; Yoshioka, S.; Takeoka, Y. *Langmuir* **2019**, *35*, 13983–13990.
- (100) Demirors, A. F.; Poloni, E.; Chiesa, M., et al. *Nature Communications* **2022**, *13*, 4397.
- (101) Park, J. G.; Kim, S. H.; Magkiriadou, S., et al. *Angewandte Chemie* **2014**, *53*, 2899–903.
- (102) Velikov, K. P.; Christova, C. G.; Dullens, R. P.; van Blaaderen, A. *Science* **2002**, *296*, 106–109.
- (103) Vogel, N.; de Viguerie, L.; Jonas, U.; Weiss, C. K.; Landfester, K. *Advanced Functional Materials* **2011**, *21*, 3064–3073.
- (104) Forster, J. D.; Noh, H.; Liew, S. F., et al. *Advanced Materials* **2010**, *22*, 2939–2944.
- (105) Kim, S. H.; Magkiriadou, S.; Rhee, D. K., et al. *ACS Applied Materials & Interfaces* **2017**, *9*, 24155–24160.
- (106) Zhang, Y.; Dong, B.; Chen, A., et al. *Advanced Materials* **2015**, *27*, 4719–4724.
- (107) Katagiri, K.; Tanaka, Y.; Uemura, K., et al. *NPG Asia Materials* **2017**, *9*, e355–e355.
- (108) Li, Z.; Ma, T.; Li, S., et al. *ACS Nano* **2022**, *16*, 11473–11482.
- (109) Kawamura, A.; Kohri, M.; Morimoto, G., et al. *Scientific Reports* **2016**, *6*, 33984.
- (110) Pedrotti, F. L.; Pedrotti, L. M.; Pedrotti, L. S., *Introduction to optics*; Cambridge University Press: 2017.
- (111) Starr, C.; Evers, C.; Starr, L., *Biology: concepts and applications*; Cengage Learning: 2014.
- (112) Tilley, R. J., *Understanding solids: the science of materials*; John Wiley & Sons: 2004.
- (113) Fowles, G. R., *Introduction to modern optics*; Courier Corporation: 1989.
- (114) Yin, H.; Shi, L.; Sha, J., et al. *Physical review E: Statistical, nonlinear, and soft matter physics* **2006**, *74*, 051916.

- (115) Gao, L.; Lemarchand, F.; Lequime, M. *Journal of the European Optical Society-Rapid publications* **2013**, *8*.
- (116) Jolivet, A.; Labbé, C.; Frilay, C., et al. *Applied Surface Science* **2023**, *608*, 155214.
- (117) Hart, S. D.; Maskaly, G. R.; Temelkuran, B., et al. *Science* **2002**, *296*, 510–513.
- (118) Thompson, R., *Optical waves in layered media*; Taylor & Francis: 1990.
- (119) Sharhan, A. A. *Journal of Physics: Conference Series* **2020**, *1535*, 012018.
- (120) Keskar, D.; Survase, S.; Thakurdesai, M. *Journal of Physics: Conference Series* **2021**, *1913*, 012051.
- (121) Anaya, M.; Rubino, A.; Calvo, M. E.; Míguez, H. *Journal of Materials Chemistry C* **2016**, *4*, 4532–4537.
- (122) Joannopoulos, J. D.; Villeneuve, P. R.; Fan, S. *Nature* **1997**, *386*, 143–149.
- (123) Joannopoulos, J. D.; Villeneuve, P. R.; Fan, S. *Solid State Communications* **1997**, *102*, 165–173.
- (124) John, S. *Physical Review Letters* **1987**, *58*, 2486–2489.
- (125) Yablonovitch, E. *Physical Review Letters* **1987**, *58*, 2059–2062.
- (126) Joannopoulos, J. D.; Johnson, S. G.; Winn, J. N.; Meade, R. D. *Princeton Univ. Press. Princeton, NJ* **2008**.
- (127) Soukoulis, C. M., *Photonic band gap materials*; Springer Science & Business Media: 2012; Vol. 315.
- (128) Borchardt-Ott, W., *Crystallography*, 2012.
- (129) Setyawan, W.; Curtarolo, S. *Computational materials science* **2010**, *49*, 299–312.
- (130) Bohm, J.; Heimann, R. B.; Bohm, M. *Crystal Research and Technology* **1996**, *31*, 1069–1075.
- (131) Monkhorst, H. J.; Pack, J. D. *Physical Review B* **1976**, *13*, 5188–5192.
- (132) Rumpf, R. empossible.net, Web Page.
- (133) Comoretto, D., *Organic and Hybrid Photonic Crystals*, 2015.
- (134) Maurin, F.; Claeys, C.; Deckers, E.; Desmet, W. *International Journal of Solids and Structures* **2018**, *135*, 26–36.
- (135) Johnson, S.; Joannopoulos, J. *Opt Express* **2001**, *8*, 173–90.
- (136) Johnson, S. G. <https://github.com/NanoComp/mpb>, Web Page.
- (137) Choi, S. S.; Morris, S. M.; Huck, W. T. S.; Coles, H. J. *Advanced Materials* **2009**, *21*, 3915–3918.
- (138) Xiong, R.; Wu, W.; Lu, C.; Colfen, H. *Advanced Materials* **2022**, *34*, e2206509.
- (139) Urbas, A. M.; Maldovan, M.; DeRege, P.; Thomas, E. L. *Advanced Materials* **2002**, *14*, 1850–1853.
- (140) Kang, Y.; Walish, J. J.; Gorishnyy, T.; Thomas, E. L. *Nature Materials* **2007**, *6*, 957–960.
- (141) Colvin, V. L. *MRS Bulletin* **2011**, *26*, 637–641.

- (142) Anselmann, R.; Winkler, H. *Advanced Engineering Materials* **2003**, *5*, 560–562.
- (143) Lange, B.; Fleischhaker, F.; Zentel, R. *Macromolecular Rapid Communications* **2007**, *28*, 1291–1311.
- (144) Marlow, F.; Muldarisnur; Sharifi, P.; Brinkmann, R.; Mendive, C. *Angewandte Chemie* **2009**, *48*, 6212–6233.
- (145) Kim, J. B.; Lee, S. Y.; Lee, J. M.; Kim, S. H. *ACS Applied Materials & Interfaces* **2019**, *11*, 14485–14509.
- (146) Kim, S.-H.; Lee, S. Y.; Yang, S.-M.; Yi, G.-R. *NPG Asia Materials* **2011**, *3*, 25–33.
- (147) Aguirre, C. I.; Reguera, E.; Stein, A. *Advanced Functional Materials* **2010**, *20*, 2565–2578.
- (148) Huang, G.; Yin, Y.; Pan, Z., et al. *Biomacromolecules* **2014**, *15*, 4396–4402.
- (149) Mekis, A.; Chen, J. C.; Kurland, I. I., et al. *Physical Review Letters* **1996**, *77*, 3787–3790.
- (150) Lin, S. Y.; Chow, E.; Hietala, V. V.; Villeneuve, P. R.; Joannopoulos, J. D. *Science* **1998**, *282*, 274–276.
- (151) Cubukcu, E.; Aydin, K.; Ozbay, E.; Foteinopoulou, S.; Soukoulis, C. M. *Nature* **2003**, *423*, 604–605.
- (152) Kosaka, H.; Kawashima, T.; Tomita, A., et al. *Applied Physics Letters* **1999**, *74*, 1212–1214.
- (153) Zhang, W.; Zhang, G. *Optik* **2016**, *127*, 7162–7166.
- (154) Yan, J.; Zhang, J.; Sun, Q.; Yan, X.; Sheng, J. *Dyes and Pigments* **2021**, *184*, 108753.
- (155) Armstrong, E.; O'Dwyer, C. *Journal of Materials Chemistry C* **2015**, *3*, 6109–6143.
- (156) Iler, R. K. *Nature* **1965**, *207*, 472–473.
- (157) Xia, Y.; Gates, B.; Li, Z. Y. *Advanced Materials* **2001**, *13*, 409–413.
- (158) Von Freymann, G.; Kitaev, V.; Lotsch, B. V.; Ozin, G. A. *Chemical Society Reviews* **2013**, *42*, 2528–2554.
- (159) Maldovan, M.; Thomas, E. L. *Nature Materials* **2004**, *3*, 593–600.
- (160) Yablonovitch, E.; Gmitter, T. J.; Leung, K. M. *Physical Review Letters* **1991**, *67*, 2295–2298.
- (161) Maiwald, L.; Sommer, T.; Sidorenko, M. S., et al. *Advanced Optical Materials* **2021**, *10*, 2100785.
- (162) Mandal, C.; Donthula, S.; Soni, R., et al. *Journal of Sol-Gel Science and Technology* **2018**, *90*, 127–139.
- (163) Olmos-Trigo, J.; Sanz-Fernandez, C.; Abujetas, D. R., et al. *Physical Review Letters* **2020**, *125*, 073205.
- (164) Zhang, Y.; Chen, S.; Han, J. *Molecules* **2021**, *26*, 6106.
- (165) Bohren, C. F.; Huffman, D. R., *Absorption and Scattering of Light by Small Particles*, 1998.
- (166) Christoffel, H.; Hulst, v. d., *Light scattering by small particles*; Courier Corporation: 1981.

- (167) Platt, U.; Pfeilsticker, K.; Vollmer, M. In *Springer Handbook of Lasers and Optics*, 2007; Chapter Chapter 19, pp 1165–1203.
- (168) Zagury, F. *Atmospheric and Climate Sciences* **2012**, *02*, 510–517.
- (169) Deirmendjian, D., *Electromagnetic Scattering on Spherical Polydispersions*; American Elsevier Pub. Co.: New York, 1969.
- (170) Mie, G. *Annalen der Physik* **1908**, *330*, 377–445.
- (171) Wang, H.; Fu, K.; Drezek, R. A.; Halas, N. J. *Applied Physics B* **2006**, *84*, 191–195.
- (172) Wiscombe, W. J., *Mie scattering calculations: Advances in technique and fast, vector-speed computer codes*; National Technical Information Service, US Department of Commerce: 1979; Vol. 10.
- (173) Prahl, S. <https://github.com/scottprahl/miepython>, Web Page.
- (174) Väisänen, T.; Martikainen, J.; Muinonen, K. *Journal of Quantitative Spectroscopy and Radiative Transfer* **2020**, *241*, 106719.
- (175) Chýlek, P. *Journal of the Optical Society of America* **1976**, *66*, 285–287.
- (176) Wiersma, D. S. *Nature Photonics* **2013**, *7*, 188–196.
- (177) Karg, M.; König, T. A. F.; Retsch, M., et al. *Materials Today* **2015**, *18*, 185–205.
- (178) Syurik, J.; Siddique, R. H.; Dollmann, A., et al. *Scientific Reports* **2017**, *7*, 46637.
- (179) Hou, J.; Wang, L.; Wang, C., et al. *Journal of Environmental Sciences* **2019**, *75*, 40–53.
- (180) Vukusic, P.; Hallam, B.; Noyes, J. *Science* **2007**, *315*, 348–348.
- (181) Cortese, L.; Pattelli, L.; Utel, F., et al. *Advanced Optical Materials* **2015**, *3*, 1337–1341.
- (182) Wilts, B. D.; Sheng, X.; Holler, M., et al. *Advanced Materials* **2018**, *30*, e1702057.
- (183) Jacucci, G.; Schertel, L.; Zhang, Y.; Yang, H.; Vignolini, S. *Advanced Materials* **2021**, *33*, e2001215.
- (184) Caixeiro, S.; Peruzzo, M.; Onelli, O. D.; Vignolini, S.; Sapienza, R. *ACS Applied Materials & Interfaces* **2017**, *9*, 7885–7890.
- (185) Vasileva, E.; Chen, H.; Li, Y., et al. *Advanced Optical Materials* **2018**, *6*, 1800999.
- (186) Yang, H.; Jacucci, G.; Schertel, L.; Vignolini, S. *ACS Nano* **2022**, *16*, 7373–7379.
- (187) Jacucci, G.; Bertolotti, J.; Vignolini, S. *Advanced Optical Materials* **2019**, *7*, 1900980.
- (188) Jacucci, G.; Longbottom, B. W.; Parkins, C. C.; Bon, S. A. F.; Vignolini, S. *Journal of Materials Chemistry C* **2021**, *9*, 2695–2700.
- (189) Utel, F.; Cortese, L.; Wiersma, D. S.; Pattelli, L. *Advanced Optical Materials* **2019**, *7*, 1900043.

- (190) Raman, A. P.; Anoma, M. A.; Zhu, L.; Rephaeli, E.; Fan, S. *Nature* **2014**, *515*, 540–544.
- (191) Jaramillo-Fernandez, J.; Yang, H.; Schertel, L., et al. *Advanced Science* **2022**, *9*, e2104758.
- (192) Ishimaru, A., *Wave Propagation and Scattering in Random Media*; Academic Press: New York, 1978.
- (193) Fang, Z.; Zhu, H.; Bao, W., et al. *Energy & Environmental Science* **2014**, *7*, 3313–3319.
- (194) Liang, G.; Yu, S.; Huang, Z., et al. *Advanced Photonics Research* **2021**, *2*, 2100185.
- (195) Toivonen, M. S.; Onelli, O. D.; Jacucci, G., et al. *Advanced Materials* **2018**, *30*, e1704050.
- (196) Semmler, J.; Bley, K.; Klupp Taylor, R. N.; Stingl, M.; Vogel, N. *Advanced Functional Materials* **2019**, *29*, 1806025.
- (197) Romanov, S. G.; Orlov, S.; Ploss, D., et al. *Scientific Reports* **2016**, *6*, 27264.
- (198) Galisteo-López, J. F.; Ibisate, M.; Sapienza, R., et al. *Advanced Materials* **2011**, *23*, 30–69.
- (199) García, P. D.; Sapienza, R.; Blanco, A.; López, C. *Advanced Materials* **2007**, *19*, 2597–2602.
- (200) Goerlitzer, E. S. A.; Klupp Taylor, R. N.; Vogel, N. *Advanced Materials* **2018**, *30*, e1706654.
- (201) Elaloufi, R.; Carminati, R.; Greffet, J. J. *Journal of the Optical Society of America. A, Optics, image science, and vision* **2004**, *21*, 1430–1437.
- (202) Shang, G.; Maiwald, L.; Renner, H., et al. *Scientific Reports* **2018**, *8*, 7804.
- (203) Shang, G.; Eich, M.; Petrov, A. *APL Photonics* **2020**, *5*, 060901.
- (204) Liew, S. F.; Yang, J.-K.; Noh, H., et al. *Physical Review A* **2011**, *84*, 063818.
- (205) Schertel, L.; Siedentop, L.; Meijer, J.-M., et al. *Advanced Optical Materials* **2019**, *7*, 1900442.
- (206) Noh, H.; Liew, S. F.; Saranathan, V., et al. *Advanced Materials* **2010**, *22*, 2871–2880.
- (207) Xiao, M.; Hu, Z.; Wang, Z., et al. *Science Advances* **2017**, *3*, e1701151.
- (208) Takeoka, Y.; Iwata, M.; Seki, T., et al. *Langmuir* **2018**, *34*, 4282–4288.
- (209) Kohri, M.; Yanagimoto, K.; Kawamura, A., et al. *ACS Applied Materials & Interfaces* **2018**, *10*, 7640–7648.
- (210) Takeoka, Y.; Yoshioka, S.; Takano, A., et al. *Angewandte Chemie* **2013**, *52*, 7261–7265.
- (211) Hwang, V.; Stephenson, A. B.; Barkley, S., et al. *Proceedings of the National Academy of Sciences of the United States of America* **2021**, *118*, e2015551118.

- (212) Dyachenko, P. N.; do Rosário, J. J.; Leib, E. W., et al. *ACS Photonics* **2014**, *1*, 1127–1133.
- (213) Shang, G.; Häntsch, Y.; Furlan, K. P., et al. *APL Photonics* **2019**, *4*, 046101.
- (214) Atiganyanun, S.; Plumley, J. B.; Han, S. J., et al. *ACS Photonics* **2018**, *5*, 1181–1187.
- (215) Li, Z.; Yin, Y. *Advanced Materials* **2019**, *31*, e1807061.
- (216) Däntl, M.; Jiménez-Solano, A.; Lotsch, B. V. *Materials Advances* **2022**, *3*, 7406–7424.
- (217) Liu, S.; Yang, Y.; Zhang, L.; Xu, J.; Zhu, J. *Journal of Materials Chemistry C* **2020**, *8*, 16633–16647.
- (218) Xu, H.; Cao, K. D.; Ding, H. B., et al. *ACS Applied Materials & Interfaces* **2012**, *4*, 6752–6757.
- (219) Shen, P.; Zhang, Y.; Cai, Z., et al. *Journal of Materials Chemistry C* **2021**, *9*, 5840–5857.
- (220) Ge, J.; Yin, Y. *Angewandte Chemie* **2011**, *50*, 1492–522.
- (221) Hawkeye, M. M.; Brett, M. J. *Advanced Functional Materials* **2011**, *21*, 3652–3658.
- (222) Mohd-Noor, S.; Jang, H.; Baek, K., et al. *Journal of Materials Chemistry A* **2019**, *7*, 10561–10571.
- (223) Fenzl, C.; Hirsch, T.; Wolfbeis, O. S. *Angewandte Chemie* **2014**, *53*, 3318–3335.
- (224) Zhang, Y.; Fu, Q.; Ge, J. *Nature Communications* **2015**, *6*, 7510.
- (225) Yang, Y.; Kim, H.; Xu, J., et al. *Advanced Materials* **2018**, *30*, e1707344.
- (226) Muscatello, M. M.; Asher, S. A. *Advanced Functional Materials* **2008**, *1186*, 18–18.
- (227) Holtz, J. H.; Asher, S. A. *Nature* **1997**, *389*, 829–832.
- (228) Lim, H. S.; Lee, J. H.; Walish, J. J.; Thomas, E. L. *ACS Nano* **2012**, *6*, 8933–8939.
- (229) Cai, Z.; Kwak, D. H.; Punihaole, D., et al. *Angewandte Chemie* **2015**, *54*, 13036–13040.
- (230) Teyssier, J.; Saenko, S. V.; van der Marel, D.; Milinkovitch, M. C. *Nature Communications* **2015**, *6*, 6368.
- (231) Chan, E. P.; Walish, J. J.; Thomas, E. L.; Stafford, C. M. *Advanced Materials* **2011**, *23*, 4702–4706.
- (232) Missinne, J.; Teigell Benítez, N.; Lamberti, A., et al. *Advanced Engineering Materials* **2018**, *20*, 1701127.
- (233) Hu, Y.; He, L.; Yin, Y. *Angewandte Chemie* **2011**, *123*, 3831–3834.
- (234) Foelen, Y.; Schenning, A. *Advanced Science* **2022**, *9*, e2200399.
- (235) Chiappelli, M. C.; Hayward, R. C. *Advanced Materials* **2012**, *24*, 6100–6104.
- (236) Chen, M.; Zhang, Y.; Jia, S., et al. *Angewandte Chemie* **2015**, *54*, 9257–9261.

- (237) Jurewicz, I.; King, A. A. K.; Shanker, R., et al. *Advanced Functional Materials* **2020**, *30*, 2002473.
- (238) Foelen, Y.; van der Heijden, D. A. C.; Verdurmen, A. M. J., et al. *Advanced Optical Materials* **2022**, *10*, 2201462.
- (239) Lee, S. Y.; Lee, J. S.; Kim, S. H. *Advanced Materials* **2019**, *31*, e1901398.
- (240) Ferry, J. D., *Viscoelastic properties of polymers*; John Wiley & Sons: 1980.
- (241) Ha, N.; Xu, K.; Ren, G.; Mitchell, A.; Ou, J. Z. *Advanced Intelligent Systems* **2020**, *2*, 2000063.
- (242) Othong, J.; Boonmak, J.; Kielar, F.; Youngme, S. *ACS Applied Materials & Interfaces* **2020**, *12*, 41776–41784.
- (243) Ramalho, J. F. C. B.; Correia, S. F. H.; Fu, L., et al. *Advanced Science* **2019**, *6*, 1900950.
- (244) Ramalho, J. F. C. B.; Dias, L. M. S.; Fu, L., et al. *Advanced Photonics Research* **2021**, *3*, 2100206.
- (245) Döring, A.; Rogach, A. L. *ACS Applied Nano Materials* **2022**, *5*, 11208–11218.
- (246) Pandit, S.; Banerjee, T.; Srivastava, I.; Nie, S.; Pan, D. *ACS Sensors* **2019**, *4*, 2730–2737.
- (247) Zhang, Y.; Yu, L.; Hu, Z., et al. *Journal of Lightwave Technology* **2021**, *39*, 1537–1543.
- (248) Lewis, C.; Erikson, J. W.; Sanchez, D. A., et al. *ACS Applied Nano Materials* **2020**, *3*, 4045–4053.
- (249) Ramalho, J. F. C. B.; Carlos, L. D.; André, P. S.; Ferreira, R. A. S. *Advanced Photonics Research* **2021**, *2*, 2000211.
- (250) Burgess, I. B.; Mishchenko, L.; Hatton, B. D., et al. *Journal of the American Chemical Society* **2011**, *133*, 12430–12432.
- (251) Bai, L.; Xie, Z.; Wang, W., et al. *ACS Nano* **2014**, *8*, 11094–11100.
- (252) Xie, Z.; Cao, K.; Zhao, Y., et al. *Advanced Materials* **2014**, *26*, 2413–2418.
- (253) Huang, Y.; Li, F.; Qin, M.; Jiang, L.; Song, Y. *Angewandte Chemie* **2013**, *52*, 7296–7299.
- (254) Potyrailo, R. A.; Bonam, R. K.; Hartley, J. G., et al. *Nature Communications* **2015**, *6*, 7959.
- (255) Yu, Y.; Brandt, S.; Nicolas, N. J.; Aizenberg, J. *ACS Applied Materials & Interfaces* **2020**, *12*, 1924–1929.
- (256) Claussen, K. U.; Giesa, R.; Scheibel, T.; Schmidt, H. W. *Macromolecular Rapid Communications* **2012**, *33*, 206–211.
- (257) Zhu, C.; Qiu, J.; Pongkitwitoon, S.; Thomopoulos, S.; Xia, Y. *Advanced Materials* **2018**, e1706706.
- (258) Hesse, S. A.; Werner, J. G.; Wiesner, U. *ACS Macro Letters* **2015**, *4*, 477–482.

- (259) Holtappels, P.; Sorof, C.; Verbraeken, M. C.; Rambert, S.; Vogt, U. *Fuel Cells* **2006**, *6*, 113–116.
- (260) Ye, F.; Cui, C.; Kirkeminde, A., et al. *Chemistry of Materials* **2010**, *22*, 2970–2977.
- (261) Giri, D.; Hanks, C. N.; Collinson, M. M.; Higgins, D. A. *Journal of Physical Chemistry C* **2014**, *118*, 6423–6432.
- (262) Ashraf, K. M.; Wang, C.; Nair, S. S., et al. *Langmuir* **2017**, *33*, 4207–4215.
- (263) Giri, D.; Li, Z.; Ashraf, K. M.; Collinson, M. M.; Higgins, D. A. *ACS Applied Materials & Interfaces* **2016**, *8*, 24265–24272.
- (264) Li, J.; Han, Y. *Langmuir* **2006**, *22*, 1885–1890.
- (265) Faustini, M.; Ceratti, D. R.; Louis, B., et al. *ACS Applied Materials & Interfaces* **2014**, *6*, 17102–17110.
- (266) Schedl, A. E.; Howell, I.; Watkins, J. J.; Schmidt, H. W. *Macromolecular Rapid Communications* **2020**, *41*, e2000069.
- (267) Schedl, A. E.; Neuber, C.; Fery, A.; Schmidt, H. W. *Langmuir* **2018**, *34*, 14249–14253.
- (268) Li, X.; Gao, J.; Xue, L.; Han, Y. *Advanced Functional Materials* **2010**, *20*, 259–265.
- (269) Kubrin, R.; Pasquarelli, R. M.; Waleczek, M., et al. *ACS Applied Materials & Interfaces* **2016**, *8*, 10466–10476.
- (270) Zhang, L.; Wang, J.; Tao, S.; Geng, C.; Yan, Q. *Advanced Optical Materials* **2018**, *6*, 1701344.
- (271) Mamedov, A. A.; Belov, A.; Giersig, M.; Mamedova, N. N.; Kotov, N. A. *Journal of the American Chemical Society* **2001**, *123*, 7738–7739.
- (272) Fu, Y.; An, Y.; Xu, Y.; Dai, J.-G.; Lei, D. *EcoMat* **2022**, *4*, e12169.
- (273) Hayran, Z.; Kurt, H.; Staliunas, K. *Scientific Reports* **2017**, *7*, 3046.
- (274) Shen, Y.; Ye, D.; Celanovic, I., et al. *Science* **2014**, *343*, 1499–1501.
- (275) Cassan, E.; Do, K.-V.; Caer, C.; Marris-Morini, D.; Vivien, L. *Journal of Lightwave Technology* **2011**, *29*, 1937–1943.
- (276) Skibina, J. S.; Iliew, R.; Bethge, J., et al. *Nature Photonics* **2008**, *2*, 679–683.
- (277) Vaidya, N.; Solgaard, O. *Microsystems & Nanoengineering* **2022**, *8*, 69.
- (278) Ludwig, A. *npj Computational Materials* **2019**, *5*, 70.
- (279) Müller, M. B.; Kuttner, C.; König, T. A., et al. *ACS Nano* **2014**, *8*, 9410–9421.
- (280) Kuttner, C.; Piotta, V.; Liz-Marzán, L. M. *Chemistry of Materials* **2021**, *33*, 8904–8914.
- (281) Collins, B. E.; Dancil, K. P. S.; Abbi, G.; Sailor, M. J. *Advanced Functional Materials* **2002**, *12*.
- (282) Von Freymann, G.; John, S.; Kitaev, V.; Ozin, G. A. *Advanced Materials* **2005**, *17*, 1273–1276.

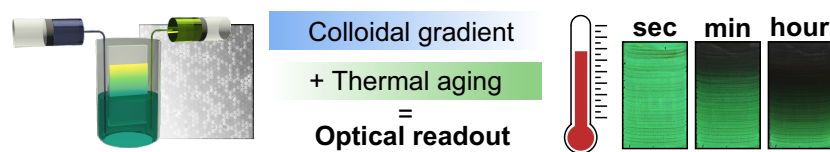
- (283) Elsing, J.; Quell, A.; Stubenrauch, C. *Advanced Engineering Materials* **2017**, *19*, 1700195.
- (284) Spinnrock, A.; Schupp, D.; Colfen, H. *Small* **2018**, *14*, e1803518.
- (285) Xu, X.; Franke, T.; Schilling, K.; Sommerdijk, N.; Colfen, H. *Nano Lett* **2019**, *19*, 1136–1142.
- (286) Liu, W.; Midya, J.; Kappl, M.; Butt, H. J.; Nikoubashman, A. *ACS Nano* **2019**, *13*, 4972–4979.
- (287) Chen, M.; Colfen, H.; Polarz, S. *ACS Nano* **2015**, *9*, 6944–50.
- (288) Chen, M.; Hagedorn, K.; Colfen, H.; Polarz, S. *Advanced Materials* **2017**, *29*, 1603356.
- (289) Bahner, J.; Klinkenberg, N.; Frisch, M.; Brauchle, L.; Polarz, S. *Advanced Functional Materials* **2019**, *29*, 1904058.
- (290) Gates, B.; Xia, Y. *Advanced Materials* **2000**, *12*, 1329–1332.
- (291) Kim, S. H.; Jeong, W. C.; Hwang, H.; Yang, S. M. *Angewandte Chemie* **2011**, *50*, 11649–11653.
- (292) Chi, J.; Shao, C.; Zhang, Y., et al. *Nanoscale* **2019**, *11*, 12898–12904.
- (293) Ding, H.; Liu, C.; Ye, B., et al. *ACS Applied Materials & Interfaces* **2016**, *8*, 6796–6801.
- (294) Ding, H.; Liu, C.; Gu, H., et al. *ACS Photonics* **2014**, *1*, 121–126.
- (295) Schöttle, M.; Tran, T.; Feller, T.; Retsch, M. *Advanced Materials* **2021**, *33*, 2101948.
- (296) Schöttle, M.; Lauster, T.; Roemling, L. J.; Vogel, N.; Retsch, M. *Advanced Materials* **2023**, *35*, 2208745.
- (297) Olympus, *Handbook: LEXT - OLS5100*, 2023.
- (298) OceanOptics, *Handbook: USB4000 Spectrometer*, 2023.
- (299) Schöttle, M.; Tran, T.; Oberhofer, H.; Retsch, M. *Advanced Science* **2023**, *10*, 2205512.
- (300) Schöttle, M.; Theis, M.; Lauster, T.; Hauschild, S.; Retsch, M. *Advanced Optical Materials* **2023**, *11*, 2300095.

Part II

Publications

Time–temperature integrating optical sensors based on gradient colloidal crystals

Marius Schöttle, Thomas Tran, Tanja Feller, and Markus Retsch, „Time temperature integrating optical sensors based on gradient colloidal crystals“, *Advanced Materials*, **2021**, 33(40), 2101948.

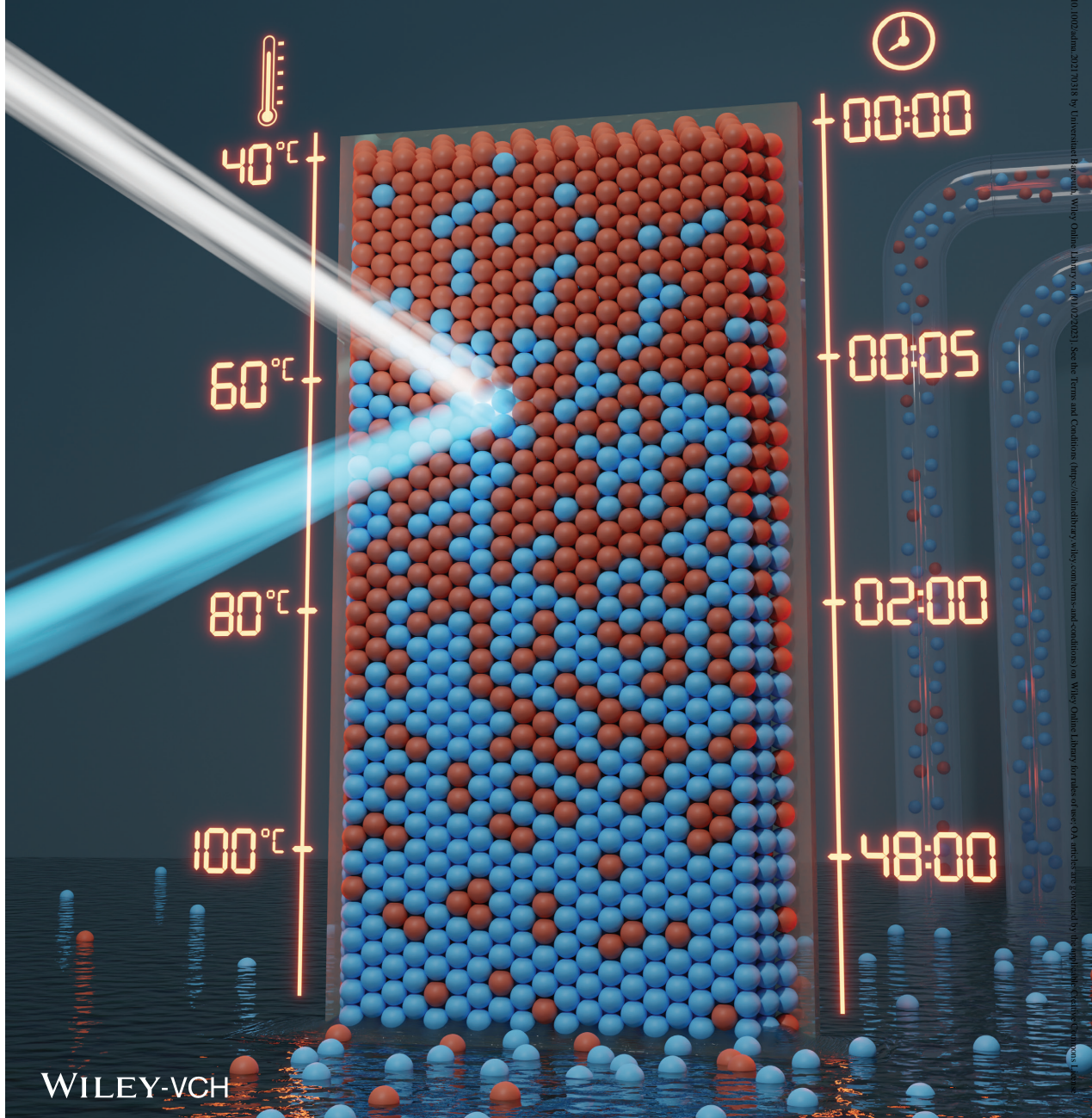


We introduce a colloidal stopband-based time-temperature integrator, which can monitor the thermal history of a specific system over an adjustable time and temperature range. The fabrication of a binary colloidal crystal gradient comprising same sized, monodisperse particles with distinct glass transition temperatures are the key components for this type of integrating sensor.

Vol. 33 • No. 40 • October 7 • 2021

www.advmat.de

ADVANCED MATERIALS



WILEY-VCH

1521-4095, 2021, 40, Downloaded from https://onlinelibrary.wiley.com/doi/10.1002/adma.202121018 by Universitaet Bayreuth, Wiley Online Library on [02/02/2023]. See the Terms and Conditions (https://onlinelibrary.wiley.com/terms-and-conditions) on Wiley Online Library for rules of use; OA articles are governed by the applicable Creative Commons License

Time–Temperature Integrating Optical Sensors Based on Gradient Colloidal Crystals

Marius Schöttle, Thomas Tran, Tanja Feller, and Markus Retsch*

Manipulation-free and autonomous recording of temperature states for extended periods of time is of increasing importance for food spoilage and battery safety assessment. An optical readout is preferred for low-tech visual inspection. Here, a concept for time–temperature integrators based on colloidal crystals is introduced. Two unique features in this class of advanced materials are combined: 1) the film-formation kinetics can be controlled by orders of magnitude based on mixtures of particles with distinct glass transition temperatures. 2) A gradual variation of the particle mixture along a linear gradient of the colloidal crystal enables local readout. Tailor-made latex particles of identical size but different glass transition temperatures provide a homogenous photonic stopband. The disappearance of this opalescence is directly related to the local particle ratio and the exposure to a time and temperature combination. This sensing material can be adjusted to report extended intermediate and short excessive temperature events, which makes it specifically suitable for long-term tracing and threshold applications.

and catalysis,^[8,9] to name a few. By far most prominent is, however, their periodic refractive index modulation, resulting in vivid structural colors. Consequently, colloidal crystals are predestined for sensing, where significant color changes can often be recognized with the bare eye.^[10–12] A shift of the optical stopband, as well as a change of the opalescence intensity, can serve as an indicator for changes inflicted to the colloidal ensemble. Such changes can be caused by temperature,^[13,14] force,^[15,16] humidity,^[17–19] pH,^[20,21] ionic strength/complexation,^[22] wettability,^[23,24] or biodegradation^[25] and either alter the refractive index contrast (change in intensity), the periodicity of the structure (change in bandgap), or both. The sensing performance can be further tuned, for example, by the introduction of fluorescence for organic vapor detection.^[26–28]


1. Introduction

Particle-based colloidal crystals (CCs) and inverse opals have been subject to extensive research for a long time.^[1] For homogeneous and patterned colloidal assembly structures a wide range of fabrication techniques has been investigated and established, which render such nanostructured films a mature area of research.^[2] The intricate nanostructure on a length scale of a few to hundreds of nanometers raised interest in fields such as granular mechanics,^[3,4] heat transport,^[5,6] phononics,^[7]

An important and general distinction of sensors is their classification into reversible and irreversible ones. Reversible sensors indicate the actual condition of a system in real-time. Temperature-dependent color changes of liquid crystals are a wide-spread example of this. In the case of monitoring certain predefined limits, irreversible sensors are more suitable as they allow judging the history of a certain state. Irreversible sensors are especially relevant in food or drug transportation and storage.^[29,30] When the readout response changes in a gradual and slow manner, irreversible sensors can also indicate the degree to which a certain state has been exceeded. This provides additional information either regarding the time or intensity that a certain state has been reached. Considering the role of colloidal crystals in the field of irreversible sensors, the loss of opalescence at the film-forming temperature is obvious. This process is also called dry-sintering and has been studied already.^[31–33] The onset of dry-sintering is related to the glass transition temperature (T_g) in the case of polymer colloidal crystals. At this point, the optical and thermal properties change abruptly, corresponding to the structural degradation process. The concomitant loss of contrast and periodicity diminishes both photonic opalescence and thermal insulation properties.^[34,35] Introduction of additives can alter the kinetics and reversibility of this film formation process, which allows correlating time and temperature processes.^[36] Random mixtures of two monodisperse particle types with different glass transition temperatures allowed to change the abrupt jump in thermal conductivity at the glass transition temperature to a gradual one.^[37] An even more elaborate microstructural design

M. Schöttle, T. Tran, T. Feller, Prof. M. Retsch
Department of Chemistry
Physical Chemistry I
University of Bayreuth
Universitätsstr. 30, 95447 Bayreuth, Germany
E-mail: markus.retsch@uni-bayreuth.de

Prof. M. Retsch
Bavarian Center for Battery Technology (BayBatt)
Bavarian Polymer Institute
and Bayreuth Center for Colloids and Interfaces
University of Bayreuth
Universitätsstr. 30, 95447 Bayreuth, Germany

 The ORCID identification number(s) for the author(s) of this article can be found under <https://doi.org/10.1002/adma.202101948>.

© 2021 The Authors. Advanced Materials published by Wiley-VCH GmbH. This is an open access article under the terms of the Creative Commons Attribution License, which permits use, distribution and reproduction in any medium, provided the original work is properly cited.

DOI: 10.1002/adma.202101948

with locally controlled film formation kinetics was introduced by Lee et al.^[38] Polymer inverse opals with locally varied cross-linking densities allowed to determine the temperature and exposure time simultaneously.

The aforementioned work is an excellent example of the emerging possibilities of future functional materials, where unconventional properties can be realized by a local control on the fundamental material properties. Lithographic (micro) patterning of colloidal structures has been investigated by various groups already.^[39] Much fewer systems have been reported in the case of CCs and inverse opals, where the structure or composition is gradually altered. First examples for tuning the lattice spacing have been realized by means of diffusion,^[40,41] compression,^[42,43] wrinkling,^[44,45] or an external magnetic field.^[46] Ultracentrifugation has also been used for the preparation of colloidal gradients.^[47–49]

In this work, we demonstrate how a controlled spatial variation of the colloidal crystal composition allows realizing a time–temperature integrator. We introduce two new aspects to the field of colloidal materials. First, we elaborate a logarithmic dry-sintering kinetic behavior based on random binary CCs consisting of high- and low- T_g polymer particles. Second, we introduce a method to fabricate thin-film colloidal crystals with a compositional gradient. The synergistic combination of composition-dependent kinetics and local composition control results in an adjustable time–temperature integrating sensor with a position-dependent optical readout.

2. Results and Discussion

The dry-sintering kinetic properties of a homogeneous CC consisting of purely low- T_g particles are well known (Figure 1a). We, therefore, fabricated homogeneous colloidal crystals comprising monodisperse poly[(methyl methacrylate)-*random*-(butyl acrylate)] (PMMA-*r*-nBA) colloids via dip-coating from aqueous dispersions. As a larger contact area between neighboring particles is formed and the air is expelled from the structure, the periodic variation of the refractive index is lost. Concomitantly, the structural color vanishes and the cracks between crystalline domains become larger to accommodate shrinkage, which can be seen in the microscopy images from top to bottom (Figure 1a). Transmission UV–vis spectra (Figure 1b) show a slight blueshift of the photonic stopband of approximately 10 nm and an even more pronounced decrease of the intensity (purple to yellow color). The normalized stopband intensity can be used as a measure for the kinetics of the film formation process (Figure 1c, details in Figures S1 and S2, Supporting Information). We use a semi-logarithmic scale for a clearer representation of the temporal evolution of the sintering behavior. For the specific case shown here ($T_g = 49$ °C, sintering temperature $T = 60$ °C), the film formation process is complete after about 4 min (normalized intensity decayed to ≈ 0). Scanning electron microscopy (SEM) images of the colloidal crystal before and after sintering at 60 °C for 100 min (Figure 1d,g) confirm the expected loss of porosity during the film formation.

Adding various amounts of a second latex bead of the same size but with a different glass transition temperature ($T_g = 94$ °C, Figure S3, Supporting Information) to the

dip-coating dispersion does not compromise the colloidal crystal formation, but it strongly influences the film formation process. When 50% high- T_g particles are added, the hexagonal lattice structure is retained, but only half of the particles experience deformation during sintering at 60 °C (Figure 1e,h). This leads to particle patches with retained shape and interstitial space. The surface impression provided by SEM is confirmed by the bulk behavior of the stopband, where a blue structural color is retained (Figure 1h, inset). Heating a CC composed purely of high- T_g particles at 60 °C shows no effect, and the structure remains unaltered (Figure 1f,i).

Analogous to the pure low- T_g system, we quantified the sintering kinetics of various binary CC compositions by in situ UV–vis measurements at 60 °C. Figure 1k summarizes the time-dependent decay of the normalized stopband intensity for these systems. Quite strikingly, the binary compositions shift the film formation kinetics by orders of magnitude to longer time scales with an increasing amount of high- T_g particles. Each individual system follows an exponential decay at first glance. We, nevertheless, want to stress that this optical analysis is not sufficient to unravel the detailed mechanics of this process. Dry-sintering of polymer colloids takes place in a number of different steps, including, for example, contact area formation.^[32] The underlying refractive index matching is presumed to arise from viscous polymer flow of the low- T_g component and capillary infiltration of cavities between non-sintered particles. Each step most likely shows a unique temperature dependence, and we will therefore compare these results only qualitatively. One may infer a jump in decay kinetics between the 50% and 60% low- T_g particle composition in Figure 1k. We rationalize this by examining SEM images of all sample compositions sintered at 60 °C (Figure S4, Supporting Information). A gradual change in composition results in a transition from a continuous low- T_g particle network to isolated domains. This is most evident between 40–60% low- T_g particles, where the majority phase inverts. The presence of islands of one particle type is not an effect of phase separation. In Figure S5, Supporting Information, SEM images of partially sintered CCs are compared to a 2D-simulation of a random distribution of two particle types. An analysis of the mean absolute number of neighboring, non-sintered particles in the first, second, and third generation is performed for both the measured and simulated images. The relative intensities as well as the absolute values show a significant overlap between the experimental and simulated data. This comparison confirms the statistical distribution expected due to the same size and surface chemistry of the two particle types.

The observed sintering behavior is rather intriguing as it allows an adjustment of the thermal response simply by mixing particles at a defined ratio with two distinct glass transition temperatures. The dependence of time, composition, and normalized stopband intensity result in a wide parameter space that can be difficult to grasp. We, therefore, introduce an alternative way to visualize the film formation kinetics (Figure 1l,m). Here, the normalized intensity is plotted versus the composition and color-coded with respect to the sintering time. Each line represents one specific composition. Figure 1l connects the time-scale to the crystal composition. It also helps to understand the representation in Figure 1m, from which the expected stopband intensity can be derived for any sintering time and any particle

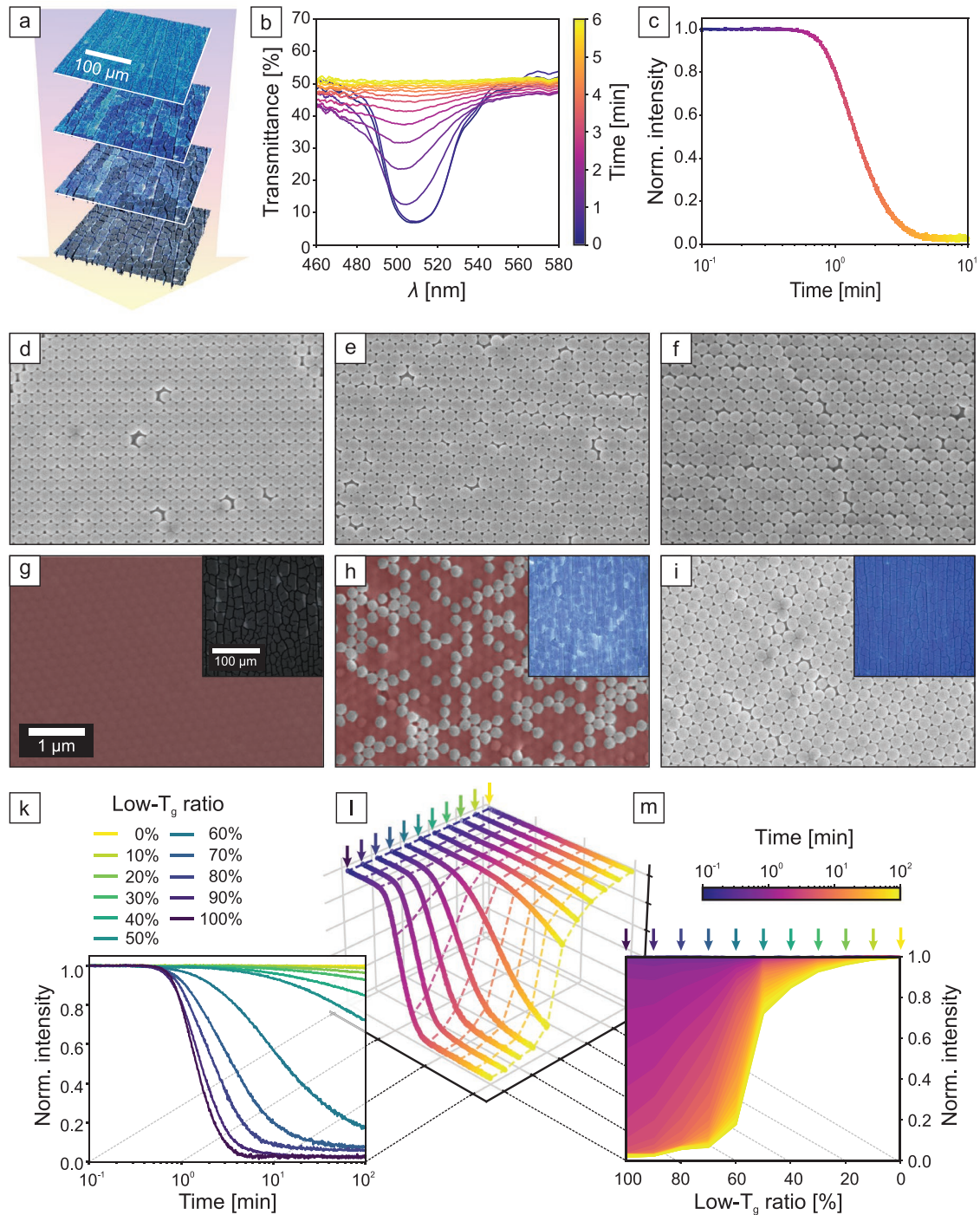


Figure 1. Characterization of the film-formation of colloidal crystals at 60 °C. a) Optical microscopy images show the simultaneous color fading (blue to gray) and crack formation (thin dark lines) during the film-formation of 100% low- T_g particles. b) In situ transmission UV–vis spectra showing the temporal change of the photonic stopband during the film-formation process shown in (a). c) Time-dependent decay curve calculated from the normalized stopband intensity shown in (b) to quantify the loss of opalescence. d–f) Scanning electron microscopy images of pristine colloidal crystals consisting of 100%, 50%, and 0% low- T_g particles, respectively. g–i) Images of the same samples after 100 min at 60 °C. Dense, sintered regions are color-coded in red, original SEM images are shown in Figure S4, Supporting Information. Insets show light microscopy images, where a loss of the photonic stopband and the appearance of cracks is visible when transitioning from a pristine to a sintered film. k) Stopband decay curves of various compositions between 100% and 0% low- T_g particles. (l) and (m) show how the data in (k) can be transformed to convert the time-dependent measurement into a composition-dependent analysis.

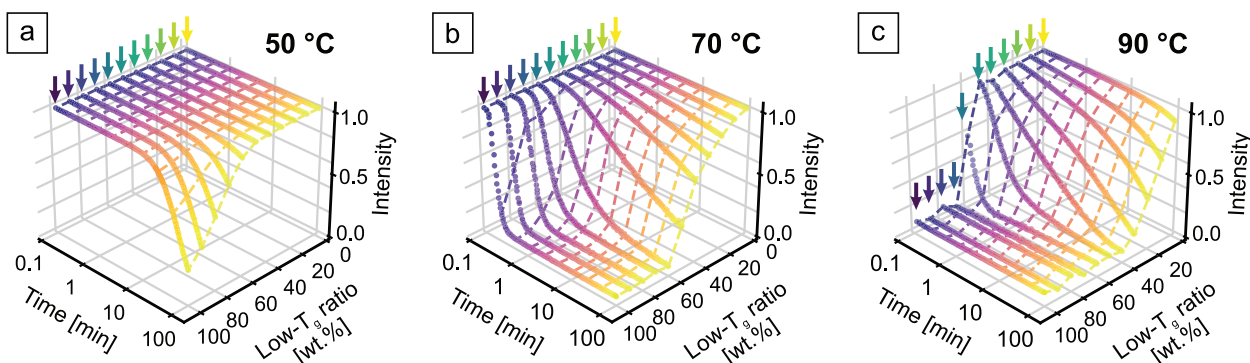


Figure 2. Three-dimensional representation of stopband decay curves. Several compositions are measured at temperatures of 50 °C (a), 70 °C (b), and 90 °C (c). The dashed lines are guides to the eye. They represent the composition-dependent intensity profile expected for the sintering behavior after certain time steps.

composition. For the sake of clarity, we point out to the reader that throughout this work, the color scheme shown in Figure 1k (yellow to turquoise) corresponds to a change in composition, while a time dependency is indicated by the color scheme in Figure 1m (yellow to purple).

Further in situ measurements of the various particle ratios are conducted at temperatures of 50, 70, and 90 °C (Figure 2a–c). As 50 °C is close to the lower glass transition temperature, the observable effect is comparatively small. None of the samples showed complete thermal degradation during 100 min of measurement time. A gradual change from 100–50% low- T_g particles is present beyond which none of the curves exhibit a discernible decay. Increasing the temperature to 70 °C causes the low- T_g dominated samples to degrade in a matter of seconds to minutes. The perceptible change of the profile shape at longer sintering times is shifted to the range between 70–20%. This is amplified when the temperature is raised further to 90 °C. Here, a slight degradation even of the pure high- T_g particles sets in. In total, the temperature and time-dependent behavior shows how binary CCs could be used as time–temperature integrators. The combination of various compositions and their normalized intensities correlate to certain combinations of the sintering time at a certain temperature. Limits of this particular system are given by a lower temperature where no effect is observed at approximately 45 °C and an excessively fast film formation of all particles above 100 °C (Figure S6, Supporting Information).

To fully exploit the potential of this composition-dependent film formation behavior, we demonstrate now how to arrange the binary particles in a gradient colloidal crystal. For this, we took inspiration from infusion-withdrawal-coating (IWC), which has been reported for sol–gel-derived gradients.^[50–53] This method is based on dip-coating by the use of two syringe pumps (Figure 3a). A glass substrate is dipped in a dispersion of one particle type, which is extracted with a syringe pump. Simultaneously, a second syringe pump infuses a dispersion of the second particles at a slower rate. The water level, thereby, decreases continuously, mimicking dip-coating, while the composition changes in a slow and gradual fashion. This time-dependent concentration change translates directly into a compositional gradient along the coated substrate. Similar to dip-coating, this produces a continuous thin-film with a strong

iridescent color throughout the entire sample. Figure 3b also shows a typical colloidal crystal with a film thickness between 4–8 μm . The periodic roughness, especially on the top half of the sample, is a consequence of meniscus pinning and stick-slip behavior.^[54] Transmission UV–vis spectra in Figure 3c measured at equidistant points along the coating axis corroborate the successful colloidal assembly. The stopband of this photonic crystal is distinct at all points. Peak intensities vary slightly, which is attributed to the observed thickness modulation. Peak position and FWHM by and large remain constant, emphasizing the homogeneity and high quality of the gradient colloidal crystal. To visualize and quantify the gradual composition change, we introduced red-fluorescent polystyrene particles to the infusion dispersion. These fluorescent tracer beads (100 nm diameter) are small enough to theoretically occupy octahedral gaps in the structure and were added in a trace amount of 1 wt% with respect to the PMMA/nBA particles.

Fluorescence microspectroscopy (Figure 3d,e) confirms the targeted composition gradient. A gradual increase of the fluorescence intensity is spectroscopically measured and corroborated by microscopy images exhibiting a transition from black to red. Modulation of the layer thickness can also be observed in the microscopy images. The fluorescence intensity is expected to be proportional to the number of tracer particles and to the film thickness. Quantification of the gradient is, therefore, performed by integration of the fluorescence signal between 560–650 nm. The integrated fluorescence is then corrected to the local layer thickness by normalization to the stopband intensity measured at the same position. The validity of this analytic procedure is assessed by measuring homogeneously dip-coated samples with defined tracer particle concentrations between 0–1.0 wt% (Figure S7, Supporting Information). The expected linear trend of the tracer particle concentration could be reconstructed when normalizing to the stopband intensity. This analysis confirms the direct relation between fluorescence particle concentration and fluorescence intensity. We use this direct relationship to measure the normalized fluorescence integral at identical positions along three individual gradient samples. Figure 3f shows that the composition profile follows a linear trend. Despite the homogeneous photonic stopband of this binary system, we were able to prepare a linear gradient of the tracer particle incorporation. Due to some limitations

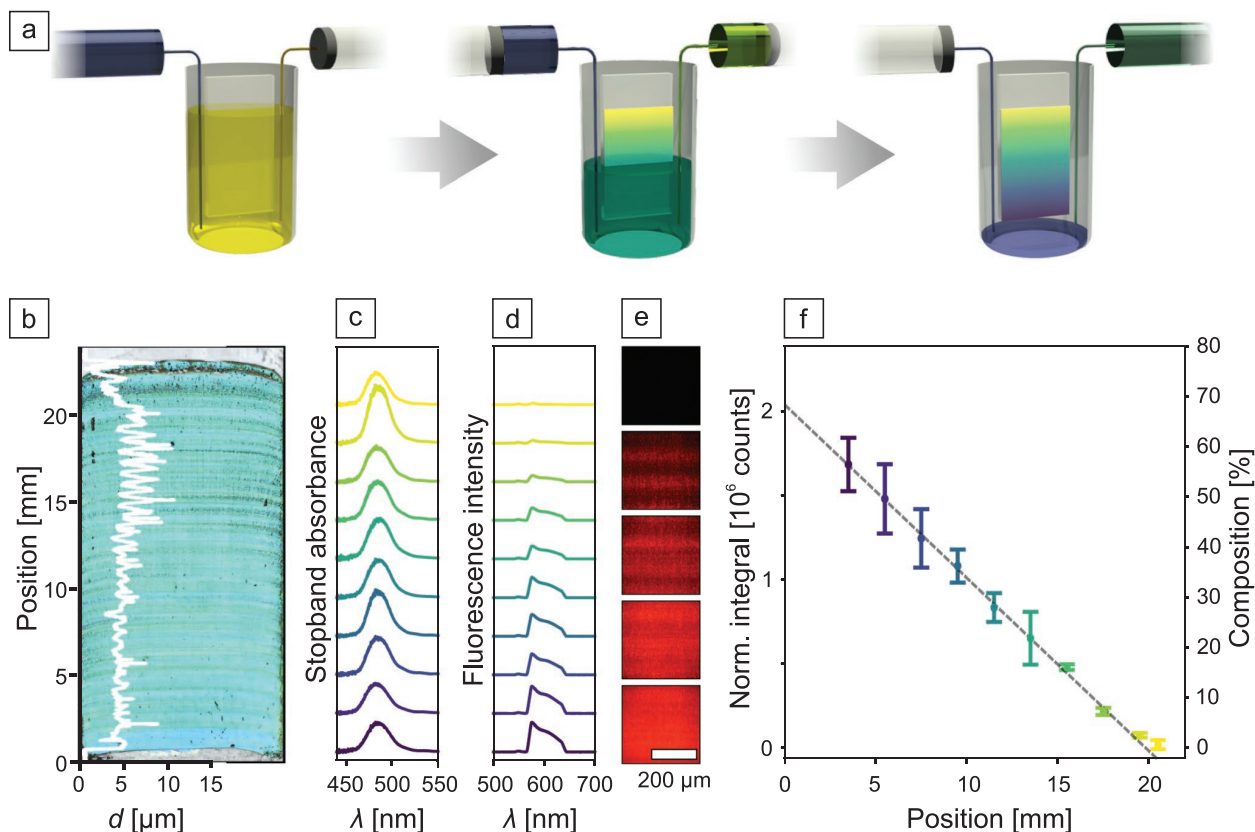


Figure 3. Infusion withdrawal coating technique to fabricate gradient colloidal crystals. a) Simultaneous infusion and extraction of the colloidal dispersion at different rates leads to a continuous composition gradient. This gradient is coated on the submerged glass substrate by continuous extraction of the mixed dispersion. b) Stitched light microscopy image of a colloidal crystal prepared via infusion withdrawal coating. The overlay (white line) shows the thickness of the colloidal film measured along the coating axis. This sample comprises a gradient of fluorescently labeled tracer particles. c,d) Stopband absorbance and fluorescence intensity at various gradient positions, respectively. e) Example fluorescence microscopy images taken along the gradient. f) Change of the normalized fluorescence intensity versus gradient position. A linear profile of the change in composition is obtained. The error bars result from measurements on three individual samples.

inherent to the IWC setup, we can access gradients ranging from 0–60% composition.

Using this approach, we prepared CCs with a gradually changing ratio of high- and low- T_g particles. Two identical gradients are subjected to sintering temperatures of 70 and 90 °C, respectively (Figure 4a,b). In both cases, dry-sintering and loss of structural color sets in first at the bottom of the sample where the amount of low- T_g particles is highest. While the temperature persists, the threshold between the colorful and degraded regions moves along the gradient. As expected, this film-forming process proceeds faster at a higher temperature. To better quantify these observations, we evaluate the normalized peak intensity along the gradient sintered at 90 °C (Figure 3c). This data is obtained from ex situ UV–vis measurements (Figure S8, Supporting Information) after the gradient structure has been subjected to the respective time and temperature. The stopband decay correlates well with the aforementioned observations. It becomes especially clear how sintering times on a logarithmic scale can be distinguished. The profiles at 1 and 10 min are just as well separated as those of 10 and 100 min. We further corroborate the reproducibility

of the kinetic behavior by including the expected composition-dependent intensity decay derived from Figure 2c as dotted lines in Figure 4c. This is possible by translating the position along the gradient into a low- T_g ratio via the results from the fluorescence measurements. Expected and measured data overlap quite well and substantiate the controlled and predictable sintering behavior of the nanostructure. Measurements along the same gradient heated to 70 °C in Figure S9, Supporting Information, show a profile where dry-sintering is primarily observed at the bottom of the sample where more low- T_g particles are present. This is corroborated by SEM images of the partially sintered gradient (Figure S10, Supporting Information). In this case, distinguishing sintering times between 1, 10, and 100, and even 10^3 and 10^4 min is possible. Further examination shows that similar intensity profiles can be reached by various time–temperature combinations. For the case shown here, annealing at 70 °C for 100 min and 90 °C for 1 min result in comparable measurements. This behavior portrays the expected sensitivity to both temperature and time. We point out that a correction coefficient is applied to the expected data to shift the axis of the particle composition relative to the position

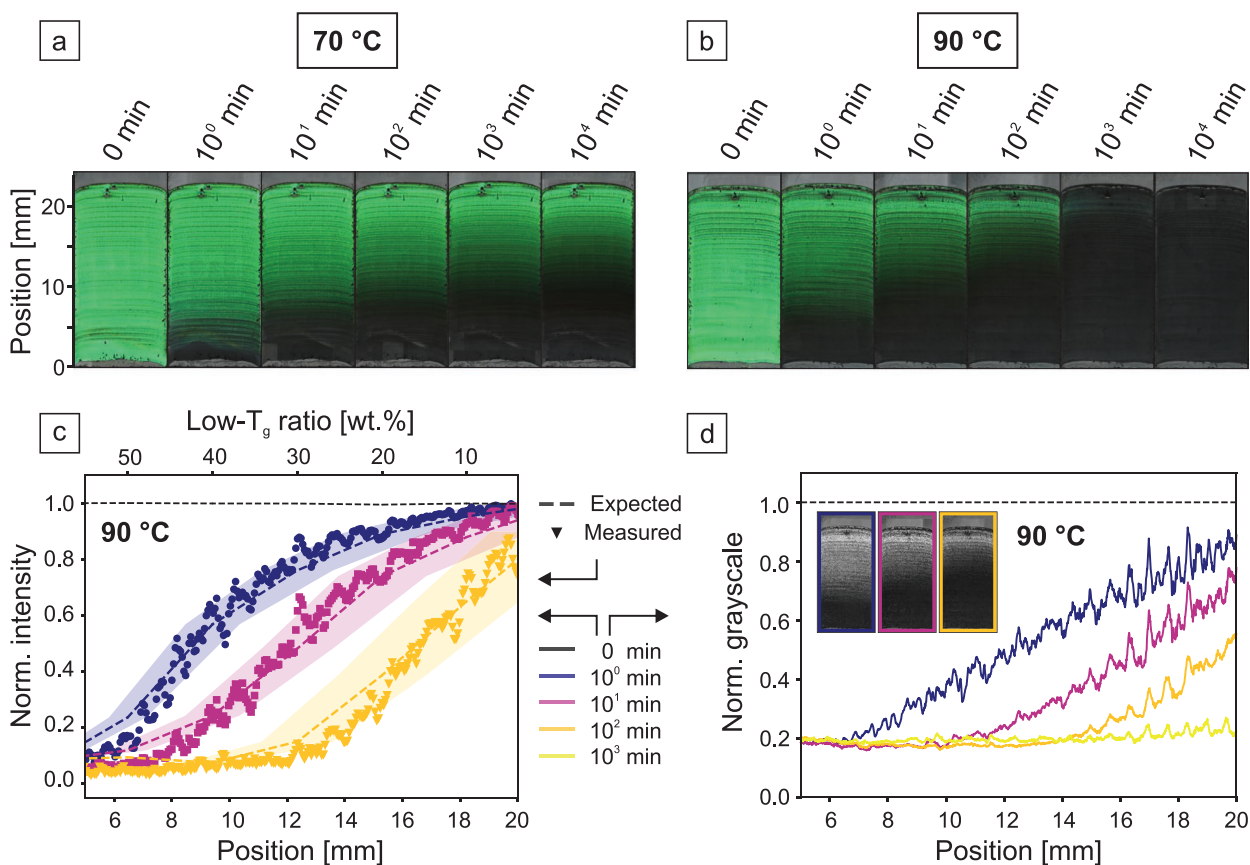


Figure 4. Colloidal crystals with a gradual change of the ratio of high- and low- T_g particles. (a) and (b) show identically prepared gradients and the sintering procedure at 70 and 90 °C, respectively. Images are obtained via stitching of light microscopy images and ex situ during the sintering process. The respective sintering times increase on a logarithmic scale. c) Normalized intensity obtained from ex situ UV–vis transmission measurements along the gradient axis. The dotted lines correspond to expected profiles originating from in situ measurements shown in Figure 2c. The shaded areas arise from the errors in the linear fit in Figure 3f, which is needed to correlate distance and composition. d) The inset shows green-channel images after color-channel separation of the pictures in (b). Profile analysis normalized to the measurement of the pristine gradient shows analogous results to the ex situ UV–vis measurements.

on the substrate in Figure 4c. This is necessary due to subtle and non-systematic variations during the individual coating processes. Such variations are likely caused by inconsistent pinning of the meniscus, variations of the substrate wettability, and the relative humidity during coating. The correction is done by optimizing a shift parameter to overlap the expected and measured data at a sintering time of 1 min. In the case of the 90 °C measurement, the axis is shifted by 0.8 mm. This is a reasonably small variability given the dynamic position of the wetting meniscus. Profiles of ensuing measurements at longer sintering times then all show a good agreement between the expected and measured intensity profiles.

The simplest method of analyzing the sintering behavior is the observation of the structural color at different degrees of sintering. The sintering difference along the composition gradient is obvious to the bare eye (Figure 4a,b). Simple image analysis is sufficient to obtain a more quantitative analysis, which reaches a comparable significance compared to the spectral analysis shown in Figure 4c. The separation of the color channels and profile analysis of the green channel image is shown

in Figure 4d. The distinction of sintering times on the same logarithmic time-scale is clearly visible. To provide a benchmark, the accuracy of temperature and time determination by green-channel evaluation is provided in Figures S11 and S12, Supporting Information, respectively. These experiments show that, depending on the absolute temperature region, temperature steps between 5–10 °C can clearly be distinguished. Regarding the temporal evaluation, approximately 1–2 steps can be resolved between each decade. Despite the uniquely simple measurement and evaluation, reproducibility is not impaired as shown in Figure S13, Supporting Information. Identically prepared colloidal crystal gradients show green-channel profiles with a strong overlap when subjected to the same thermal history.

This method of evaluation requires no elaborate equipment and works with a low-level software realization. We expect that given correct lighting conditions and a reference region on each sample, this analysis could be readily achieved by modern smartphones. This provides the context for a potential application of such gradient-based time–temperature integrators. These structures operate autonomously and cannot be restored

nor refreshed once the film formation sets in and are, therefore, not susceptible to manipulation. The distinct property of this gradient sensor is its sensitivity to prolonged moderate temperature exposures and short high-temperature excesses. The temperature can be imposed by the environmental conditions or caused by an operating device serving as heat source. Hence, a continuous monitoring of, for example, the thermal history of high-power batteries is readily conceivable, where heat management is gaining increased attention. High operating temperatures have pronounced negative effects regarding, for example, capacity fading.^[55,56] Batteries that experience excessive temperatures can additionally become a safety hazard.^[57] As batteries are an ubiquitous part of everyday life, it is of great importance to make an assessment of the thermal history as simple as possible. The colloidal gradients introduced here provide a visual way to judge on the time–temperature history based on the position-dependent stopband intensity. Beyond a certain threshold of local film formation, either the desired life expectancy would have been surpassed, or an undesired high-temperature excursion appeared. In either case, a thorough analysis of the battery state would be required before further usage. For such potential applications the current model system needs to be improved by a specific design of the required sensitive temperature range. This can be achieved by fine-tuning the composition range, by realizing non-linear composition gradients, and by creating gradient strips with particles of different, pre-defined T_g .

3. Conclusion

We have demonstrated a novel approach to functional colloidal crystals, which can be used as time–temperature integrators. Two key advancements in colloidal material fabrication made this sensor based on structural color detection possible. First, mixing of two equally sized, monodisperse latex particles with distinct glass transition temperatures provides access to composite colloidal crystals with specific time-dependent film formation properties. The film formation kinetics at a certain temperature can be varied from a few seconds to hours, days, and weeks by choosing the right particle composition. Second, the fabrication of gradient colloidal crystals allows the translation of the particle composition to a local position. We, therefore, introduced infusion-withdrawal coating for the fabrication of linear composition gradients at a retained optical stopband. The gradient structures exhibit the expected film-formation kinetic behavior and, consequently, change the intensity of the optical stopband locally. The gradual and local transition can be analyzed spectroscopically or through simple image analysis and provides a simple, autonomous, and manipulation-free way to assess the colloidal gradient's thermal history. Our contribution demonstrates how space-specific material engineering allows fabricating structures that exceed their individual components' properties.

4. Experimental Section

Details on the particle synthesis, coating procedures, and characterization methods, as well as details regarding the data evaluation of UV–vis spectroscopy, fluorescence spectroscopy, and

scanning electron microscopy images can be found in the Supporting Information.

Supporting Information

Supporting Information is available from the Wiley Online Library or from the author.

Acknowledgements

This project was supported by the Bavarian Center for Battery Technology (BayBatt). The help from the Keylab Electron Microscopy is appreciated. Tobias Lauster is thanked for discussions on the optical characterization, Celina Bräutigam is thanked for help with the microscopy images. M.S. and T.T. acknowledge support from the Elite Network Bavaria (ENB). This project has received funding from the European Research Council (ERC) under the European Union's Horizon 2020 research and innovation programme (grant agreement No 714968).

Open access funding enabled and organized by Projekt DEAL.

Conflict of Interest

The authors declare no conflict of interest.

Data Availability Statement

The data that supports the findings of this study are available in the supplementary material of this article.

Keywords

binary mixtures, film formation kinetics, infusion withdrawal coating, photonic crystals, structural colors

Received: March 11, 2021

Revised: June 15, 2021

Published online: August 21, 2021

- [1] A. Stein, F. Li, N. R. Denny, *Chem. Mater.* **2008**, *20*, 649.
- [2] N. Vogel, M. Retsch, C. A. Fustin, A. Del Campo, U. Jonas, *Chem. Rev.* **2015**, *115*, 6265.
- [3] J. Yin, M. Retsch, E. L. Thomas, M. C. Boyce, *Langmuir* **2012**, *28*, 5580.
- [4] N. Boechler, J. K. Eliason, A. Kumar, A. A. Maznev, K. A. Nelson, N. Fang, *Phys. Rev. Lett.* **2013**, *111*, 036103.
- [5] J. Ma, B. R. Parajuli, M. G. Ghossoub, A. Mihi, J. Sadhu, P. V. Braun, S. Sinha, *Nano Lett.* **2013**, *13*, 618.
- [6] M. T. Barako, A. Sood, C. Zhang, J. Wang, T. Kodama, M. Asheghi, X. Zheng, P. V. Braun, K. E. Goodson, *Nano Lett.* **2016**, *16*, 2754.
- [7] W. Cheng, J. Wang, U. Jonas, G. Fytas, N. Stefanou, *Nat. Mater.* **2006**, *5*, 830.
- [8] C. M. A. Parlett, K. Wilson, A. F. Lee, *Chem. Soc. Rev.* **2013**, *42*, 3876.
- [9] A. Stein, B. E. Wilson, S. G. Rudisill, *Chem. Soc. Rev.* **2013**, *42*, 2763.
- [10] Z. Li, Y. Yin, *Adv. Mater.* **2019**, *31*, 1807061.
- [11] J. Hou, M. Li, Y. Song, *Nano Today* **2018**, *22*, 132.
- [12] Y. Yu, S. Brandt, N. J. Nicolas, J. Aizenberg, *ACS Appl. Mater. Interfaces* **2020**, *12*, 1924.

- [13] M. Tsuchiya, Y. Kurashina, H. Onoe, *Sci. Rep.* **2019**, *9*, 17059.
- [14] J. M. Weissman, H. B. Sunkara, A. S. Tse, S. A. Asher, *Science* **1996**, *274*, 959.
- [15] W. Wohlleben, F. W. Bartels, S. Altmann, R. J. Leyrer, *Langmuir* **2007**, *23*, 2961.
- [16] A. C. Arsenault, T. J. Clark, G. von Freymann, L. Cademartiri, R. Sapienza, J. Bertolotti, E. Vekris, S. Wong, V. Kitaev, I. Manners, R. Z. Wang, S. John, D. S. Wiersma, G. A. Ozin, *Nat. Mater.* **2006**, *5*, 179.
- [17] E. T. Tian, J. X. Wang, Y. M. Zheng, Y. L. Song, L. Jiang, D. B. Zhu, *J. Mater. Chem.* **2008**, *18*, 1116.
- [18] R. A. Barry, P. Wiltzius, *Langmuir* **2006**, *22*, 1369.
- [19] Y. Wang, D. Aurelio, W. Li, P. Tseng, Z. Zheng, M. Li, D. L. Kaplan, M. Liscidini, F. G. Omenetto, *Adv. Mater.* **2017**, *29*, 1702769.
- [20] S. Jia, Z. Tang, Y. Guan, Y. Zhang, *ACS Appl. Mater. Interfaces* **2018**, *10*, 14254.
- [21] M. Chen, Y. Zhang, S. Jia, L. Zhou, Y. Guan, Y. Zhang, *Angew. Chem., Int. Ed.* **2015**, *54*, 9257.
- [22] J. H. Holtz, S. A. Asher, *Nature* **1997**, *389*, 829.
- [23] I. B. Burgess, L. Mishchenko, B. D. Hatton, M. Kolle, M. Lončar, J. Aizenberg, *J. Am. Chem. Soc.* **2011**, *133*, 12430.
- [24] Y. Heo, H. Kang, J.-S. Lee, Y.-K. Oh, S.-H. Kim, *Small* **2016**, *12*, 3819.
- [25] J.-W. Kim, J.-S. Lee, S.-H. Kim, *Adv. Mater. Interfaces* **2018**, *5*, 1701658.
- [26] M. Pelton, *Nat. Photonics* **2015**, *9*, 427.
- [27] J. F. Olorunyomi, M. M. Sadiq, M. Batten, K. Konstas, D. Chen, C. M. Doherty, R. A. Caruso, *Adv. Opt. Mater.* **2020**, *8*, 2000961.
- [28] F. Fleischhaker, R. Zentel, *Chem. Mater.* **2005**, *17*, 1346.
- [29] B. Liu, P. A. Gurr, G. G. Qiao, *ACS Sens.* **2020**, *5*, 2903.
- [30] A. Saha, Y. Tanaka, Y. Han, C. M. W. Bastiaansen, D. J. Broer, R. P. Sijbesma, *Chem. Commun.* **2012**, *48*, 4579.
- [31] F. A. Nutz, P. Ruckdeschel, M. Retsch, *J. Colloid Interface Sci.* **2015**, *457*, 96.
- [32] E. A. Sulyanova, A. Shabalin, A. V. Zozulya, J. M. Meijer, D. Dzhibaev, O. Gorobtsov, R. P. Kurta, S. Lazarev, U. Lorenz, A. Singer, O. Yefanov, I. Zaluzhnyy, I. Besedin, M. Sprung, A. V. Petukhov, I. A. Vartanyants, *Langmuir* **2015**, *31*, 5274.
- [33] G. Herzog, M. M. Abul Kashem, G. Benecke, A. Buffet, R. Gehrke, J. Perlich, M. Schwartzkopf, V. Korstgens, R. Meier, M. A. Niedermeier, M. Rawolle, M. A. Ruderer, P. Muller-Buschbaum, W. Wurth, S. V. Roth, *Langmuir* **2012**, *28*, 8230.
- [34] F. A. Nutz, M. Retsch, *Phys. Chem. Chem. Phys.* **2017**, *19*, 16124.
- [35] F. A. Nutz, A. Philipp, B. A. F. Kopera, M. Dulle, M. Retsch, *Adv. Mater.* **2018**, *30*, 1704910.
- [36] I. Jurewicz, A. A. K. King, R. Shanker, M. J. Large, R. J. Smith, R. Maspero, S. P. Ogilvie, J. Scheerder, J. Han, C. Backes, J. M. Razal, M. Florescu, J. L. Keddie, J. N. Coleman, A. B. Dalton, *Adv. Funct. Mater.* **2020**, *30*, 2002473.
- [37] F. A. Nutz, M. Retsch, *Sci. Adv.* **2017**, *3*, eaao5238.
- [38] S. Y. Lee, J. S. Lee, S. H. Kim, *Adv. Mater.* **2019**, *31*, 1901398.
- [39] T. Ding, Q. Zhao, S. K. Smoukov, J. J. Baumberg, *Adv. Opt. Mater.* **2014**, *2*, 1098.
- [40] S. H. Kim, W. C. Jeong, H. Hwang, S. M. Yang, *Angew. Chem., Int. Ed.* **2011**, *50*, 11649.
- [41] C. Zhu, J. Qiu, S. Pongkitwitoon, S. Thomopoulos, Y. Xia, *Adv. Mater.* **2018**, *30*, 1706706.
- [42] H. Ding, C. Liu, B. Ye, F. Fu, H. Wang, Y. Zhao, Z. Gu, *ACS Appl. Mater. Interfaces* **2016**, *8*, 6796.
- [43] H. Ding, C. Liu, H. Gu, Y. Zhao, B. Wang, Z. Gu, *ACS Photonics* **2014**, *1*, 121.
- [44] A. E. Schedl, I. Howell, J. J. Watkins, H. W. Schmidt, *Macromol. Rapid Commun.* **2020**, *41*, 2000069.
- [45] A. E. Schedl, C. Neuber, A. Fery, H. W. Schmidt, *Langmuir* **2018**, *34*, 14249.
- [46] J. Chi, C. Shao, Y. Zhang, D. Ni, T. Kong, Y. Zhao, *Nanoscale* **2019**, *11*, 12898.
- [47] A. Spinnrock, D. Schupp, H. Colfen, *Small* **2018**, *14*, 1803518.
- [48] M. Chen, K. Hagedorn, H. Colfen, S. Polarz, *Adv. Mater.* **2017**, *29*, 1603356.
- [49] J. Bahner, N. Klinkenberg, M. Frisch, L. Brauchle, S. Polarz, *Adv. Funct. Mater.* **2019**, *29*, 1904058.
- [50] K. M. Ashraf, M. R. K. Khan, D. A. Higgins, M. M. Collinson, *Langmuir* **2018**, *34*, 663.
- [51] K. M. Ashraf, C. Wang, S. S. Nair, K. J. Wynne, D. A. Higgins, M. M. Collinson, *Langmuir* **2017**, *33*, 4207.
- [52] D. Giri, C. N. Hanks, M. M. Collinson, D. A. Higgins, *J. Phys. Chem. C* **2014**, *118*, 6423.
- [53] F. Ye, C. Cui, A. Kirkemide, D. Dong, M. M. Collinson, D. A. Higgins, *Chem. Mater.* **2010**, *22*, 2970.
- [54] J. Huang, R. Fan, S. Connor, P. Yang, *Angew. Chem., Int. Ed.* **2007**, *46*, 2414.
- [55] J. Shim, R. Kostecki, T. Richardson, X. Song, K. A. Striebel, *J. Power Sources* **2002**, *112*, 222.
- [56] F. Leng, C. M. Tan, M. Pecht, *Sci. Rep.* **2015**, *5*, 12967.
- [57] J. Hou, M. Yang, D. Wang, J. Zhang, *Adv. Energy Mater.* **2020**, *10*, 1904152.

ADVANCED MATERIALS

Supporting Information

for *Adv. Mater.*, DOI: 10.1002/adma.202101948

Time–Temperature Integrating Optical Sensors Based on
Gradient Colloidal Crystals

*Marius Schöttle, Thomas Tran, Tanja Feller, and Markus
Retsch**

Supporting Information

Time-temperature integrating optical sensors based on gradient colloidal crystals*Marius Schöttle¹, Thomas Tran¹, Tanja Feller¹, and Markus Retsch^{1,2,*}***Experimental Section****Materials:**

Methyl methacrylate (MMA), n-butyl acrylate (nBA), 3-styrenesulfonic acid sodium salt hydrate (NaSS, $\geq 99\%$), and potassium persulfate (KPS, $\geq 99\%$) were obtained from Sigma-Aldrich. MMA and nBA are destabilized over Alox B prior to use. Sulfate-modified, fluorescent red polystyrene particles (100 nm diameter) were obtained from Sigma-Aldrich as an aqueous suspension, diluted to 0.025 wt.%, and sonicated for 20 minutes before further use. Water is taken from a Millipore Direct Q3UV unit for all experiments.

Particle synthesis: Monodisperse polymer colloids are prepared via an emulsifier free emulsion polymerization. 13 mL monomer mixture (MMA/nBA, either 70:30 or 90:10) are added to 250 mL water and heated to 80 °C. After stirring at 850 rpm for 60 minutes under nitrogen flow, 10 mg NaSS and subsequently 100 mg KPS, both dissolved in 5 mL water, are added quickly. After 15 minutes, the stirring speed is reduced to 650 rpm. The reaction is left to proceed over-night and terminated by exposure to ambient oxygen.

Substrates: Glass substrates are cleaned carefully prior to all coating procedures.

Ultrasonication proceeds twice in 2 vol.% aqueous Hellmanex III solution and once in ethanol (p.a.). Subsequently, substrates are immediately dried under a nitrogen stream.

Directly before coating, the surface is hydrophilized via oxygen plasma treatment.

Dip-coating: Homogeneous colloidal crystals are prepared via dip-coating. Several dispersions with varying ratios of particle types are prepared. Mixtures are adjusted to 1.0 total wt% and stirred over-night to ensure statistical distribution of the two particle types.

Clean glass substrates are inserted, and dip-coating proceeds with a velocity of $0.25 \mu\text{m s}^{-1}$ and a controlled atmosphere of $25 \text{ }^\circ\text{C}$ and 75% relative humidity.

Infusion-withdrawal-coating: Gradient colloidal crystals are prepared via an infusion-withdrawal-coating process. A clean glass substrate is dipped in a 10 mL PTFE-beaker filled with 8.7 mL of the starting dispersion and equipped with a stirrer bar. The stirring speed is set to 80 rpm. Two cannulas are inserted vertically on opposite sides of the beaker, and each is connected to a syringe pump. One injects the second dispersion at 0.6 mLh^{-1} , the other extracts the resulting mixture at 1.1 mLh^{-1} . Taking into account a determined evaporation rate of 0.1 mLh^{-1} , this ensures that the extraction rate is twice the infusion rate. The first part of the colloidal crystal is especially subject to pinning and defect formation. Therefore, before the infusion is started, extraction is set to 0.5 mLh^{-1} for one hour. The corresponding top part of the sample is not regarded in the evaluation. The concentration of both dispersions is 1.3 wt%, and the ambient conditions lie between $19 - 21 \text{ }^\circ\text{C}$ and 25 - 35% relative humidity. For the fluorescence measurements, one PMMA/nBA type is used, and 1.0 wt.% (with respect to PMMA/nBA) red-fluorescent polystyrene particles are added to the infusion dispersion.

Methods:

Differential scanning calorimetry: Measurements are conducted using a TA Instruments Discovery DSC 2500. The second of two heating cycles is used for the evaluation. Samples are measured between $-20 - 200 \text{ }^\circ\text{C}$ at 10 K min^{-1} and in a nitrogen atmosphere.

Imaging microscopy: 2D color images and 3D reconstructed images are obtained using a laser scanning microscope (Olympus, LEXT). High magnification images are taken using a 50x lens with N.A. 0.95. Overview images are obtained by stitching several domains with a 5x lens with N.A. 0.15.

UV-Vis/Fluorescence microspectroscopy: The setup is based on an Olympus IX71 inverted microscope. Throughout all measurements, a 4x lens with N.A. 0.10 is used. UV-Vis spectra are obtained in transmission geometry with a halogen light source. An OceanOptics USB4000

spectrometer is coupled via fiber optics. *In-situ* measurements are conducted by using an Instec HCS622HV heating stage with a silver heating block and transmission capability to the setup. The lid of the stage is lifted briefly while the sample is placed on the preheated silver block, and the measurement is immediately started. Spectra are obtained every 500 ms over a period of 100 minutes. Ex-situ measurements are performed by externally heating samples on the same heating stage for a defined amount of time. Subsequently, a motorized μm -stage is used to automatically measure spectra at defined positions along the samples.

Fluorescence spectroscopy is performed with the same setup but with a mercury vapor lamp in reflection geometry. A Chroma 49005 Cy3 filter cube is used, allowing excitation between 530 - 560 nm and emission detection between 590 - 650 nm. The integration time is set to 2 seconds, and 10 scans are measured for averaging. Gradients are measured at defined positions using a μm -stage. Thereby, fluorescence and transmission UV-Vis spectra can be measured at the same position.

Scanning electron microscopy: Images were taken with a Zeiss Ultra plus (Carl Zeiss AG, Germany) at an operating voltage of 3 kV and with in-lens detection after sputtering of 2 - 4 nm platinum.

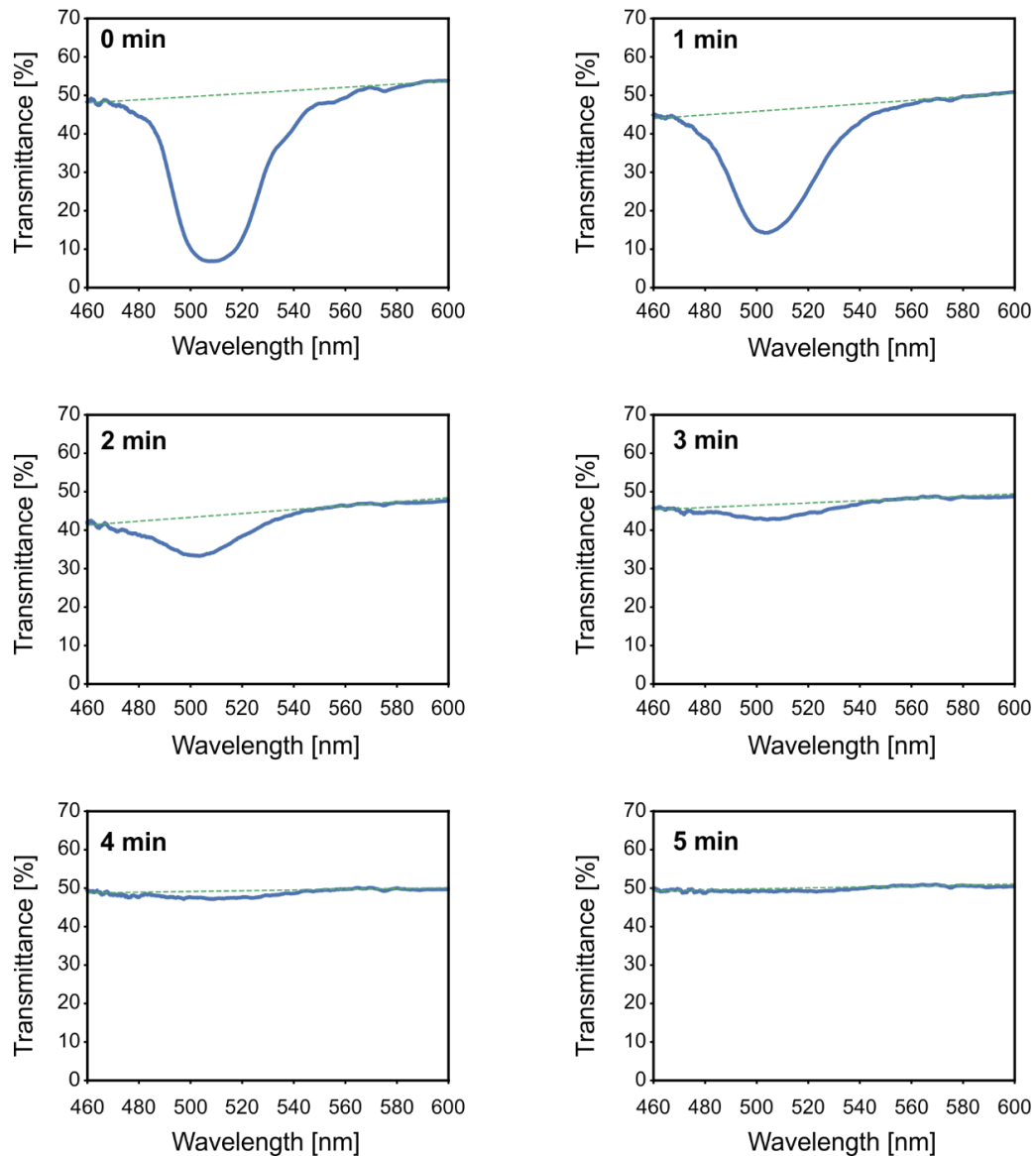


Figure S1. Transmission UV-Vis spectra during the film-formation of a 100% low- T_g colloidal crystal at 60 °C. Dotted green lines show the baseline used for the evaluation. Division of the spectrum by the baseline and subsequent normalization to the stopband intensity at 0 minutes leads to the decay curve in **Figure 1c**.

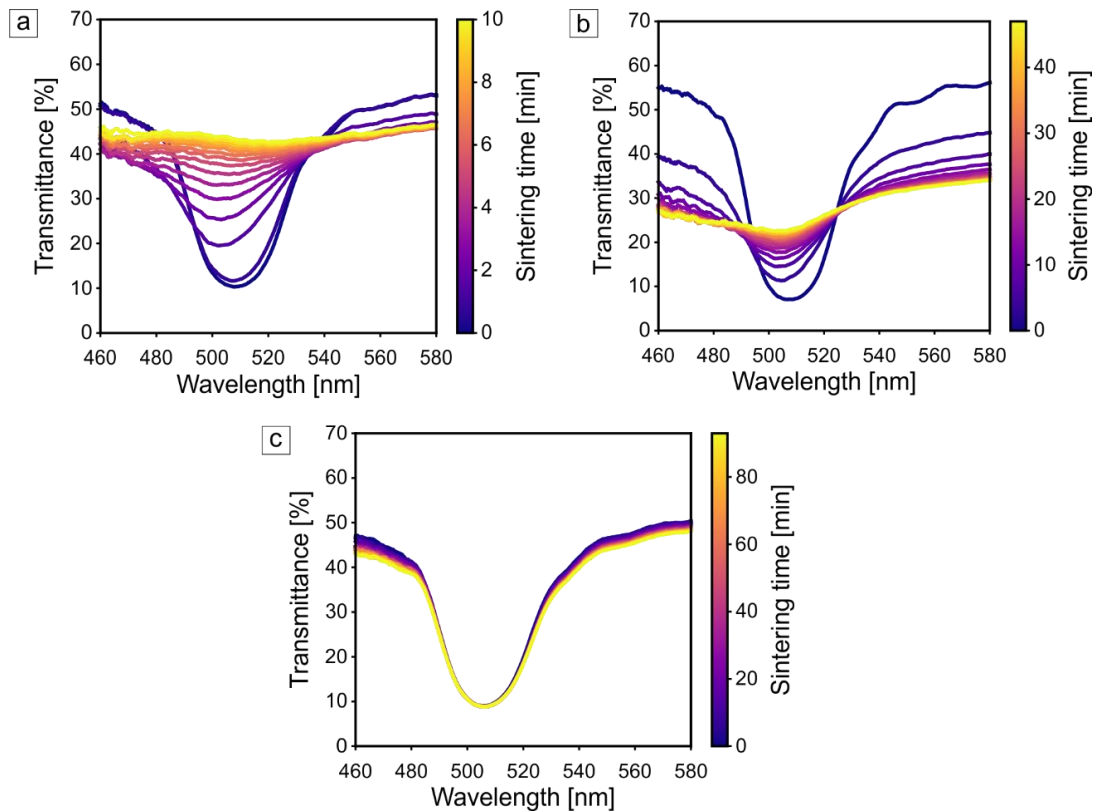


Figure S2. Exemplary *in-situ* UV-Vis measurements of samples with a) 80, b) 60, and c) 10% low- T_g particles at 60°C . After 5 minutes, the spectra in a) show slight minima and maxima that arise from thin-film interference. This cannot accurately be distinguished from the stopband and is therefore not corrected. As an effect, the normalized intensity decays to a value slightly above zero.

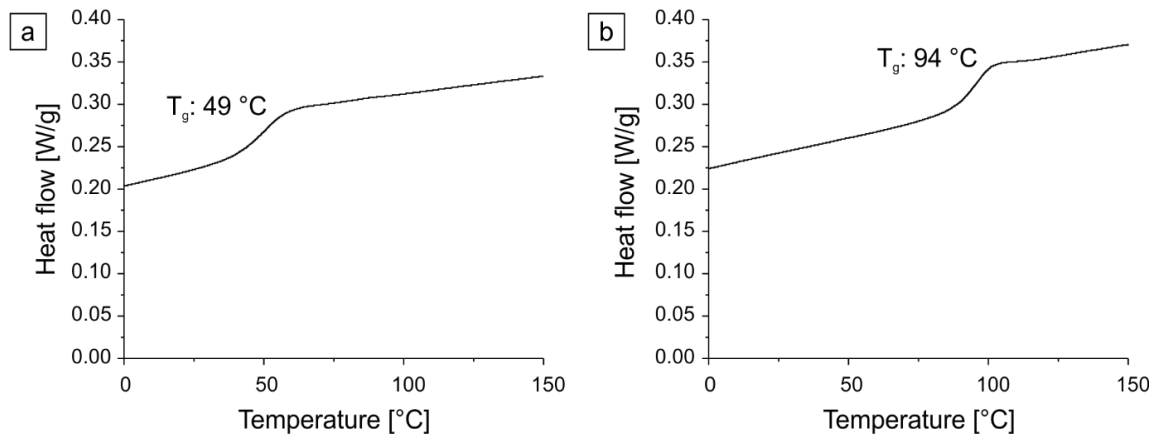


Figure S3. The second heating curve of DSC measurements of PMMA/nBA particles with a monomer ratio of a) 70:30 and b) 90:10.

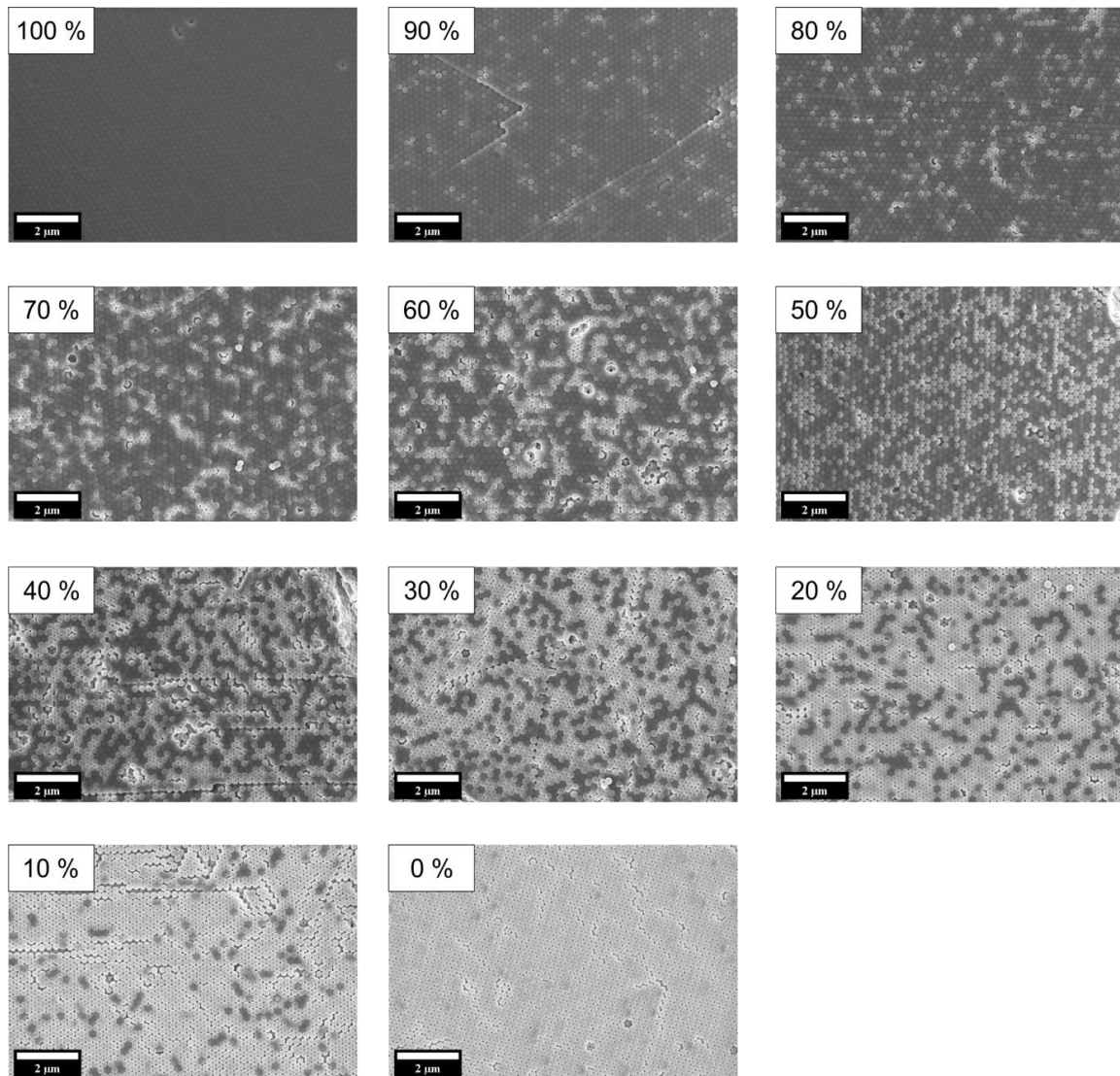


Figure S4. Scanning electron microscopy images of colloidal crystals after film formation for 100 minutes at 60 °C. Different compositions are labeled with the amount of low- T_g particles in the mixture.

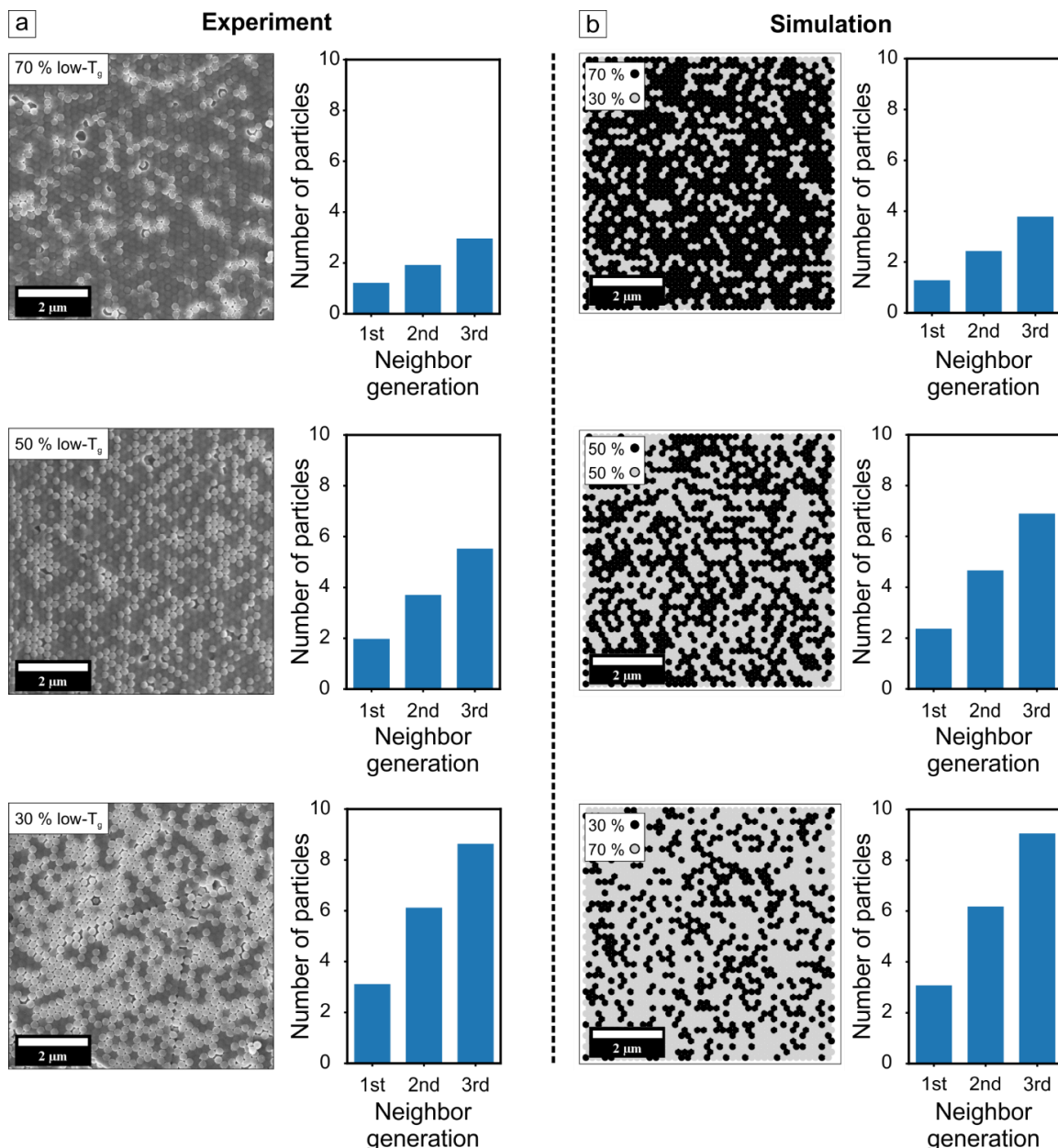


Figure S5. a) Scanning electron microscopy images of colloidal crystals with a different amount of low- T_g particles after film formation. b) Simulated distributions of two different particle types randomly mixed in a 2D-hexagonal structure. The images are calculated by randomly assigning each particle with a black or grey color. The probability of each color is chosen according to the particle ratio in the SEM counterpart.

For the quantitative evaluation, the positions of non-sintered particles in the SEM images and grey particles in the simulations are examined. The mean number of neighbors is evaluated in both cases. First generation neighbors are integrated between 0 - 0.3 μm distance between particle centers, second generation between 0.3 - 0.5 μm and third generation between 0.5 - 0.7 μm . The distributions of experiments and simulations correlate very well. Relative intensities of the three generations as well as the absolute values are comparable. This concludes that the particles are indeed randomly distributed in the colloidal crystals. The lack of phase separation and prevention of heterogeneous film formation kinetics is a prerequisite for the characterization shown in this work.

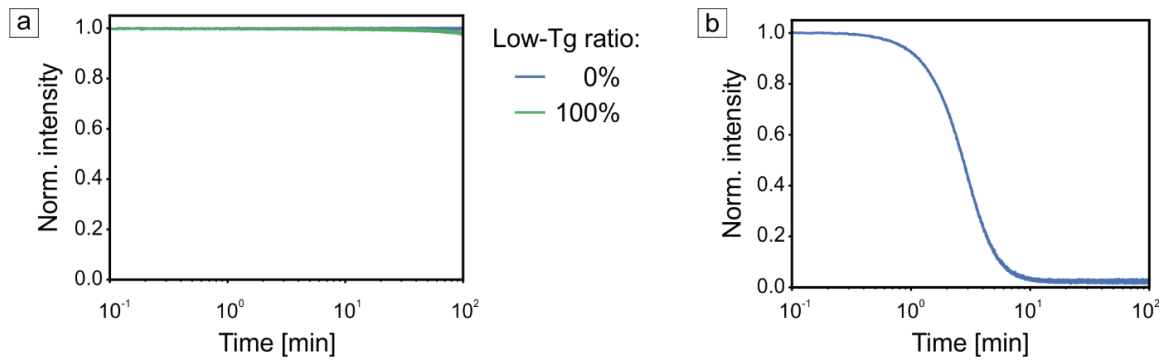


Figure S6. a) Stopband decay curves of colloidal crystals consisting purely of high- and low- T_g particles, respectively, at 45 °C. b) Stopband decay curve of 100% high- T_g particles at 100 °C. These measurements show the temperature limits accessible with the present combination of copolymer colloids.

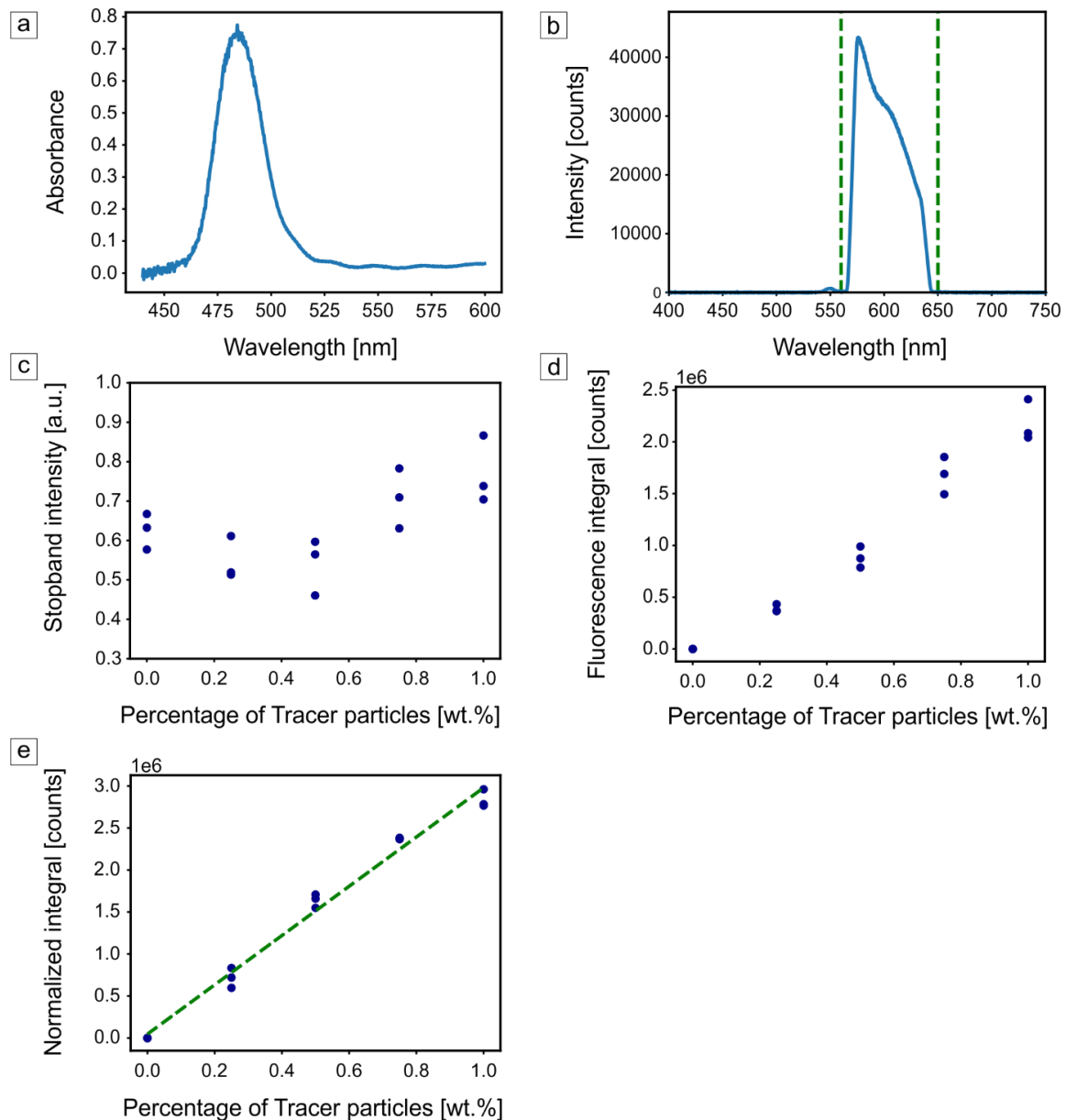


Figure S7. Exemplary a) baseline-corrected transmission UV-Vis and b) fluorescence emission spectra of a PMMA/nBA colloidal crystal prepared via dip-coating with 1.0 wt.% red-fluorescent polystyrene particles. Green lines in b) show the integration boundaries required for further evaluation. c) Determined stopband intensity and d) fluorescence integral of all measurements. e) Normalized fluorescence integral obtained for the various percentages of tracer particles. The green dotted line represents the linear fit used for the correlation of position and composition of the gradient in **Figure 3f**.

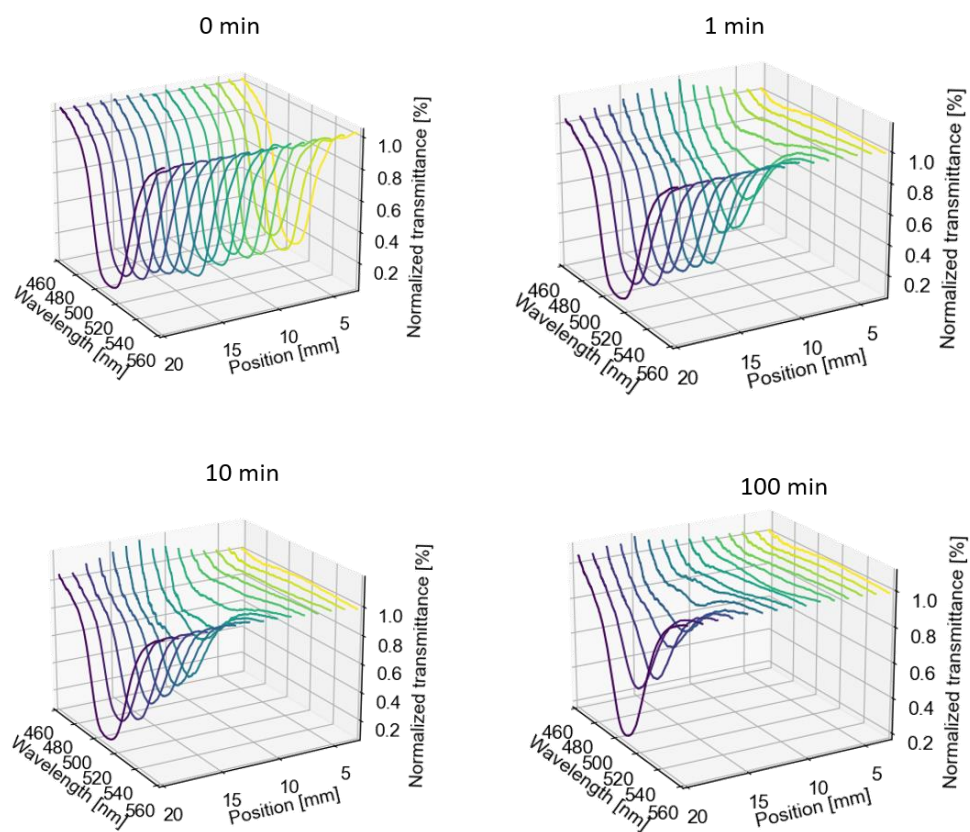


Figure S8. Baseline corrected transmission UV-Vis spectra measured *ex-situ* along a gradient colloidal crystal. These show the film formation process at 90 °C and how the degradation proceeds along the gradient.

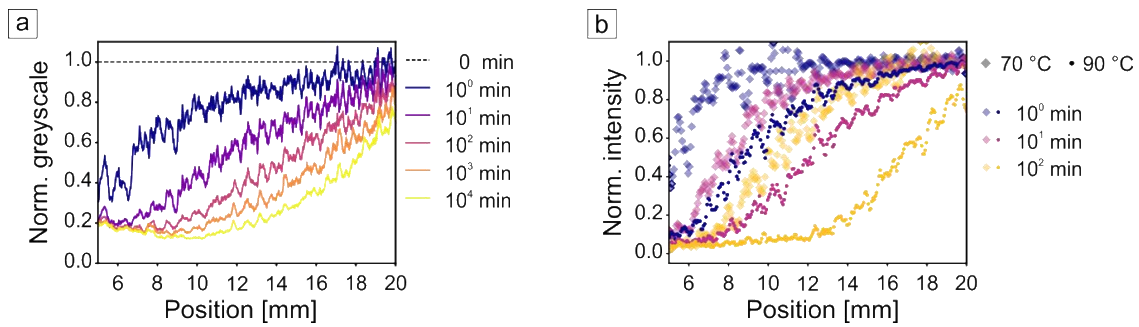


Figure S9. Measurements of the colloidal crystal gradient after different sintering times at 70 °C. a) Greyscale profile analysis *via* green channel separation of photographs shown in **Figure 4a**. b) *Ex-situ* UV-Vis results of a gradient sintered at 70 °C (large symbols) and 90 °C (small symbols) at equivalent sintering-times. The near overlap of the time-temperature pairs 100 min / 70 °C and 1 min / 90 °C shows the mutual influence of both time and temperature on the local film formation.

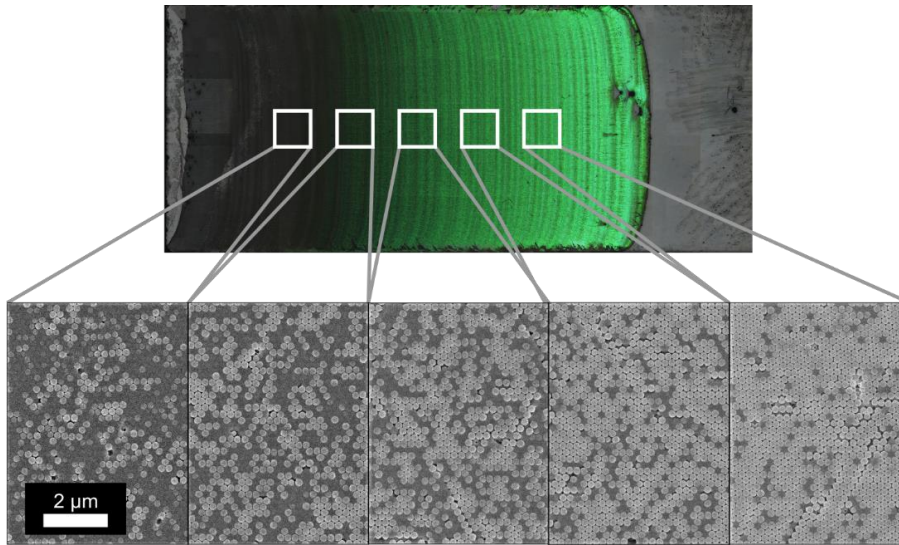


Figure S10. Scanning electron microscope images of a colloidal crystal gradient sintered at 70 °C for 100 minutes. A gradual decrease in the percentage of low- T_g particles is observed from left to right. The random particle distribution corresponds well to the individually prepared mixtures shown in **Figure S4**.

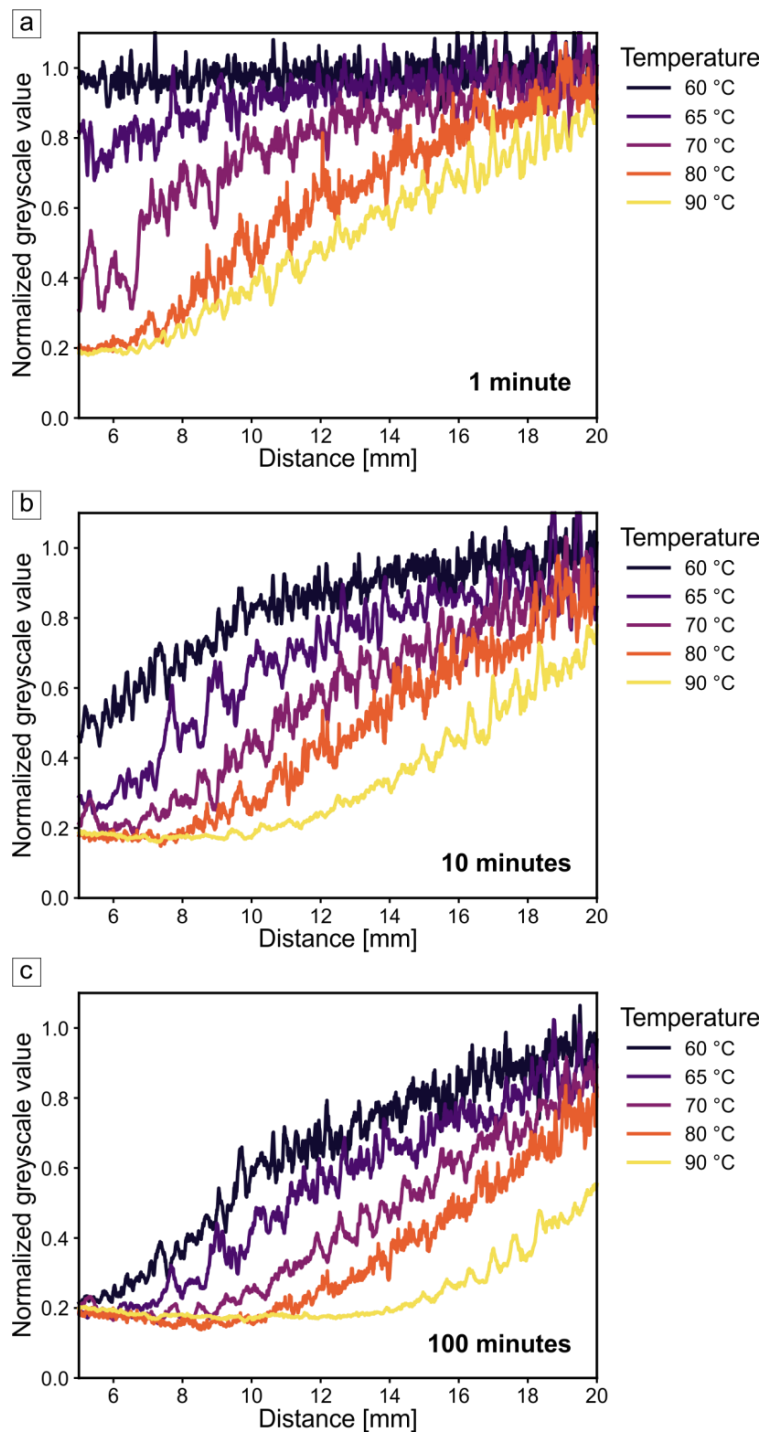


Figure S11. Temperature accuracy evaluation. Five gradient colloidal crystals are subjected to temperatures between 60 – 90 °C and the respective profiles are determined via green-channel image analysis. Three sintering times of a) 1 minute, b) 10 minutes and c) 100 minutes are presented. Temperature difference of 5 °C and higher can be distinguished.

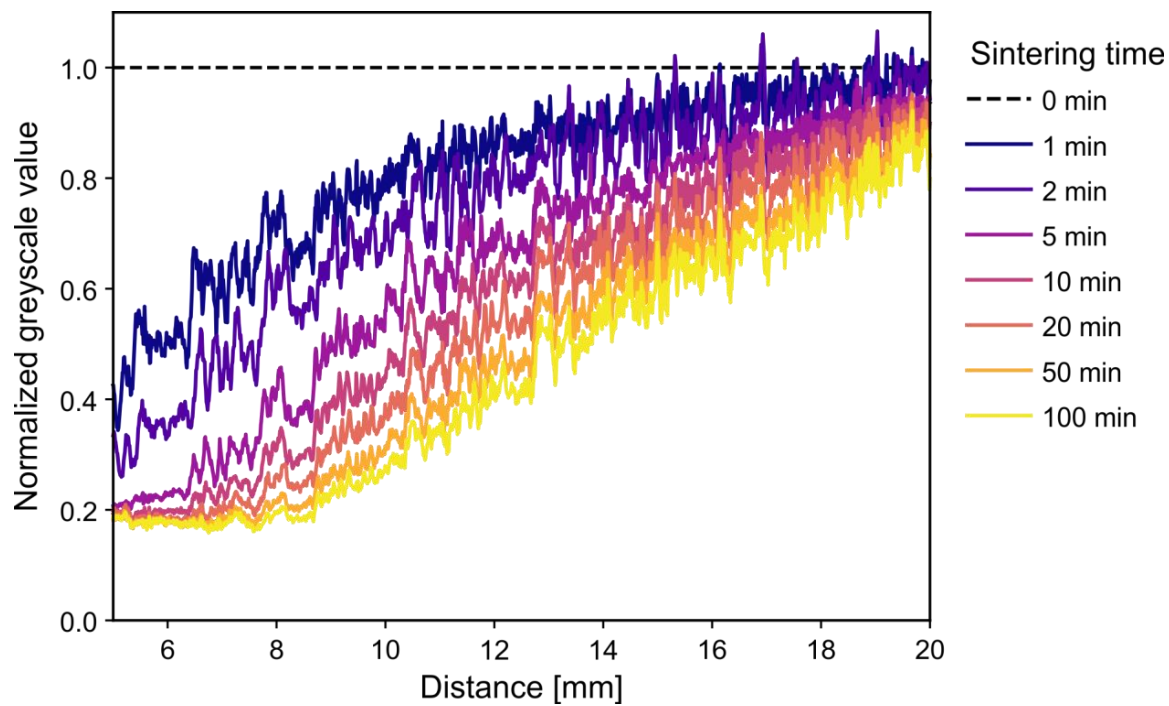


Figure S12. Time accuracy evaluation. A gradient colloidal crystal is subjected to a temperature of 70 °C and ex-situ profiles are obtained at various sintering times. The respective time decades (1 min, 10 min, 100 min) are well separated, inferring a temporal accuracy of a fraction of the sintering time of interest.

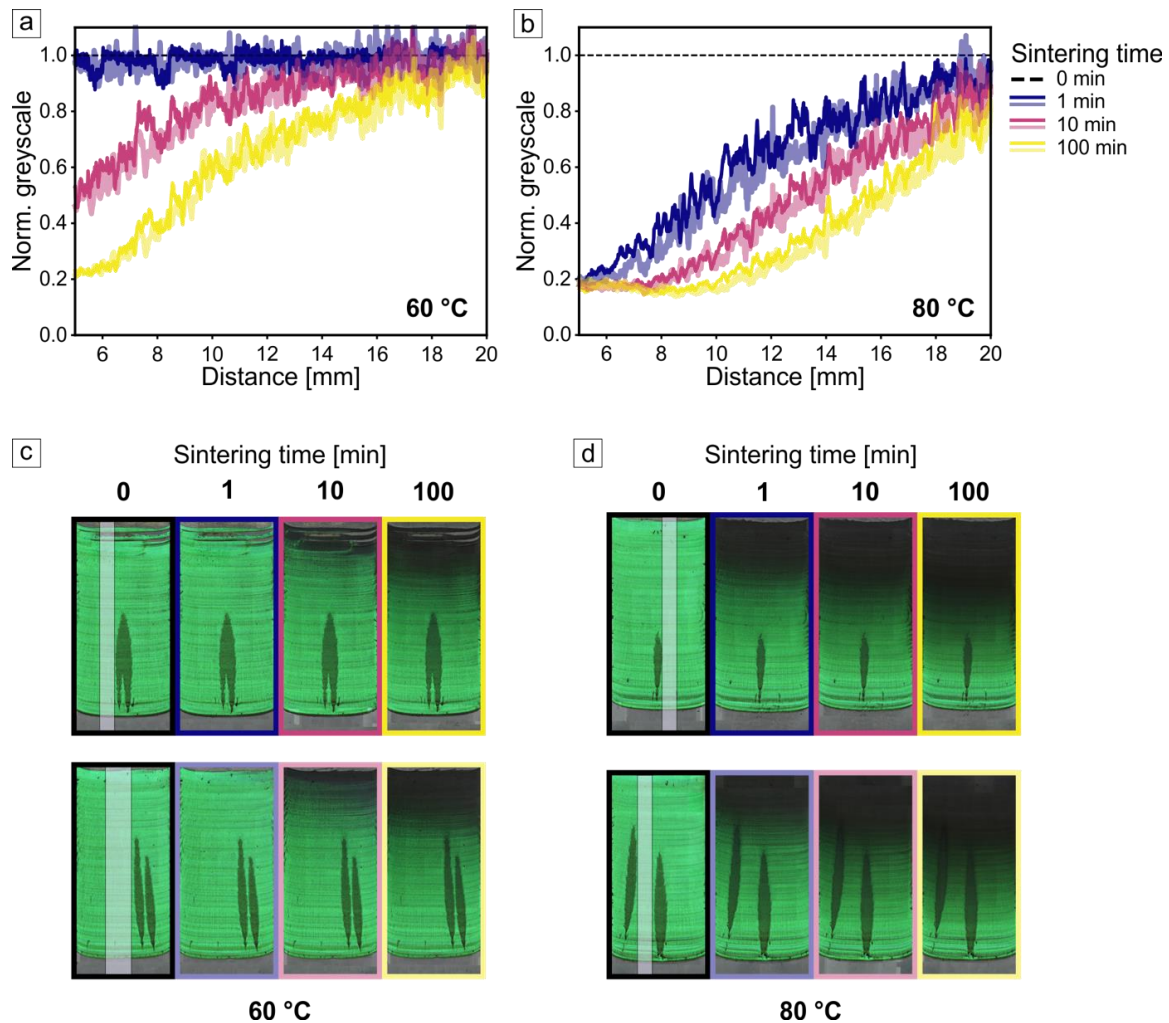
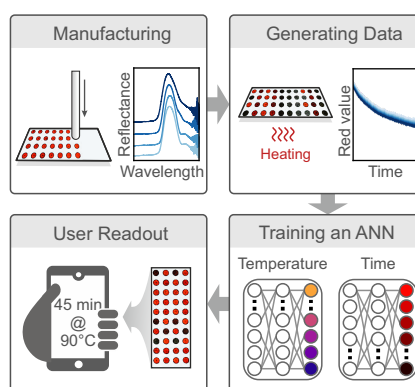


Figure S13. Reproducibility evaluation. Gradient colloidal crystals are subjected to sintering temperatures of a) 60 °C and b) 80 °C and profiles are determined via green-channel image analysis. Two samples are measured at each temperature and the resulting profiles are presented together (shown as an overlay of dark and light curve for each sintering time). The corresponding samples at the given sintering times are shown in c) and d), respectively. The high agreement between the two samples at both temperatures showcases the reproducibility of the time-temperature integrator. The green-channel profile analysis is conducted in regions of the samples (white shaded area) unaffected by the dark-green defects.

Machine learning enabled image analysis of time-temperature sensing colloidal arrays

Marius Schöttle*, Thomas Tran,* , and Markus Retsch, „Machine Learning Enabled Image Analysis of Time-Temperature Sensing Colloidal Arrays“, *Advanced Science* **2023**, *Early View*, 2205512.

**These authors contributed equally to the work.*



The optical response of multicomponent photonic crystals contains intricate information regarding a sample's thermal history. In this work, the authors present a reproducible sensor fabrication method coupled with fast data acquisition via digital photography. Machine learning assisted evaluation allows smartphone-based sensing of thermal events. Time and temperature can thereby be obtained independently and without specialized equipment.

Machine Learning Enabled Image Analysis of Time-Temperature Sensing Colloidal Arrays

Marius Schöttle, Thomas Tran, Harald Oberhofer, and Markus Retsch*

Smart, responsive materials are required in various advanced applications ranging from anti-counterfeiting to autonomous sensing. Colloidal crystals are a versatile material class for optically based sensing applications owing to their photonic stopband. A careful combination of materials synthesis and colloidal mesostructure rendered such systems helpful in responding to stimuli such as gases, humidity, or temperature. Here, an approach is demonstrated to simultaneously and independently measure the time and temperature solely based on the inherent material properties of complex colloidal crystal mixtures. An array of colloidal crystals, each featuring unique film formation kinetics, is fabricated. Combined with machine learning-enabled image analysis, the colloidal crystal arrays can autonomously record isothermal heating events — readout proceeds by acquiring photographs of the applied sensor using a standard smartphone camera. The concept shows how the progressing use of machine learning in materials science has the potential to allow non-classical forms of data acquisition and evaluation. This can provide novel insights into multiparameter systems and simplify applications of novel materials.

batteries, food, and medicine requires tamper-proof sensors independent of an external power supply.^[1–3] Color-coded systems are advantageous since they allow user-friendly readout.^[4] This prerequisite is often realized using the responsive photonic properties of nanostructured (often polymeric) materials.^[5,6] These can react to external stimuli by changing the spacing, effective refractive index, or via loss of order.^[7–9] Beside the sensing of, e.g., pH-value^[10] and (bio-)analytes,^[11] temperature monitoring plays a key role in tracking degradation and spoilage.^[12,13] Depending on the application, both reversible sensors and irreversible indicators have been shown.^[14,15] More intricate systems can provide further information regarding the thermal history. Time-temperature integrators (TTIs) additionally provide temporal readout, which is highly relevant for establishing the safety of products.^[16–18] Often, this is achieved by controlling the kinetics

of the deformation process in structured polymeric materials.^[19] A system shown by Lee et al. even allows the independent evaluation of time and temperature.^[20] This was possible by semi-analytical characterization of the creep-deformation process in polymeric inverse opals using local UV-vis spectroscopy. Recently, we showed a related material class: mixed colloidal crystals.^[21] These make use of adjustable dry-sintering kinetics^[22,23] and show great potential regarding evaluation using simple image analysis.

Sensing via RGB channels of images obtained with digital cameras greatly enhances the applicability compared to a spectral analysis. Examination using commercial, hand-held devices rather than expensive (micro-)spectrometers makes these appliances much more user-friendly and more easily distributable. Research on such methods has been shown for, e.g., pH-sensing^[24] and water-content determination.^[25] Other materials for smartphone-based temperature sensing allow readout via luminescence thermography.^[26–29] Another path towards combining materials science with digital advancements is beginning to evolve in the form of machine learning.^[30] The application of these tools stretches from the prediction of optical properties^[31] to optimizing synthetic parameters to create the desired materials.^[32] For sensors, machine learning allows automated readout of complex, multiparameter systems that often cannot be described analytically. Examples comprise biomolecular sensing,^[33] ethanol content,^[34] and temperature.^[35,36]


1. Introduction

Autonomous sensing has become increasingly important for various aspects of everyday life. For example, lifetime monitoring of

M. Schöttle, T. Tran, M. Retsch
Department of Chemistry
Physical Chemistry I
University of Bayreuth
95447, Universitätsstr. 30 Bayreuth, Germany
E-mail: markus.retsch@uni-bayreuth.de

H. Oberhofer
Department of Physics
Theoretical Physics VII
University of Bayreuth
Universitätsstr. 30, 95447 Bayreuth, Germany

H. Oberhofer, M. Retsch
Bavarian Center for Battery Technology (BayBatt)
University of Bayreuth
Universitätsstr. 30, 95447 Bayreuth, Germany

 The ORCID identification number(s) for the author(s) of this article can be found under <https://doi.org/10.1002/adv.202205512>

© 2023 The Authors. Advanced Science published by Wiley-VCH GmbH. This is an open access article under the terms of the Creative Commons Attribution License, which permits use, distribution and reproduction in any medium, provided the original work is properly cited.

DOI: 10.1002/adv.202205512

Here, we introduce a TTI based on multicomponent colloidal crystals, using smartphone-based image acquisition and machine learning analysis for the data evaluation. Four monodisperse polymer particle types are synthesized with varying glass transition temperatures to span a quaternary phase diagram. We use a fast, automated, and reproducible drop-casting method to fabricate colloidal crystal arrays of mixed compositions. The composition correlates to the dry-sintering kinetics and concomitantly to the loss of structural color. However, the quaternary particle system is too complex to allow an analytical description. Instead, we demonstrate that an artificial neural network can accurately measure our colloidal crystal arrays' time and temperature history. A system that initially is too intricate for conventional characterization is thereby made applicable for multiparameter sensing. Our analysis demonstrates a general approach to improve the sensing capabilities of well-established photonic structures drastically. Due to the scalable fabrication process, the modular adjustment to other sensing tasks by a specific particle selection, and the user-friendly, low-tech characterization method, this TTI concept opens the pathway toward cheap multiparameter sensors.

2. Results and Discussion

We aim to fabricate a sensor enabling a simple readout of two independent parameters: time and temperature. One main difficulty, thereby, is designing a system that is complex enough to over-determine the parameter space yet remains feasible to analyze. The concept presented here is based on an array of polymer colloidal crystals (CCs). The first step, therefore, is the realization of a suitable self-assembly process. Prerequisites for sample preparation are site selectivity, reproducibility, automation, and a fast preparation rate. Consequently, we apply a combination of array-printing and drop-casting that meets these criteria and additionally is scalable, resource-efficient, and non-toxic.

A spring-loaded pin with a hydrophilic, round tip is dipped into a particle suspension that adheres via wetting. When brought into contact with a glass substrate, a defined dispersion volume is deposited and subsequently forms a CC via evaporative self-assembly (Figure 1a). The interplay of capillary and Marangoni flow in these sessile droplets at room temperature results in a pronounced coffee-stain effect (Figure 1b).^[37] Structural colors appear faint and far from homogeneous, and the droplet itself shows an irregular shape. When heating the substrate to 70 °C, the interactions favor a homogeneous layer of particles, facilitated by the formation of a "milk-skin"-like particle layer during the accelerated evaporation.^[38] Additionally, evaporation occurs at the edges immediately after contact, forcing the assembly to occur in a well-defined circular area. This greatly enhances the reproducibility and, thereby, the readability of the sensor during the analysis described later. Scanning electron microscopy (SEM) images of the surface show large domain sizes of densely packed, monodisperse particles, corroborating the vivid structural colors observed via light microscopy (Figure 1c). Another significant feature of this process is efficiency, as almost none of the suspension is wasted. Therefore, a given laboratory-scale batch of particles (typically a few 100 mL with 5 wt.% particle concentration) can theoretically be used to prepare several thousand samples.

Having established a robust array fabrication method, we now present the cornerstones of the particulate system. The polymer latex particles used in this work consist of random copolymers of methyl methacrylate (MMA) and *n*-butyl acrylate (nBA). Four different particle types are prepared with varying comonomer volume ratios between 85:15 and 100:0 while maintaining a consistent particle diameter of 320 ± 5 nm. Self-assembly of all four particle types and subsequent UV-vis spectroscopy (Figure 1d) show an optical stop band at 635 ± 3 nm in each case. Both the assembly behavior and the periodicity of the resulting nanostructure are thereby proven to be uniform. The differences between the four particle types are elucidated via differential scanning calorimetry (DSC). Heating curves show the glass transition temperature (T_g) shifting towards higher temperatures when increasing the MMA content (Figure 1e). This dependency of T_g and comonomer composition is linear (Figure 1f).

The key aspects of these building blocks are the same size and surface chemistry of the particles with different thermal properties. This allows the fabrication of multicomponent yet crystalline nanostructures from mixed particle suspensions. Depending on the number of components in an ensemble, the film formation process can be tailored to a specific temperature range. The thermal parameter space, we apply for sensing, can be elucidated in a quaternary phase diagram (Figure 1g) showing all utilized particle mixtures. The automated array-printing setup facilitates the realization of this large parameter space. We, therefore, drop-cast a total of 20 different particle mixtures onto defined positions on a glass substrate (Figure 1h). Two spots are prepared with each composition to introduce some redundancy and improve later readout. The setup allows reproducible fabrication of samples with circular spots of CCs, all with the same vivid, red structural coloration due to a consistent periodicity, geometry, and effective refractive index (Figure 1i). Differences can later be observed at elevated temperatures, where the thermal response of each composition is tracked.

The question now is how to characterize such a sample appropriately. Classic laboratory characterization methods can be divided into two groups: 1) Methods that exhaustively cover the entire sample but can only be measured *ex situ*. 2) *In situ* methods that are, however, limited to one spot at a time. An example of *ex situ* characterization is scanning light and electron microscopy (Figure 2a–d). A pristine sample (RT), as well as three samples subjected to isothermal sintering at different temperatures between 83 and 112 °C for 120 min are shown. Depending on the thermal history, specific CCs remain (nearly) pristine, while others show various degrees of discoloration. We examine three representative positions post-sintering via SEM to corroborate the expected structural change (Figure 2b–d). The respective CCs consist of particles with 90%, 95%, and 100% MMA and show compositions of 0:1:2 (spot i), 1:1:1 (spot ii), and 2:1:0 (spot iii). When the CC consists of only high- T_g particles (spot i), the structure remains intact after heating (blue-shaded particles). When only the minority phase is affected by the temperature increase, and these particles deform (spot ii), an interconnected nanostructure of periodically arranged particles remains. As the temperature persists, these voids are slowly filled by the creeping polymer. The overall refractive index contrast between spheres and voids is concomitantly reduced, and the saturation diminishes. If the majority of particles are heated above their T_g (spot iii), only small

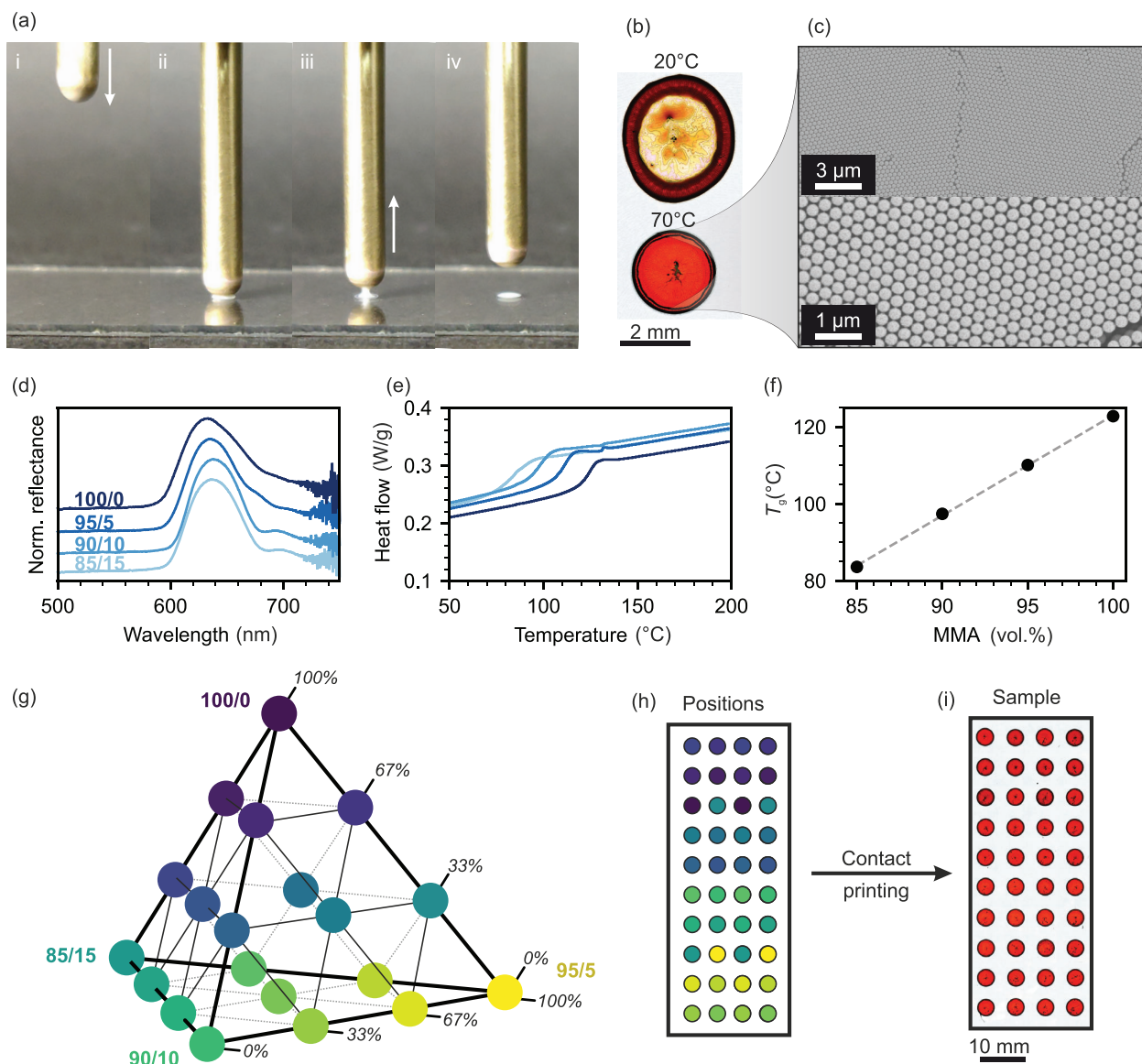


Figure 1. Fabrication process of multi-spot colloidal crystal sensors. a) Snapshots of the array-printing procedure, showing the (i) advancing, loaded tip, (ii,iii) the tip in contact with the substrate, and (iv) the receding pin. b) Microscopy images of spots prepared at different substrate temperatures, elucidating the importance of accelerated evaporation during self-assembly. c) SEM images of the colloidal crystal shown in panel (b). d) UV-vis reflectance spectra of four spots prepared from copolymer particles of identical size but different comonomer compositions. e) DSC heating curves of the four different copolymers. f) Glass transition temperatures obtained from panel (e), showing a linear dependence regarding the comonomer composition. g) Quaternary phase diagram of all particle mixtures obtained from mixing the four different particle types. h) Positions of these mixtures on the substrates. i) Microscopy image of a substrate prepared via the array-printing of the mixed particle suspensions shown in panels (g) and (h).

islands remain and (nearly) all symmetry and periodicity are lost. No discernable color remains.

Complementary to this ex situ evaluation, in situ UV-vis spectroscopy provides temporal information regarding the sintering process. Three spots are measured, one after the other (Figure 2e–g). The spectrum of spot i shows little to no change during 60 min at an elevated temperature. Spot ii, however, shows a slow and consistent degradation of the stop-band to approximately half of its previous reflectance. Spot iii shows a fast response, with

almost complete loss of any indication of a photonic stop-band during the first 10–15 min. Quantifying the time-dependent UV-vis spectra is possible, e.g., in the form of the normalized stop-band intensity (Figure 2h). However, it is unfeasible to perform this measurement at all 40 spots at once. Spectroscopic methods, therefore, fail to provide a holistic evaluation of the sensor's response to thermal events. Additionally, while similar optical studies of inverse polymeric opals have been conducted by applying, e.g., the Kelvin–Voigt model and WLF theory,^[20] our

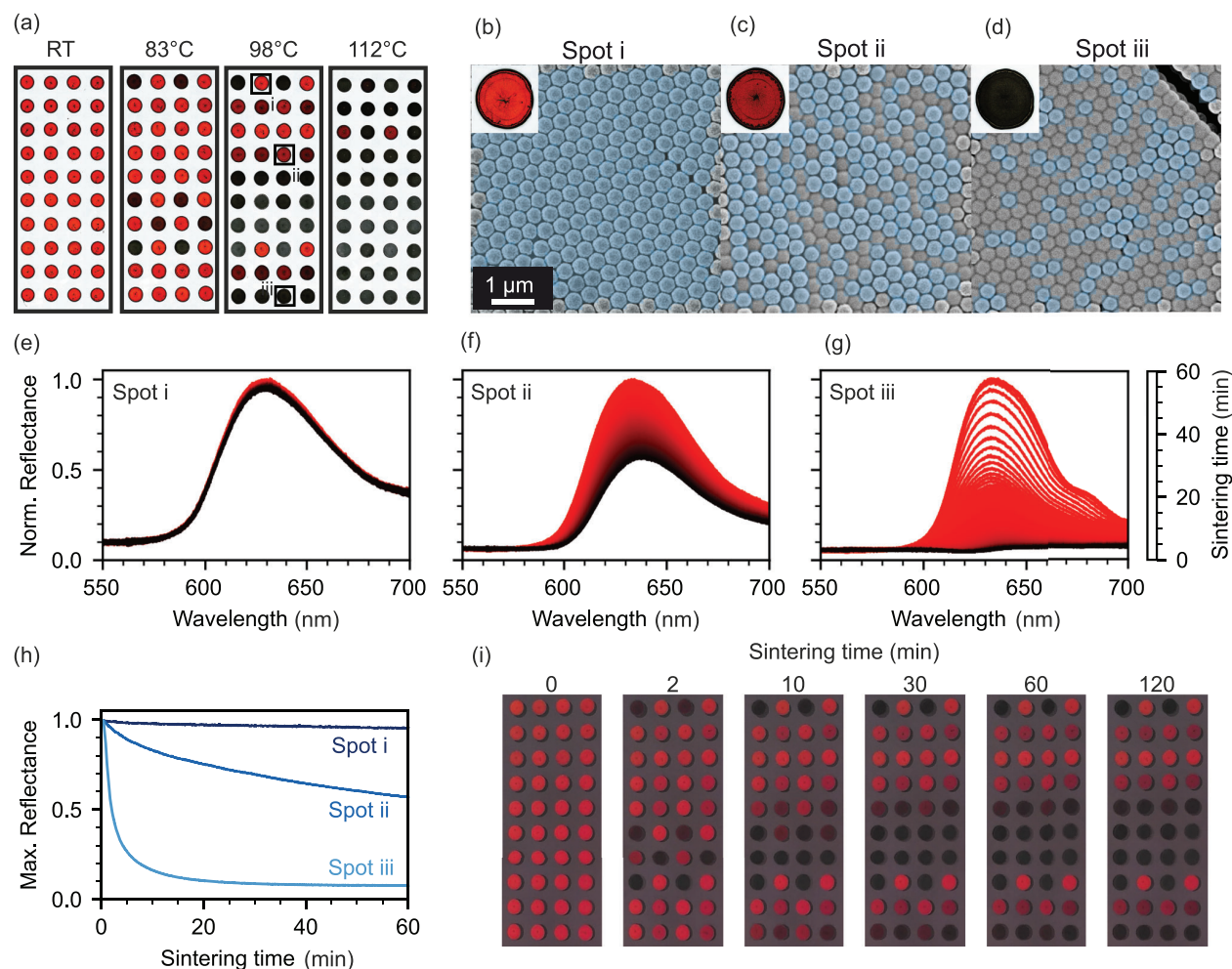


Figure 2. Thermal response of the sensors. a) Light microscopy images of samples held at different temperatures for 120 min. The width of each image is 27 mm. b–d) SEM images of the spots indicated in panel (a). The blue overlay shows intact, non-sintered particles. e–g) In situ UV–vis spectra of equivalent spots during the sintering process at 98 °C showing the gradual stop-band degradation. These, however, have to be measured consecutively. h) Time-dependent decrease of the normalized stop-band intensity. i) Photographs taken in situ of a sample during the sintering process at 98 °C with a smartphone camera.

system is difficult to be studied (semi-)analytically.^[21] Sintering of particulate systems, in general, is a multi-step process,^[39,40] and the binary and ternary mixtures increase this intricacy. Besides the polymer and particle composition, the surface chemistry may influence the film formation kinetics. All this renders an analytical description of the film formation increasingly difficult.

Machine learning lends itself as a prime candidate for evaluating the behavior of our sensors. It can describe nonlinear behavior without requiring extensive physical modeling. Instead, a prerequisite for machine learning is a large amount of data. We acquire the necessary data by capturing the time-dependent optical response of the sensor using a smartphone camera. This unconventional yet convenient method has the additional benefit of being widely applicable and providing a user-friendly and non-expert evaluation. Capturing the response with a smartphone combines the time-resolution of the in-situ UV–vis spectroscopy

with the ability to measure the entire sensor of scanning microscopy (Figure 2i).

An evaluation of the full images is computationally expensive and includes many pixels of the substrate background that contain no relevant information. Furthermore, slight differences between spot sizes will complicate the training process. We, therefore, determine the mean red value of each spot by dividing every image into 40 sub-images containing one spot each (Figure 3a). We use the mean brightness of the 5%, 10%, 15%, 20%, and 25% of pixels with the highest red value for the evaluation (Figure 3b). For each substrate, 40 spots with five mean values each correspond to 200 inputs for a given image. Compared to the RGB images with a size of 420×1060 pixels, the number of inputs is reduced by a factor of ≈6700, significantly speeding up computations. The mean red value of each spot (Figure 3c) changes similarly to the stop-band intensity shown in Figure 2h. Spots i and ii both show little to no change during 120 min of isothermal

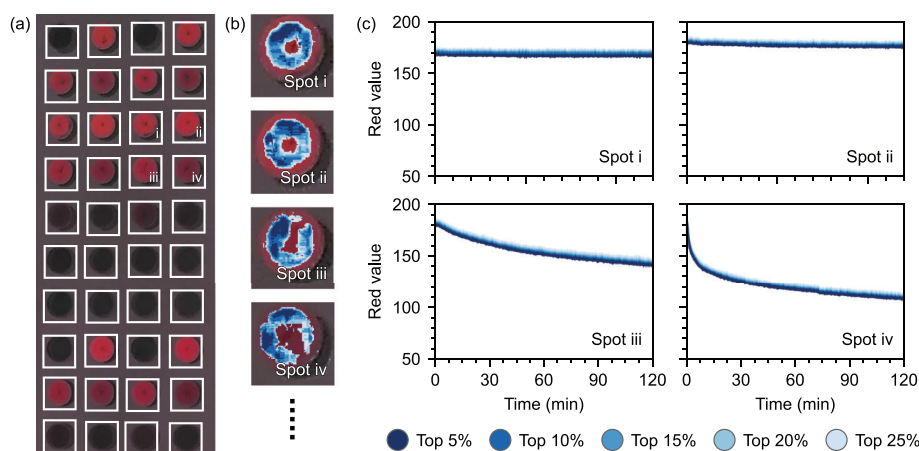


Figure 3. Preprocessing of the image data for the neural network. The shown image was taken after heating the sample for 80 min at 98 °C. a) The digital image of the sensor is divided into 40 sub-images containing one spot each. b) For each sub-image, the pixels with the highest red value are used for further evaluation. c) The mean red values follow the same trend as the stop-band decay.

heating. Also, the absolute red value of the two spots is nearly identical, corroborating the homogeneity and structural integrity of the CCs. The mean red value of spot iii decreases continuously throughout the measurement, while spot iv shows a fast degradation during the first 10 min. Combining these different response types to an elevated temperature is important for making a reasonable readout possible. For comparison, we also show analogue plots for samples measured 5 K above and below this temperature (Figure S1, Supporting Information). The influence of the change in temperature on the sintering kinetics is clearly visible in each decay curve. Therefore, we conclude that thermal and temporal information is hidden in the 200 inputs and continue to establish a model capable of deciphering the results.

We use artificial neural networks (ANNs) with ten hidden layers to predict the time and temperature of a single image. The design idea for our ANN is to model the distinct sintering kinetics of each particle composition at each temperature. Therefore, the model consists of two parts (Figure 4). First, the model estimates the probability of an image being taken at a specific temperature by detecting the pattern of spots with no, little, and high red intensities. The resulting probability density and the mean red values are the inputs for the time prediction layer. Finally, the model reports the most probable temperature and predicts the time as a continuous variable. A detailed description of the network architecture and training procedure is in the Experimental Section.

We trained the ANN with nine different temperatures between 100 and 140 °C. Here, we report the hot plate set point as the temperature for better readability. The set point is slightly higher than the actual sensor temperature (Figure S2, Supporting Information). At each temperature, we measured eight samples for 2 h at intervals of 5 s, corresponding to >94000 training images. Supervised training optimizes the model parameters, and after 20 training epochs, the model assigns 96.7% of training images to the correct temperature (Figure S3a, Supporting Information). The predicted time also correlates very well with the measured time. More than 80% of training inputs deviate <10 min from the correct value (Figure S3b, Supporting Information). We notice that the wrong assignment of temperatures occurs primarily

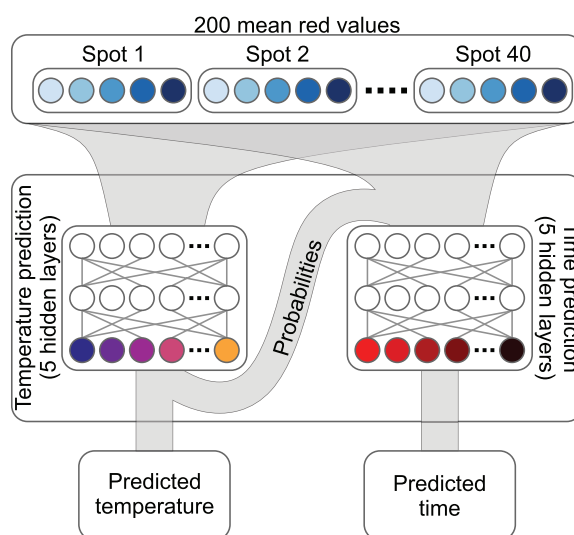


Figure 4. Artificial neural network architecture. The model consists of two parts. The first half predicts the temperature by using only the mean red values. The second half predicts the heating time, with the inputs being the mean red values and the temperature probabilities.

at short times and that the incorrectly predicted temperature is directly below the correct temperature (Figure S3c, Supporting Information).

Next, we investigate the generalization of our ANN by predicting the time and temperature for two validation samples per temperature. Our model has never seen these samples before and is unaware of the correct values. We can validate our system over the whole time–temperature regime because both the sensor creation and the sensor evaluation are automated. In total, the validation set consists of >23000 images. As shown in Figure 5, the resulting predictions resemble the training results well. Temperature predictions are correct for the most part (96.4%). If images are mislabeled, the temperature error is mainly only 5 K (3.3%).

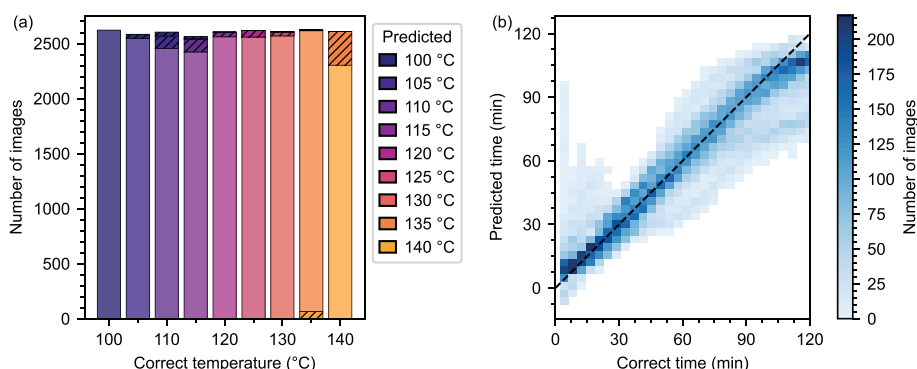


Figure 5. Prediction results for two samples per temperature, corresponding to >23000 validation images. a) Correlation of correct and predicted temperatures. Incorrect predictions (hatched areas) are minimal and mostly show a deviation of only 5 K from the correct value. Underestimations are shown at the top, and overestimations at the bottom. b) Correlation between correct and predicted time values.

Concerning the time, the majority of the predictions closely follow the correct value (Figure 5b). However, some predictions deviate from expectations. The large number of validation images allows us to investigate these deviations in more detail by grouping the time predictions by the correct temperature.

Figure 6a shows how the prediction quality varies with the correct sensor temperature. Each point in the graphs corresponds to one validation image. For most temperatures, no difference between the two used validation samples is visible, demonstrating that both the creation and evaluation of our sensors are highly reproducible. While predictions at temperatures below 135 °C are very accurate, some images at the highest temperatures show incorrectly predicted time values. As the same phenomenon occurs in the training data (although less pronounced), this is not a generalization issue but a limitation of the applied system itself.

Without a large amount of validation data, it is impossible to identify the prediction capabilities in the distinct areas shown above. Previous publications about TTIs validated their system with a small number of validation samples,^[15,18,20,21] thus, not covering the whole time–temperature regime. Our large amount of validation data allows us to state individual uncertainties for each pair of predicted temperature and time (Figure 7). The mean absolute difference between the predicted and the measured time is generally below 10 min for temperatures below 135 °C. For high temperatures, the uncertainty is larger. These individual errors can be used as an output for the end user. Examples of single images as recorded by a potential user are shown in Figure 6b.

Further examples are in Figures S4–S6 (Supporting Information), showing how our integrators behave with multiple temperature steps. As expected, if the sensors cool down between two isothermal heating steps, the predicted time is the sum of the two heating durations (Figure S4, Supporting Information). If multiple heating events in the temperature range of the sensors occur, the prediction refers to the higher temperature and further heating at lower temperatures does not affect the readout (Figure S5, Supporting Information). For small temperature differences, a slight overestimation of the time is possible (Figure S6, Supporting Information). Consequently, this type of TTI sensor is most suitable and applicable for the recording of the highest temperature events, which are, in many cases, the most relevant ones to judge on safety or spoilage issues.

The evaluation of a single photograph takes <1 s and is based solely on an image taken by a smartphone camera. No knowledge of photonic systems or the underlying physical processes is necessary to utilize our system. The software will immediately predict the time and temperature of the photographed sensor and state the corresponding uncertainty. Consequently, non-specialists can employ our system effortlessly. This concept can conceivably be adjusted to adapt the prerequisites to various applications. The time and temperature ranges that can be determined are related only to the thermal properties of the respective polymer particles. Changing the glass transition temperature of these can easily be done by varying the monomer composition. Alternatively, high-temperature applications can be made possible by adding inorganic components such as silica colloids to the phase diagram. Since the process is irreversible, tamper-proof monitoring of goods such as food or batteries becomes a simple process. Further advancements can be readily implemented by miniaturizing the colloidal arrays down to the image resolution limit of commercial cameras. Thereby, an even larger number of CC spots and, consequently, particle mixtures could be examined at once. Increasing the number of CC spots will also provide flexibility to include particle mixtures with different stop-bands allowing for a multi-color analysis specific to certain temperature ranges.

3. Conclusion

We established a concept that applies a combinatorial approach to add significant functionality to the well-known material class of polymer colloidal crystals. Mixed photonic systems described by a quaternary phase diagram were assembled using a scalable and efficient array-printing method. This allowed us to examine the thermal response of numerous samples, which formed a solid training set for our measurement evaluation. The sensor state can be optically read out by digital photography using a standard smartphone. The evaluation was performed using an artificial neural network. Using only the photograph of a sample subjected to isothermal heating, the model correctly predicts time and temperature independently. Our concept can be readily transferred to specific sensing applications comprising photonic structures and integrating sensing capabilities. The case demonstrated here

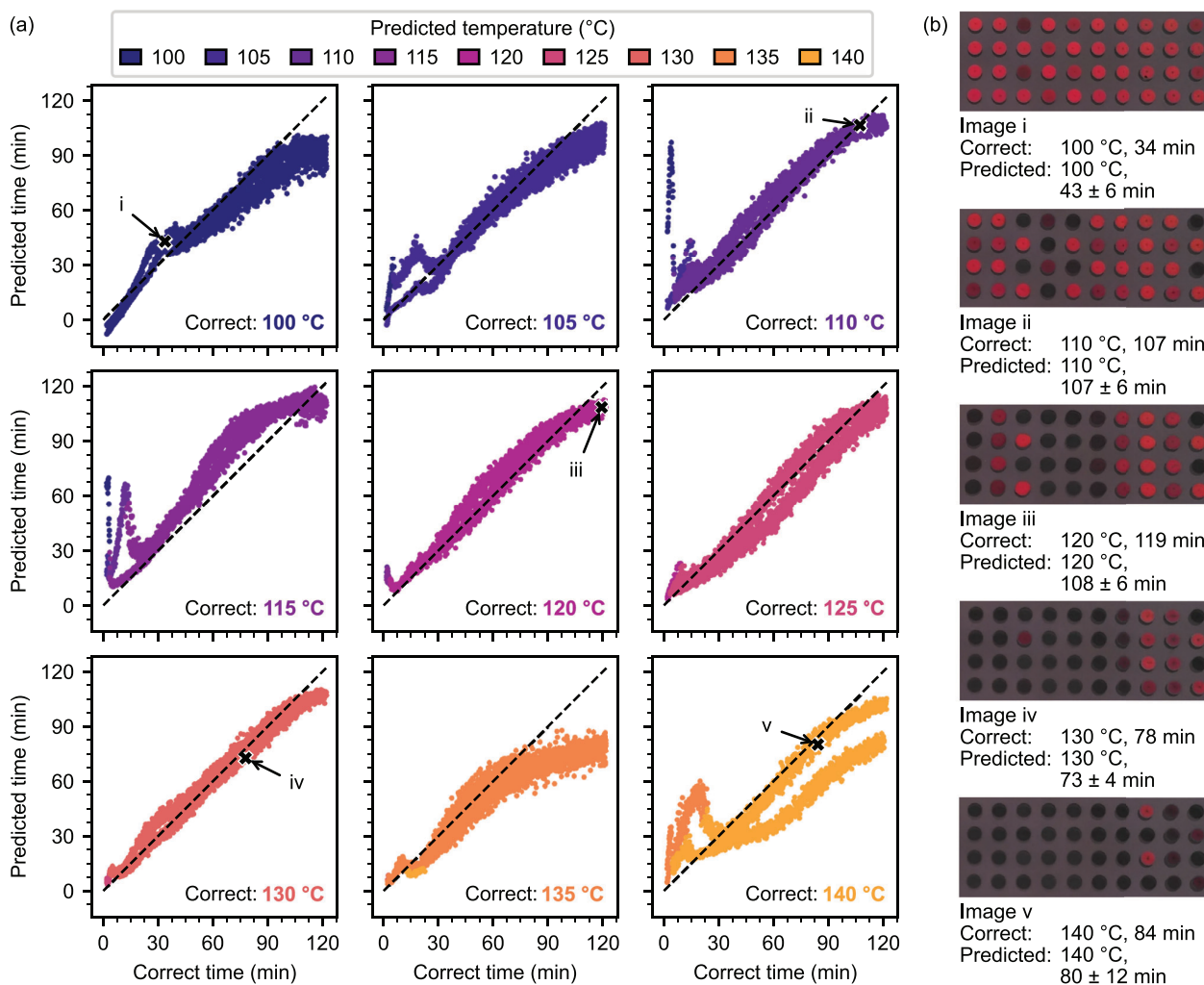


Figure 6. Detailed prediction results for the validation images. a) Predictions for the first seven temperatures are very close to the true values. At higher temperatures, the time predictions begin to deviate. b) Input images of five validation points from (a) with their corresponding predictions.

is particularly simple owing to the robust array fabrication procedure and the optical readout, which make this sensor useful for non-expert users. Overall, we showed how the combination of materials chemistry and advanced computational methods are starting to enable a multiparametric analysis from complex colloidal systems.

4. Experimental Section

Materials: Methyl methacrylate (MMA), *n*-butyl acrylate (nBA), 3-styrenesulfonic acid sodium salt hydrate (NaSS, 99%), and potassium persulfate (KPS, 99%) were obtained from Sigma–Aldrich. Before further use, both MMA and nBA were destabilized over Alox B. Water of MilliQ quality was used throughout all experiments. Glass substrates were cleaned via sonication in an aqueous 2 vol.% Helmanex III solution and in ethanol.

Particle Synthesis: Monodisperse particles were prepared via a surfactant-free emulsion polymerization. 240 mL water were heated to 80 °C and degassed in a 250 mL three-necked flask for 75 min. While stir-

ring at 600 rpm, 19 mL of the respective monomer mixture were added, together with 10 mg NaSS dissolved in 5 mL water. After 5 min, the polymerization was initiated by adding 200 mg KPS dissolved in 5 mL water. The reaction was left to proceed overnight and terminated by exposure to ambient oxygen. The different particle dispersions were each filtered over a 125 μm mesh and otherwise used directly for preparing the binary and ternary mixtures. The concentration of all dispersions was 5.7 ± 0.1 wt.%.

Self-Assembly via Array-Printing: The printing procedure was fully automated using an XYZ stage to ensure full reproducibility. A clean glass substrate was placed on a hot-plate set to 70 °C. A spring-loaded, rounded brass pin with a diameter of 5 mm was dipped into a dispersion and then brought in contact with the substrate for a duration of 1 s. The pin was then mechanically cleaned in a water bath and dried with a non-woven fabric. The process then repeated with the next dispersion.

Characterization Methods: Microscopy images were obtained using a laser scanning confocal microscope (Olympus, OLS5000) with a white light source as well as a 405 nm laser with a 5x-magnification lens and stitching of 7×18 images.

Scanning electron microscopy images were obtained with a Zeiss Leo 1530 (Carl Zeiss AG, Germany) at an operating voltage of 1 kV and both

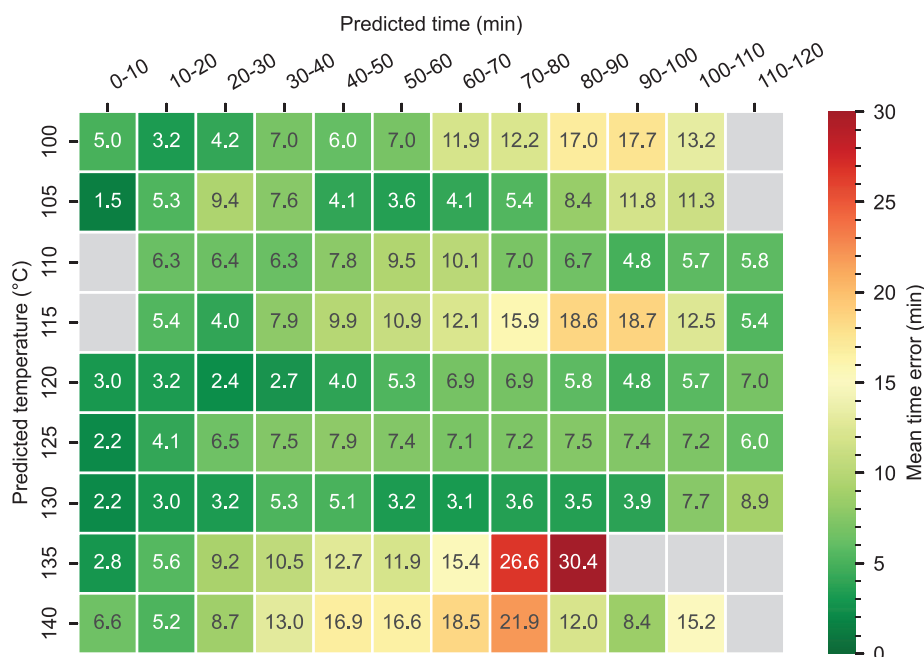


Figure 7. Mean errors between predicted and correct time. The validation over the whole time–temperature regime allows estimating uncertainties precisely. Lower temperatures show a smaller deviation from the correct value. For high predicted temperatures, the uncertainty increases.

in-lens as well as secondary electron detection after sputtering of 2 nm platinum. Images, where a false-colored overlay was applied, are shown in their original form in Figure S7 (Supporting Information).

UV–vis spectra of drop-cast suspensions were measured on an Olympus IX71 inverted microscope with a 10x lens in reflection geometry and a halogen light source. An OceanOptics USB4000 spectrometer was coupled via fiber optics. In situ measurements were conducted using an Instec HCS622HV heating stage with a silver heating block set to 110 °C. Samples were attached to the stage using double-sided carbon tape, and the sample was heated to 98 ± 3 °C. Spectra were obtained at intervals of 2 s.

Differential scanning calorimetry was conducted using a TA Instruments Discovery DSC 2500. The second of two heating cycles was used for the evaluation. Samples were measured between 20 and 200 °C at 10 K min^{-1} and in a nitrogen atmosphere.

The hydrodynamic diameter was measured using diluted dispersions with a Zetasizer (Malvern) with 175° backscattering geometry.

Image Acquisition and Feature Extraction: Each sample was placed on a black-coated hot plate (PZ 28-2, Harry Gestigkeit GmbH). A full-spectrum lamp (Walimex pro LED Niova 600 Plus Daylight) with a light diffuser illuminated the sample at an angle of 10° and a distance of 30 cm. A smartphone (Fairphone 3+) took photographs (ISO 100, $1/10647$ s exposure time) of the sample at an angle of 10° and a distance of 10 cm every 5 s, stored in the WebP format. The full 3000×4000 pixel images were cut into 40 squares of 75×75 pixels at pre-defined positions. The cropped images are available online.^[41] For each square, the 5%, 10%, 15%, 20%, and 25% pixels with the highest red value were used to determine five distinct mean values used as the input for the ANN. Each input vector of length 200 was standardized by z-score normalization using the mean and standard deviation of the training set.

ANN Architecture: PyTorch^[42] was used for the network creation and we made the code available online.^[43] To choose a suitable model structure, different architectures were compared. Details are in the Supporting Information. The final machine learning approach encompasses two almost identical, sequential models for temperature and time. They consist of an initial batch normalization layer and five hidden, linear layers each.

The hidden layers have node sizes of 8192, 2048, 2048, 2048, and 512, respectively. Each hidden layer uses a leaky ReLU function^[44] as its activation. After the final hidden layer, a dropout layer with a dropout probability of 50% was introduced to improve generalization. For the temperature module, the output layer was a softmax function creating a probability density for the nine temperature categories. For the time module, the output layer was a final linear layer of size one.

Training Process: The time series images of eight samples per temperature were labeled and used for training. The initial 2 min of each sample were discarded due to temperature equilibration (Figure S2, Supporting Information). Prior to training, the time labels were scaled by min–max normalization with a minimum time of 2 min and a maximum of 122 min. Stochastic gradient descent was employed. Different hyperparameters were tested (Table S2, Supporting Information). The final model was trained with a batch size of 32, a learning rate of 5×10^{-4} , a Nesterov momentum of 0.9 and a weight decay of 1×10^{-3} . The loss function is the sum of the cross-entropy loss for the temperature prediction and the mean squared error for the time predictions. The training concluded after 20 epochs.

Statistical Analysis: The errors indicated for the predicted times are mean deviations between the correct and predicted times of the validation data. To determine those, predictions were grouped into the temperature and time bins shown in Figure 7. For each bin, the mean absolute difference between the correct and predicted value is shown. The training set consists of 94032 and the validation set of 23433 images. Preprocessing of the photographs is explained in the subsection “Image Acquisition and Feature Extraction”. The data and software are available online.^[41,43]

Supporting Information

Supporting Information is available from the Wiley Online Library or from the author.

Acknowledgements

M.S. and T.T. contributed equally to this work. The authors thank the keylabs of the Bavarian Polymer Institute (BPI) for access to the scanning electron microscopy. H.O. acknowledges support by the DFG within the Heisenberg scheme (grant no. OB425/9-1). T.T. and M.S. appreciate the support by the Elite Network Bavaria (ENB). Funded by the Deutsche Forschungsgemeinschaft (DFG, German Research Foundation) – 491183248. Funded by the Open Access Publishing Fund of the University of Bayreuth. Open Access funding enabled and organized by Projekt DEAL.

Open access funding enabled and organized by Projekt DEAL.

Conflict of Interest

The authors declare no conflict of interest.

Data Availability Statement

The data that support the findings of this study are available from the corresponding author upon reasonable request.

Keywords

artificial neural network, film formation, photonic crystals, sensors, smart-phone, structural colors

Received: September 22, 2022

Revised: December 23, 2022

Published online:

- [1] R. A. Barry, P. Wiltzius, *Langmuir* **2006**, *22*, 1369.
- [2] L. H. J. Raijmakers, D. L. Danilov, R. A. Eichel, P. H. L. Notten, *Appl. Energy* **2019**, *240*, 918.
- [3] B. Liu, P. A. Gurr, G. G. Qiao, *ACS Sens.* **2020**, *5*, 2903.
- [4] Z. Li, Y. Yin, *Adv. Mater.* **2019**, *31*, 1807061.
- [5] J. H. Holtz, S. A. Asher, *Nature* **1997**, *389*, 829.
- [6] M. Tsuchiya, Y. Kurashina, H. Onoe, *Sci. Rep.* **2019**, *9*, 17059.
- [7] J. Hou, M. Li, Y. Song, *Nano Today* **2018**, *22*, 132.
- [8] I. B. Burgess, L. Mishchenko, B. D. Hatton, M. Kolle, M. Lončar, J. Aizenberg, *J. Am. Chem. Soc.* **2011**, *133*, 12430.
- [9] S. Jia, Z. Tang, Y. Guan, Y. Zhang, *ACS Appl. Mater. Interfaces* **2018**, *10*, 14254.
- [10] M. Chen, Y. Zhang, S. Jia, L. Zhou, Y. Guan, Y. Zhang, *Angew. Chem., Int. Ed.* **2015**, *54*, 9257.
- [11] Z. Ma, P. Chen, W. Cheng, K. Yan, L. Pan, Y. Shi, G. Yu, *Nano Lett.* **2018**, *18*, 4570.
- [12] M. Weston, S. Geng, R. Chandrawati, *Adv. Mater. Technol.* **2021**, *6*, 2001242.
- [13] J. Reichstein, S. Mussig, H. Bauer, S. Wintzheimer, K. Mandel, *Adv. Mater.* **2022**, *34*, 2202683.
- [14] K. Ueno, K. Matsubara, M. Watanabe, Y. Takeoka, *Adv. Mater.* **2007**, *19*, 2807.
- [15] I. Jurewicz, A. A. K. King, R. Shanker, M. J. Large, R. J. Smith, R. Maspero, S. P. Ogilvie, J. Scheerder, J. Han, C. Backes, J. M. Razal, M. Florescu, J. L. Keddie, J. N. Coleman, A. B. Dalton, *Adv. Funct. Mater.* **2020**, *30*, 2002473.
- [16] C. Zhang, A. X. Yin, R. Jiang, J. Rong, L. Dong, T. Zhao, L. D. Sun, J. Wang, X. Chen, C. H. Yan, *ACS Nano* **2013**, *7*, 4561.
- [17] S. Choi, Y. Eom, S. M. Kim, D. W. Jeong, J. Han, J. M. Koo, S. Y. Hwang, J. Park, D. X. Oh, *Adv. Mater.* **2020**, *32*, 1907064.
- [18] J.-W. Kim, J.-S. Lee, S.-H. Kim, *Adv. Mater. Interfaces* **2018**, *5*, 1701658.
- [19] Y. Foelen, A. Schenning, *Adv. Sci.* **2022**, *9*, e2200399.
- [20] S. Y. Lee, J. S. Lee, S. H. Kim, *Adv. Mater.* **2019**, *31*, 1901398.
- [21] M. Schöttle, T. Tran, T. Feller, M. Retsch, *Adv. Mater.* **2021**, *33*, 2101948.
- [22] F. A. Nutz, M. Retsch, *Sci. Adv.* **2017**, *3*, eaao5238.
- [23] F. A. Nutz, M. Retsch, *Phys. Chem. Chem. Phys.* **2017**, *19*, 16124.
- [24] P. Das, S. Paul, S. S. Bhattacharya, P. Nath, *IEEE Sens. J.* **2020**, *21*, 2839.
- [25] J. Othong, J. Boonmak, F. Kielar, S. Youngme, *ACS Appl. Mater. Interfaces* **2020**, *12*, 41776.
- [26] J. F. C. B. Ramalho, S. F. H. Correia, L. Fu, L. L. F. Antonio, C. D. S. Brites, P. S. Andre, R. A. S. Ferreira, L. D. Carlos, *Adv. Sci.* **2019**, *6*, 1900950.
- [27] W. Piotrowski, K. Trejgis, K. Maciejewska, K. Ledwa, B. Fond, L. Marciniak, *ACS Appl. Mater. Interfaces* **2020**, *12*, 44039.
- [28] J. F. C. B. Ramalho, L. D. Carlos, P. S. André, R. A. S. Ferreira, *Adv. Photonics Res.* **2021**, *2*, 2000211.
- [29] J. F. C. B. Ramalho, L. M. S. Dias, L. Fu, A. M. P. Botas, L. D. Carlos, A. N. Carneiro Neto, P. S. André, R. A. S. Ferreira, *Adv. Photonics Res.* **2021**, *3*, 2100206.
- [30] J. Kimmig, S. Zechel, U. S. Schubert, *Adv. Mater.* **2021**, *33*, 2004940.
- [31] S. Xu, X. Liu, P. Cai, J. Li, X. Wang, B. Liu, *Adv. Sci.* **2022**, *9*, 2101074.
- [32] J. Kimmig, T. Schuett, A. Vollrath, S. Zechel, U. S. Schubert, *Adv. Sci.* **2021**, *8*, 2102429.
- [33] S. Pandit, T. Banerjee, I. Srivastava, S. Nie, D. Pan, *ACS Sens.* **2019**, *4*, 2730.
- [34] A. Döring, A. L. Rogach, *ACS Appl. Nano Mater.* **2022**, *5*, 11208.
- [35] C. Lewis, J. W. Erikson, D. A. Sanchez, C. E. McClure, G. P. Nordin, T. R. Munro, J. S. Colton, *ACS Appl. Nano Mater.* **2020**, *3*, 4045.
- [36] Y. Zhang, L. Yu, Z. Hu, L. Cheng, H. Sui, H. Zhu, G. Li, B. Luo, X. Zou, L. Yan, *J. Lightwave Technol.* **2021**, *39*, 1537.
- [37] A. Gencer, C. Schutz, W. Thielemans, *Langmuir* **2017**, *33*, 228.
- [38] J. Zhang, Z. Zhu, Z. Yu, L. Ling, C.-F. Wang, S. Chen, *Mater. Horiz.* **2019**, *6*, 90.
- [39] G. Herzog, M. M. Abul Kashem, G. Benecke, A. Buffet, R. Gehrke, J. Perlich, M. Schwartzkopf, V. Korstgens, R. Meier, M. A. Niedermeier, M. Rawolle, M. A. Ruderer, P. Muller-Buschbaum, W. Wurth, S. V. Roth, *Langmuir* **2012**, *28*, 8230.
- [40] E. A. Sulyanova, A. Shabalin, A. V. Zozulya, J. M. Meijer, D. Dzhi-gaev, O. Gorobtsov, R. P. Kurta, S. Lazarev, U. Lorenz, A. Singer, O. Yefanov, I. Zaluzhnyy, I. Besedin, M. Sprung, A. V. Petukhov, I. A. Vartanyants, *Langmuir* **2015**, *31*, 5274.
- [41] M. Schöttle, T. Tran, H. Oberhofer, M. Retsch, Experimental Data for: Machine learning enabled image analysis of time-temperature sensing colloidal arrays, <https://doi.org/10.5281/zenodo.7464047> (accessed: January 2023).
- [42] A. Paszke, S. Gross, F. Massa, A. Lerer, J. Bradbury, G. Chanan, T. Killeen, Z. Lin, N. Gimelshein, L. Antiga, A. Desmaison, A. Kopf, E. Yang, Z. DeVito, M. Raison, A. Tejani, S. Chilamkurthy, B. Steiner, L. Fang, J. Bai, S. Chintala, in *Advances in Neural Information Processing Systems 32 (NeurIPS 2019)*, (Eds: H. Wallach, H. Larochelle, A. Beygelzimer, F. d'Alché-Buc, E. Fox, R. Garnett), Curran Associates, Inc., Red Hook, Vancouver, Canada **2019**, pp. 8024–8035.
- [43] The source code for our software, the preprocessed data, model, and training scripts, <https://github.com/thomas-tran-de/tti-analysis> (accessed: January 2023).
- [44] B. Xu, N. Wang, T. Chen, M. Li, Empirical evaluation of rectified activations in convolutional network, arXiv 2015, 1505.00853.

Supporting Information

for *Adv. Sci.*, DOI 10.1002/adv.202205512

Machine Learning Enabled Image Analysis of Time-Temperature Sensing Colloidal Arrays

*Marius Schöttle, Thomas Tran, Harald Oberhofer and Markus Retsch**

Supporting Information: Machine learning enabled image analysis of time-temperature sensing colloidal arrays

*Marius Schöttle Thomas Tran Harald Oberhofer Markus Retsch**

M. Schöttle, T. Tran, Prof. M. Retsch

Department of Chemistry, University of Bayreuth, Universitätsstr. 30, 95447 Bayreuth, Germany

Email Address: markus.retsch@uni-bayreuth.de

Prof. H. Oberhofer

Department of Physics, Theoretical Physics VII, University of Bayreuth, Universitätsstr. 30, 95447 Bayreuth, Germany

Prof. H. Oberhofer, Prof. M. Retsch

Bavarian Center for Battery Technology (BayBatt), University of Bayreuth, Universitätsstr. 30, 95447 Bayreuth, Germany

1 ANN Architecture

We compared five different model and chose the best one to be our final architecture (Tab. S1).

Full images The input for this model are the RGB images of our sensors instead of the average red values. Multiple convolutional layers precede the fully connected layers.

Single model Instead of splitting the model into parts dedicated to the temperature and time prediction, we use the outputs of the second to last layer to one independent layer for time and temperature, each.

Small model The number of nodes of this model is reduced to 1/16th of the final model.

Medium model The model architecture described in the main text.

Large model The number of nodes of this model is four times larger than that of the final model.

Table S1: Comparison between different network architectures. The final model is highlighted.

Model	Traning loss	Validation loss
Full images	1.38	1.62
Single model	1.45	1.48
Small model	1.52	1.54
Medium model	1.41	1.42
Large model	1.43	1.49

Table S2: Comparison between different training parameters. Shaded parameters are used to train our model.

Batch size	Learning rate	Momentum	Weight decay	Traning loss	Validation loss
32	5×10^{-4}	0.7	1×10^{-3}	1.56	1.54
32	5×10^{-4}	0.98	1×10^{-3}	1.44	1.49
32	5×10^{-4}	0.9	1×10^{-4}	1.45	1.42
32	5×10^{-4}	0.9	5×10^{-3}	1.53	1.50
16	5×10^{-4}	0.9	1×10^{-3}	1.46	1.44
64	5×10^{-4}	0.9	1×10^{-3}	1.50	1.49
32	1×10^{-4}	0.9	1×10^{-3}	1.61	1.54
32	5×10^{-4}	0.9	1×10^{-3}	1.41	1.42
32	1×10^{-3}	0.9	1×10^{-3}	1.44	1.44

2 Supporting Figures

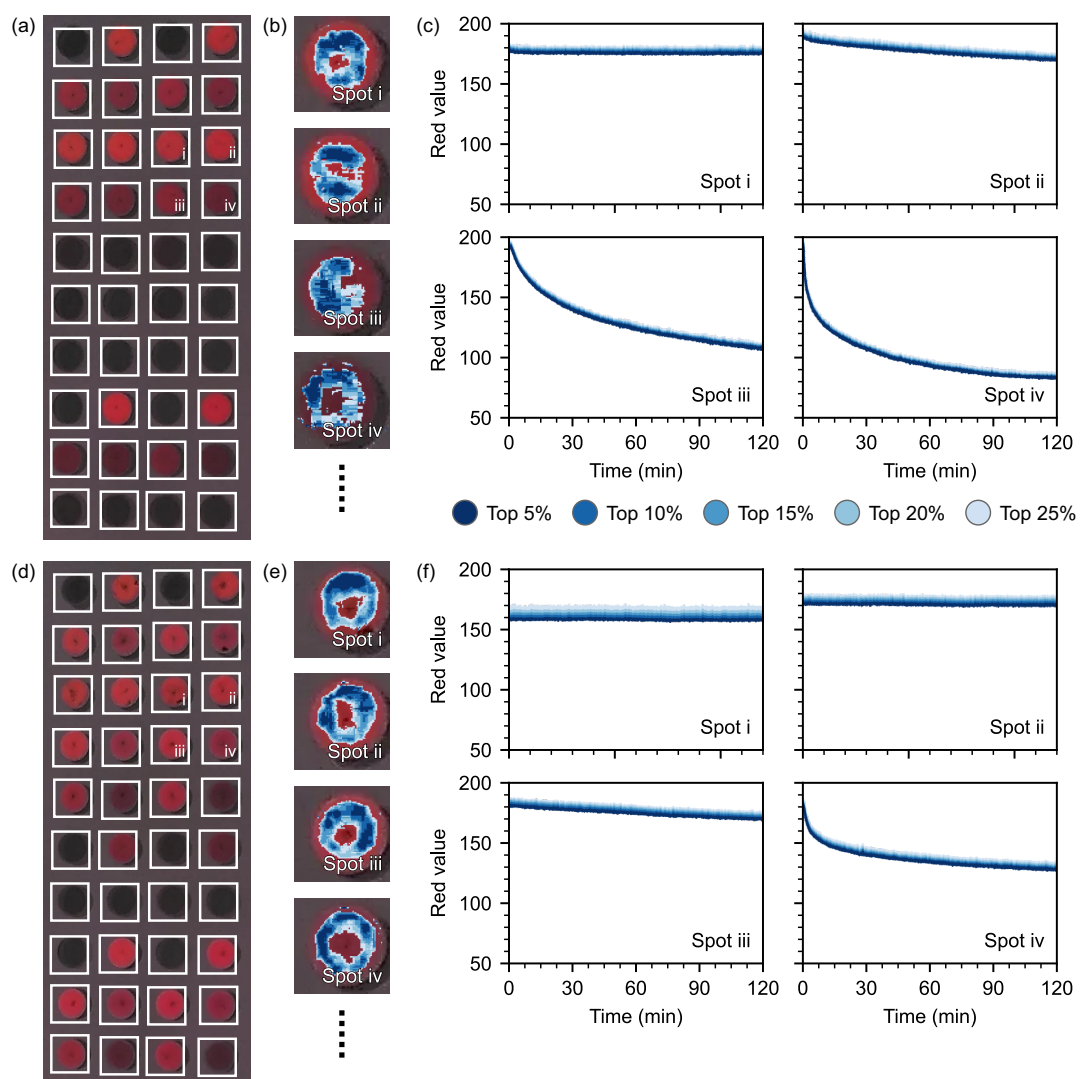


Figure S1: Detection of mean red values for samples at different temperatures. (a-c) 125 °C, (d-f) 115 °C.

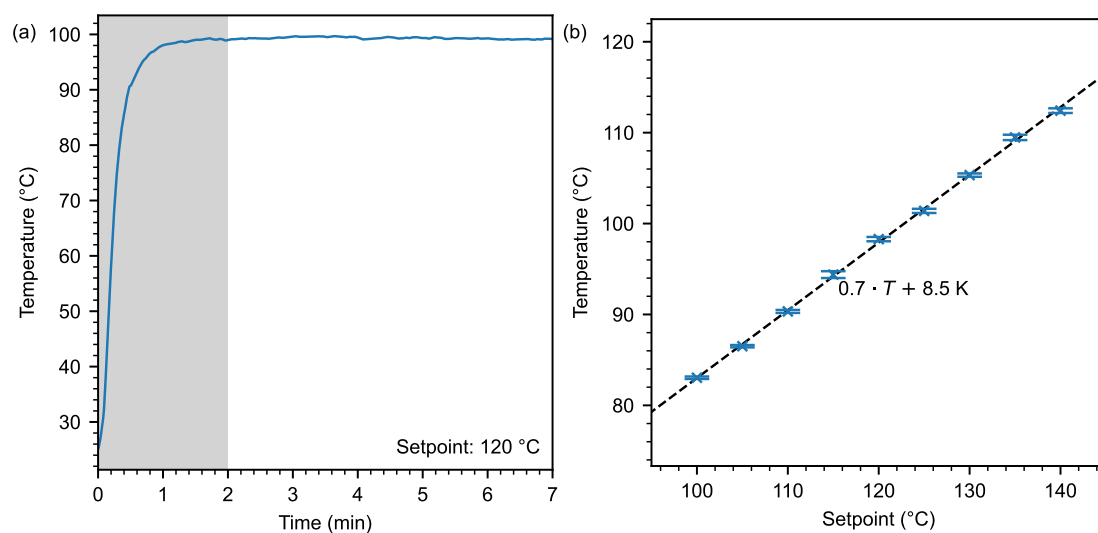


Figure S2: Sample temperature on the hotplate. The true temperature was measured by a Pt-100 placed on top of a glass substrate. (a) During the first two minutes (shaded area), the sample reaches thermal equilibrium. (b) Due to the experimental setup, the sample temperature is lower than the setpoint of the hotplate.

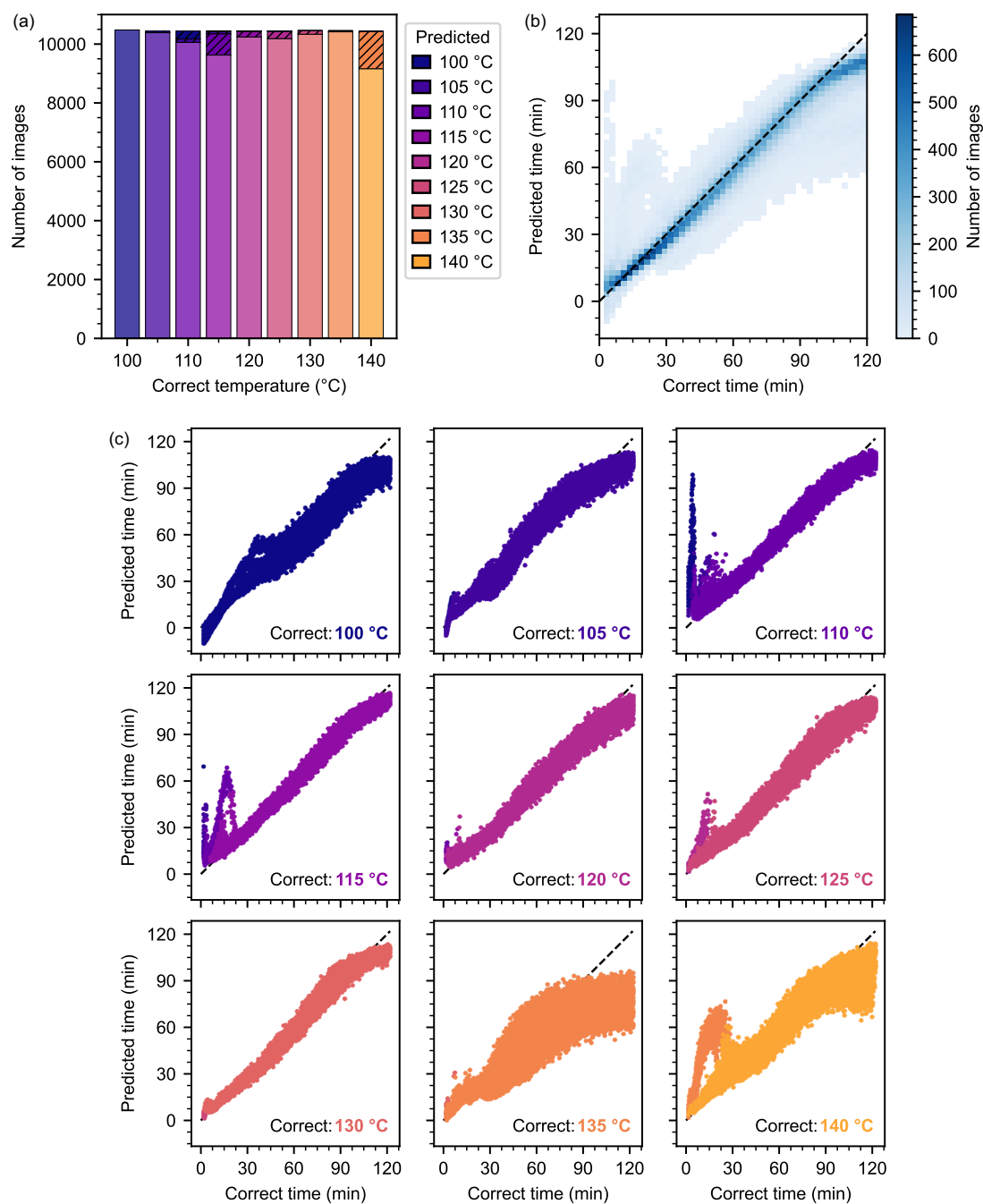


Figure S3: Prediction results for the training data. (a) Temperature prediction. (b) Correlation between predicted and correct time. (c) Detailed view of time and temperature prediction.

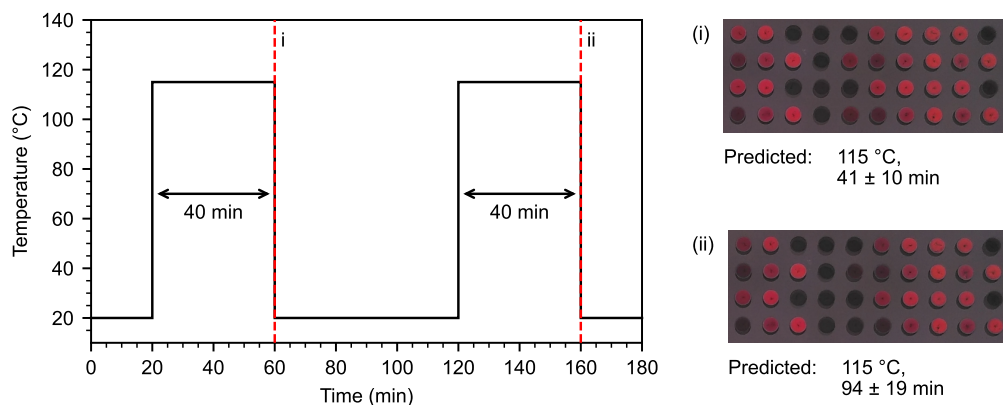


Figure S4: Prediction results with complete cooldown. The graph shows the applied temperature profile. Evaluation of the sensor after both heating steps shows is as expected. The sensors integrate the total time at the elevated temperature.

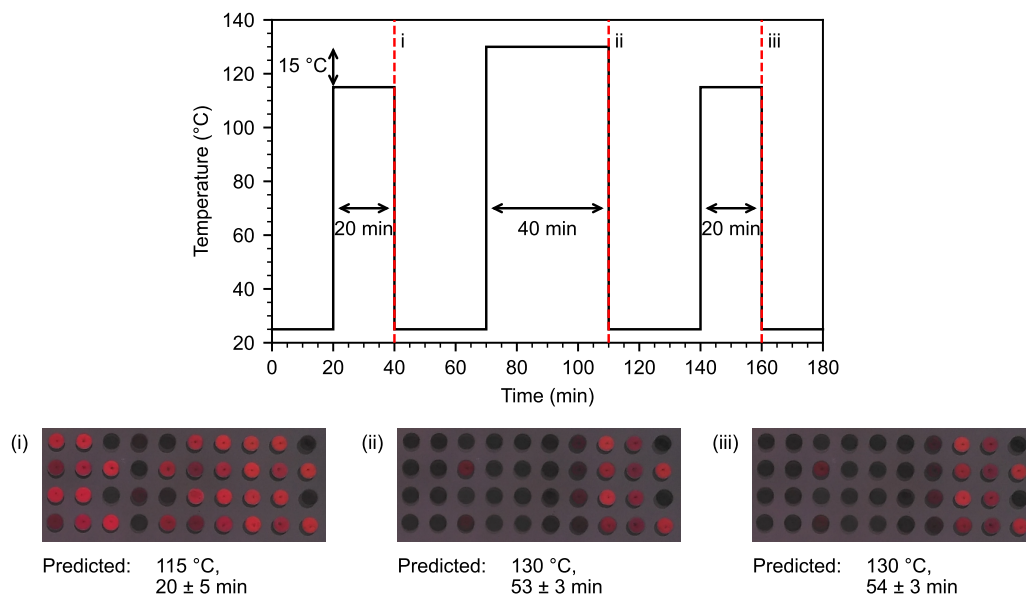


Figure S5: Multiple heating events inside the operating range of the sensor. The sensor reports the highest detected temperature and the corresponding heating time.

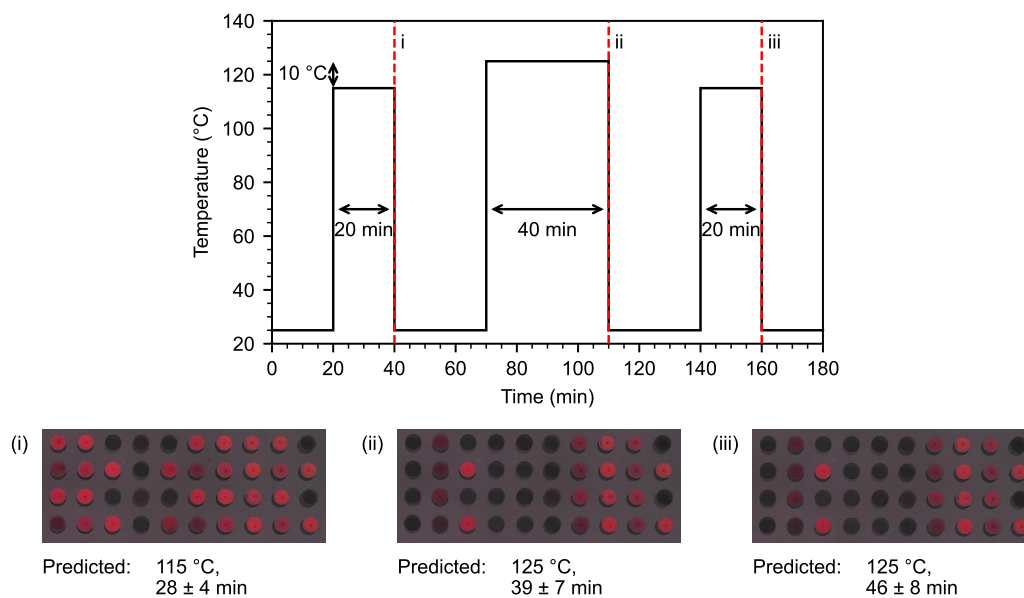


Figure S6: Multiple heating steps with a small temperature difference. Our sensor shows the expected result after the first and second heating step. After the third heating step, the predicted time slightly increases.

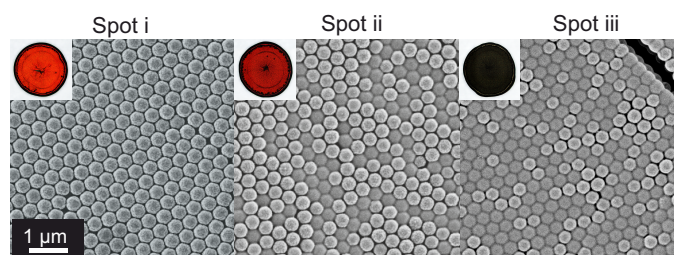
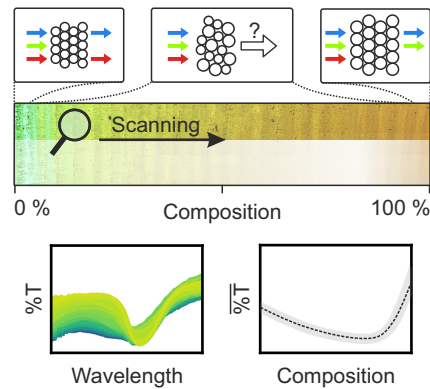


Figure S7: Original SEM images of partially sintered colloidal crystals shown in Fig 2b-d.

Microspectroscopy on Thin Films of Colloidal Mixture Gradients for Data-Driven Optimization of Optical Properties

Marius Schöttle, Maximilian Theis, Tobias Lauster, Stephan Hauschild, and Markus Retsch, „Microspectroscopy on Thin Films of Colloidal Mixture Gradients for Data-Driven Optimization of Optical Properties“, *Advanced Optical Materials*, **2023**, 16(11), 2300095.



Gradient colloidal assembly is a powerful fabrication tool that provides large amounts of data from local measurements along a single sample. Here, an approach to characterize an optimal scattering efficiency of thin films comprising binary colloidal mixtures is shown. A distinct optimum can thereby be observed at the edge of the composition range.

Microspectroscopy on Thin Films of Colloidal Mixture Gradients for Data-Driven Optimization of Optical Properties

Marius Schöttle, Maximilian Theis, Tobias Lauster, Stephan Hauschild, and Markus Retsch*

Thin films comprising mixtures of different colloids provide a simple approach to materials with tunable optical properties. However, the prediction of UV–vis spectra for different compositions in colloidal crystals and glasses is difficult. The degree of disorder, for example, determines whether the optical response is dominated by incoherent scattering, coherent scattering, or Bragg diffraction. Both the volume ratio, as well as the morphology of the individual constituents, influence the properties of the ensemble, which necessitates extensive screening procedures. Here, a method for expediting such a screening approach by means of gradient colloidal crystals and glasses is shown. Continuous composition gradients, combined with local microspectroscopy, allow for the characterization of the entire composition range with high reproducibility, thereby reducing the experimental effort. This is shown for a system of spherical polymer particles with different radii. An optimum of the scattering efficiency in the visible wavelength range is shown close to the order/disorder transition at the edge of the composition range. The high-throughput screening method presented here can generate large data sets that may contribute to machine-learning-enabled optimization of self-assembled optical materials.

1. Introduction

The optical properties of non-absorbing, homogeneous bulk materials are intrinsic to the specific compound and provide little freedom for adjustment. Assemblies of colloidal microparticles, however, feature a high interface density and non-continuous refractive index (RI). This opens a variety of possibilities for engineered light-matter interactions. An especially interesting case is thin, particulate films, which lie in an intermediate regime between ballistic light transport and the opaque whiteness caused by multiple scattering.^[1] These films play an important role in elementary applications such as paint or paper, as well as in coatings for electronics, solar cells, and radiative cooling.^[2–4] The most common parameters governing the optical properties are the size, shape, and RI of the single particles, as well as the superordinate structure and filling fraction.^[5,6] Inspiration can be found, for example, in the pronounced

white appearance of highly scattering thin films in some beetle scales and butterfly wings.^[1,7,8] Biomimetic approaches to efficient scattering have been presented in the form of porous structures built from silica or cellulose-based colloids.^[9,10] Both shape anisotropy, as well as optimized Mie scattering are effective parameters, the latter providing the best results when the characteristic size is approximately half the wavelength of the incident light.^[11] This morphological optimization allows the use of low-RI (< 1.7) materials that could replace potentially harmful titania nanoparticles.^[12]

When using monodisperse, spherical colloids, various types of photonic materials can be fabricated. Ordered colloidal crystals, for example, exhibit a periodically changing refractive index. Ballistic light transport and interference cause angle-dependent structural colors.^[13,14] However, if the strong immersion capillary forces and concomitant dense packing can be prevented during the assembly process, disordered colloidal glasses are obtained.^[15] Structural coloration via dispersive light diffusion in such materials is attributed to Mie scattering of isomorphic particles and short-range order.^[16–18] Colloidal glasses provide a versatile approach to tuning optical properties such as broadband reflectance or in anti-counterfeiting applications.^[19–21] A

M. Schöttle, M. Theis, T. Lauster, M. Retsch
Department of Chemistry
Physical Chemistry I
University of Bayreuth
Universitätsstr. 30, 95447 Bayreuth, Germany
E-mail: markus.retsch@uni-bayreuth.de

S. Hauschild
Jülich Centre for Neutron Science (JCNS-1/IBI-8)
Forschungszentrum Jülich GmbH
52425 Jülich, Germany

M. Retsch
Bavarian Polymer Institute
Bayreuth Center for Colloids and Interfaces, and Bavarian Center for
Battery Technology (BayBatt)
University of Bayreuth
95447 Bayreuth, Germany

 The ORCID identification number(s) for the author(s) of this article can be found under <https://doi.org/10.1002/adom.202300095>

© 2023 The Authors. Advanced Optical Materials published by Wiley-VCH GmbH. This is an open access article under the terms of the Creative Commons Attribution License, which permits use, distribution and reproduction in any medium, provided the original work is properly cited.

DOI: 10.1002/adom.202300095

simple route to these amorphous systems is the co-assembly of two particle sizes from a bi-disperse suspension.^[22] While specific size ratios and compositions allow co-crystallization,^[23] most combinations induce disorder. Binary particle monolayers have been prepared to determine optimum haze properties depending on the composition of large and small particles as well as the filling fraction.^[24] These particle monolayers have also been utilized to specifically examine the transition from an ordered monodisperse system to the disordered binary case.^[25] Spectroscopic analysis and simulations revealed the crossover from collective diffraction to single-particle scattering. 3D assemblies have also been characterized regarding their photonic, phononic, and thermal properties.^[26,27] However, such screening approaches are tedious due to the large number of samples that must be prepared, especially if various combinations of different particle types are examined.

An efficient approach for screening the optical properties of colloidal materials has been shown for gold nanoparticles assembled in the form of a particle-size gradient.^[28,29] Local spectroscopic characterization thereby allows large data sets to be obtained from a single sample. Continuous gradients in assemblies of microparticles are an emerging topic as well.^[30–32] For example, structural analysis of the order to disorder transition has been shown via analytical ultracentrifugation.^[33,34] However, an efficient platform tailored toward screening the optical properties of colloidal crystals and glasses has not been shown. We recently presented a method to gradient colloidal crystals via a modified vertical deposition method known as infusion-withdrawal coating (IWC).^[35,36] Now, we present a screening platform based on leveraging the advantages of colloidal gradient compositions. Thin films formed from binary colloidal mixtures with a gradual composition gradient are examined via microspectroscopy. This provides a thorough analysis of the optical properties over the entire composition range. The large amount of UV–vis transmittance spectra provided by each gradient sample allows extensive data analysis. To directly correlate the optical transmittance with a specific composition, we introduce an orthogonal calibration technique based on two types of fluorescent tracer particles. Different combinations of relative particle diameters are shown to provide adjustable degrees of disorder and, thereby, tailored light scattering. We verify these results by additional measurements of colloidal assemblies with pre-defined layer thicknesses via patterned substrates. We find a markedly non-symmetric evolution of the scattering efficiency with the particle composition, indicative of an optimum scattering performance at the order-disorder transition of the large colloidal spheres. Furthermore, we expect this type of combinatorial sample preparation and characterization to expedite current research regarding the optical properties of particulate systems.

2. Results and Discussion

The system examined in this work is based on different combinations of poly(methyl methacrylate-co-*n*-butyl acrylate) (PMMA/*n*BA) particles. Four particle suspensions are prepared via surfactant-free emulsion polymerization with hydrodynamic diameters of 305, 282, 255, and 222 nm, respectively. Binary combinations of the largest particles with each of the three smaller

particles are fabricated via vertical deposition and characterized regarding the respective transmittance in the visible wavelength range. For the calibration of gradients, fluorescent tracers are prepared from the pristine particles via post-synthesis staining and added to the assemblies. Red fluorescent tracers are added to the large particles, and blue tracers to the smaller particles. Therefore, the ratio of red and blue fluorescence enables the accurate calibration of the composition. In **Figure 1**, we will discuss the optical properties of discrete (non-gradient) samples, and in **Figure 2**, the fluorescence-enabled calibration of gradient samples is presented. For the sake of clarity, we will use the term ‘composition’ for the binary particle mixture, which coincides with the ratio of red and blue fluorescent tracer particles.

For calibration reasons of the pursued methodology, we first fabricated discrete samples via vertical deposition of binary particle combinations on glass substrates (**Figure 1**). Each combination of particles is characterized by the according size ratio (R_s). As a proof of principle, samples consisting only of large particles ($R_s = 1.0$) with different compositions of blue and red tracers are also prepared (**Figure 1a**). The colloidal crystals formed from these monodisperse suspensions exhibit structural coloration and stop bands at approximately 600 nm. Importantly, the addition of fluorescent tracers does not affect the transmittance. The five spectra with different combinations of blue and red tracers are nearly identical. Mixing particles with similar diameters (**Figure 1b**, $R_s = 0.9$) also results in photonic colloidal crystals, but the optical properties change with the composition. The systems appear to accommodate the difference in particle size, retaining the periodic nature and allowing co-crystallization. The mean lattice spacing is reduced when adding smaller particles, and the color transitions from orange to green while the stop band shifts from 600 to 550 nm. A size ratio of 0.8 increases the level of disorder to the extent that binary systems cannot co-crystallize but rather form amorphous ensembles (**Figure 1c**). Reflectance microscopy images show vivid structural coloration only for the monodisperse samples but not for the mixtures. A difference can also be observed regarding the formation of micro-cracks. The density of cracks is much lower in the amorphous samples, and the crack orientation is mainly parallel to the coating direction. UV–vis absorbance spectra of the mixtures are dominated by diffuse scattering, which increases toward shorter wavelengths. An exception is the sample with 75% large particles, which shows a broad peak at 550 nm attributed to Mie scattering of the majority component. Similar observations can be made for $R_s = 0.7$ (**Figure 1d**). The binary mixtures are disordered, and the photonic glass peak of the 75% sample is slightly broader and less pronounced than for $R_s = 0.8$.

Scanning electron microscopy (SEM) of assemblies with $R_s = 0.8$ corroborate a periodicity of the monodisperse and an isotropic, disordered structure of the mixed case. Fast Fourier Transforms (FFT) of the images show a much more detailed structure factor when one particle type is the majority (25 and 75% large particles) as compared to the 50:50 mixture (**Figure 1e**; **Figure S1**, Supporting Information). This elucidates how dissimilar amorphous compositions can be and why a thorough optical characterization of the entire composition range is indispensable to fully understand the influence of disorder on the optical transmission properties. The discrete samples do not provide

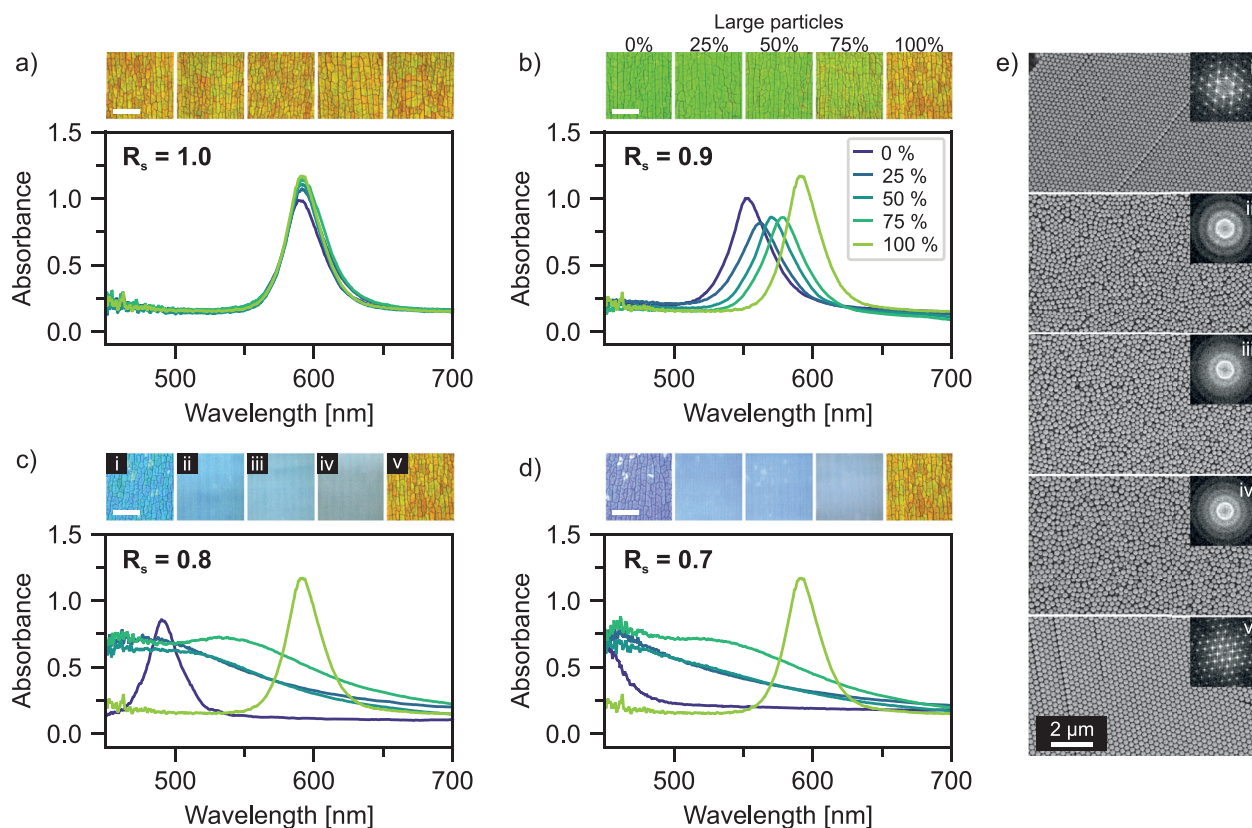


Figure 1. Characterization of discrete samples of binary colloidal assemblies. a) UV-vis absorbance spectra and reflectance microscopy images of colloidal crystal thin films prepared from large particles with different compositions of added red and blue tracer particles. b–d) Analogous characterization of binary systems with several different size ratios (R_s). The composition here corresponds both to the relative amount of large and small particles as well as the relative amount of red and blue tracer particles. e) SEM images and corresponding Fast Fourier Transforms of the samples indicated in (c). The scale bar in microscopy images is $100\mu\text{m}$.

enough information for the entire picture, which necessitates the following use of gradient colloidal assembly as a suitable screening platform.

Fully continuous composition gradients ranging between a composition of zero to one can theoretically contain every possible binary combination of two particles. A broad screening of this range, as well as a detailed examination of a specific section, is possible and entails large data sets. Practically, these gradient samples are prepared via IWC, a dual syringe pump method that is a modified version of vertical deposition (Figure S2a, Supporting Information). The method used in this work does not produce linear gradients (Figure S2b, Supporting Information), which necessitates a post-fabrication correlation of the lateral position along the gradient and the corresponding composition. Fluorescence labeling presents an elegant, orthogonal calibration method that relies on an optical signal and is, therefore, non-invasive. Pristine PMMA/nBA particles are stained via a reversible swelling/diffusion mechanism (Figure 2a) with a solution of one of two different dyes (red and blue, Figure 2b; Figure S3, Supporting Information).^[37] The resulting stained particles remain monodisperse, and self-assembly into colloidal crystals proceeds unhindered (Figure S4, Supporting Information). Since the size of the stained particles is identical to the pristine

ones, the tracers can be added at a total of 5 vol% without affecting the assembly process. The reference samples in Figure 1 are used to verify this approach. Independently acquired fluorescence spectra show how the blue signal increases and the red signal decreases as the composition changes (Figure 2c). The normalized ratio of the red and blue fluorescence signals is shown to correlate correctly with the applied composition (Figure 2d). The coincidence of the spectrally determined and gravimetrically controlled composition is a strong indication of the validity of the calibration technique. This holds for both crystalline assemblies (Figure S5a,b, Supporting Information) as well as disordered structures (Figure S5c,d, Supporting Information). An influence of the photonic properties on the fluorescence integral is not observed. Additionally, both the red and blue absolute fluorescence signals are shown to have a linear thickness dependency. This, in turn, ensures a thickness-independent determination of the composition (Figure 2e; Figure S6, Supporting Information).

To showcase the gradient calibration, we prepared a sample consisting only of large particles ($R_s = 1.0$) with a gradual change in the composition of red and blue tracer particles. Several thousand fluorescence microspectra are measured along the gradient, providing the red and blue fluorescence signal as a function of position (Figure 2f,g). Pronounced oscillations can be seen in

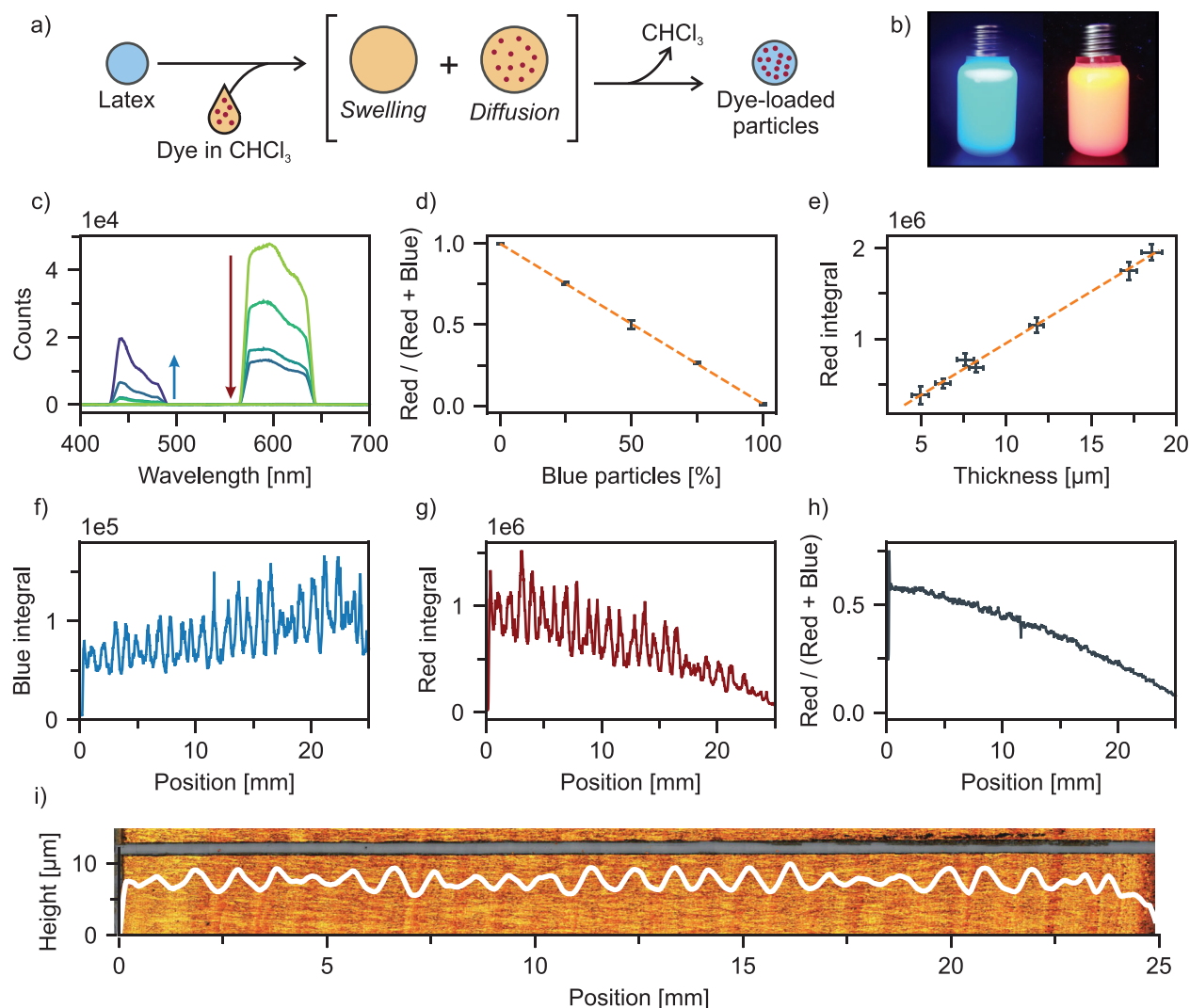


Figure 2. Workflow elucidating how fluorescent tracer particles are used as a calibration of the particle composition. a) Schematic showing the post-synthesis staining. This provides tracer particles that can co-crystallize with the pristine particles and do not influence the colloidal crystal structure. b) Photograph of the stained particle suspensions under UV light. c) Fluorescence spectra of the samples in Figure 1a showing how the red fluorescence decreases and the blue fluorescence increases when the composition is changed. d) Corrected signal ratios showing a linear relation between fluorescence signal and particle composition. e) Linear dependence of the red fluorescence integral with respect to the sample thickness. f, g) Position-dependent fluorescence signals of a gradient colloidal crystal. h) Ratio of these fluorescence signals along the sample. This is used to correlate the position with the respective composition. i) Reflectance microscopy image of the gradient sample with an overlay showing the thickness profile along the coating direction. The thickness profile (white line) was measured via LSCM along the scratch shown at the top of the image, which was used as the reference for the height determination. Oscillations in the profile are caused by meniscus pinning during the assembly process.

both, which elucidates why the information from just one dye is not sufficient. The ratio of red and blue signals at each position (Figure 2h), however, provides a continuous signal with very little noise. A calibration curve can now be obtained that accurately maps the composition to the respective lateral position (Figure S7, Supporting Information). The oscillations in the pure red and blue curves can be explained by variations in the sample thickness (Figure 2i). The height profile obtained via laser scanning confocal microscopy (LSCM) along the gradient exhibits an oscillating thickness that occurs due to meniscus pinning during the coating process.^[38] Fluorescence and thickness profiles

can be brought to a convincing overlap to verify this assumption (Figure S8, Supporting Information).

Besides the oscillations observed in the height profile, inhomogeneities on smaller length scales in the form of micro-cracks also play a role in colloidal systems. Transmittance microscopy along a colloidal crystal shows the influence that these defects impose on the optical measurements (Figure 3a–c). While the stop band position and dip remain fairly constant, the baseline oscillates $\pm 12\%$. This is caused by wavelength-independent scattering at the edges of crystalline domains, which arise during the drying process.^[39] For further analysis,

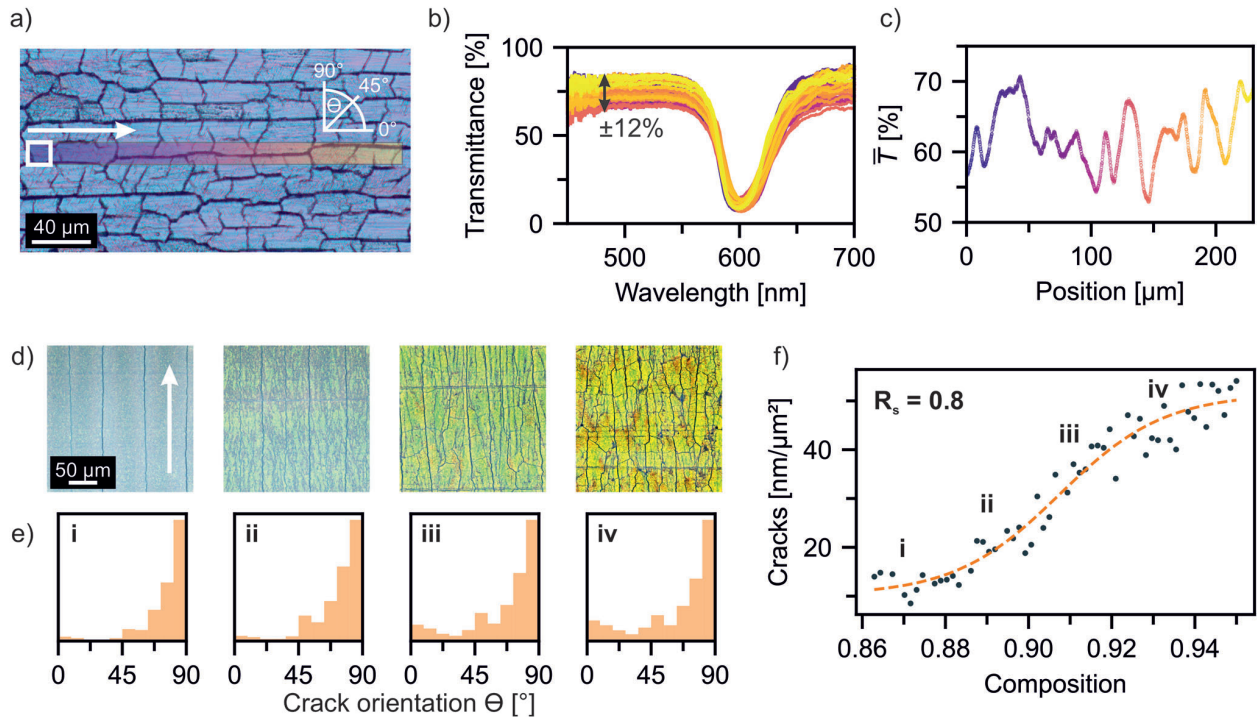


Figure 3. Characterization of micro-cracks in colloidal crystals and glasses. a) Transmission microscopy image of a non-gradient colloidal crystal. The white square indicates the spot size of microspectroscopy (determined in Figure S9, Supporting Information), and the shaded area shows the measured path. b) Spectra measured along this path. c) Scatter plot of the average transmittance of these spectra in the visible range with respect to the position. d) Equidistant reflectance microscopy images of a gradient sample transitioning between a colloidal glass and crystal. The arrow indicates the coating direction, which corresponds to $\theta = 0^\circ$. The gradient comprises a composition range of 0.85–0.95 with two particle types that have a size ratio of 0.8. The exemplary images shown here correspond to compositions of i) 0.86, ii) 0.90, iii) 0.93, and iv) 0.95, respectively. The difference in crack density and orientation of the cracks with respect to the coating direction are analyzed by image thresholding and a ridge detection algorithm. e) Distribution of the crack orientations in four evenly spaced regions along the sample. f) Crack density of all images correlated with the respective composition that was determined via the fluorescence-based calibration. The sigmoidal fit (orange) shows a gradual decrease of the crack density between compositions of 0.93 - 0.88 as the sample transitions from crystalline to amorphous.

the average transmittance over the visible range (\bar{T}) is plotted versus the position. This value fluctuates $\pm 10\%$ with a frequency that fits well to the crack density. As it is obvious that the micro-cracks have a significant influence regarding the local optical characterization, we examined potential differences that occur regarding crack formation in colloidal crystals and glasses, respectively. Therefore, a gradient sample is prepared that specifically targets the transition region between order and disorder, which for $R_s = 0.8$ is found between 85% and 95% large particles. The gradient allows extensive analysis, and more than 60 positions are examined with reflectance microscopy (Figure 3d).

Each position can be mapped to the respective composition via calibration with the fluorescent tracer particles. Image analysis and crack characterization (Figure S10, Supporting Information) proceed with respect to both the crack density as well as the orientation of cracks. Equidistant positions show a gradual transition from the colloidal glasses with cracks exclusively parallel to the coating direction to more randomly distributed cracks in the crystalline case (Figure 3e). Simultaneously, the crack density increases by a factor of 5. It does so gradually, in a composition range between 0.88 and 0.93 (Figure 3f). Evaporation-induced assembly involves shrinkage upon drying. It thereby induces in-

plane stress, which, when the tensile strength is surpassed, dissipates via crack formation.^[40,41] For most close-packed examples, these fractures occur along the 111 planes.^[42] When transitioning to amorphous systems, however, no facets exist that facilitate crack propagation. Additionally, we expect a non-close packed system with a filling fraction < 0.74 to enable local dissipation via reorganization. The fact that cracks parallel to the coating direction are most frequent in the crystalline case and dominate in the amorphous case is due to the most stress being developed parallel to the meniscus. This effectively tears the domains apart.^[43] Besides enabling the analysis of the crack formation, the microscopy images of this gradient sample present a library of colors (Figure S11, Supporting Information) that are accessible simply by mixing the two particle types. In order to examine these optical properties in more detail, transmission UV–vis spectroscopy is performed along several gradient samples.

We start this gradient optical analysis with an assembly of monodisperse large particles ($R_s = 1.0$) with a gradient in the composition of added red and blue tracer particles. For example: a composition of 0.0 indicates 0% red particles and 100% blue particles. Several thousand transmittance spectra are obtained along this gradient and correlated both with the composition via

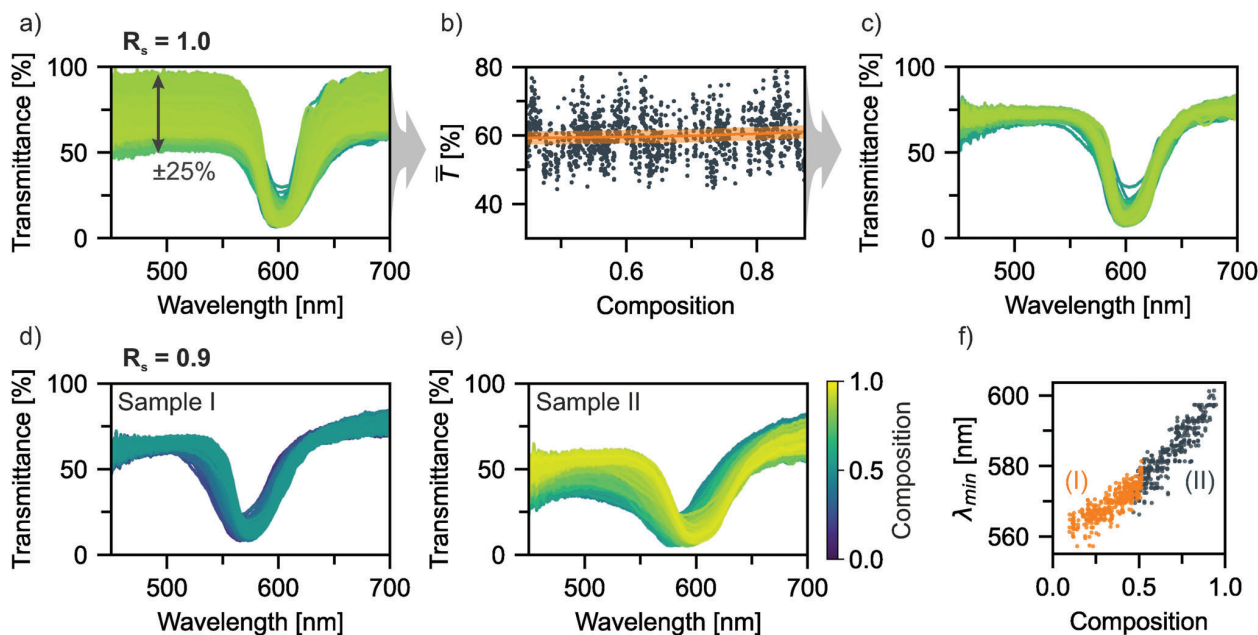


Figure 4. Microspectroscopic characterization of crystalline gradients. a) All transmittance spectra obtained along the coating direction of a sample consisting entirely of large particles with a gradient of the composition of red and blue tracer particles. The baseline shows strong oscillations due to scattering at micro-cracks and a modulated thickness. b) Average transmittance of all the spectra in (a), along with a first-order Savitzky–Golay filter in orange. By excluding all data that does not lie inside a 2% margin of the filter, only spectra from comparable positions along the sample remain. As shown in c), these consequently overlap very well. d,e) Filtered spectra obtained from two gradient samples consisting of two particles with a size ratio of 0.9 that show co-crystallization over the entire composition range. Only two samples are needed to cover the majority of this range and, as shown in f), allow a determination of the stop band position with respect to the composition.

fluorescence analysis as well as with the thickness obtained from LSCM. The spectra show strong fluctuations of the baseline (Figure 4a). Oscillations of the sample thickness, as well as the formation of micro-cracks, both have an impact on the local optical properties and result in this scattering of $\pm 25\%$. The unwanted noise makes a comparison of adjacent measurement spots difficult. However, both the thickness oscillation as well as the crack formation occur at high but distinct spatial frequencies (see FFT in Figure S12, Supporting Information) compared to the gradual change in composition, which is stretched over the entire sample. A standard procedure to eliminate unwanted, high-frequency noise is the use of the Savitzky–Golay filtering algorithm.^[44] The average transmittance is plotted as a function of the composition, which shows substantial noise (Figure 4b). The filter shown in orange is applied and remains at a constant value of approximately 60% over the entire composition range. Spectra that do not lie in a 2% margin of the filter profile are now excluded from further analysis. The remaining, filtered spectra overlap and do not exhibit these baseline fluctuations (Figure 4c). This elucidates how spectra are obtained with a similar influence of the micro-cracks and allows a more reasonable comparison of spectra along the sample. We applied this data filtering procedure to two gradient samples prepared from particles with $R_s = 0.9$, which together span almost the entire range of compositions (Figure 4d,e; Figures S13 and S14, Supporting Information). The filtered spectra show a gradual shift of the stop band toward shorter wavelengths as more of the small particles are present in the ensemble. Figure 4f shows the combined stop band position

with respect to the composition, which ranges between 560 and 595 nm. The data sets from the two samples converge and prove that co-crystallization of the two particles is indeed possible over the entire range. This information would require countless discrete samples but using the gradient colloidal assembly, only two experiments are necessary.

Next, gradient samples, transitioning from crystalline to amorphous regions, are examined. Figure 5 shows the average transmittance, the filtering approach, and the filtered spectra for gradient colloidal assemblies with $R_s = 0.8$ (For raw data: see Figures S15–S17, Supporting Information). For most of the composition range, the average transmittance decreases monotonously with an increasing amount of large particles (Figure 5a–d). The origin of this trend becomes clear when observing the corresponding spectra. While diffuse scattering persists in all cases, the effect of Mie scattering of large particles becomes increasingly more visible as a shoulder that shifts toward longer wavelengths. A greater part of the visible spectrum is thereby affected by the material, and ballistic transport through the sample is minimized. This increase in the scattering efficiency progresses until a composition is reached where the system is capable of compensating for the defects and crystallizes. In Figure 5e,f, results are shown for a sample specifically prepared to target this order-to-disorder transition. Between compositions of 0.85 and 0.95, the stop band originating from the periodic crystalline structure evolves. Simultaneously, the baseline moves to substantially higher transmittance values. This is especially pronounced at shorter wavelengths, as the transition from

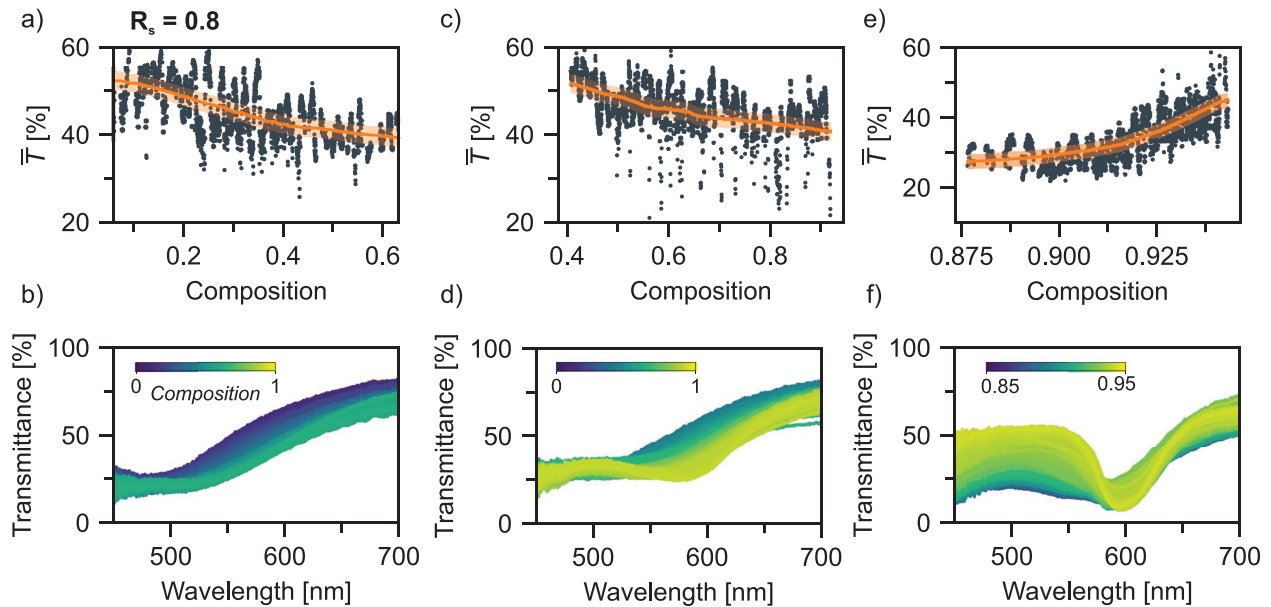


Figure 5. Microspectroscopic characterization of gradient samples ranging between crystalline and amorphous colloidal assemblies with a size ratio of $R_s = 0.8$. a) Average transmittance along the sample and b) filtered spectra. The shoulder in the spectra shifts to higher wavelengths as the amount of large particles increases, which explains the downward trend in (a). This trend persists when extending the composition range in (c) and (d). e, f) A sample designed to target the transition from order to disorder exhibits an increasing average transmittance as the composition approaches 1. The spectra show that this originates from less scattering at smaller wavelengths concomitant with the ballistic rather than diffusive light transport as the stop band begins to evolve.

diffusive to ballistic light transport reduces the number of scattered photons in this spectral range the most. The results show that an optimum of the scattering capability is found at a composition of approximately 0.9 for binary mixtures with $R_s = 0.8$. At this composition, a maximum of large particles are present, with enough small particles in the mixture to induce disorder. A correlation between the defect concentration caused by polydispersity and the reduction of the stop band intensity stands in accordance with results published for discrete samples.^[45] The transition region observed via spectroscopy overlaps with the region observed in Figure 3f for the change of the micro-crack density. This stands to reason since both are attributed to an evolving crystallinity.

Gradient colloidal assemblies with a greater difference in particle size ($R_s = 0.7$) show a similar trend. An increasing amount of large particles results in more scattering over the entire visible spectrum and a monotonously decreasing average transmittance (Figures S18–S21, Supporting Information). However, even at a composition of 0.95, no stop band can be observed. The increased difference of the diameters compared to $R_s = 0.8$ causes greater disruption of the periodic structure, which cannot be accommodated as easily. Even minute addition of small particles hinders the crystallization of the large particles. Measuring beyond a composition of 0.95 is not possible on these samples due to macroscopic defects that compromise the structure at the beginning of the coating process. Additionally, another difference between crystalline and amorphous assembly can be found when observing the overall trend of the film thickness (Figure S22, Supporting Information). While purely crystalline or purely amorphous samples show a reasonably constant thickness (exclud-

ing the oscillations caused by meniscus pinning), this is not the case for the transition regime. Even though all external parameters, such as particle concentration, coating speed, and humidity, are constant, ordered assemblies from a monodisperse suspension result in considerably lower thicknesses compared to the bidisperse, amorphous case. Therefore, samples ranging between crystalline and amorphous show an overall trend in the film thickness. This must be taken into account, as the transmittance of light-scattering materials shows a pronounced thickness dependency.^[5] We, therefore, confirm our findings based on the gradient assemblies with a selection of discrete samples that exhibit a defined film thickness.

The organization of colloids can be directed via topographically patterned substrates.^[46] Self-assembly in 1D micro-trenches, for example, results in lines of colloidal crystals that exhibit a defined width and height, as dictated by the substrate and the shape of the meniscus.^[47] Here we apply patterned, hydrophilized poly(dimethyl siloxane) (PDMS) substrates to ensure unimpeded optical transmittance. Colloidal crystals and glasses are selectively deposited in the trenches via vertical deposition from (mixed) suspensions (Figure 6a). Height profiles of both the empty trenches and the coated substrate (Figure 6b) indicate how the colloidal assembly proceeds in lines with 30 μm width and a height of 14 μm . Reflectance light microscopy and SEM images of monodisperse particles assembled in the trenches show structural coloration and the hexagonal structure of colloidal crystals (Figure 6c,d). This is the case for both small and large particles (Figure S24, Supporting Information). Analogous images are presented for an amorphous assembly (Figure 6e,f). Besides the more vivid structural coloration of the crystalline samples, it also

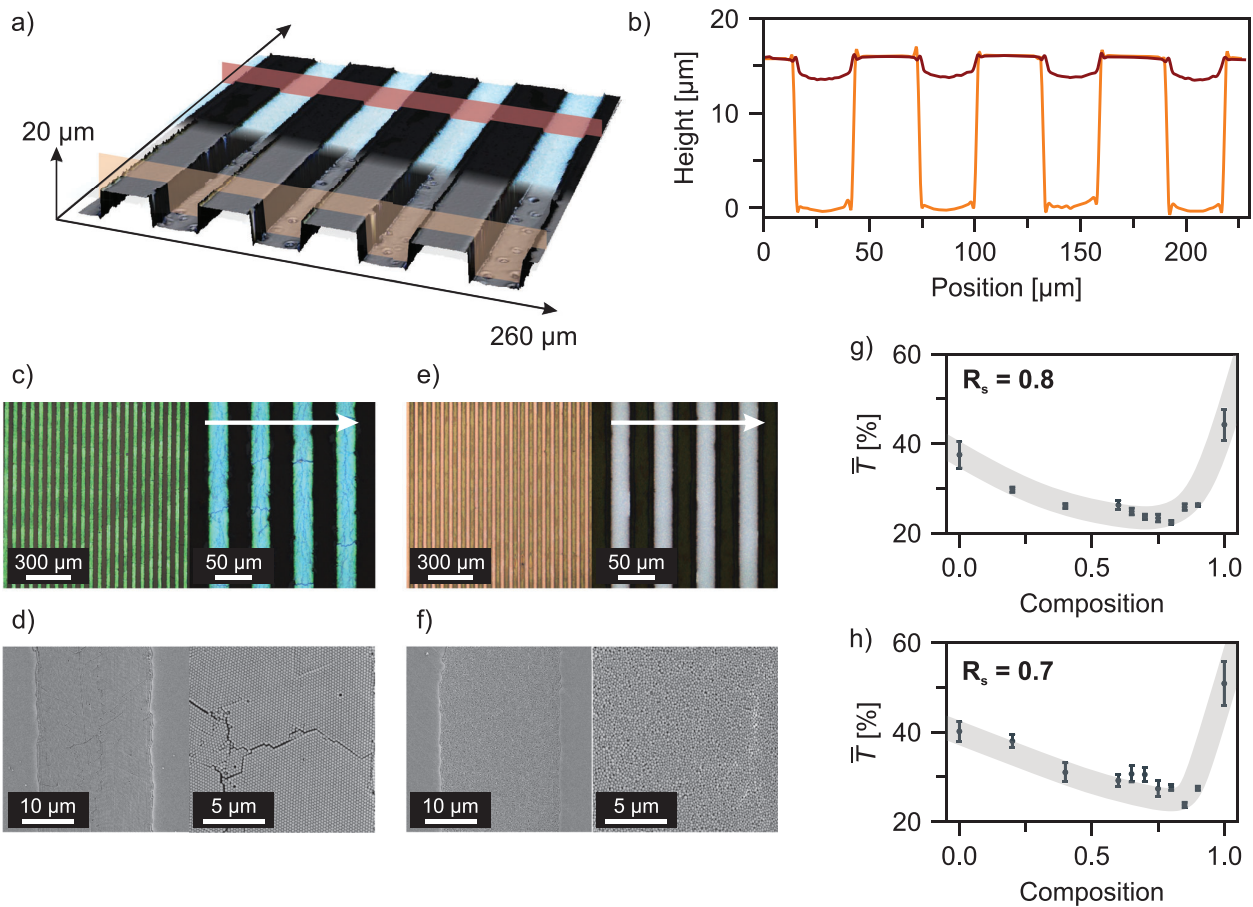


Figure 6. Discrete colloidal assemblies in ridges of a topographically patterned substrate. a) 3D reconstructed images obtained via laser scanning confocal microscopy of an empty PDMS substrate (front) and a coated sample (back) (Separate data in Figure S23, Supporting Information). The orange and red cross sections indicate where the height profile shown in b) was evaluated. A height profile with x- and y-axis to scale is shown in Figure S26 (Supporting Information). c,d) Reflectance microscopy and scanning electron microscopy of the top surface of monodisperse particles assembled to colloidal crystals inside the micro-ridges. The arrow indicates the direction of the path along which UV-vis spectra are measured later. e,f) Analogous images for an amorphous mixture of large and small particles assembled on the substrate. g,h) Average transmittance obtained from discrete samples consisting of mixtures of particles with size ratios of 0.8 and 0.7. Each point is the mean value obtained from the UV-vis transmittance spectra measured in five consecutive ridges. Details regarding the measurement are shown in Figure S25 (Supporting Information). The grey lines are guides to the eye.

becomes obvious that amorphous assembly proceeds with little or no crack formation compared to the ordered case.

UV-vis transmission microspectroscopy of these samples is performed by slowly moving perpendicular to the trenches while acquiring spectra. In five consecutive trenches, a spectrum is chosen in the middle of each trench. This is possible by examining the position-dependent average transmittance which plateaus in this region (Figure S25, Supporting Information). This is done for several samples over the entire composition range for both $R_s = 0.8$ and 0.7. The average transmittance of all spectra is shown in Figure 6g,h. An analogous trend, as observed before for the continuous gradients, can be seen. With an increasing amount of large particles, the scattering efficiency increases, and the average transmittance shows a downward trend. At the point where self-assembly to crystalline structures is possible, ballistic transport dominates, and the average transmittance increases

strongly. The agreement between the large data sets procured from gradient colloidal assemblies with the measurements on thickness-controlled, patterned substrates shows how the two approaches are complementary. Comprehensive optical characterization of several particle size ratios and compositions was thereby possible, and the results were independently corroborated.

Since all measurements so far were conducted with a fairly high numerical aperture (and, therefore, also a high acceptance angle), we also examined this parameter. Scans along the gradient in Figure 5c,d ($R_s = 0.8$) were conducted with different objectives and acceptance angles between 29° and 67°. The mean transmittance of all three sets of microspectroscopy measurements shows identical trends (Figure S27, Supporting Information). A difference that can be seen, is that the measured transmittance is greater with a higher numerical aperture. This directly correlates with the higher acceptance angle, which,

consequently, results in the detection of more scattered photons. Since the shape of the profile and the position of the minimum does not change when switching objectives, the assertions made in the previous sections hold true in this spectral range.

Finally, we performed a set of measurements to showcase the versatility of this approach and to touch on the possibilities opened by the optical screening platform. Machine learning-enabled prediction of structural color based on the specific geometry of dielectric arrays is becoming an important tool in the materials science community.^[48] While in some cases, the training data can be obtained via simulations, other approaches require measured data. These data sets can become quite extensive, as was shown for the correlation of color and absorption spectra.^[49] A set of images and spectroscopy data was used to train an artificial neural network and predict one from the other for a range of complex mixed oxides. This type of data structure can be obtained analogously with our gradient approach for the optical properties of binary colloidal mixtures. To increase the amount of information and allow a more complete characterization, both transmittance as well as reflectance microspectra and spectroscopy images were evaluated along a sample. A gradient with ($R_s = 0.8$), transitioning between order and disorder, was characterized this way (Figures S28–S31, Supporting Information). A qualitative evaluation of the data shows that both in reflection as well as transmission, the stop band begins to evolve between 88% and 92% large particles. For the reflectance measurements, this occurs earlier, which we attribute to a higher degree of order near the surface, masking a more disordered region underneath. While some pre-processing, such as filtering, is necessary, the output is a large number of correlated spectra and microscopy images. We expect that this approach will allow data-driven studies (i.e., machine learning) for tailored optical properties in complex systems of particle mixtures in the future.

3. Conclusion

We presented an integrated screening platform for the optical properties of binary colloidal mixtures. Thin films with a gradient of the particle composition were prepared. Fluorescent tracer particles were used as an orthogonal and non-invasive calibration routine to reveal the local particle composition with high lateral resolution. Mixing particles with a size ratio of $R_s = 0.9$ allowed co-crystallization over the entire composition range and showed a gradually shifting stop band. At $R_s = 0.8$, diffuse scattering dominated most parts of the particle composition, and light scattering proved to be most efficient when 90% large particles were present. A detailed examination of the transition regime between order and disorder was possible and elucidated the change from diffusive to ballistic light transport, which previously had been shown for a few discrete samples.^[25,50] Further increase of the size difference at $R_s = 0.7$ induced disorder and pronounced light scattering even at minute addition of small particles. Finally, these results were verified by measuring transmittance spectra of discrete samples prepared with a defined thickness which was ensured via assembly on patterned substrates.

We expect this screening approach to go beyond the particle system presented here. Various mixtures are conceivable, such as organic/inorganic, spherical/anisotropic, or hollow/solid. This can be coupled with an evaluation of the respective structure fac-

tor via, reconstruction, scattering or simulations, and then allow theoretical studies of the optical properties.^[51–54] Since measurements in the UV–vis, as well as the IR-range, can be performed locally, this will allow efficient screening of optimized colloidal materials for, for example, radiative cooling applications.^[55–57] In a more general sense, obtaining large data sets is becoming increasingly important. Advanced analysis methods such as machine learning or Bayesian statistics are rapidly being improved and introduced into the field of materials science.^[58] These rely on copious amounts of data which, in most cases, must be provided experimentally. Efficient screening techniques like the one presented in this work are, therefore, crucial to meet this requirement for implementing novel, data-driven analyses.

4. Experimental Section

Materials: Water used in this work was of Millipore quality. Methyl methacrylate (MMA 99%), n-butyl acrylate (nBA, 99%), sodium styrene sulfonate (NaSS, 99.99%), potassium persulfate (KPS, 99.99%), Nile red (NR), and Coumarin 1 (C1) were obtained from Sigma Aldrich. Chloroform was obtained from VWR. Poly(dimethyl siloxane) (PDMS) elastomer (SYLGARD 184) was obtained from Dow Corning.

Polymer Latex Synthesis: A 250 mL three-necked flask equipped with a reflux condenser and septa was loaded with 240 mL water and degassed for 75 min under a constant nitrogen stream at 80°C and 650 rpm stirring speed. With 5 min of homogenization time between each addition, the following reactants are added: 1) 7, 10, 13, or 16 mL of a 90:10 mixture of MMA/nBA, 2) 10 mg NaSS in 5 mL water, 3) 200 mg KPS in 5 mL water. The reaction was then allowed to proceed for 120 min before termination with ambient oxygen.

Particle Staining: Particle suspensions were diluted to 1.5wt% and 50 mL are stirred at 600 rpm. 5 mg of either NR or C1 were dissolved in 1.5 mL chloroform and added dropwise. Stirring proceeds in a closed container for 24 h to allow swelling and diffusion of the dye. Subsequently, the lid was opened, and stirring was continued for 72 h to slowly remove the chloroform via diffusion and evaporation.^[59] Finally, the suspensions were passed through a 5 μm syringe filter.

Assembly of Discrete Samples: Vertical deposition of discrete samples proceeded in a climate chamber set to 25°C and 75% relative humidity. Hellmanex III and plasma-cleaned glass substrates were dipped into particle suspensions of 1.0wt% that are stirred at 50 rpm. The substrate was then pulled out of the suspension at 0.25 $\mu\text{m s}^{-1}$.

Assembly of Gradient Samples: Gradient fabrication via infusion-withdrawal coating was done analogously to the discrete substrates except for the addition of two syringe pumps. The glass substrate was dipped into a suspension of one particle type with 1.0wt% and two cannulas attached to syringes were added to the system. One syringe pump extracts the suspension at 0.60 mL h^{-1} , the other infuses a suspension of a second particle type with 0.79wt% at 0.76 mL h^{-1} . The difference between the infusion and withdrawal speed was adjusted to account for the evaporation of water which was determined to be 0.16 mL h^{-1} . Thereby, both the water level as well as the particle concentration remain constant.

Assembly on Patterned Substrates: Masters for the patterned substrates were prepared via photo-lithography of SU8 resin on a silicon wafer by way of spin coating, soft bake, exposure at 365 nm (MaskAligner MJB4 by SUSS Microtec), post-exposure bake, development and hard bake. The two-component PDMS was cast on the wafer. Air bubbles were removed via vacuum treatment, and curing subsequently proceeded for 2h at 90°C. The PDMS substrates were then cut into 3×1cm pieces, hydrophilized in oxygen plasma for 5 s and immediately thereafter coated via vertical deposition, analogously to the flat substrates. The trenches were oriented parallel to the coating direction.

Microspectroscopy: Measurements proceed on an Olympus IX71 inverted microscope with a 40x Lens (N.A. 0.55). An OceanOptics USB4000 spectrometer was coupled via fiber optics. UV–vis spectra were obtained

in transmission geometry with a halogen light source. The integration time was set to 100 ms. Fluorescence spectroscopy was performed on the same setup with a mercury vapor lamp in reflection geometry. For the red fluorescence, a Chroma 49004 ET Cy3 filter cube was used, allowing excitation between 530 and 560 nm and emission detection between 570 and 640 nm. The integration time was set to 10 ms, and 10 spectra were measured for averaging. For the blue fluorescence, a Chroma 49000 ET DAPI filter cube was used, allowing excitation between 325 and 375 nm and emission detection between 435 and 485 nm. The integration time was set to 100 ms. Gradient samples were moved at $100 \mu\text{m s}^{-1}$ with a motorized μm -stage while measuring. The sample was moved along the same path three times, to allow UV-vis and the two fluorescence measurements at analogous positions. UV-vis spectra along the patterned substrates are obtained analogously, but while moving at a speed of $5 \mu\text{m s}^{-1}$.

Dynamic Light Scattering: Diluted dispersions were measured with a Zetasizer (Malvern) with 173° backscattering geometry.

Laser Scanning Confocal Microscopy: 2D color images and 3D reconstructions were obtained using a laser scanning microscope (Olympus, LEXT). High-magnification images were taken using a 50x lens (N.A. 0.95). Overview images were obtained by stitching images with a 5x lens (N.A. 0.15).

Scanning Electron Microscopy: Images were obtained with a Zeiss Leo 1530 (Carl Zeiss AG, Germany) at an operating voltage of 3 kV with in-lens detection after sputtering 2 nm platinum.

Data Analysis: The mean transmittance was determined from the UV-vis spectra by averaging the transmittance values between 450 and 700 nm. This was done for each spectrum and correlated with the respective position via the speed of the motorized stage and the time at which the spectrum was acquired. A correlation with the thickness at each position was thereby possible, and only spectra acquired in a specific range of thicknesses were examined (see Figures S13–S21, Supporting Information). A first-order Savitzky-Golay filter with a window length of approximately a third of the amount of spectra was applied, and for later characterization, only spectra that were in a range $\pm 2\%$ of this filter were used for further characterization.

For both UV-vis as well as fluorescence spectroscopy, the integration time and number of spectra for averaging were adjusted so that the total time per acquired spectrum was always 100 ms, and measurement spots coincided. The blue fluorescence was integrated between 420 and 490 nm and the red fluorescence between 560 and 650 nm. Before each measurement, a sample comprising a 50:50 mixture of red and blue particles was measured as a reference. The ratio of the red and blue integral was used as a correction factor for the ratios determined from gradient samples.

Supporting Information

Supporting Information is available from the Wiley Online Library or from the author.

Acknowledgements

The help from the Keylab Electron Microscopy was appreciated. M.S. and T.L. acknowledge support from the Elite Network of Bavaria (ENB). This project has received funding from the European Research Council (ERC) under the European Union's Horizon 2020 research and innovation program (grant agreement no. #714968).

Open access funding enabled and organized by Projekt DEAL.

Conflict of Interest

The authors declare no conflict of interest.

Data Availability Statement

The data that support the findings of this study are available in the supplementary material of this article.

Keywords

combinatorial materials science, composition gradients, photonic crystals, photonic glasses, self-assembly

Received: January 13, 2023

Revised: March 27, 2023

Published online: May 15, 2023

- [1] G. Jacucci, L. Schertel, Y. Zhang, H. Yang, S. Vignolini, *Adv. Mater.* **2021**, *33*, 2001215.
- [2] D.-Y. Zhou, X.-B. Shi, C.-H. Gao, S.-D. Cai, Y. Jin, L.-S. Liao, *Appl. Surf. Sci.* **2014**, *314*, 858.
- [3] M. Karg, T. A. F. König, M. Retsch, C. Stelling, P. M. Reichstein, T. Honold, M. Thelakkar, A. Fery, *Mater. Today* **2015**, *18*, 185.
- [4] J. Jaramillo-Fernandez, H. Yang, L. Schertel, G. L. Whitworth, P. D. Garcia, S. Vignolini, C. M. Sotomayor-Torres, *Adv. Sci.* **2022**, *9*, 2104758.
- [5] S. Caixeiro, M. Peruzzo, O. D. Onelli, S. Vignolini, R. Sapienza, *ACS Appl. Mater. Interfaces* **2017**, *9*, 7885.
- [6] G. Jacucci, J. Bertolotti, S. Vignolini, *Adv. Opt. Mater.* **2019**, *7*, 23.
- [7] L. Cortese, L. Pattelli, F. Utel, S. Vignolini, M. Burrelli, D. S. Wiersma, *Adv. Opt. Mater.* **2015**, *3*, 1337.
- [8] B. D. Wilts, X. Sheng, M. Holler, A. Diaz, M. Guizar-Sicairos, J. Raabe, R. Hoppe, S. H. Liu, R. Langford, O. D. Onelli, D. Chen, S. Torquato, U. Steiner, C. G. Schroer, S. Vignolini, A. Sepe, *Adv. Mater.* **2018**, *30*, 1702057.
- [9] M. S. Toivonen, O. D. Onelli, G. Jacucci, V. Lovikka, O. J. Rojas, O. Ikkala, S. Vignolini, *Adv. Mater.* **2018**, *30*, 1704050.
- [10] G. Jacucci, B. W. Longbottom, C. C. Parkins, S. A. F. Bon, S. Vignolini, *J. Mater. Chem. C* **2021**, *9*, 2695.
- [11] H. Yang, G. Jacucci, L. Schertel, S. Vignolini, *ACS Nano* **2022**, *16*, 7373.
- [12] J. Hou, L. Wang, C. Wang, S. Zhang, H. Liu, S. Li, X. Wang, *J. Environ. Sci.* **2019**, *75*, 40.
- [13] S. John, *Phys. Rev. Lett.* **1987**, *58*, 2486.
- [14] J. D. Joannopoulos, P. R. Villeneuve, S. Fan, *Nature* **1997**, *386*, 143.
- [15] P. D. García, R. Sapienza, C. López, *Adv. Mater.* **2010**, *22*, 12.
- [16] J. F. Galisteo-López, M. Ibisate, R. Sapienza, L. S. Froufe-Pérez, A. Blanco, C. López, *Adv. Mater.* **2011**, *23*, 30.
- [17] S. F. Liew, J. Forster, H. Noh, C. F. Schreck, V. Saranathan, X. Lu, L. Yang, R. O. Prum, C. S. O'Hern, E. R. Dufresne, H. Cao, *Opt. Express* **2011**, *19*, 8208.
- [18] E. S. A. Goerlitzer, R. N. Klupp Taylor, N. Vogel, *Adv. Mater.* **2018**, *30*, 1706654.
- [19] P. N. Dyachenko, J. J. do Rosário, E. W. Leib, A. Y. Petrov, R. Kubrin, G. A. Schneider, H. Weller, T. Vossmeier, M. Eich, *ACS Photonics* **2014**, *1*, 1127.
- [20] G. Shang, Y. Häntsch, K. P. Furlan, R. Janßen, G. A. Schneider, A. Petrov, M. Eich, *APL Photonics* **2019**, *4*, 4.
- [21] L. Bai, Y. Lim, Y. He, Q. Xiong, S. Hou, J. Zhang, H. Duan, *Adv. Opt. Mater.* **2020**, *8*, 24.
- [22] P. D. García, R. Sapienza, A. Blanco, C. López, *Adv. Mater.* **2007**, *19*, 2597.
- [23] N. Vogel, L. de Viguier, U. Jonas, C. K. Weiss, K. Landfester, *Adv. Funct. Mater.* **2011**, *21*, 3064.
- [24] J. Semmler, K. Bley, R. N. Klupp Taylor, M. Stingl, N. Vogel, *Adv. Funct. Mater.* **2019**, *29*, 4.
- [25] S. G. Romanov, S. Orlov, D. Ploss, C. K. Weiss, N. Vogel, U. Peschel, *Sci. Rep.* **2016**, *6*, 27264.
- [26] T. Still, W. Cheng, M. Retsch, R. Sainidou, J. Wang, U. Jonas, N. Stefanou, G. Fytas, *Phys. Rev. Lett.* **2008**, *100*, 194301.

- [27] F. A. Nutz, A. Philipp, B. A. F. Kopera, M. Dulle, M. Retsch, *Adv. Mater.* **2018**, *30*, 1704910.
- [28] M. B. Müller, C. Kuttner, T. A. König, V. V. Tsukruk, S. Forster, M. Karg, A. Fery, *ACS Nano* **2014**, *8*, 9410.
- [29] C. Kuttner, V. Piotto, L. M. Liz-Marzán, *Chem. Mater.* **2021**, *33*, 8904.
- [30] S. H. Kim, W. C. Jeong, H. Hwang, S. M. Yang, *Angew. Chem., Int. Ed.* **2011**, *50*, 11649.
- [31] H. Ding, C. Liu, H. Gu, Y. Zhao, B. Wang, Z. Gu, *ACS Photonics* **2014**, *1*, 121.
- [32] M. Schöttle, T. Lauster, L. J. Roemling, N. Vogel, M. Retsch, *Adv. Mater.* **2022**, 2208745.
- [33] M. Chen, H. Cölfen, S. Polarz, *ACS Nano* **2015**, *9*, 6944.
- [34] M. Chen, K. Hagedorn, H. Cölfen, S. Polarz, *Adv. Mater.* **2017**, *29*, 1603356.
- [35] M. Schöttle, T. Tran, T. Feller, M. Retsch, *Adv. Mater.* **2021**, *33*, 2101948.
- [36] F. Ye, C. Cui, A. Kirkemide, D. Dong, M. M. Collinson, D. A. Higgins, *Chem. Mater.* **2010**, *22*, 2970.
- [37] J. H. Lee, I. J. Gomez, V. B. Sitterle, J. C. Meredith, *J. Colloid Interface Sci.* **2011**, *363*, 137.
- [38] G. Lozano, H. Miguez, *Langmuir* **2007**, *23*, 9933.
- [39] B. Hatton, L. Mishchenko, S. Davis, K. H. Sandhage, J. Aizenberg, *Proc. Natl. Acad. Sci. USA* **2010**, *107*, 10354.
- [40] W. B. Russel, *AIChE J.* **2011**, *57*, 1378.
- [41] W. P. Lee, A. F. Routh, *Langmuir* **2004**, *20*, 9885.
- [42] K. R. Phillips, C. T. Zhang, T. Yang, T. Kay, C. Gao, S. Brandt, L. Liu, H. Yang, Y. Li, J. Aizenberg, L. Li, *Adv. Funct. Mater.* **2019**, *30*, 26.
- [43] Y. Xu, G. K. German, A. F. Mertz, E. R. Dufresne, *Soft Matter* **2013**, *9*, 14.
- [44] S. R. Krishnan, C. S. Seelamantula, *IEEE Trans. Signal Process.* **2013**, *61*, 380.
- [45] R. Rengarajan, D. Mittleman, C. Rich, V. Colvin, *Phys. Rev. E: Stat., Nonlinear, Soft Matter Phys.* **2005**, *71*, 016615.
- [46] N. Vogel, M. Retsch, C.-A. Fustin, A. del Campo, U. Jonas, *Chem. Rev.* **2015**, *115*, 6265.
- [47] J. Li, S. Luan, W. Huang, Y. Han, *Colloids Surf., A* **2007**, *295*, 107.
- [48] Z. Huang, X. Liu, J. Zang, *Nanoscale* **2019**, *11*, 21748.
- [49] H. S. Stein, D. Guevarra, P. F. Newhouse, E. Soedarmadji, J. M. Gregoire, *Chem. Sci.* **2019**, *10*, 47.
- [50] D. S. Wiersma, *Nat. Photonics* **2013**, *7*, 188.
- [51] L. Schertel, L. Siedentop, J. Meijer, P. Keim, C. M. Aegerter, G. J. Aubry, G. Maret, *Adv. Opt. Mater.* **2019**, *7*, 15.
- [52] G. Shang, K. P. Furlan, R. Janssen, A. Petrov, M. Eich, *Opt. Express* **2020**, *28*, 7759.
- [53] V. Hwang, A. B. Stephenson, S. Barkley, S. Brandt, M. Xiao, J. Aizenberg, V. N. Manoharan, *Proc. Natl. Acad. Sci. USA* **2021**, *118*, 4.
- [54] K. Shavit, A. Wagner, L. Schertel, V. Farstey, D. Akkaynak, G. Zhang, A. Upcher, A. Sagi, V. J. Yallapragada, J. Haataja, B. A. Palmer, *Science* **2023**, *379*, 695.
- [55] J. Jaramillo-Fernandez, G. L. Whitworth, J. A. Pariente, A. Blanco, P. D. Garcia, C. Lopez, C. M. Sotomayor-Torres, *Small* **2019**, *15*, 1905290.
- [56] H. H. Kim, E. Im, S. Lee, *Langmuir* **2020**, *36*, 6589.
- [57] Y. Fu, Y. An, Y. Xu, J.-G. Dai, D. Lei, *EcoMat* **2022**, *4*, 12169.
- [58] A. Ludwig, *npj Comput. Mater.* **2019**, *5*, 1.
- [59] A. Steinhaus, R. Chakroun, M. Mullner, T. L. Nghiem, M. Hildebrandt, A. H. Gröschel, *ACS Nano* **2019**, *13*, 6269.

ADVANCED OPTICAL MATERIALS

Supporting Information

for *Adv. Optical Mater.*, DOI 10.1002/adom.202300095

Microspectroscopy on Thin Films of Colloidal Mixture Gradients for Data-Driven
Optimization of Optical Properties

*Marius Schöttle, Maximilian Theis, Tobias Lauster, Stephan Hauschild and Markus Retsch**

Microspectroscopy on thin films of colloidal mixture gradients for data-driven optimization of optical properties (Supporting information)

Marius Schöttle Maximilian Theis Tobias Lauster Stephan Hauschild Markus Retsch*

M. Schöttle, M. Theis, T. Lauster, Prof. M. Retsch

Department of Chemistry, Physical Chemistry I, University of Bayreuth, Universitätsstr. 30, 95447 Bayreuth, Germany

Email Address: markus.retsch@uni-bayreuth.de

Prof. M. Retsch

Bavarian Polymer Institute, Bayreuth Center for Colloids and Interfaces, and Bavarian Center for Battery Technology (BayBatt), University of Bayreuth, 95447 Bayreuth, Germany

S. Hauschild

Jülich Centre for Neutron Science (JCNS-1/IBI-8), Forschungszentrum Jülich GmbH, 52425 Jülich, Germany

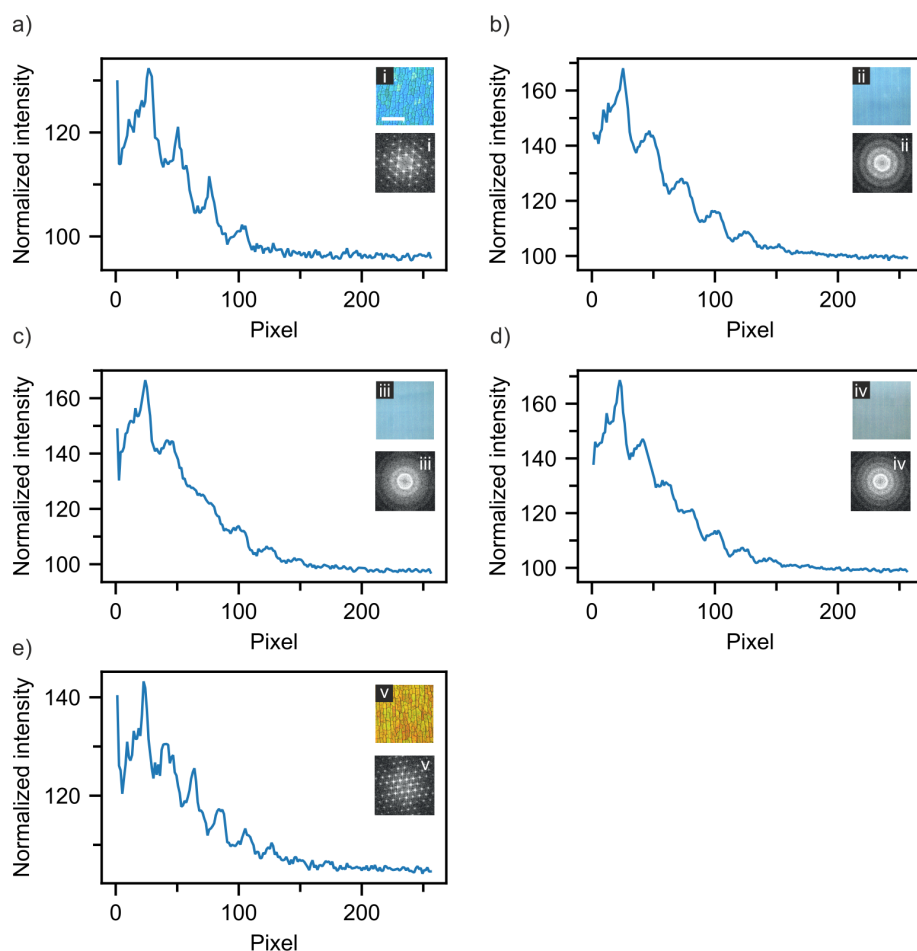


Figure S1: Radial intensity distribution of the FFTs generated from SEM images of binary colloidal assemblies with $R_s = 0.8$.

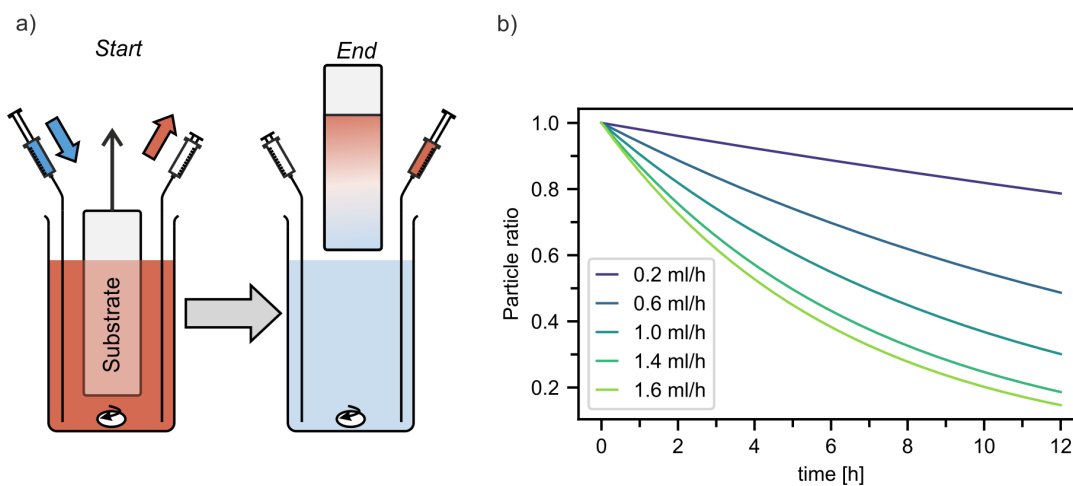


Figure S2: a) Infusion-withdrawal coating setup. A substrate is dipped into a colloidal suspension and coated by slowly moving it upwards. Simultaneously, the composition in the particle suspension is changed by infusing a different suspension while extracting at the same rate. This time-dependent composition change translates to a positional dependency along the gradient thin-film. b) Calculated change of the particle composition in the suspension over time at different pumping rates.

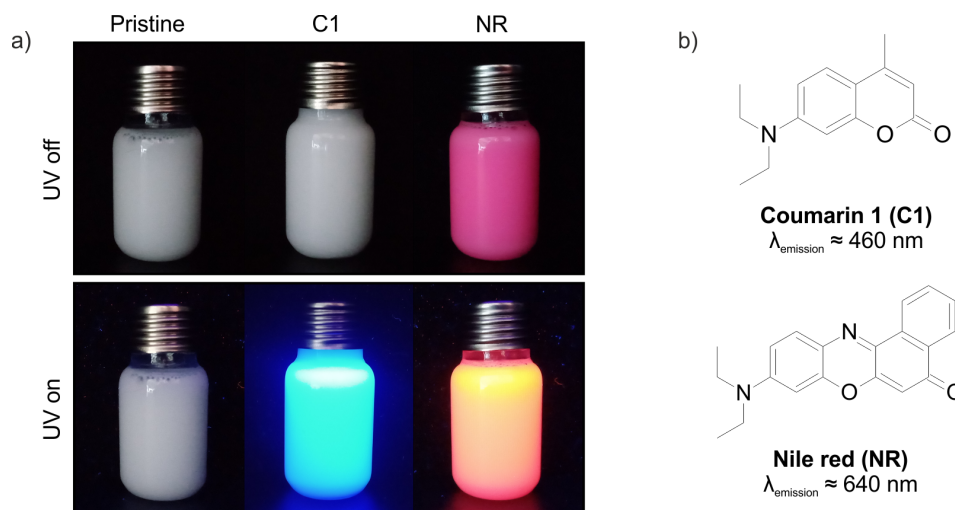


Figure S3: a) Pristine and stained colloidal suspensions under ambient and UV-light, respectively. b) The two dyes used in the swelling/diffusion procedure.

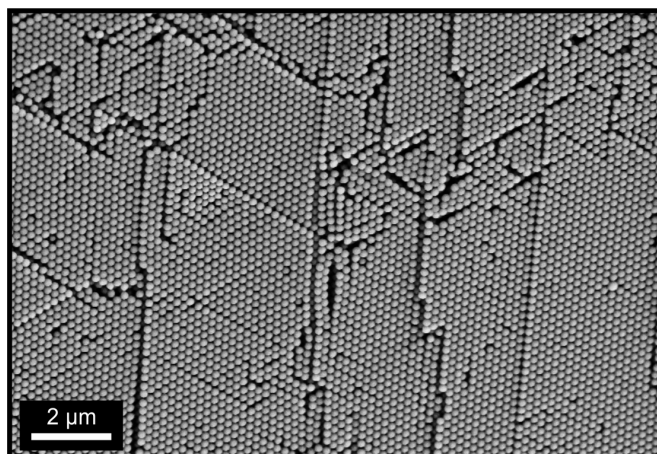


Figure S4: Colloidal crystal prepared via assembly of a 50:50 mixture of blue and red-stained particles.

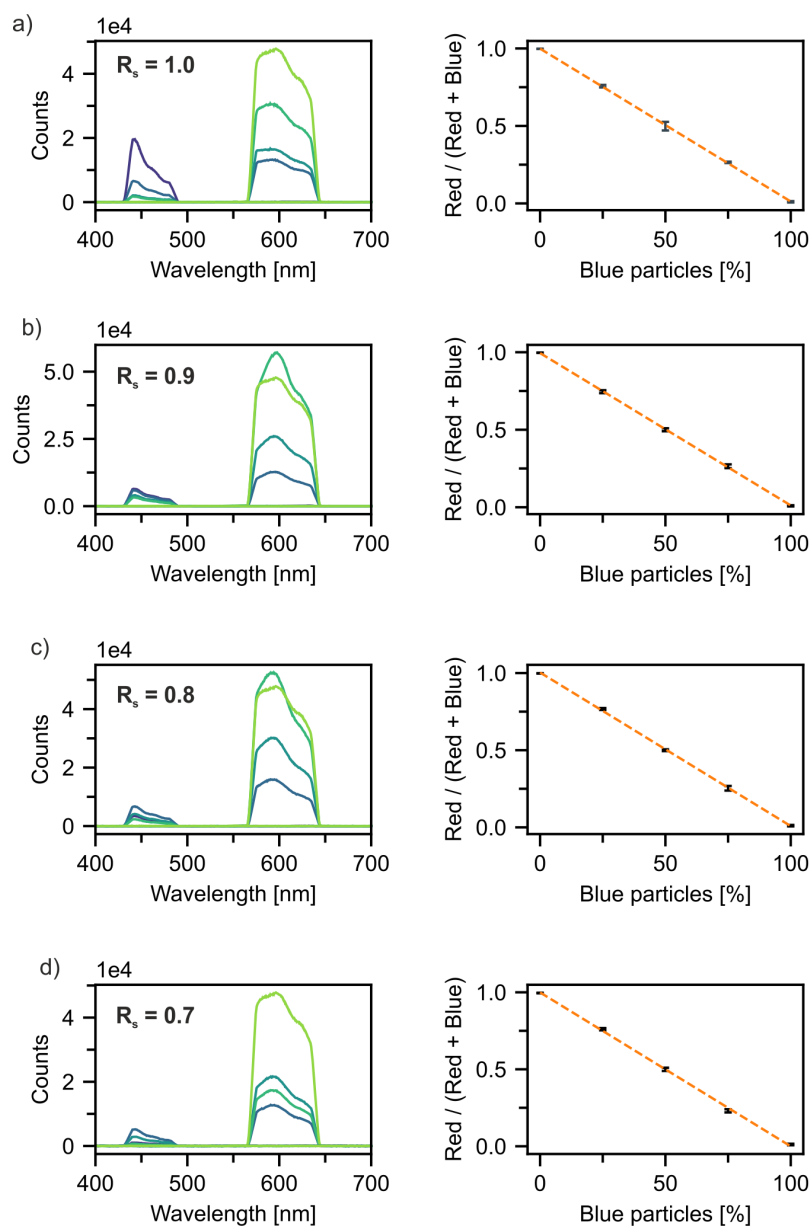


Figure S5: a)-d) Results of the fluorescence calibration for the four different types of combinations with different size ratio (R_s). For each combination, five different compositions are applied between 0-100%. The ratio of the red and blue fluorescence is shown to correlate perfectly with the known, input-composition. This proves that local fluorescence spectroscopy can be utilized to non-invasively determine an unknown composition at any position of a sample.

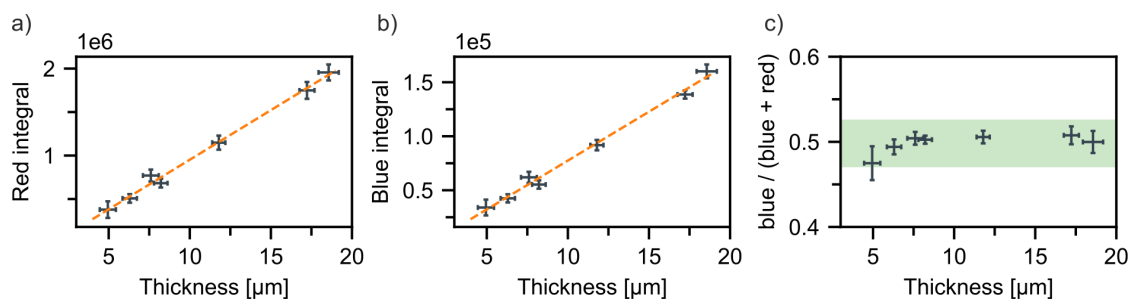


Figure S6: Measurement of samples with a 50:50 mixture of red and blue particles. a),b) Absolute integral of the fluorescence signal with respect to the sample thickness for both the red and blue channel, respectively. c) Ratio of red and blue fluorescence shows that the calibration provides consistent results over the entire examined thickness range.

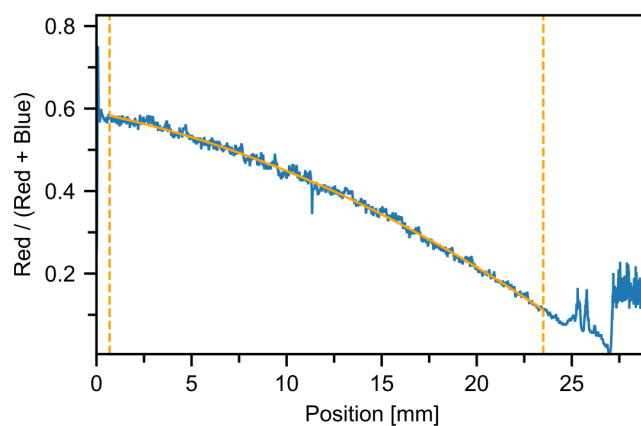


Figure S7: Composition vs. position along a gradient colloidal crystal with a second order polynomial fit (orange) and the chosen borders of the evaluation range. This curve is used to map the particle composition to the position, and thereby to the transmission spectra at these positions.

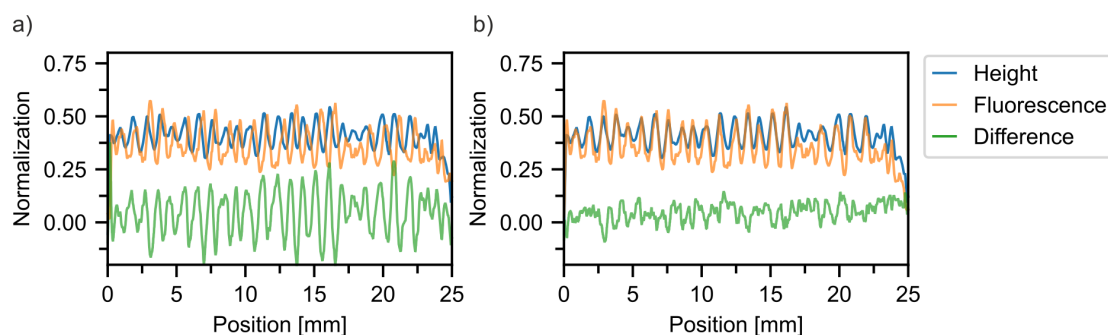


Figure S8: a) Height profile and cumulative (red + blue) fluorescence signal along a gradient colloidal crystal. Due to slight misalignment of the two measurements, a correction factor must be applied before the overlap is ideal. b) Corrected profiles showing a minimum of the difference plot.

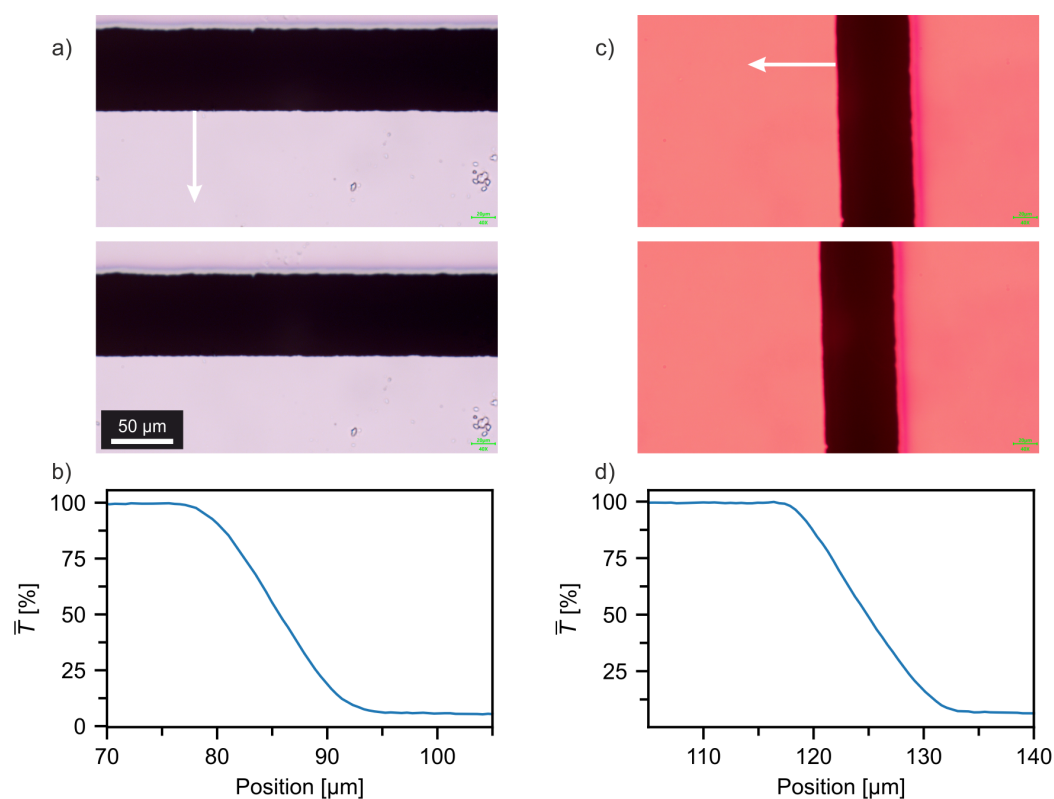


Figure S9: a) Snapshots of a mask being moved along the microscope stage vertically. b) Average transmittance during this movement, showing how the light is blocked entirely in a range of 10 μm . c),d) Analogous evaluation in horizontal direction.

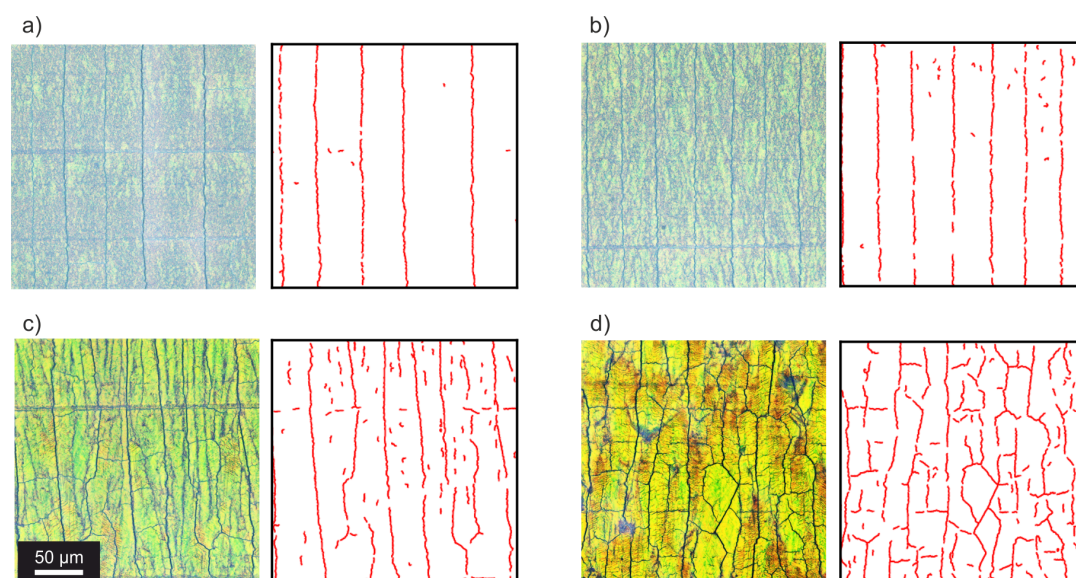


Figure S10: Exemplary microscopy images together with masks of the cracks obtained via thresholding and a ridge-detection algorithm. [Thorsten Wagner, Mark Hiner, & xraynaud. (2017). thorstenwagner/ij-ridgedetection: Ridge Detection 1.4.0 (v1.4.0). Zenodo. <https://doi.org/10.5281/zenodo.845874>]

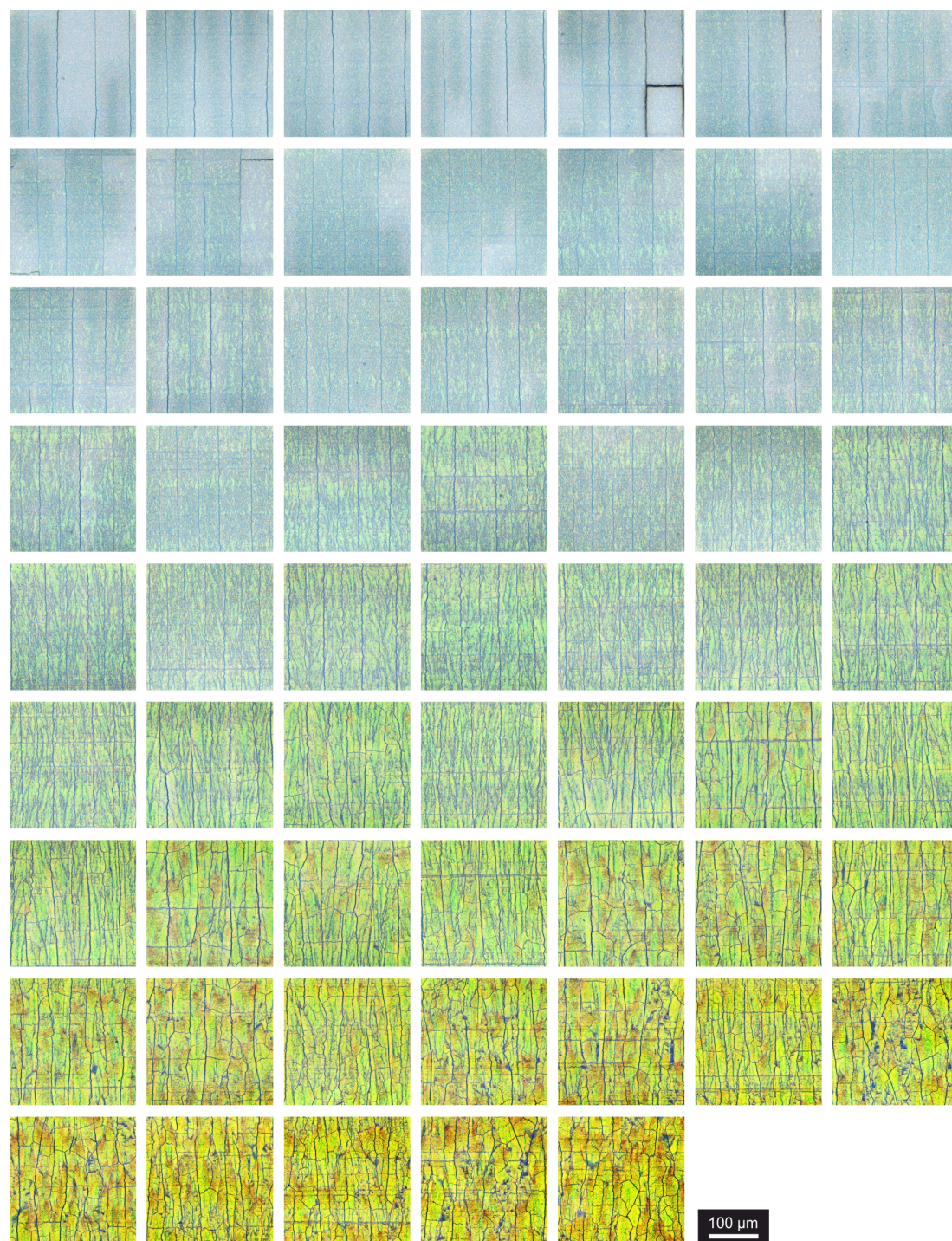


Figure S11: All microscopy images obtained along the gradient sample transitioning between order and disorder. The color gradually changes with the composition. Images are ordered left to right and top to bottom.

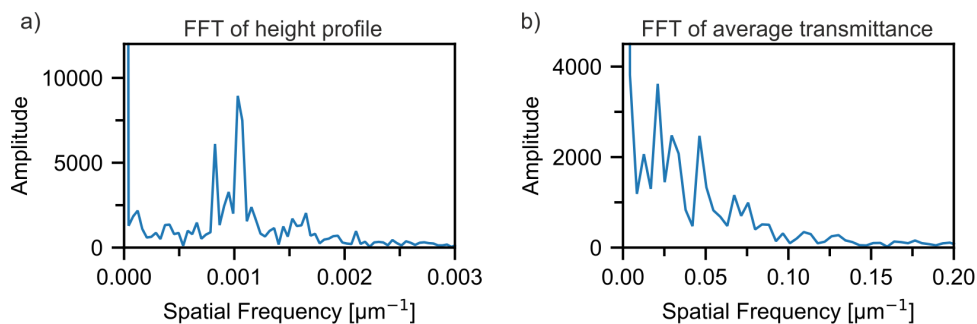


Figure S12: FFTs of a) the height-profile in Figure 2i and b) the average transmittance along the cracks in a colloidal crystal in Figure 3c.

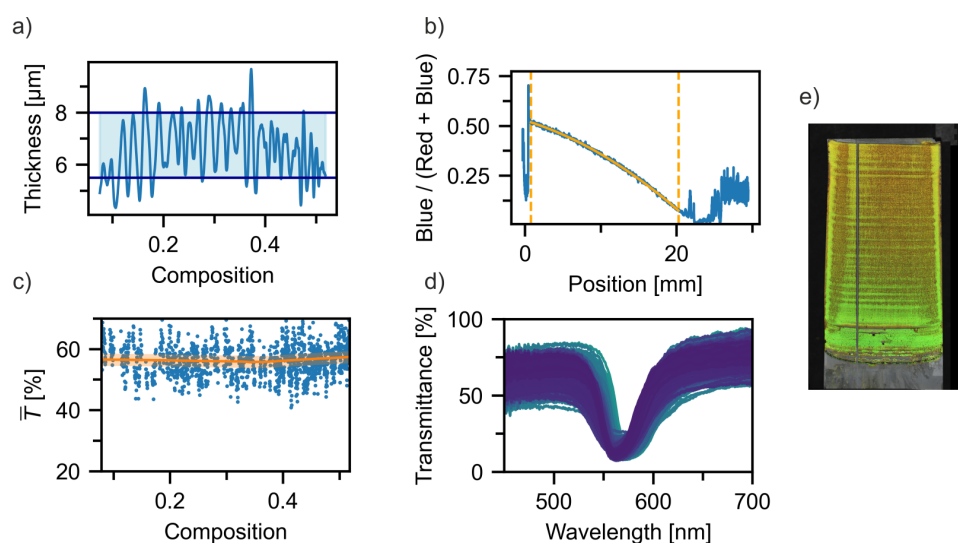


Figure S13: Raw data obtained from a sample starting with 282 nm with a gradually increasing amount of 305 nm particles. a) Height profile with the ranges showing which part of the data was used for further analysis. b) Calibration curve mapping the composition to the position. c) Scatter plot of all values of the average transmittance. The orange curve shows a first order Savitzky-Golay filter. d) All transmittance spectra (unfiltered). e) Stitched microscopy images showing the entire sample prepared via IWC.

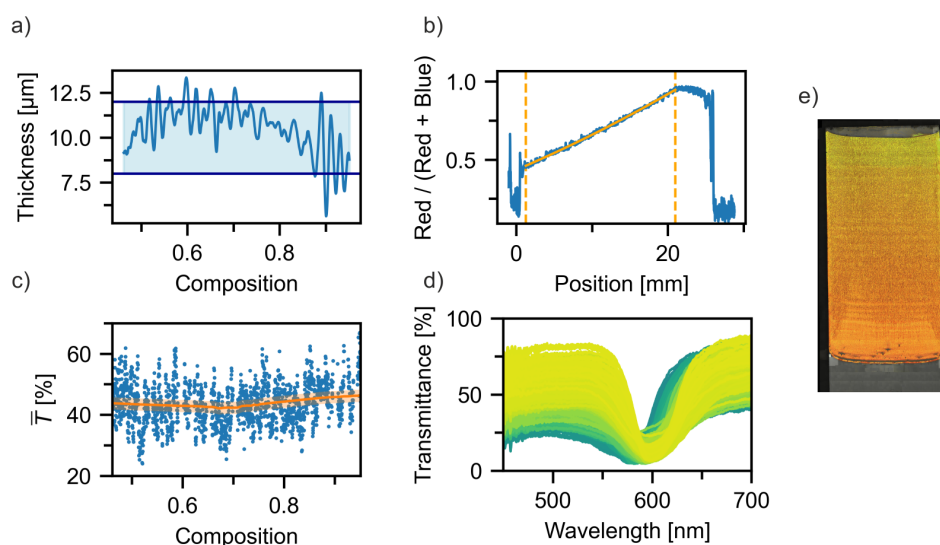


Figure S14: Raw data obtained from a sample starting with 305 nm with a gradually increasing amount of 282 nm particles. a) Height profile with the ranges showing which part of the data was used for further analysis. b) Calibration curve mapping the composition to the position. c) Scatter plot of all values of the average transmittance. The orange curve shows a first order Savitzky-Golay filter. d) All transmittance spectra (unfiltered). e) Stacked microscopy images showing the entire sample prepared via IWC.

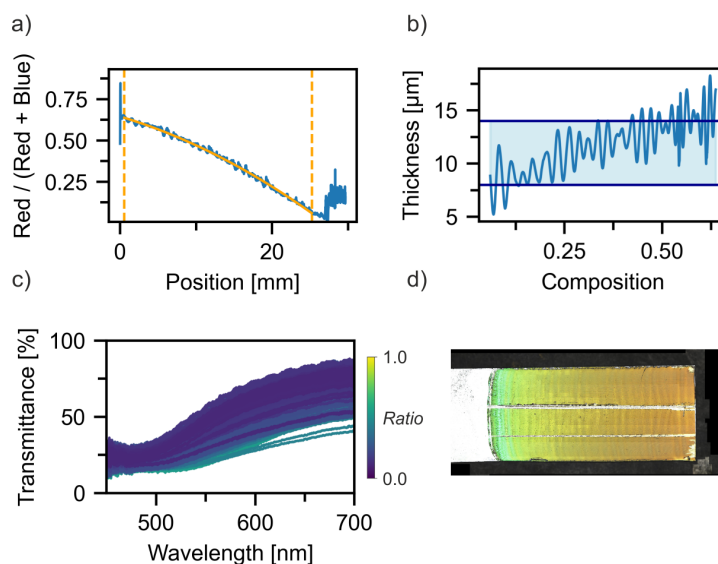


Figure S15: Raw data obtained from a sample starting with 255 nm with a gradually increasing amount of 305 nm particles. a) Calibration curve mapping the composition to the position. b) Height profile with the ranges showing which part of the data was used for further analysis. c) All transmittance spectra (unfiltered). d) Stacked microscopy images showing the entire sample prepared via IWC.

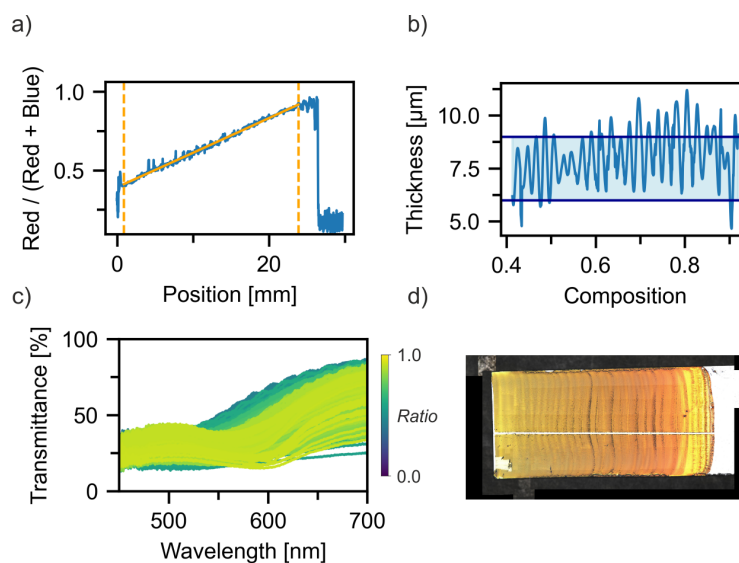


Figure S16: Raw data obtained from a sample starting with 305 nm with a gradually increasing amount of 255 nm particles. a) Calibration curve mapping the composition to the position. b) Height profile with the ranges showing which part of the data was used for further analysis. c) All transmittance spectra (unfiltered). d) Stitched microscopy images showing the entire sample prepared via IWC.

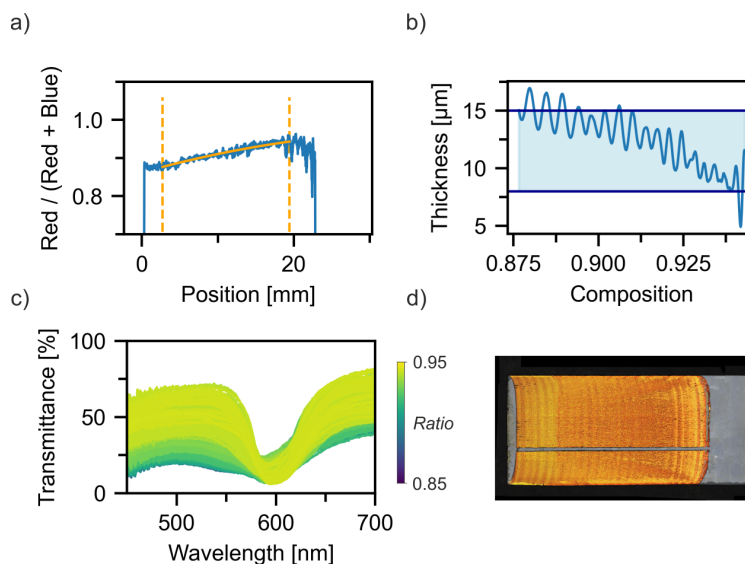


Figure S17: Raw data obtained from a sample starting with 305 nm with a gradually increasing amount of 255 nm particles. A slower addition rate of small particles results in a sample that can provide a detailed analysis of this specific composition range where the order-to-disorder transition takes place. a) Calibration curve mapping the composition to the position. b) Height profile with the ranges showing which part of the data was used for further analysis. c) All transmittance spectra (unfiltered). d) Stitched microscopy images showing the entire sample prepared via IWC.

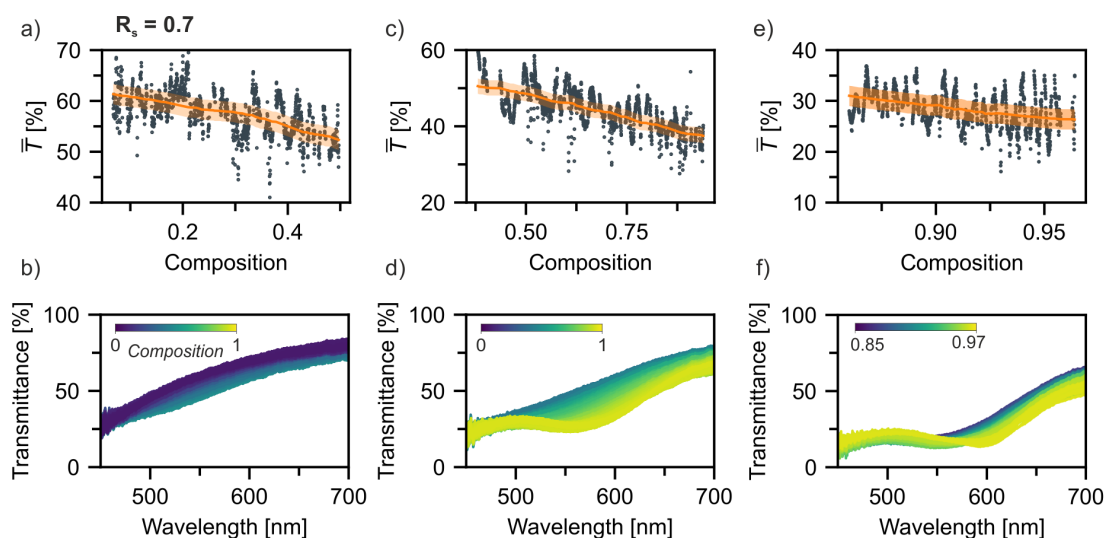


Figure S18: Local spectroscopic characterization of gradient samples with a size ratio of $R_s = 0.7$. a) Average transmittance along the sample and b) filtered spectra. The shoulder in the spectra shifts to higher wavelengths as the amount of large particles increases, which explains the downward trend in a). This trend persists when extending the composition range in c) and d) as well as when examining a smaller range in more detail in e) and f).

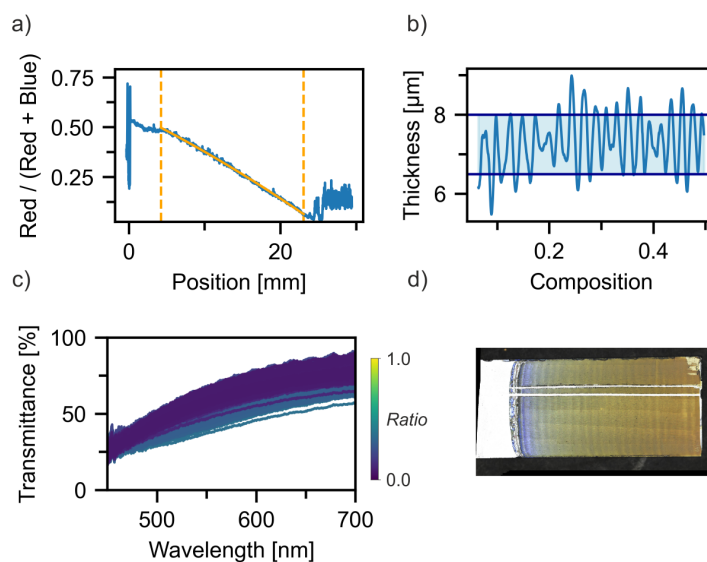


Figure S19: Raw data obtained from a sample starting with 222 nm with a gradually increasing amount of 305 nm particles. a) Calibration curve mapping the composition to the position. b) Height profile with the ranges showing which part of the data was used for further analysis. c) All transmittance spectra (unfiltered). d) Stitched microscopy images showing the entire sample prepared via IWC.

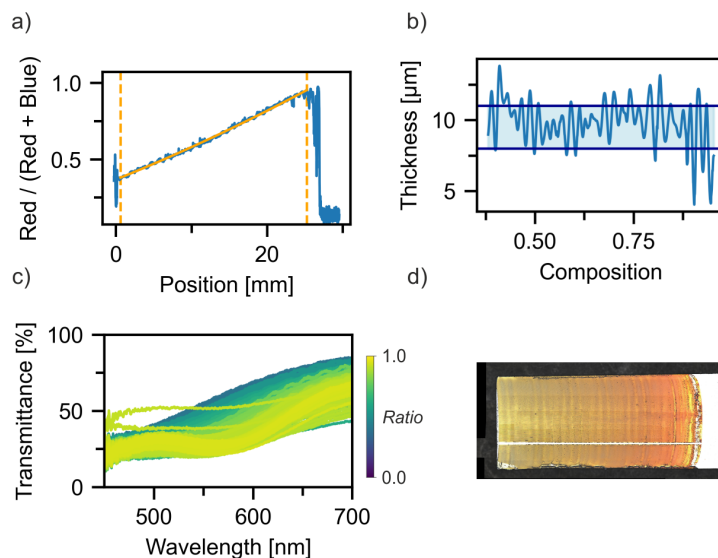


Figure S20: Raw data obtained from a sample starting with 305 nm with a gradually increasing amount of 222 nm particles. a) Calibration curve mapping the composition to the position. b) Height profile with the ranges showing which part of the data was used for further analysis. c) All transmittance spectra (unfiltered). d) Stitched microscopy images showing the entire sample prepared via IWC.

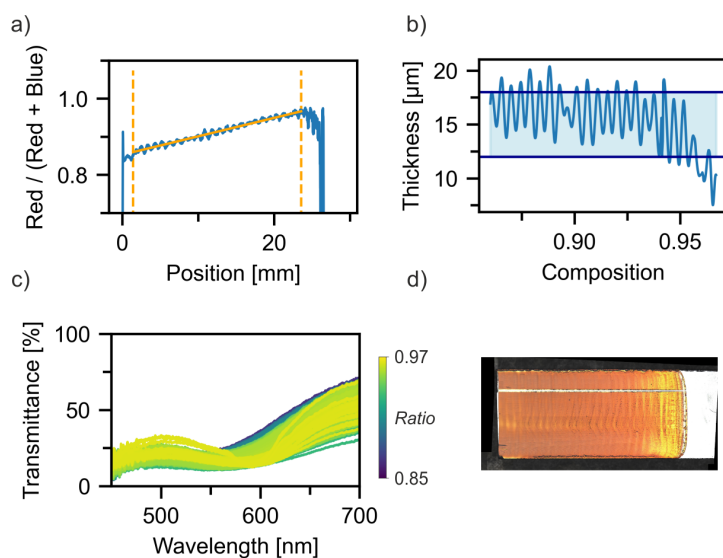


Figure S21: Raw data obtained from a sample starting with 305 nm with a gradually increasing amount of 222 nm particles. A slower addition rate of small particles results in a sample that can provide a detailed analysis of this specific composition range close to the order-to-disorder transition. a) Calibration curve mapping the composition to the position. b) Height profile with the ranges showing which part of the data was used for further analysis. c) All transmittance spectra (unfiltered). d) Stitched microscopy images showing the entire sample prepared via IWC.

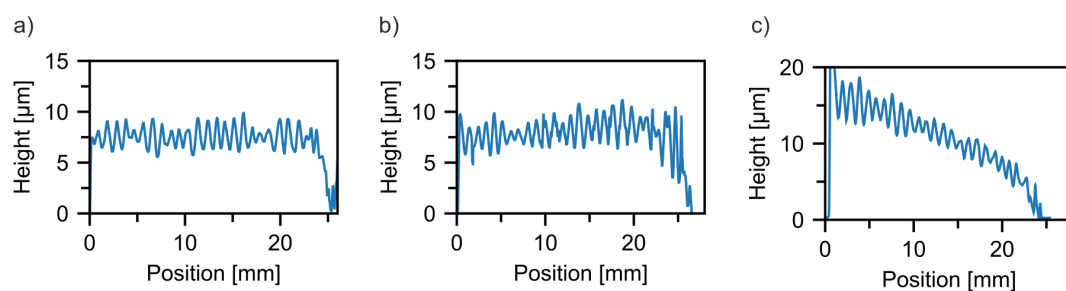


Figure S22: a) Height profile of a sample that is crystalline over the entire range. b) Height profile of a sample that is amorphous over the entire range. c) Height profile of a sample that gradually transitions from amorphous to crystalline. The thickness shows a trend in the transition regime between crystalline and amorphous in c).

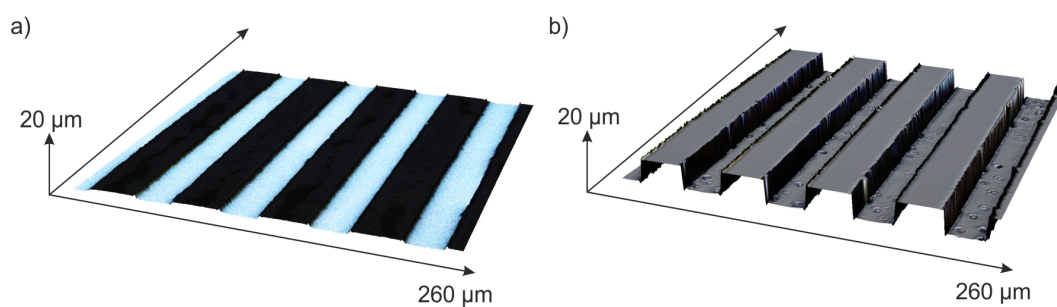


Figure S23: 3D reconstructed images obtained via laser scanning confocal microscopy of a) the empty, patterned PDMS and b) a coated substrate.

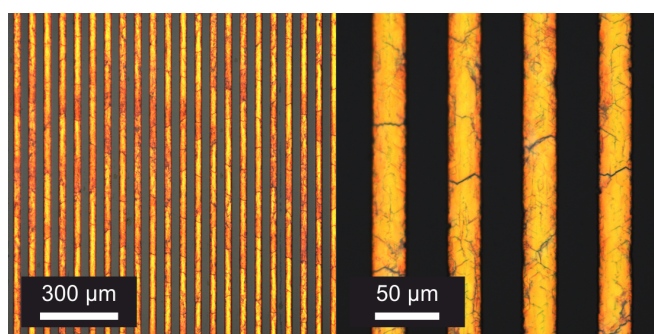


Figure S24: Reflectance microscopy images of 305 nm particles assembled to a colloidal crystal in the PDMS trenches.

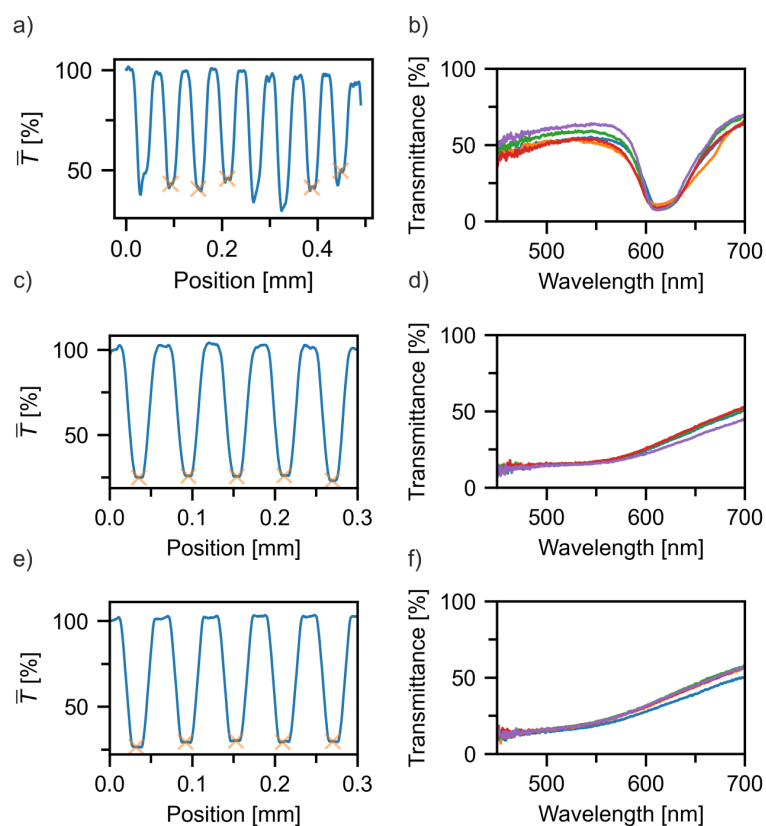


Figure S25: a) Average transmittance while measuring perpendicular to the trenches on a substrate coated with monodisperse large particles in the trenches. The orange markers show which positions (and therefore which spectra) were chosen for further analysis. b) The five spectra selected in (a). c,d) and e,f) show an analogous evaluation for binary (amorphous) samples with a composition of 0.6 (60% large particles) and $R_S = 0.8$ and 0.7 respectively. The markers are set at positions where the average transmittance plateaus. The evaluation is more consistent for the amorphous samples, as these are not compromised by cracks.

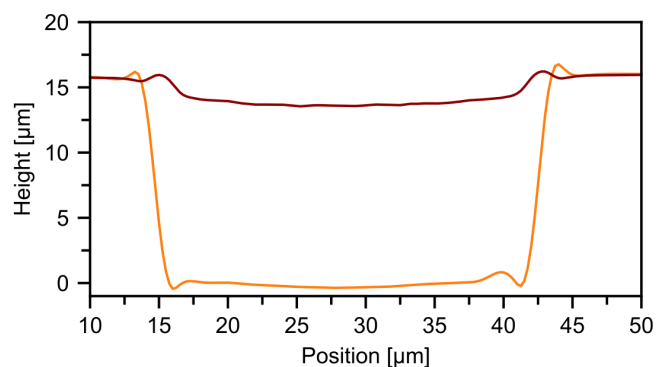


Figure S26: Height profile of one single trench. Orange: empty, Red: filled with a colloidal glass. The scaling of x-, and y-axis is identical in this plot and therefore shows the true geometry of a cross-section through the trench.

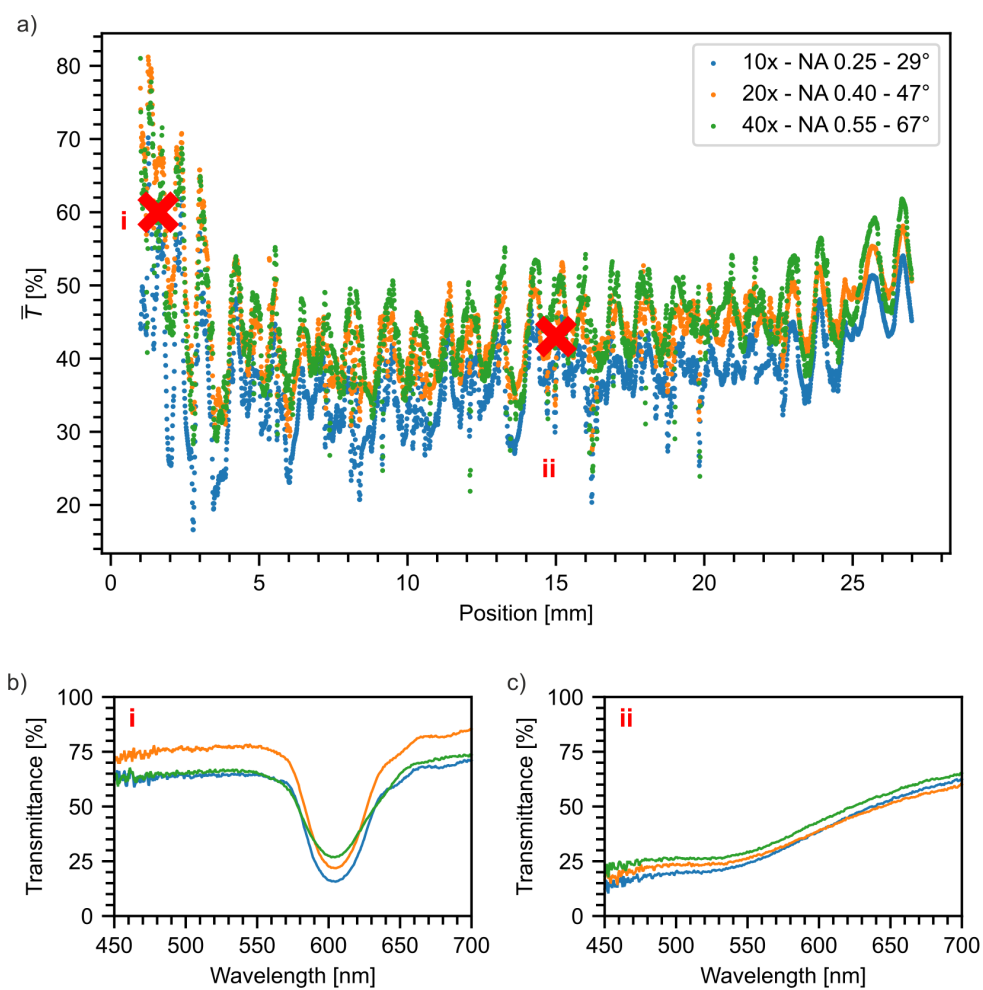


Figure S27: a) Mean transmittance along the gradient that was presented in Figure 5c,d. Different objectives are used to compare the effect of a varying acceptance angle. b),c) Representative spectra with obtained with all three objectives, measured at the positions indicated in (a).

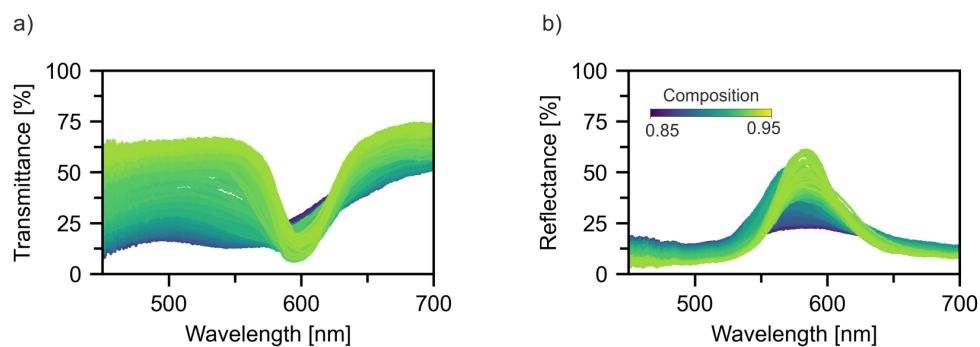


Figure S28: Transmittance and reflectance spectra along the gradient presented in Figure 3. The size ratio of the two particles here is 0.8 and the composition gradually changes between 0.85 and 0.95 (where 1.0 denotes 100 % large particles).

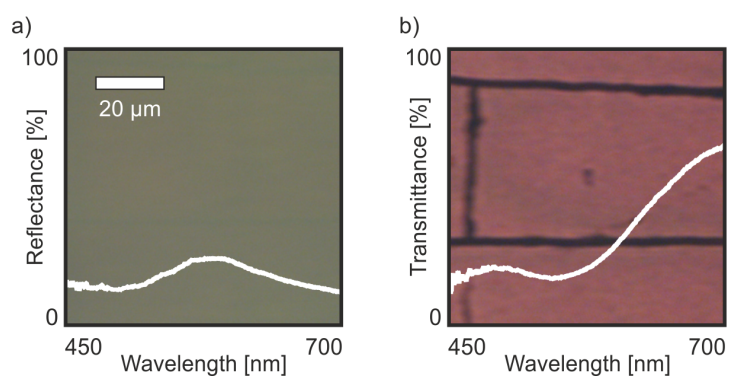


Figure S29: Exemplary microspectra and microscopy images in reflection (a) and transmission (b) geometry to show the scale for all images in Figures S30 and S31.

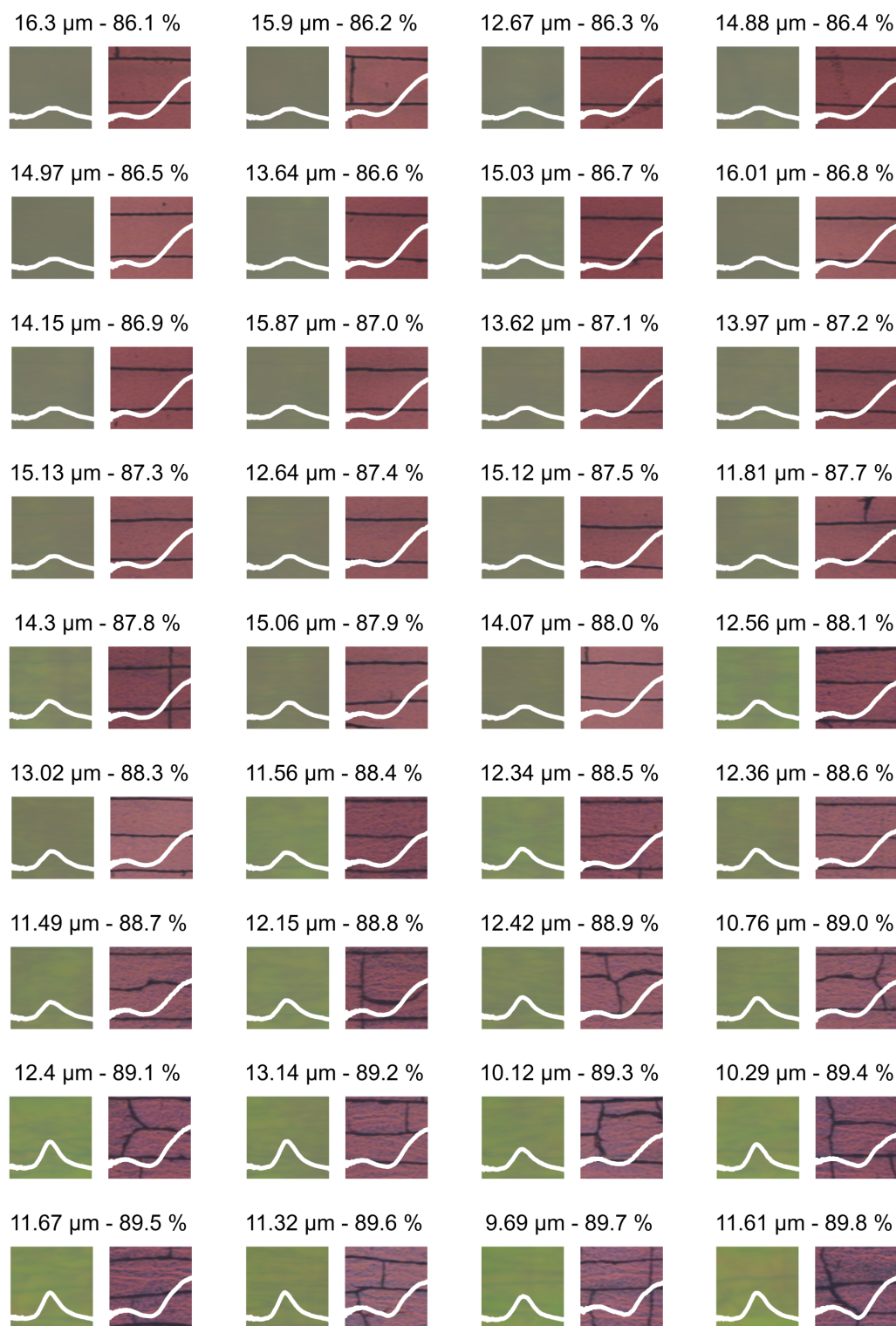


Figure S30: Reflectance and transmittance spectra as well as the according microscopy images along the gradient measured in Figure S28. The thickness (in μm) is measured via LSCM along the scratch and the composition (of large particles in %) is determined via local fluorescence measurements.

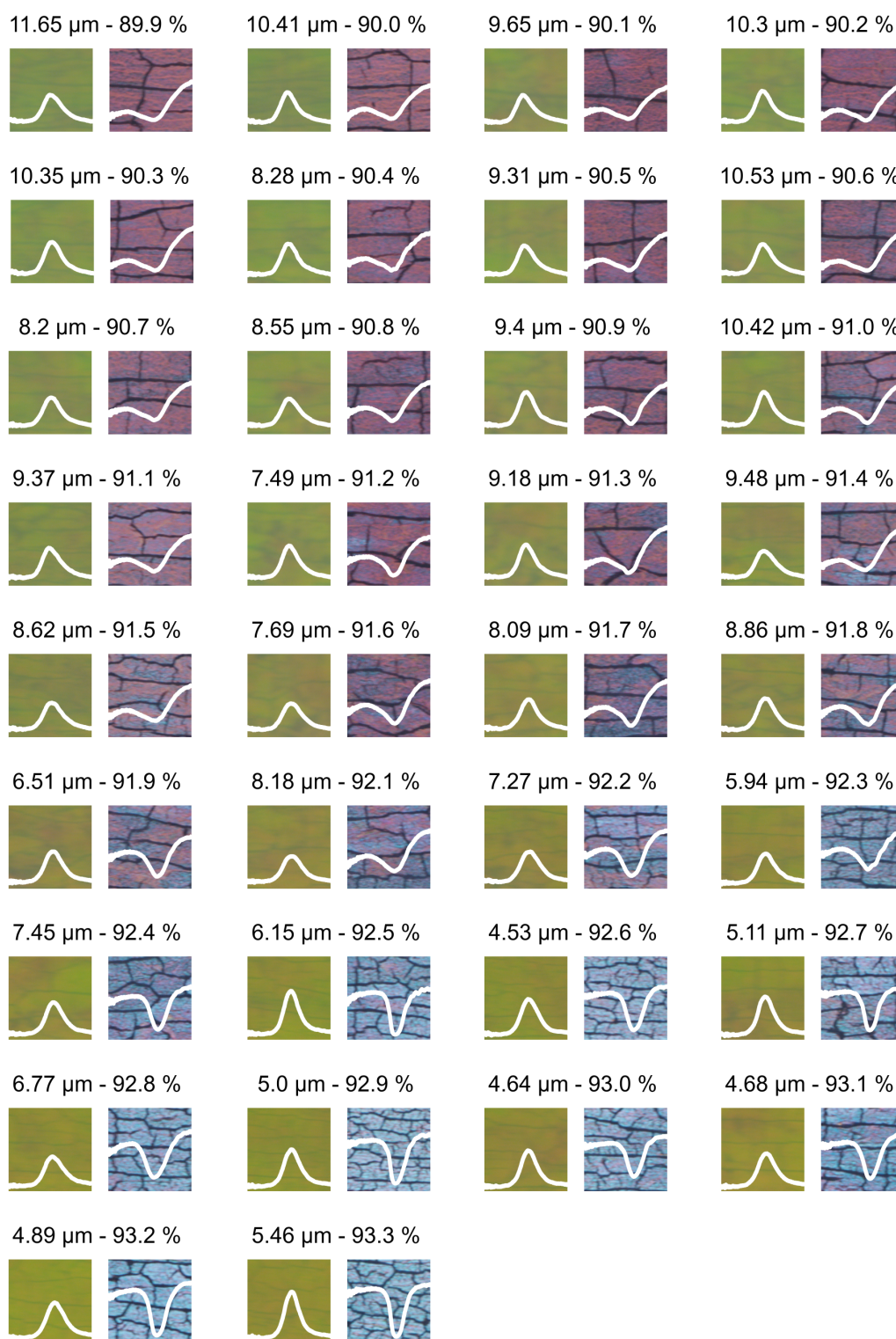
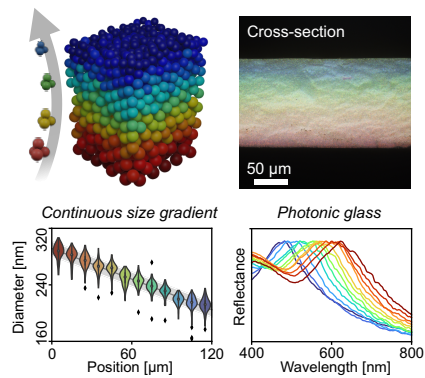


Figure S31: Continued data from Figure S30.

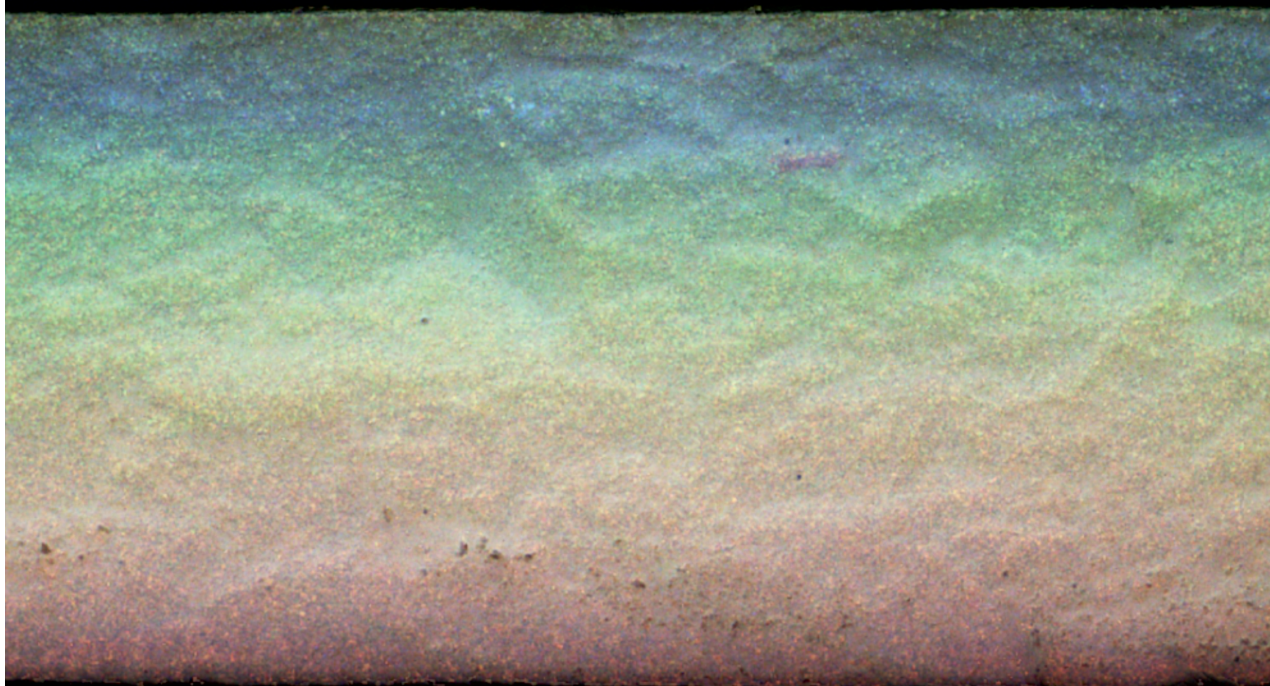
A Continuous Gradient Colloidal Glass

Marius Schöttle, Tobias Lauster, Lukas J. Römling, Nicolas Vogel, and Markus Retsch, „A continuous gradient colloidal glass“, *Advanced Materials*, **2023**, 35(7), 2208745.



A controlled extraction emulsion process (CrEEP) allows the synthesis of monodisperse latex particles with a continuous size gradient. Subsequent self-assembly into a photonic glass results in a thin film with a continuous photonic gradient and structural colors ranging over the full visible spectrum. This concept is shown to improve the broadband reflectance of such a mesostructure.

ADVANCED MATERIALS



Continuous gradients in self-assembled materials can provide functionality exceeding that of the homogenous case. In article number 2208745, Markus Retsch and co-workers present a synthesis method that provides gradient size distributions via a controlled extraction emulsion process (CrEEP). The high degree of control allows the fabrication of a continuous-gradient photonic glass with enhanced broadband reflectance.

WILEY-VCH

PHOTONIC COLLOIDAL GLASS

A Continuous Gradient Colloidal Glass

Marius Schöttle, Tobias Lauster, Lukas J. Roemling, Nicolas Vogel, and Markus Retsch*

Colloidal crystals and glasses manipulate light propagation depending on their chemical composition, particle morphology, and mesoscopic structure. This light–matter interaction has been intensely investigated, but a knowledge gap remains for mesostructures comprising a continuous property gradient of the constituting particles. Here, a general synthetic approach to bottom-up fabrication of continuous size gradient colloidal ensembles is introduced. First, the technique synthesizes a dispersion with a specifically designed gradual particle size distribution. Second, self-assembly of this dispersion yields a photonic colloidal glass with a continuous size gradient from top to bottom. Local and bulk characterization methods are used to highlight the significant potential of this mesostructure, resulting in vivid structural colors along, and in superior light scattering across the gradient. The process describes a general pathway to mesoscopic gradients. It can expectedly be transferred to a variety of other particle-based systems where continuous gradients will provide novel physical insights and functionalities.

1. Introduction

Structured materials show perceptible photonic properties when the characteristic length scale is similar to the wavelength of visible light. The interaction of photons with a periodically changing refractive index (n) in photonic crystals (PCs) creates a dispersion relation with wave-vector dependent gaps analogous to that of electrons in semiconductors.^[1] These stop bands are the cause of characteristic, iridescent structural colors.^[2] From sensors to optical metamaterials, increasingly complex structures allow tailoring of these properties.^[3,4] However, many are only accessible via simulations or in the microwave range,^[5,6] others are limited to high- n materials.^[7]

Complementary to the phenomenon of ballistic light transport in ordered structures is the dispersive light diffusion

in photonic glasses (PGs).^[8–10] These jammed packings of monodisperse, dielectric spheres show coherent scattering due to Mie resonances and short-range order.^[11,12] Because of the isotropic nature, the resulting colors are angle-independent.^[13,14] Particle size and morphology, such as core-shell and hollow sphere structures, have been shown to influence the optical properties and provide tunable scattering and broadband reflectance of PGs.^[15–19] Recently, anisotropic particles have also been shown to be useful for the adjustment of the scattering properties of the ensembles.^[20,21]

Hierarchical structural design can introduce further complexity to particulate system.^[22] For example, multilayer PC films with a cross-plane, stepwise change of the lattice constant show properties not found in single-component systems. These range from broadband reflectivity^[23] to angular selectivity.^[24] However, fabrication methods are often tedious and typically apply physical vapor deposition or repetitive colloidal assembly.^[25,26] Without precise optimization, the latter can suffer from degradation of preformed layers and delamination. Further issues include incoherent light scattering at the interfaces and small sample sizes.

Despite the intense research on photonic crystals and glasses, one major category of colloidal mesostructure has received surprisingly little attention: continuous gradient structures. Continuous gradients in colloidal assemblies is an emerging topic, with few examples and approaches being reported in literature. Gradual changes, e.g., in the interparticle distance or composition can be formed via centrifugation,^[27,28] post-assembly deformation^[29] or modified coating procedures.^[30,31] From a fundamental point of view, a better physical understanding of photonic materials with gradually changing properties needs to be developed and compared to experimental results.^[32–34] To our knowledge, no experimental realization of a photonic colloidal assembly with a continuous particle size gradient has been presented to date. To achieve such a structure, two major challenges need to be addressed: First, particle dispersions with precise control of size and a continuous size variation need to be reliably available. Second, self-assembly must retain, not mix, the particle size gradient and immobilize the particles gradually in the colloidal ensemble.

Here, we provide a solution to both challenges that conceivably can also be applied to other (functional) particles. This general approach to continuous gradient colloidal glasses will add a missing piece to the field of colloidal mesostructures and opens a new field for photonic engineering and beyond. At the heart

M. Schöttle, T. Lauster, M. Retsch
Department of Chemistry
University of Bayreuth
Universitätsstr. 30, 95447 Bayreuth, Germany
E-mail: markus.retsche@uni-bayreuth.de
L. J. Roemling, N. Vogel
Insitute of Particle Technology
Friedrich-Alexander University Erlangen-Nürnberg
91058 Erlangen, Germany

 The ORCID identification number(s) for the author(s) of this article can be found under <https://doi.org/10.1002/adma.202208745>.

© 2022 The Authors. Advanced Materials published by Wiley-VCH GmbH. This is an open access article under the terms of the Creative Commons Attribution License, which permits use, distribution and reproduction in any medium, provided the original work is properly cited.

DOI: 10.1002/adma.202208745

of our work is a controlled emulsion extraction process (CrEEP) that enables us to store the time-dependent size increase of monodisperse latex particles in a thin extraction tube, where laminar flow prevails. Subsequent filtration assembly translates the gradient dispersion into a film with a fully continuous, cross-plane gradient of the particle size. First, we present the synthesis method and then show the characteristics of the 3D self-assembled colloidal gradient material.

2. Results and Discussion

Surfactant-free emulsion polymerization is an established method for the preparation of monodisperse latex particle suspensions.^[35,36] Further control can be obtained via a semibatch process by first preparing seed particles that then increase in size when more monomer is added.^[37,38] In our CrEEP-approach (Figures S1 and S2, Supporting Information), the monomer is added gradually, and the growing particle suspension is simultaneously extracted into a thin tube. The resulting time-dependent change of the particle diameter is thereby stored in the extraction tube and turned into a positional dependency. Slow extraction and the small diameter of the tube provide controlled laminar flow. To verify the controlled nature of this process, we show that the reaction rate of the emulsion polymerization is fast compared the rate of monomer addition by evaluating the kinetics of the particle growth during seed synthesis (Figure S3, Supporting information). Mixing is further inhibited by fractionation via the injection of air bubbles as separators inside the tube. Thereby the monodisperse nature inherent to the emulsion polymerization is maintained. Analogous experiments without injection of air result in a slightly less ordered assembly (Figure S4, Supporting information). The air bubbles have the additional benefit of quenching the remaining initiator molecules with ambient oxygen, inhibiting any further polymerization. The fact that the continuous particle growth and extraction take place in the same reactor as the seed synthesis ensures reproducible starting conditions. Combined with the slow monomer addition, this results in a highly controlled reaction. Ultimately, a large number of equidistant fractions (in this case 110) are retained in the tube (Figure 1a). We examine every 10th fraction via dynamic light scattering (DLS) and correlate it to the respective reaction time during the extraction process (Figure 1b,c). We observe a near-linear increase of the hydrodynamic particle diameter and a low polydispersity throughout the synthesis. Both confirm the high degree of control that is necessary for the self-assembly process, which is dramatically influenced by both size and size distribution. In our example, we prepare a diameter range between 220–310 nm to specifically target photonic materials in the visible range. In combination with the number of fractions, this implies a sub-nm step size between neighboring fractions. Naturally, this is smaller than the size distribution of any given latex particle synthesis. Consequently, this constitutes a smooth and gradual size increase, a feature not accessible using a multi-pot approach.

To demonstrate the quality of fractions obtained via CrEEP, we induce self-assembly via heated drop-casting. The formation of PCs with structural colors dependent on the diameter

of the particles becomes apparent via white light microscopy (Figure 1d). Brilliant colors ranging from blue to red can be observed. Due to the fcc symmetry and the concomitant *k*-vector dependency of the optical stop-band, these are inherently angle-dependent. Increasing the angle between light source and observer causes a blue shift of all 12 drop-cast spots (Figure 1e) and verifies the crystallinity. Further optical characterization with normal incidence reflectance μ -UV-vis spectroscopy (Figure 1f) elucidates the size-dependent properties. As the particle diameter increases, the stop-band peak gradually shifts to higher wavelengths. The position of the peak with respect to the reaction time of the corresponding fraction follows a linear trend (Figure 1g). Considering the linear dependency of the lattice spacing and wavelength in the Bragg–Snell Equation,^[25] this corroborates the similar trend observed for the DLS results. Scanning electron microscopy (SEM) images of four selected PCs (Figure 1h) illustrate the monodisperse nature and hexagonal symmetry as well as the controlled increase of the particle size. An overview SEM image (Figure S5, Supporting Information) shows large domain sizes. Altogether this preliminary evaluation of the extracted fractions shows that the gradual increase of the particle size can be retained in a thin tube via CrEEP. Prevention of mixing thereby ensures that the monodisperse nature is maintained and allows self-assembly to form photonic structures.

After the CrEEP, a gradient colloidal dispersion is stored inside the extraction tube in a size-sorted manner. We now present a straightforward self-assembly process to transform this gradient dispersion into a colloidal glass with a smooth and continuous gradient. Our semicontinuous filtration technique involves dilution and subsequent filtration of each fraction. This allows us to fabricate a free-standing colloidal glass film with a gradually increasing particle size from top to bottom (Figure 2a; Figure S6a, Supporting Information). A sample 3.5 cm in diameter and with a thickness of $110 \pm 5 \mu\text{m}$ is thereby obtained (Figure S6b, Supporting Information).

We demonstrate the successful fabrication of the intended gradient colloidal glass by laser scanning confocal microscopy (LSCM)^[39] across the edge of a broken gradient film. An overlay of the height image obtained via laser-scanning and white light microscopy images from various focal positions provides a simple and intuitive impression (Figure 2b; Figure S7, Supporting Information). Complementary to the colorful appearance observed for self-assembled particles of separate fractions, we find structural colors continuously ranging from blue to red, reminiscent of a rainbow. The top and bottom faces appear blue and red, respectively, corresponding to the particle size of the first and last fraction. The addition of a broadband absorber is known to counteract the effect of diffuse scattering.^[40] We, therefore, improve the saturation of the side-view structural colors by a thin layer of carbon (10 nm) on the surface of the cross section (Figure S8, Supporting information). While the colloidal glass filtration is conducted in a semicontinuous way, we do not observe any layering or stepwise particle size increase. As outlined in the gradient dispersion synthesis, the mean particle size changes with $<1 \text{ nm}$ from fraction to fraction, which is too small to be resolved analytically. Another advantage of the filtration approach is that a large sample can be prepared with homogeneous gradient properties. The colloidal

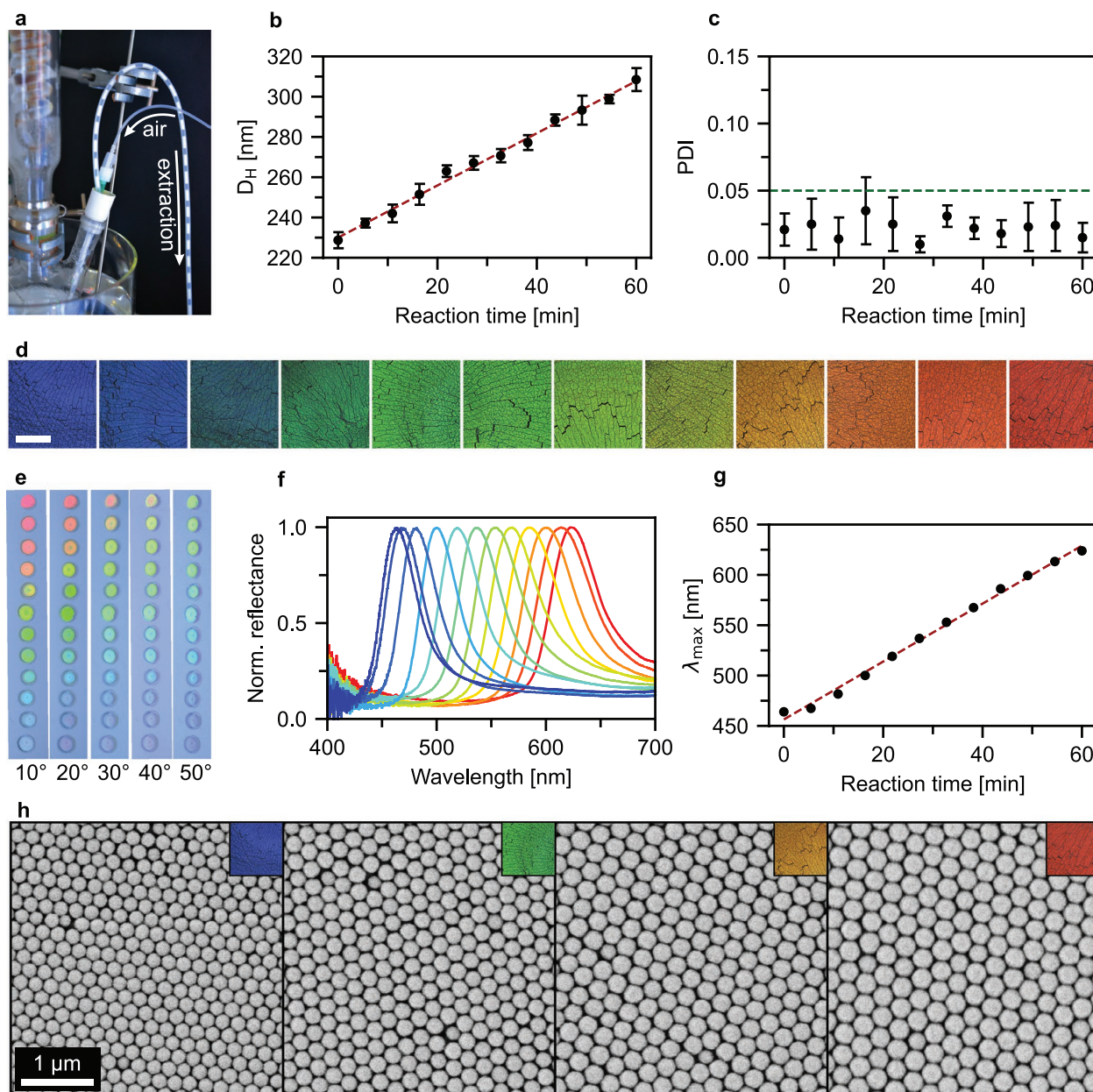


Figure 1. Characterization of equidistant fractions after the controlled emulsion extraction process (CrEEP). a) Snapshot of fractions during the extraction process showing even separation by air bubbles. b,c) Hydrodynamic diameter (D_H) and polydispersity index (PDI) obtained from DLS measurements of every 10th fraction. The reaction time noted here corresponds to the CrEEP starting with the gradual monomer addition. A linear fit shown in red elucidates the highly controlled nature of the gradual seeded growth. The polydispersity remains below 5% and is independent of the reaction time. d) Light microscopy images of these fractions after drop-casting showing size-dependent structural colors typical for colloidal crystals. Scale bar: 100 μm e) Photographs of the samples measured in (d) at different angles between camera and light source. f) μ -UV-vis reflectance spectra of the drop-cast fractions showing a gradual red-shift of the stop-band as the particle size increases. g) Peak position of the stop-band versus reaction time showing a linear relation. This stands in accordance with the DLS measurements and particle size. h) SEM images of selected drop-cast fractions. Insets show the corresponding light microscopy images. Both the increase in absolute size, as well as the consistently monodisperse nature, can be observed in the self-assembled colloidal crystals showing hexagonal symmetry.

gradient and hence the photonic properties are identical when examining cross sections via LSCM at several different macroscopic positions along the length of the filtered film (Figure S9, Supporting Information).

SEM images of selected positions along the cross section (Figure 2c) provide structural insights into the origin of colors in the gradient. The filtration assembly forces random aggregation of particles and thus a disordered structure. We

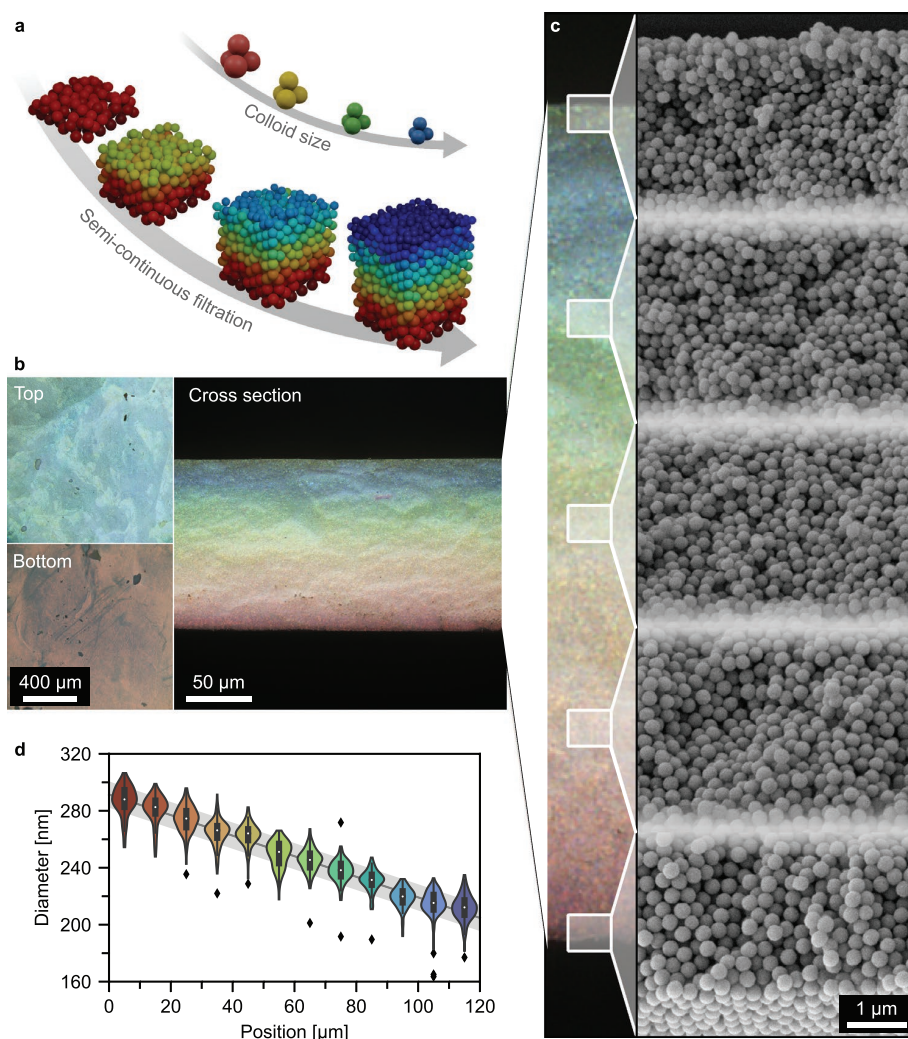


Figure 2. Gradient photonic glass prepared via semicontinuous filtration. a) Schematic illustration of the z-gradient structure resulting from the gradual assembly process. b) Light microscopy images of the top and bottom surface as well as the cross section showing the gradual transition of structural color throughout the entire visible spectrum. c) Representative SEM images of the colloidal assembly at the positions indicated in the cross-section. d) Size distribution of particles at equidistant positions along the gradient as obtained from the SEM images in Figure S10 (Supporting Information). At each position, more than 100 particles were measured. Outliers are shown as black diamonds.

attribute this to the fast kinetics of the filtration process and the absence of capillary forces.^[22] The result is a photonic glass that consists of monodisperse, dielectric Mie scatterers and shows a position-dependent resonance frequency. Measurement of particle diameters at equidistant z-positions along the cross section allowed statistical evaluation of the change in size (Figure 2d; Figure S10, Supporting Information). Two important observations can be made here: 1) The position-dependent particle size shows a linear trend. This, once more, emphasizes the high degree of control during synthesis and assembly. We achieve this linearity by careful optimization of the CrEEP (details are outlined in Figure S11, Supporting Information). 2) At any given z-position, all particles are nearly monodisperse, underlining the performance of the fractionation in our process. The efficiency of fractionation is better than the polydispersity of the emulsion polymerization itself; hence the

overlap of individual fractions is continuous. The result is one of the significant features presented in this work: the circumvention of discrete steps in a gradient particle assembly. The photonic glass shown here is consequently a fully continuous gradient structure.

For a full characterization analogous to that of discrete fractions, we show local μ -UV-vis reflectance spectra at equidistant positions along the gradient material (Figure 3a; Figure S12, Supporting Information). As the particle size increases, the reflectance peak shows a gradual red shift (Figure 3b). This positional dependency is linear, (Figure 3c) which correlates with the linear change in diameter examined via SEM evaluation. Compared to the spectra of colloidal crystals in Figure 1f, the width of these peaks is significantly larger. We attribute this to the short-range order and also partly to the fact that the measurement averages over a range

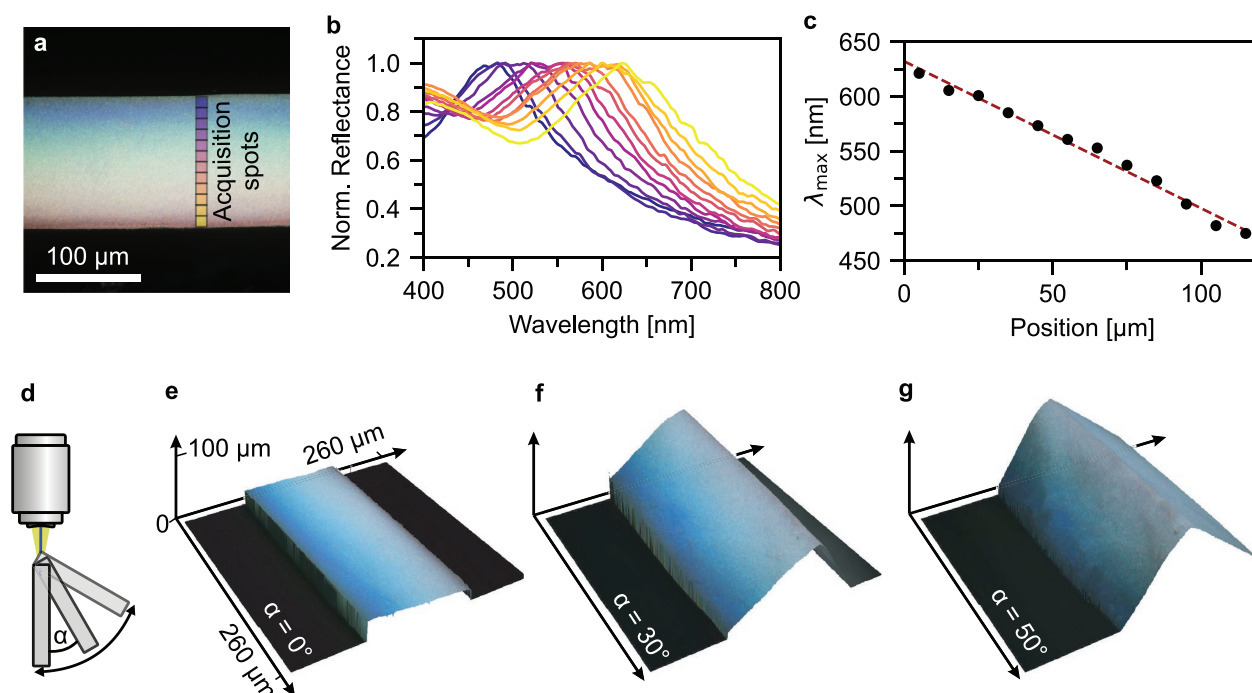


Figure 3. Local optical characterization of the gradient photonic glass. a) Microscopy image of a carbon-coated cross-section illustrating the spot size and position where individual spectra were obtained. b) Local spectra and c) wavelengths of the peak maxima showing a linear red-shift from the top to the bottom of the gradient. d) Microscopy setup used to examine different viewing angles of one gradient cross-section to prove the angle independence of the structural colors. e, f) Resulting overlay of height and white light microscopy images obtained via LSCM of a sample tilted between 0 and 50°. The color range of the gradient remains between blue and red, independent of the viewing angle.

of 10 μm , thereby covering a particle size increase of ≈ 8 nm in each area. The latter effect becomes more obvious when increasing the spot size (Figure S13d, Supporting Information). Averaging over half the cross section thereby naturally results in further peak broadening. Spectra obtained from samples without carbon-coating show stronger diffuse scattering, most visible toward smaller wavelengths (Figure S13a,c, Supporting Information).

The fact that isotropic colloidal assemblies exhibit no discrete peaks in Fourier space and, therefore, produce non-iridescent colors can be a significant advantage.^[16] We examine this property by tilting the cross section of a gradient photonic glass under a microscope and conducting LSCM measurements at different viewing angles from 0 to 50° (Figure 3d–g; Figure S14, Supporting Information). This approach is similar to previously shown characterization methods of colloidal supraparticles.^[41] Unlike the results obtained for the iridescent colloidal crystals in Figure 1e, the coloration remains unchanged and ranges between blue and red at all viewing angles. In summary, the local characterization reveals that the gradient colloidal glass exhibits angle-independent reflectivity throughout the visible spectrum.

We now compare the diffuse reflectance from the top surface of the colloidal gradient glass with different reference samples (Figure 4a–f) to establish how the continuous mesostructure affects the optical properties. Homogeneous, non-gradient samples are prepared via filtration of pure small (224 nm) and large (304 nm) particles, respectively. Additionally, these particles are

used for the fabrication of a statistical, binary mixture as well as a bilayer sample. The CrEEP technique is applied to prepare two different samples: 1) a statistical “gradient mixture” via mixing of all fractions and subsequent filtration and 2) the continuous gradient material discussed in Figure 2 and Figure 3. The two CrEEP-syntheses are shown to be identical via UV–vis spectroscopy and DLS measurements of the particles in the respective first and last fractions (Figure S15, Supporting Information). The film thickness is 112 ± 3 μm throughout all samples (Figure S16, Supporting Information).

The single-component sample consisting of small particles shows an intense blue color, whereas the large particles result in a less saturated red appearance. The latter is more compromised by diffuse light scattering and, therefore, appears fainter. The UV–vis diffuse reflectance spectra of these samples show distinct peaks at 420 and 580 nm, respectively (Figure 4g), as expected from the increase in diameter.^[42]

Next, the two disordered structures, both binary and gradient mixture, are compared. Microscopy images of cross sections of the two show a white color. However, the reflectance spectra reveal a pronounced difference (Figure 4h), even though both samples comprise particles in the same size range. The binary mixture almost exclusively results in a profile characteristic for diffuse scattering. A slight shoulder at 550 nm hints toward a rather weak contribution of coherent scattering. Conversely, in the case of the gradient mixture, a distinct peak at 515 nm can be observed. This lies roughly in the middle of the peaks observed for the pure small and large particles, respectively.

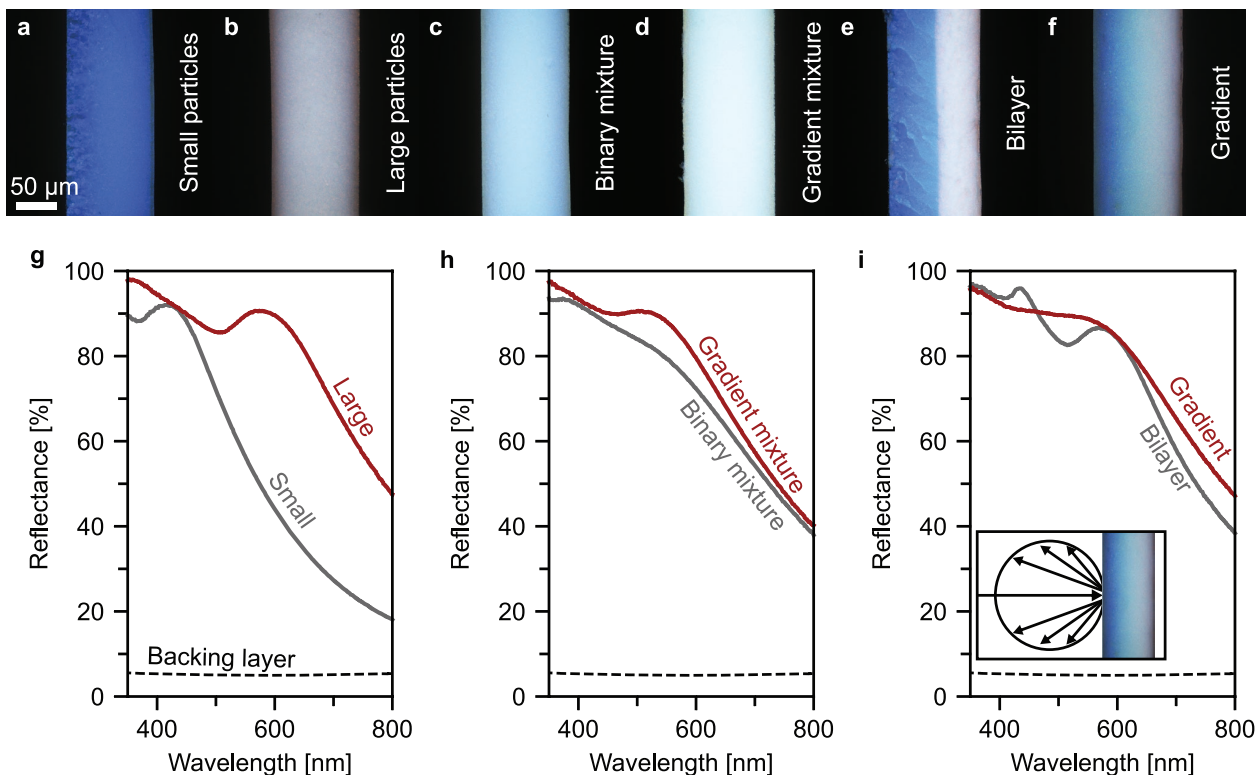


Figure 4. Diffuse reflectance UV-vis spectroscopy of colloidal assemblies prepared via filtration. a,b) Cross section light microscopy images of samples consisting of monodisperse particles. c) Disordered, binary mixture of these reference particles. d) Sample prepared by mixing all fractions obtained from the semibatch emulsion polymerization prior to filtration. e) Bilayer of small and large particles. f) Gradient sample prepared via the presented semicontinuous filtration approach after semibatch emulsion polymerization. g–i) UV-vis diffuse reflectance spectra of all samples measured with an integrating sphere. The inset in (i) elucidates the measurement geometry.

two pure SEM measurements show a statistical mixture of all particle sizes and no segregation (Figure S17, Supporting Information), corroborating that this coloration must be attributed to coherent scattering of the isotropic assembly. We rationalize the difference via the degree of disorder, elucidated by the pair distribution function, $g(r)$ of the two types of colloidal glasses. Simple 2D simulations (Figure S18, Supporting Information) of both cases and subsequent $g(r)$ evaluation^[43] show that the binary mixture shows a pair correlation function limited to a set of distinct pairs: small–small, small–large, and large–large. No additional peaks can be observed in subsequent coordination spheres. In the gradient mixture, peaks in the $g(r)$ can be observed up to the 5th coordination sphere. Since phase correlation and constructive interference of scattered waves depend on the short-range order^[8] this results in a more pronounced peak in the reflectance spectrum.

Lastly, we compare the bilayer and the gradient sample (Figure 4i). The former represents the most extreme case of a stepwise gradient, while the latter is the fully continuous counterpart. In both cases, the sample is oriented, so that the smallest particles are on top. The reasoning behind this is that waves of shorter wavelengths (blue light) are affected more by diffuse scattering of the large particles. Small particles that show Mie resonance at these frequencies should, therefore, interact with the light first.^[26] The spectrum of the

bilayer shows two discrete peaks at the same wavelengths as the single-component reference samples. This proves that the diffuse reflectance measurements are sensitive to photons coherently scattered in lower regions of the sample. This is possible due to an increased ratio of single- and multiple scattering events caused by the short-range order and near-field effects.^[13] These observations also hold for the interpretation of the optical properties of the gradient photonic glass. Here, we see a plateau over the full region between the two peaks of the bilayer. Unlike in the bilayer, no local minima and maxima are observed. Instead, a uniform reflectance results over the visible range. We attribute this unique property to the gradual mesoscale structure of this material. In comparison, step-gradient samples prepared via deposition of discrete layers always show distinct peaks (Figure S19, Supporting Information). The gradient spectrum is in accordance with the local optical characterization, as the plateau of the diffuse reflectance spans the same wavelength range as the maxima of peaks measured along the cross section in Figure 3b. Additionally, the plateau and general shape closely resemble the reflectance spectrum obtained from a non carbon-coated cross section measured with a large spot size (Figure S13c, Supporting Information). This implies the applicability of such a gradient material as a broadband reflector in a wavelength range of choice. We confirmed this possibility by a separate CrEEP synthesis with an

extended size range from 220 nm up to 450 nm (Figure S20, Supporting Information). The gradient colloidal glass, consequently, covers a much broader spectral range compared to the system outlined here (Figure S21, Supporting Information). The critical role of the mesoscopic structure becomes apparent when directly comparing the gradient superstructure to the gradient mixture (Figure S22, Supporting Information). Self-assembly of a gradient particle dispersion mixture without an additional mesoscopic gradient does not show a plateau in the visible range. Furthermore, the diffuse reflectance of the gradient photonic glass is superior to the disordered case across the entire spectral range.

Enhanced scattering of visible light is of great importance in fields such as thin reflective coatings and passive cooling applications.^[44,45] Beside the use of high-*n* materials such as titania, recent studies have examined alternative approaches such as the variation of the particle morphology of low-*n* materials to improve the scattering performance.^[21,46] An alternative/complementary approach is our optimized mesostructure. The gradient colloidal glass provides a tuneable approach to enhanced broadband reflectance, opening an alternative approach to create the whitest white. The fabrication proceeds without any stacking faults or cracks that can arise during the much more complicated fabrication of multilayer inverse opals or (2+1) photonic crystals.^[15,25] Recent theoretical work has examined the passive cooling properties of gradient particulate assemblies.^[33] These simulations are corroborated by our observation that the gradient colloidal glass shows superior diffuse reflectance compared to the mixed case. Overall, gradient mesostructures are a highly attractive materials class from which novel applications in the field of wave–matter interaction, granular mechanics, and filtration can be expected. This interest will be further expedited by the fact that this type of gradient can conceivably be assembled using any type of particle that can be fabricated via seeded growth.

3. Conclusion

We have introduced a general method that makes use of a previously untapped feature of colloid synthesis. The time-dependent growth of colloidal particles is stored in a thin extraction tube prior to self-assembly. The self-assembly process retains the gradual dispersion composition and provides access to fully continuous mesoscopic gradients. Local optical and structural characterization corroborated the gradient mesostructure, and diffuse reflectance measurements showcased the unique broadband reflectivity. Our method will be of immediate relevance for a broad interdisciplinary community investigating and optimizing photonic glasses toward highly efficient scattering systems^[44,46] with potential applications in areas such as passive cooling.^[45,47] Considering the generality of our synthetic approach, we expect that a wide range of novel, functional materials with a gradient composition will become available that reach far beyond model polymeric particles. Perfecting the self-assembly process may lead to elusive chirped colloidal crystals,^[32,48] while infiltration can provide further insight as to the superior mechanical properties of composite and porous graded materials.^[49,50]

4. Experimental Section

Materials: Water used in this work was of Millipore quality. Methyl methacrylate (MMA 99%), sodium styrene sulfonate (NaSS, 99.99%) and potassium persulfate (KPS, 99.99%) were obtained from Sigma Aldrich.

Seed Particle Synthesis: A 100 mL three-necked flask equipped with a reflux condenser and septa was loaded with 48 mL water and degassed for 75 min under a constant nitrogen stream at 80 °C and 650 rpm stirring speed. With 5 min of equilibration time between each addition, the following reactants are added: 1) 2 mg NaSS in 1 mL water, 2) 1.7 mL MMA, 3) 40 mg KPS in 1 mL water. The reaction was then allowed to proceed for 30 min before the semibatch process was initiated.

Semibatch Growth and Extraction: The setup preparation proceeds before the seed synthesis is started, so no oxygen enters the system between seed synthesis and gradual growth. Silicone tube (2 m) with an inner diameter of 2 mm was attached to a syringe, and both were filled with water. The free end of the tube was inserted through a septum and dipped into the reaction mixture. The cannula used for the injection of air was bent and inserted into this end of the tube. Two processes were started simultaneously after the 30 min of seed synthesis: 1) Monomer feed was initiated, and 3.0 mL MMA was added at 3.0 mL h⁻¹. 2) Extraction was initiated, and 5.0 mL were drawn into the tube at 5.0 mL h⁻¹. Air fractions of 16 μL were pumped into the tube end every 30 s. This resulted in 5–6 drops of monomer being added during the time it took to extract one fraction. After 60 min, 110 fractions were stored in the tube with a gradually increasing size of polymer latex particles. For the extended size range, the reaction proceeds analogously while adding 6.0 mL MMA at 6.0 mL h⁻¹. The introduction of air-bubbles to fractionate the extracted particle dispersion improved the particle size monodispersity during the filtration process (compare Figure S4, Supporting Information). It eliminated a boundary layer at the tube solid–liquid interface with zero flow velocity and quenches the polymerization. In combination with the laminar flow inside the tube any turbulent mixing was effectively suppressed by this technique and the extracted size distribution was retained.

Semicontinuous Filtration Assembly: The setup used for the filtration mediated self-assembly can schematically be seen in Figure S6 (Supporting information). The tube, filled with all fractions and still connected to the syringe, was used directly after the synthesis. Dispersion droplets were slowly pumped into an intermediate vessel at 0.4 mL h⁻¹. Water was simultaneously added dropwise at 60 mL h⁻¹. During dilution, the dispersion was mixed, and upon reaching a total volume of 5 mL, the vessel was periodically emptied via a Pythagorean cup mechanism. The diluted dispersion was thereby transferred into a vacuum filtration setup, and particles were deposited on a hydrophilized poly(tetrafluoroethylene) (PTFE) filter (Omnipore) with a pore size of 200 nm. The timing was adjusted, so that the filter process was completed before the next emptying of the intermediate vessel. During this time, the assembly did not dry but remained an aqueous paste. After completion, the swollen particle film was transferred from the filter via pressing and adhesion to a poly(dimethylsiloxane) (PDMS) substrate from which it could be removed after drying.

Reference samples were prepared via filtration of diluted dispersions of the seed particles and/or the particle dispersion remaining in the reaction vessel after the termination of the semibatch process.

Drop-Casting: Rapid self-assembly of every 10th fraction was done by direct drop-casting of 2 μL dispersion onto a clean glass substrate preheated to 80 °C.

Dynamic Light Scattering: Diluted dispersions were measured with a Zetasizer (Malvern) with 175° backscattering geometry to obtain the hydrodynamic diameter and the size distribution of the latex particles.

Viscosimetry: The relative viscosity of two dispersions with small (224 nm) and large (304 nm) particles in water was determined with an Ubbelohde viscosimeter at 30 °C. An Ubbelohde capillary type 0c in combination with a visco-clock was used to determine the flow times, respectively. The relative viscosity of the dispersion was calculated by $\eta_{\text{Disp.}} = t(\eta_{\text{H}_2\text{O}}/t_{\text{H}_2\text{O}})$.

Carbon-Coating: A Leica EM ACE 600 coater with planetary stage and quartz crystal thickness measurement was used to deposit carbon nanolayers on the cross sections of samples with a sub-nanometer thickness accuracy.

Laser Scanning Confocal Microscopy: Both 2D color images, as well as 3D-reconstructed images, were obtained using a laser scanning confocal microscope (Olympus, OLS5000) with a white light source as well as a 405 nm laser, respectively. Cross sections were examined using a 50× lens with N.A. 0.95, and for the reconstruction, a pitch size of 0.12 μm was applied.

Scanning Electron Microscopy: Images were obtained with a Zeiss Leo 1530 (Carl Zeiss AG, Germany) at operating voltages of 1–3 kV and both in-lens as well as secondary-electron detection after sputtering of 2 nm of platinum.

Micro UV–vis Spectroscopy: UV–vis spectra of drop-cast suspensions were measured on an Olympus IX71 inverted microscope with a 4× lens (numerical aperture (NA) 0.10) in reflection geometry with a halogen light source. An OceanOptics USB4000 spectrometer was coupled via fiber optics.

The local measurements of the gradient cross section were conducted using a Zeiss Axio Imager Z2 light microscope with either a 20× lens (NA 0.5, EC Epiplan-NEOLFLUAR, Zeiss) or a 50× lens (NA 0.55, LD EC Epiplan-NEOFLUAR, Zeiss). Spectra were measured using an MCS CCD UV-NIR Spectrometer (Zeiss, Germany) coupled to the light microscope. The spot size was further adjusted using mechanical apertures in the optical path toward the detector. A silver mirror was used as reference.

Diffuse Reflectance Spectroscopy: Diffuse reflectance spectra were collected with a Cary 5000 UV–vis spectrometer (Agilent Technologies) in combination with an integrating sphere accessory (Labspheres). The samples were mounted at the reflectance port of the sphere after adhesion to a glass substrate with carbon adhesive tape. As a reference, a Spectralon diffuse white standard (Labspheres) was used.

2D Simulation of Particle Assemblies: 2D-rigid body physics of circles with different diameters falling into a rectangular basin were simulated using the Pymunk library in Python 3. Circles were initiated as dynamic bodies one after the other at a random x-position at the top of the plane. They experienced only downward directed gravitational force as well as rigid body interactions with other circles as well as the walls and floor of the basin. A total number of 4000 particles were simulated in each case in a basin measuring 1500 × 1000 units. The diameters were set to one of two specific integers (8 and 12) with a probability of 50% each for the binary case (Figure S18a,b, Supporting Information) and to random floating-point numbers between 8 and 12 for the mixed gradient case (Figure S18c,d, Supporting Information). The crystalline assembly was simulated by letting circles with a diameter of exactly 10 fall into the basin (Figure S18e,f, Supporting Information).

Supporting Information

Supporting Information is available from the Wiley Online Library or from the author.

Acknowledgements

N.V. acknowledges funding by the Deutsche Forschungsgemeinschaft (DFG, German Research Foundation) – Project-ID 416229255 – SFB 1411. M.S. and T.L. thank the Elite Network of Bavaria (ENB). The help from the Keylab Electron Microscopy is appreciated. This project has received funding from the European Research Council (ERC) under the European Union's Horizon 2020 research and innovation program (grant agreement no. #714968).

Open access funding enabled and organized by Projekt DEAL.

Conflict of Interest

The authors declare no conflict of interest.

Data Availability Statement

The data that support the findings of this study are available from the corresponding author upon reasonable request.

Keywords

colloidal self-assembly, gradient size distribution, light scattering, mesoscale gradients

Received: September 22, 2022

Revised: November 7, 2022

Published online:

- [1] J. D. Joannopoulos, P. R. Villeneuve, S. Fan, *Nature* **1997**, *386*, 143.
- [2] S. John, *Phys. Rev. Lett.* **1987**, *58*, 2486.
- [3] E. Ducrot, M. He, G. R. Yi, D. J. Pine, *Nat. Mater.* **2017**, *16*, 652.
- [4] J. H. Holtz, S. A. Asher, *Nature* **1997**, *389*, 829.
- [5] L. Maiwald, T. Sommer, M. S. Sidorenko, R. R. Yafyasov, M. E. Mustafa, M. Schulz, M. V. Rybin, M. Eich, A. Y. Petrov, *Adv. Opt. Mater.* **2021**, *10*, 2100785.
- [6] Z. Hayran, H. Kurt, K. Staliunas, *Sci. Rep.* **2017**, *7*, 3046.
- [7] Y. Takeoka, S. Yoshioka, A. Takano, S. Arai, K. Nueangnoraj, H. Nishihara, M. Teshima, Y. Ohtsuka, T. Seki, *Angew. Chem., Int. Ed.* **2013**, *52*, 7261.
- [8] E. S. A. Goerlitzer, R. N. Klupp Taylor, N. Vogel, *Adv. Mater.* **2018**, *30*, 1706654.
- [9] P. D. Garcia, R. Sapienza, A. Blanco, C. Lopez, *Adv. Mater.* **2007**, *19*, 2597.
- [10] P. D. Garcia, R. Sapienza, C. Lopez, *Adv. Mater.* **2010**, *22*, 12.
- [11] K. Ueno, A. Inaba, Y. Sano, M. Kondoh, M. Watanabe, *Chem. Commun.* **2009**, *24*, 3603.
- [12] J. F. Galisteo-Lopez, M. Ibisate, R. Sapienza, L. S. Froufe-Perez, A. Blanco, C. Lopez, *Adv. Mater.* **2011**, *23*, 30.
- [13] S. F. Liew, J. Forster, H. Noh, C. F. Schreck, V. Saranathan, X. Lu, L. Yang, R. O. Prum, C. S. O'Hern, E. R. Dufresne, H. Cao, *Opt. Express* **2011**, *19*, 8208.
- [14] M. Harun-Ur-Rashid, A. Bin Imran, T. Seki, M. Ishii, H. Nakamura, Y. Takeoka, *ChemPhysChem* **2010**, *11*, 579.
- [15] P. N. Dyachenko, J. J. do Rosário, E. W. Leib, A. Y. Petrov, R. Kubrin, G. A. Schneider, H. Weller, T. Vossmeier, M. Eich, *ACS Photonics* **2014**, *1*, 1127.
- [16] G. Shang, Y. Häntsch, K. P. Furlan, R. Janßen, G. A. Schneider, A. Petrov, M. Eich, *APL Photonics* **2019**, *4*, 046101.
- [17] M. Retsch, M. Schmelzeisen, H. J. Butt, E. L. Thomas, *Nano Lett.* **2011**, *11*, 1389.
- [18] S. Yu, C.-W. Qiu, Y. Chong, S. Torquato, N. Park, *Nat. Rev. Mater.* **2020**, *6*, 226.
- [19] V. Hwang, A. B. Stephenson, S. Barkley, S. Brandt, M. Xiao, J. Aizenberg, V. N. Manoharan, *Proc. Natl. Acad. Sci. USA* **2021**, *118*, 2015551118.
- [20] H. Yang, G. Jacucci, L. Schertel, S. Vignolini, *ACS Nano* **2022**, *16*, 7373.
- [21] G. Jacucci, B. W. Longbottom, C. C. Parkins, S. A. F. Bon, S. Vignolini, *J. Mater. Chem. C* **2021**, *9*, 2695.
- [22] N. Vogel, M. Retsch, C.-A. Fustin, A. del Campo, U. Jonas, *Chem. Rev.* **2015**, *115*, 6265.
- [23] L. Zhang, J. Wang, S. Tao, C. Geng, Q. Yan, *Adv. Opt. Mater.* **2018**, *6*, 1701344.
- [24] Y. Shen, D. Ye, I. Celanovic, S. G. Johnson, J. D. Joannopoulos, M. Soljačić, *Science* **2014**, *343*, 1499.

- [25] L. Zhang, Z. Xiong, L. Shan, L. Zheng, T. Wei, Q. Yan, *Small* **2015**, *11*, 4910.
- [26] R. Kubrin, R. M. Pasquarelli, M. Waleczek, H. S. Lee, R. Zierold, J. J. do Rosario, P. N. Dyachenko, J. M. Montero Moreno, A. Y. Petrov, R. Janssen, M. Eich, K. Nielsch, G. A. Schneider, *ACS Appl. Mater. Interfaces* **2016**, *8*, 10466.
- [27] M. Chen, H. Colfen, S. Polarz, *ACS Nano* **2015**, *9*, 6944.
- [28] J. Bahner, N. Klinkenberg, M. Frisch, L. Brauchle, S. Polarz, *Adv. Funct. Mater.* **2019**, *29*, 44.
- [29] H. Ding, C. Liu, B. Ye, F. Fu, H. Wang, Y. Zhao, Z. Gu, *ACS Appl. Mater. Interfaces* **2016**, *8*, 6796.
- [30] S. H. Kim, W. C. Jeong, H. Hwang, S. M. Yang, *Angew. Chem., Int. Ed.* **2011**, *50*, 11649.
- [31] M. Schöttle, T. Tran, T. Feller, M. Retsch, *Adv. Mater.* **2021**, *33*, 2101948.
- [32] J. S. Skibina, R. Iliew, J. Bethge, M. Bock, D. Fischer, V. I. Beloglasov, R. Wedell, G. Steinmeyer, *Nat. Photonics* **2008**, *2*, 679.
- [33] Y. Fu, Y. An, Y. Xu, J. Dai, D. Lei, *EcoMat* **2022**, *4*, e12169.
- [34] N. Vaidya, O. Solgaard, *Microsyst. Nanoeng.* **2022**, *8*, 69.
- [35] F. A. Nutz, M. Retsch, *Sci. Adv.* **2017**, *3*, eaao5238.
- [36] J. W. Goodwin, J. Hearn, C. C. Ho, R. H. Ottewill, *Colloid Polym. Sci.* **1974**, *252*, 464.
- [37] J. Q. Li, R. Salovey, *J. Polym. Sci., Part A: Polym. Chem.* **2000**, *38*, 3181.
- [38] F. J. Schork, W. H. Ray, *J. Appl. Polym. Sci.* **1987**, *34*, 1259.
- [39] L. R. P. Areias, I. Mariz, E. Macoas, J. P. S. Farinha, *ACS Nano* **2021**, *15*, 11779.
- [40] Y. Takeoka, M. Iwata, T. Seki, K. Nueangnoraj, H. Nishihara, S. Yoshioka, *Langmuir* **2018**, *34*, 4282.
- [41] J. G. Park, S. H. Kim, S. Magkiriadou, T. M. Choi, Y. S. Kim, V. N. Manoharan, *Angew. Chem., Int. Ed.* **2014**, *53*, 2899.
- [42] C. F. Bohren, D. R. Huffman, *Absorption and Scattering of Light by Small Particles*, John Wiley & Sons, New York, USA **1998**.
- [43] B. A. F. Kopera, M. Retsch, *Anal. Chem.* **2018**, *90*, 13909.
- [44] B. D. Wilts, X. Sheng, M. Holler, A. Diaz, M. Guizar-Sicairos, J. Raabe, R. Hoppe, S. H. Liu, R. Langford, O. D. Onelli, D. Chen, S. Torquato, U. Steiner, C. G. Schroer, S. Vignolini, A. Sepe, *Adv. Mater.* **2018**, *30*, 1702057.
- [45] Q. Zhang, S. Wang, X. Wang, Y. Jiang, J. Li, W. Xu, B. Zhu, J. Zhu, *Small Methods* **2022**, *6*, e2101379.
- [46] M. S. Toivonen, O. D. Onelli, G. Jacucci, V. Lovikka, O. J. Rojas, O. Ikkala, S. Vignolini, *Adv. Mater.* **2018**, *30*, 1704050.
- [47] T. Wang, Y. Wu, L. Shi, X. Hu, M. Chen, L. Wu, *Nat. Commun.* **2021**, *12*, 365.
- [48] B. Gates, Y. Xia, *Adv. Mater.* **2000**, *12*, 1329.
- [49] C. Zhu, J. Qiu, S. Pongkitwitoon, S. Thomopoulos, Y. Xia, *Adv. Mater.* **2018**, *30*, 1706706.
- [50] U. G. Wegst, H. Bai, E. Saiz, A. P. Tomsia, R. O. Ritchie, *Nat. Mater.* **2015**, *14*, 23.

ADVANCED MATERIALS

Supporting Information

for *Adv. Mater.*, DOI: 10.1002/adma.202208745

A Continuous Gradient Colloidal Glass

*Marius Schöttle, Tobias Lauster, Lukas J. Roemling,
Nicolas Vogel, and Markus Retsch**

A continuous gradient colloidal glass (Supporting information)

Marius Schöttle Tobias Lauster Lukas J. Roemling Nicolas Vogel Markus Retsch*

Marius Schöttle, Tobias Lauster, Markus Retsch
Department of Chemistry, University of Bayreuth, Universitätsstr. 30, 95447 Bayreuth, Germany
Email Address: markus.retsch@uni-bayreuth.de

Lukas J. Roemling, Nicolas Vogel
Institute of Particle Technology, Friedrich-Alexander University Erlangen-Nürnberg, 91058 Erlangen, Germany

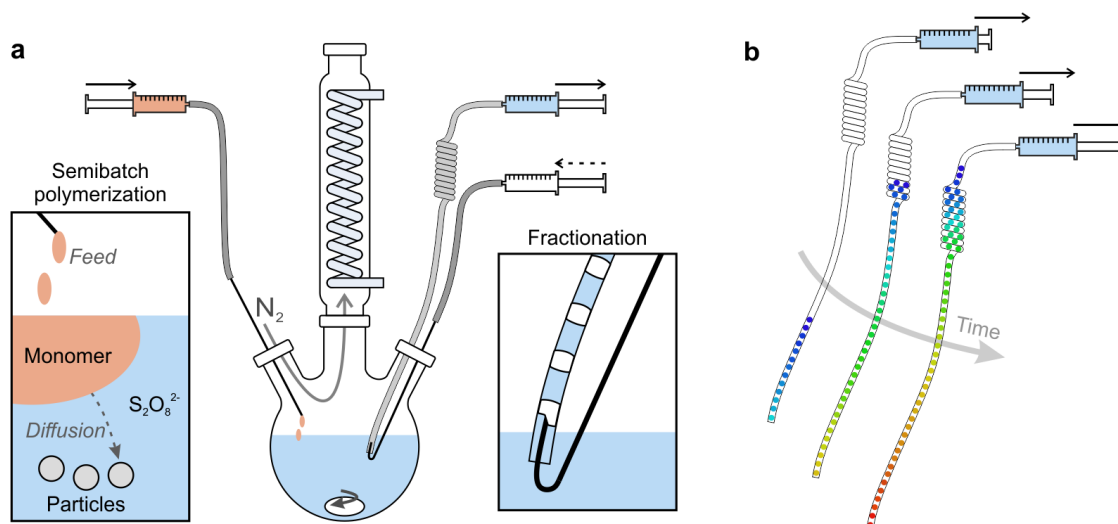


Figure S1: a) Reactor used for the controlled emulsion extraction process (CrEEP). Gradual addition of monomer (orange) to the seed particle suspension (blue) causes continuous diffusion of monomer to the growing particles. Simultaneous extraction, accompanied by fractionation via air bubble separation (white), retains the time-dependent increase of the particle diameter. Arrows indicate extraction and (periodic) infusion, respectively. b) Schematic showing the direction in which the growing particles are extracted. Blue fractions represent the smallest particles, red fractions the largest. During the assembly process, fractions are pushed out of the tube in the opposite direction.

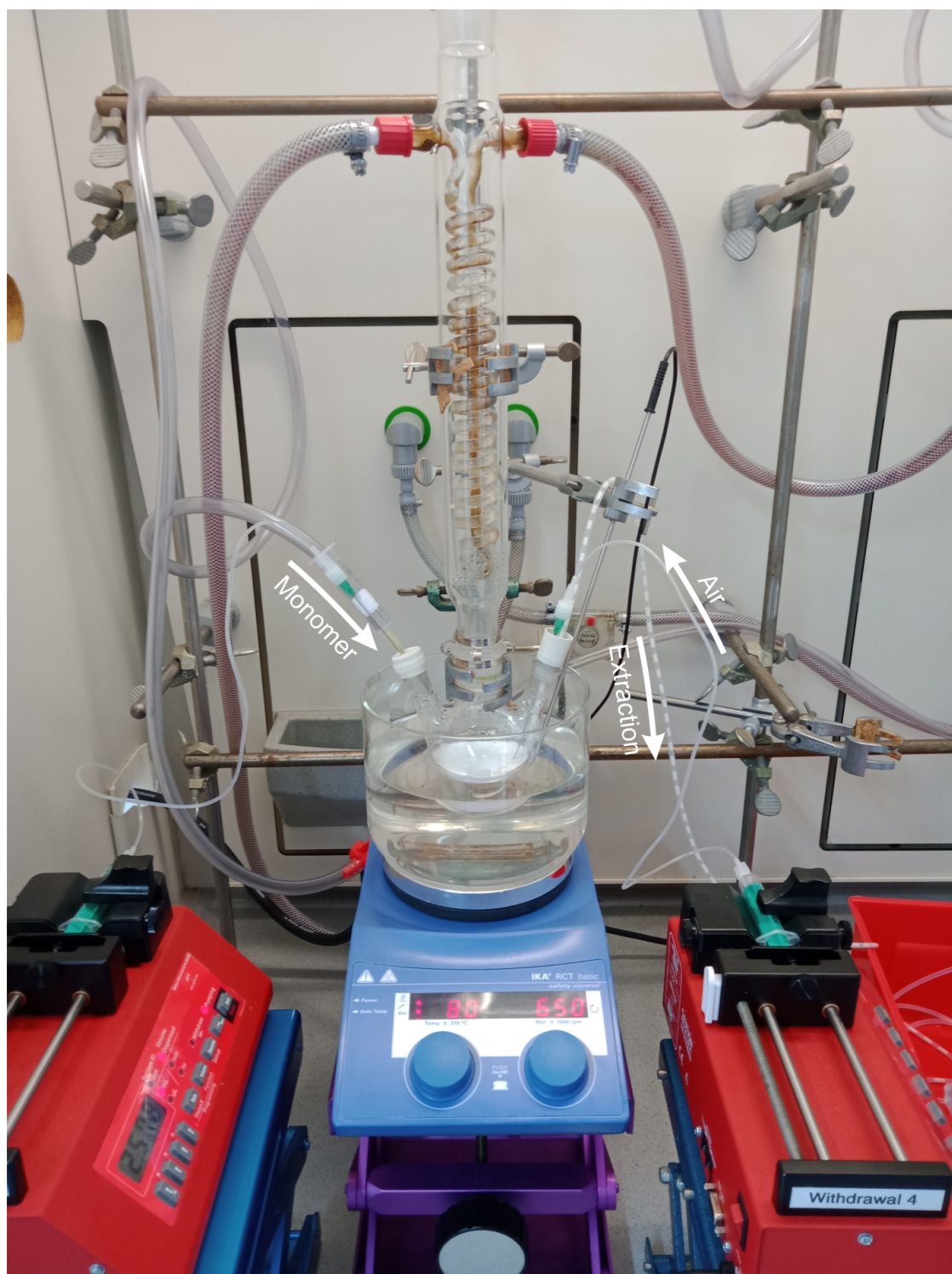


Figure S2: Photograph of the CrEEP setup during the synthesis. Infusion and withdrawal points are identical to Fig. S1. Inert gas flow and monomer feed proceed through the left joint, whereas extraction and the periodic airflow needed for fractionation can be seen on the right. The total volume in the reactor is significantly larger than the extracted volume. Thereby, a near-constant addition rate with respect to the concentration of particles is ensured.

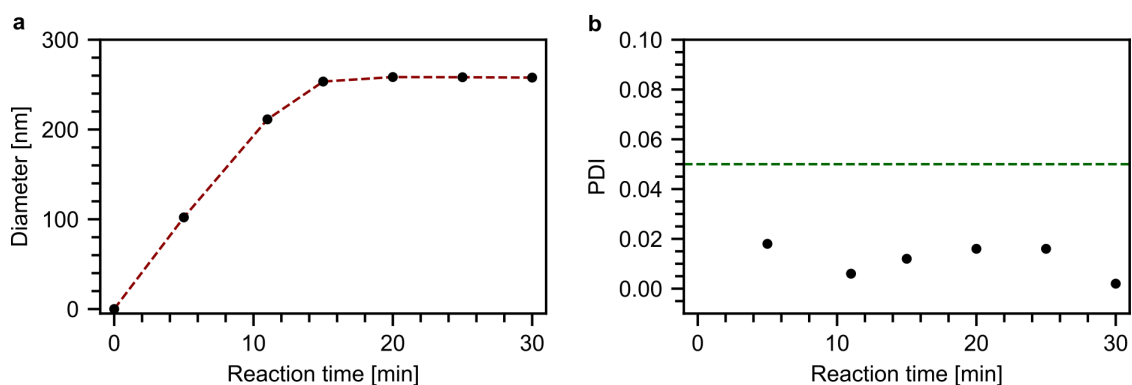


Figure S3: Evaluation of the kinetics of the particle growth during the surfactant-free emulsion polymerization to produce the seed particles. Here: 1.7 mL MMA are added at once and left to react. Samples are withdrawn every 5 minutes and examined via DLS to determine the growing particle diameter (a) and the polydispersity (b). Two important mechanistic insights can be obtained thereby: 1) Already at low conversions, the growing particles are shown to have a polydispersity index below 0.02 and can be considered monodisperse. 2) The reaction rate is fast compared to the gradual monomer addition. A volume of 1.7 mL monomer reacts in a matter of approx. 15 minutes, giving a reaction rate of 0.1 mL/min. During the 30 s it takes to extract one fraction, 25 μ L of monomer are added to the system (approx. 5-6 drops) which gives an addition rate of 0.05 mL/min. Since the monomer-addition rate is much smaller than the reaction rate we can assume monomer-starved conditions. The benefit of this starved-feed procedure is that the extracted dispersion possesses a high conversion and low polydispersity. Consequently, it can be used for self-assembly without any purification steps. The presence of any unreacted monomer would soften the latex beads leading to a film formation, which we don't observe. Overall, the CrEEP process can be considered robust and applicable for emulsion polymerizations as long as the extraction rate is lower than the reaction rate.

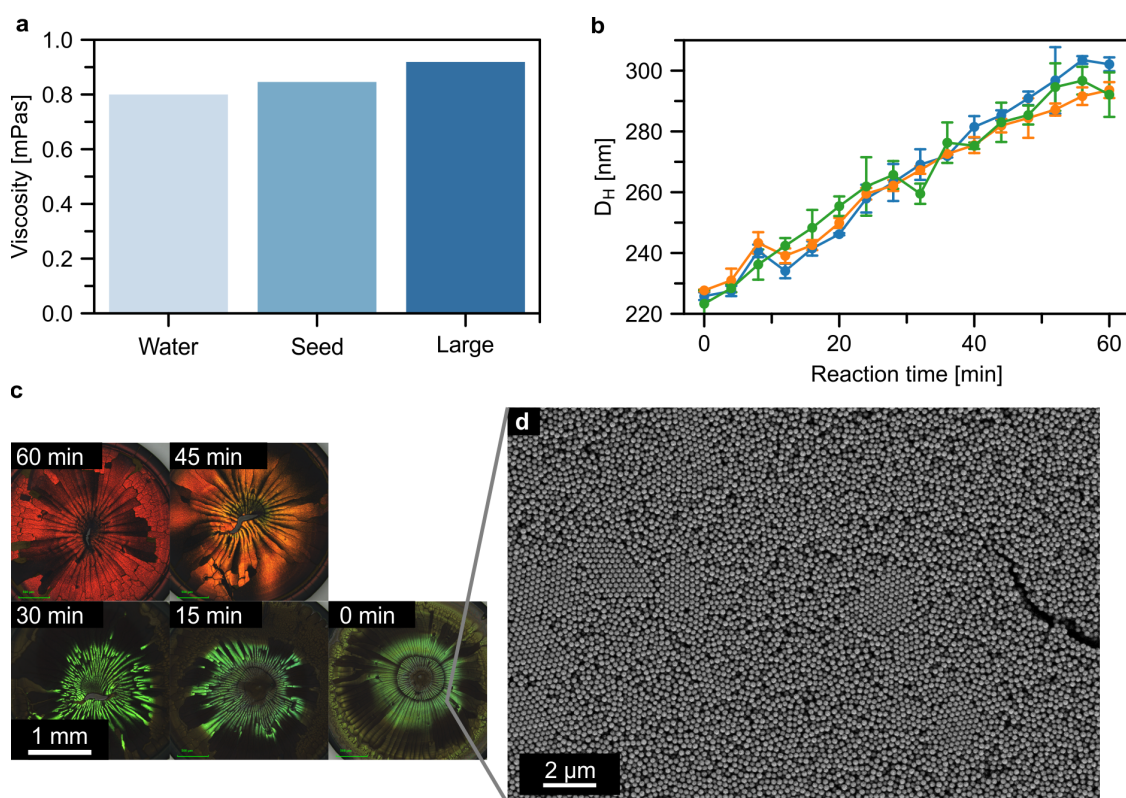


Figure S4: a) Results of viscosity measurements using an Ubbelohde viscometer. Measurements of the seed particle suspension, as well as the reaction mixture after CrEEP, show a slight increase in viscosity with a rising volume percentage of latex particles. These measurements allowed approximate calculation of the Reynolds number in the tube during extraction using a density of 10^3 kg/m^3 , a flow rate of $6 \cdot 10^{-3} \text{ m/s}$ and an inner diameter of $2 \cdot 10^{-3} \text{ m}$. The Reynolds numbers lie in the range of 1-5, which indicates laminar flow. It could, therefore, in principle, be possible to omit the fractionation and simply rely on the absence of turbulence. b) Results of DLS measurements of three identical CrEEP syntheses without air-fractionation. This shows both the pronounced reproducibility as well as the possibility of making use of the low Reynolds number system instead of fractionation to minimize mixing. In principle, the time-dependent increase in size can thereby still be translated into a positional dependency due to the laminar flow during extraction. c) Light microscopy images of drop-cast particle assemblies. For larger particles (30 - 60 minutes), the assembly into colloidal crystals seems adequate, but smaller particles do not show the characteristic blue color that can be seen with fractionation. As exhibited in the SEM image in d), small crystalline domains exist but the greater part of the structure is disordered. We attribute this to a near-zero flow rate at the tube walls, which causes mixing of large and small particles. As the assembly is known to be highly dependent on polydispersity, we, therefore, apply the fractionation approach in all further experiments to minimize the mixing of particles with different diameters.

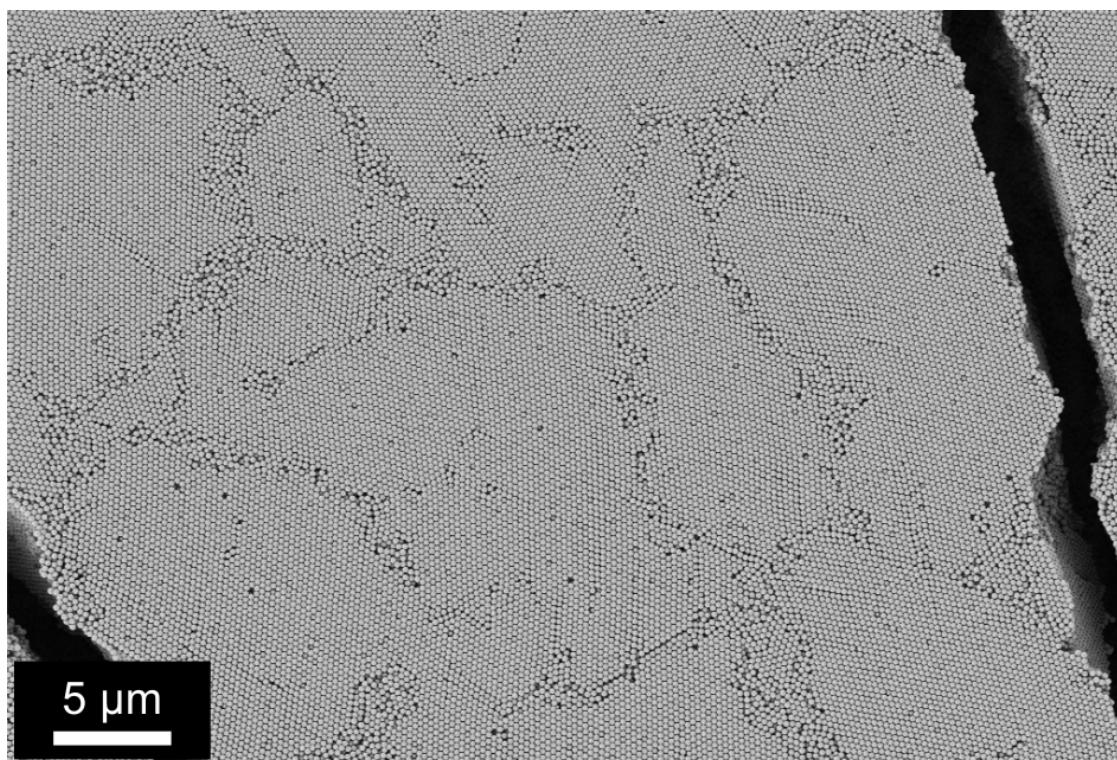


Figure S5: Overview SEM-image of the yellow sample shown in Figure 1h. The crystalline nature of the assembly proves the low polydispersity of each fraction.

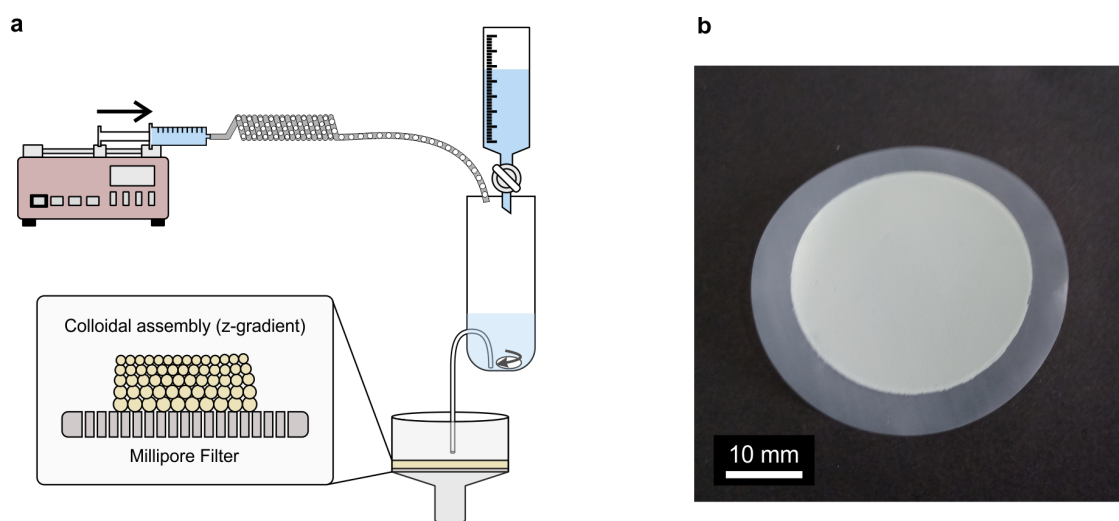


Figure S6: a) Schematic of the setup used for the semi-continuous filtration assembly of the 3D gradient structure. The fractionated suspension is added slowly and discretely into an intermediate container equipped with a stirrer bar. Here, the suspension is diluted with MilliQ water. The container is periodically emptied via a Pythagorean cup mechanism, and the diluted suspension is transferred into a filtration setup allowing a particle assembly to be formed. Due to the gradually decreasing diameters of the particles in the tube, this results in a size gradient in the z-direction. b) A photograph of the assembly after the last fraction was added.

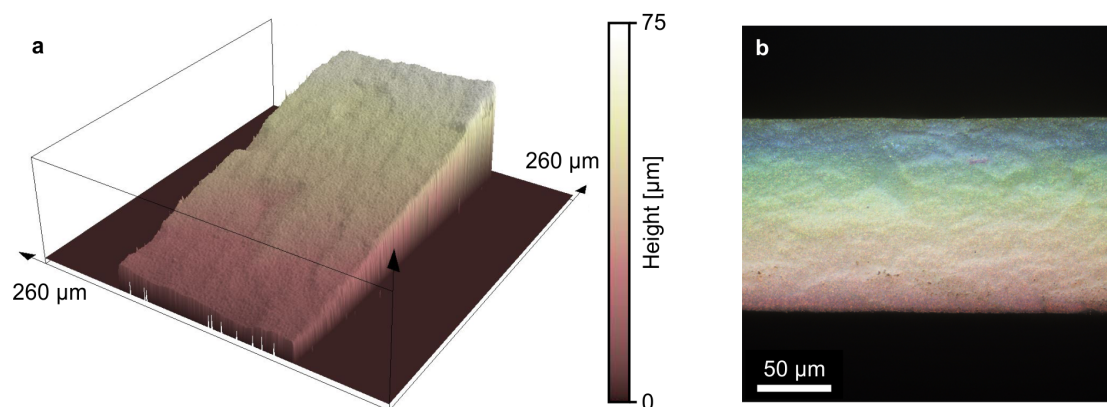


Figure S7: Microscopy images of a cross-section of a gradient colloidal glass that has been coated with 10 nm of carbon to reduce the effect of diffuse light scattering a) Height image obtained via laser scanning confocal microscopy b) The resulting image obtained from light microscopy at various focal positions after correlation with the height image.

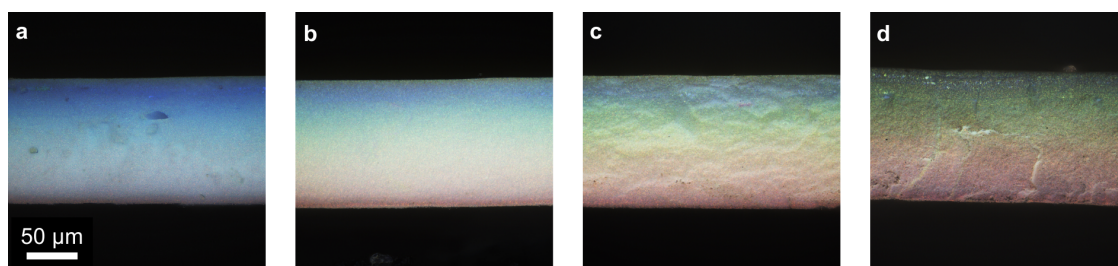


Figure S8: Cross-sections of gradient colloidal glasses coated with 0, 5, 10, and 20 nm carbon (a-d, respectively).

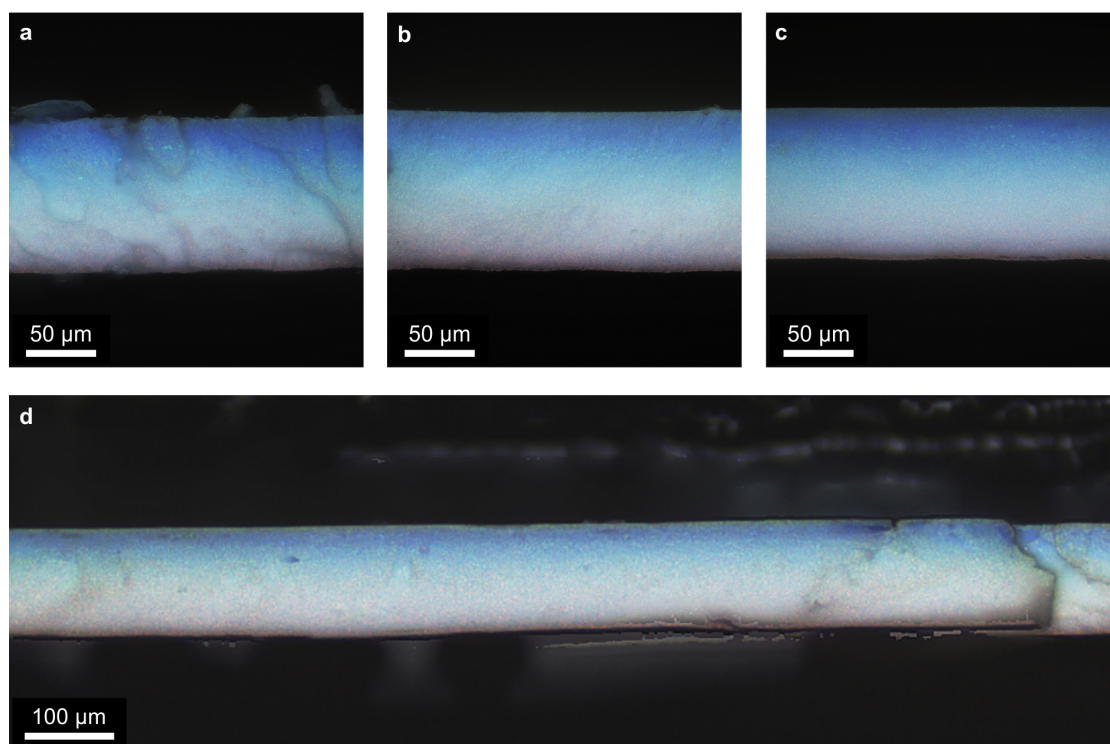


Figure S9: Microscopy images of cross-sections taken from different parts of the sample. These have not been carbon-coated prior to the measurement. This highlights the in-plane homogeneity of the gradual size distribution in the entire sample.

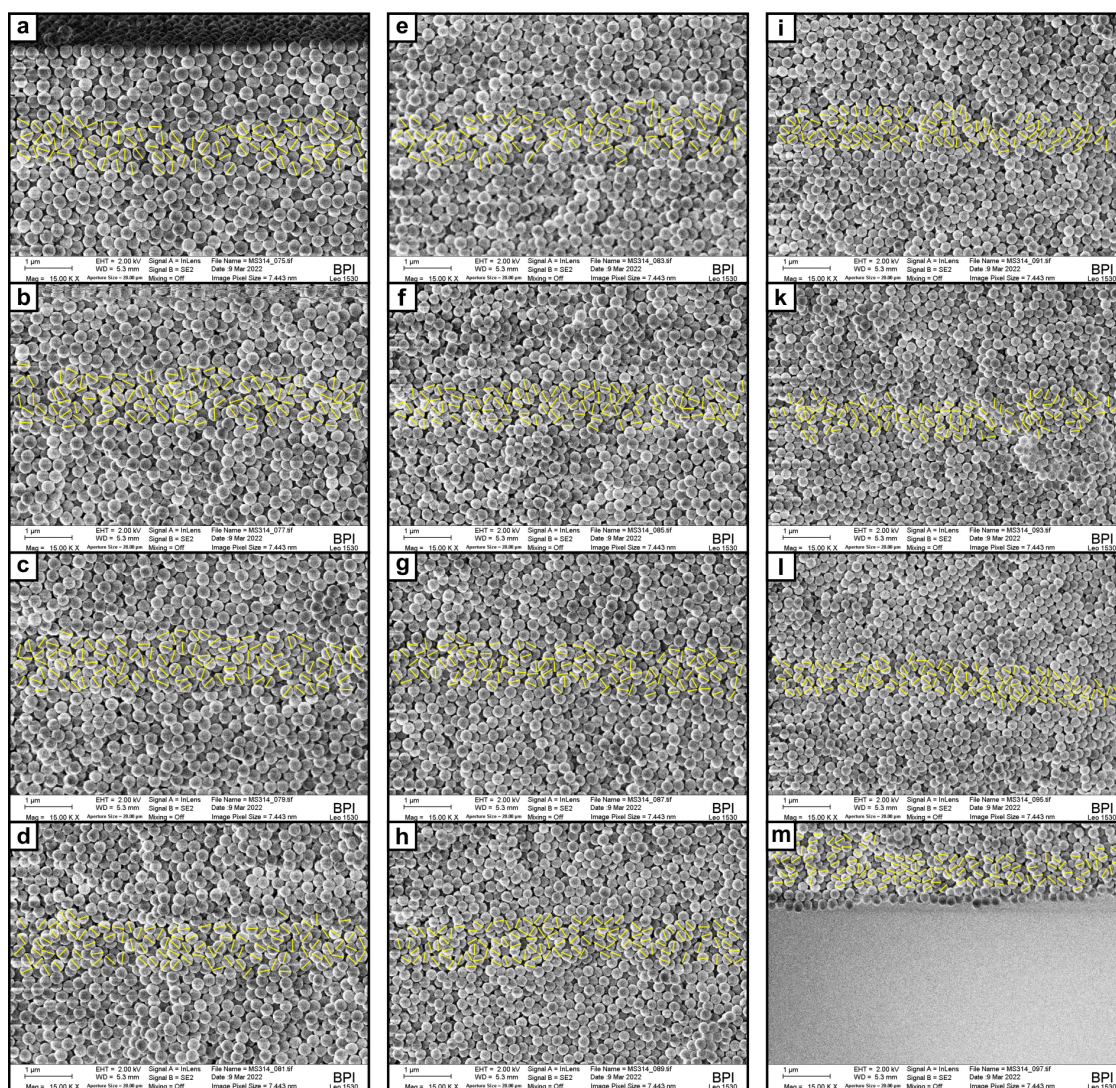


Figure S10: SEM images obtained at equidistant positions along the z-direction of a gradient colloidal glass. The yellow lines show the manual determination of the particle diameter of all evaluated particles. The examined regions are approximately 1 μm wide and 10 μm apart from each other.

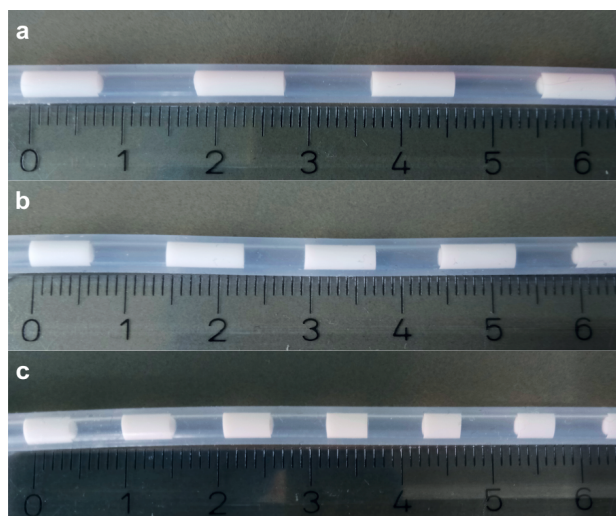


Figure S11: Comparison of the size of fractions in the beginning (a), after 30 minutes (b), and towards the end (c) of the CrEEP synthesis. The gradual decrease of the size of the fractions is an effect of the low gas barrier of the silicone tube. The extraction process is sufficiently slow for the diffusion of air from the outside of the tube into the preformed gas separators to play a role. As the reaction proceeds and the amount of these gas fractions increases, this effect becomes more pronounced, and the effective extraction speed gradually decreases. This counteracts the increase in volume percentage of latex particles during monomer feed and plays an important role in ensuring a linear gradient in later 3D self-assembly. Whereas the particle size increases from top to bottom, the optical impression of the dispersion remains white for all fractions, which is caused by multiple light scattering. The structural colors only evolve during the self-assembly process and are shown in Figure 1d and e in the main manuscript.

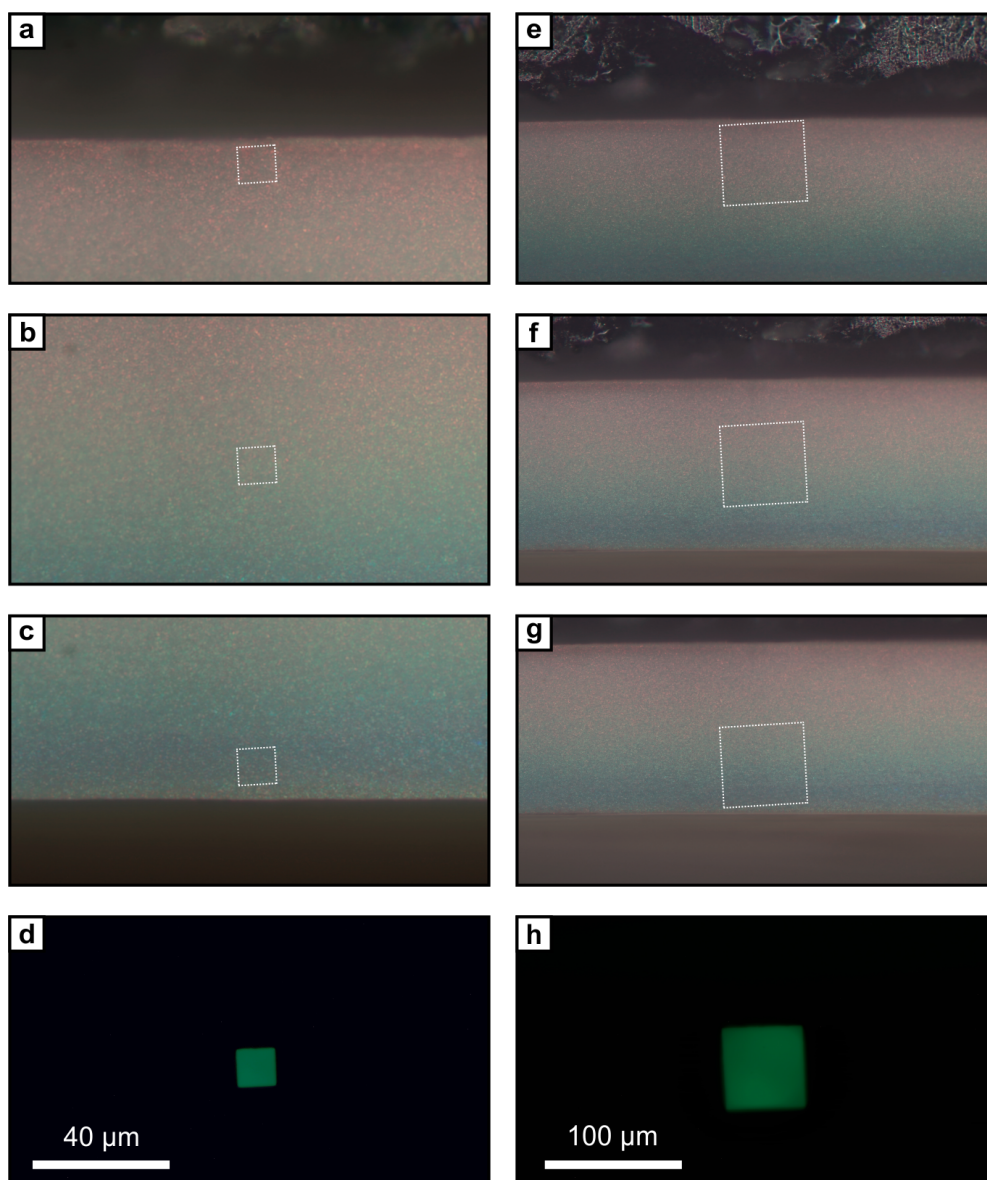


Figure S12: a)-c) Selection of microscopy images taken during microspectroscopy with a 50x-magnification objective. The white box is an overlay of the actual spot size as shown in d). The latter is determined by shining a green LED through the optical path leading to the spectrometer. e)-f) Microscopy images with overlay and g) spot-size corresponding to microspectroscopy using a 20x-magnification objective.

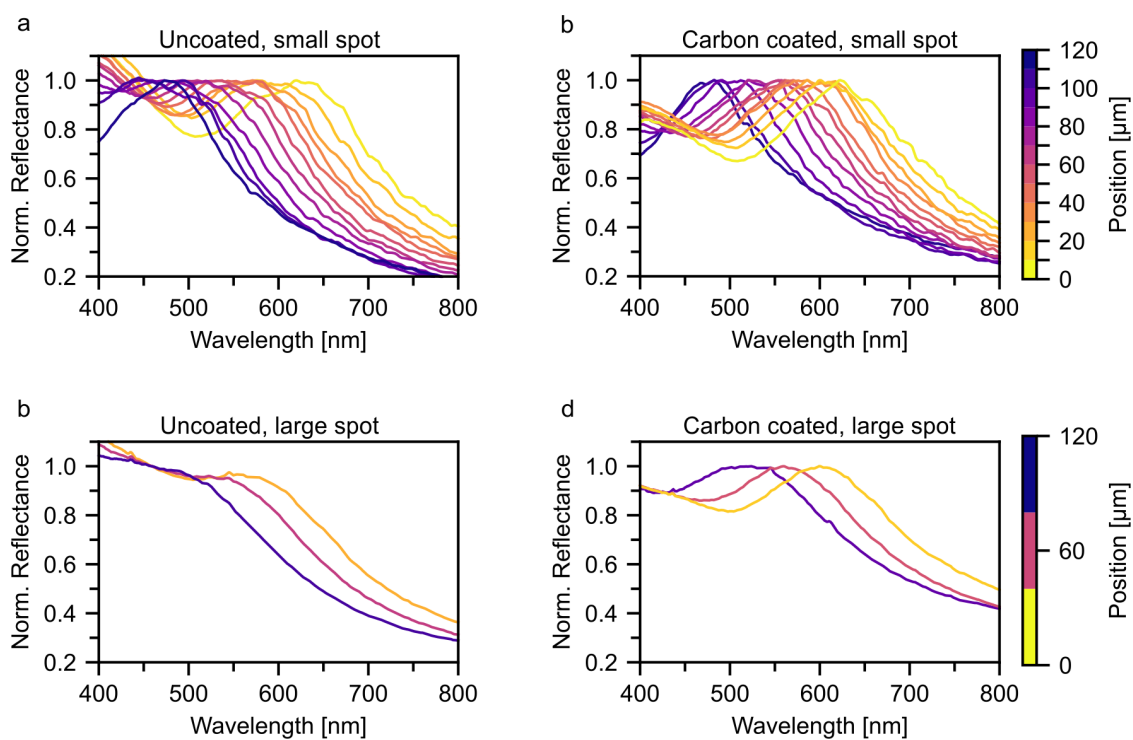


Figure S13: a), b) Spectra taken using the small spot-size at equidistant positions along cross-sections of gradient colloidal glasses without and with 5 nm carbon coating, respectively. c), d) Spectra taken using the large spot-size at equidistant positions along cross-sections of gradient colloidal glasses without and with 5 nm carbon coating, respectively.

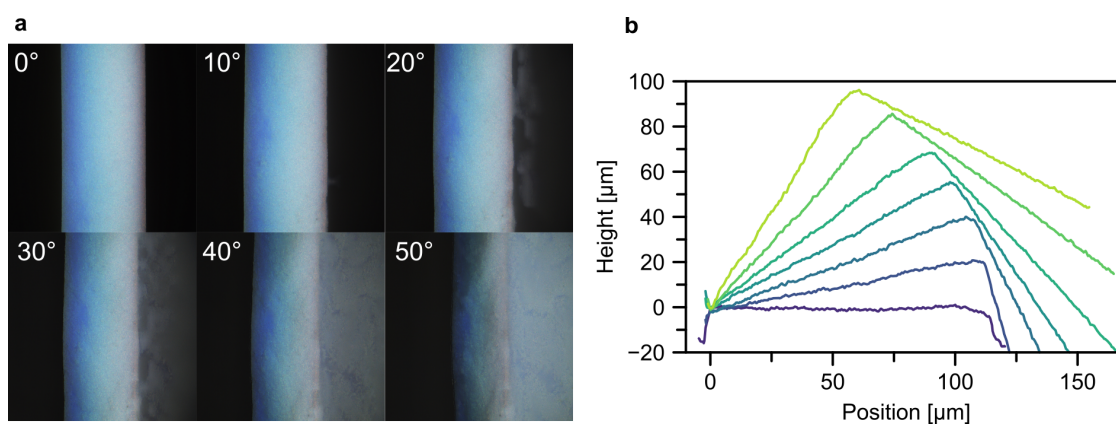


Figure S14: a) Light microscopy images of a cross-section tilted at angles between 0-50°. The range of colors observed in the gradient does not change with the viewing angle. b) Height profiles corresponding to the images in a) showing how the tilt-angle was determined from the LSCM evaluation.

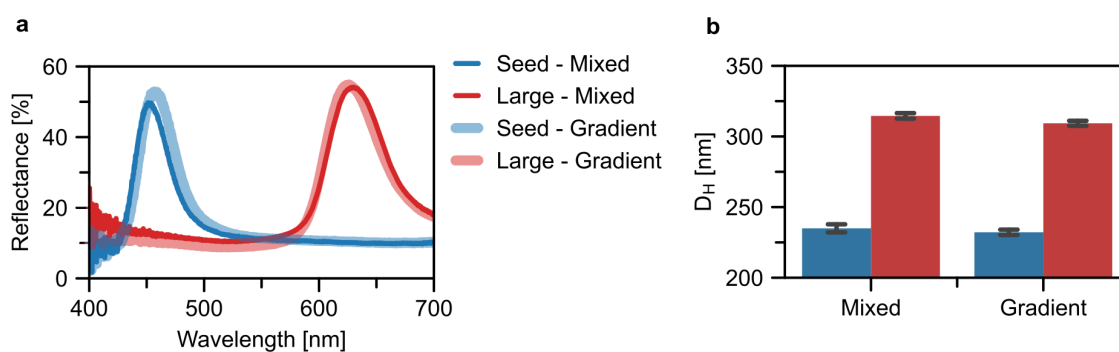


Figure S15: Comparison of the first fraction (seed particles, blue) and last fraction (large particles, red) of the two CrEEP syntheses used for the fabrication of the gradient colloidal glass and the mixed structure, respectively. a) UV-Vis microspectra of drop-cast suspensions. b) DLS results showing the hydrodynamic diameter of the dispersed particles.

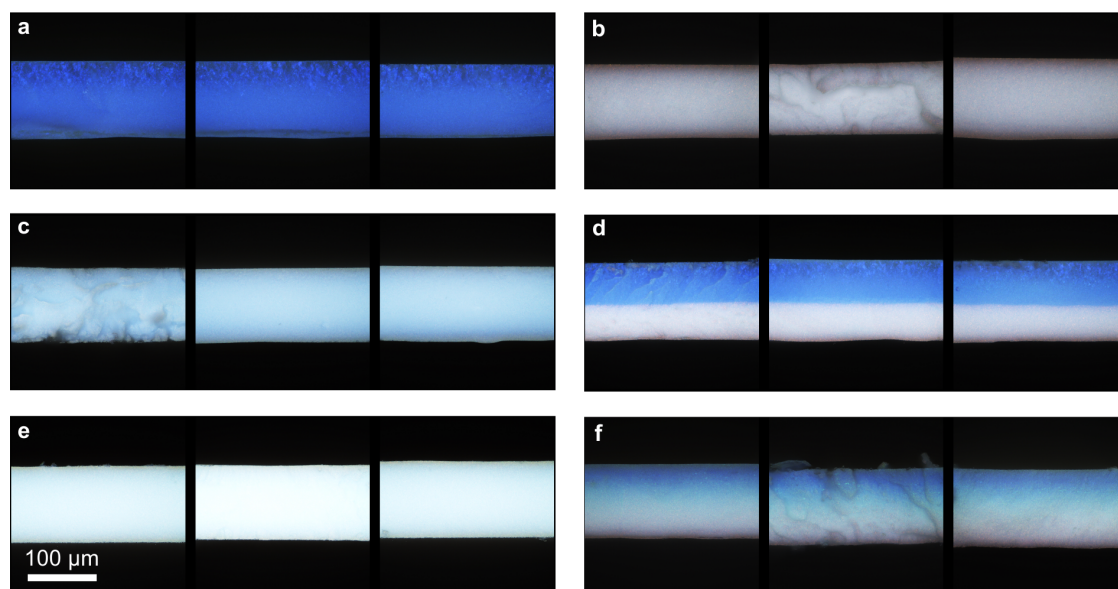


Figure S16: LSCM images of cross-sections of all samples prepared via filtration. Three different cross-sections of each sample are examined and verify that the thickness of all samples is comparable. a) small particles, b) large particles, c) binary mixture, d) bilayer, e) gradient mixture, and f) gradient colloidal glass.

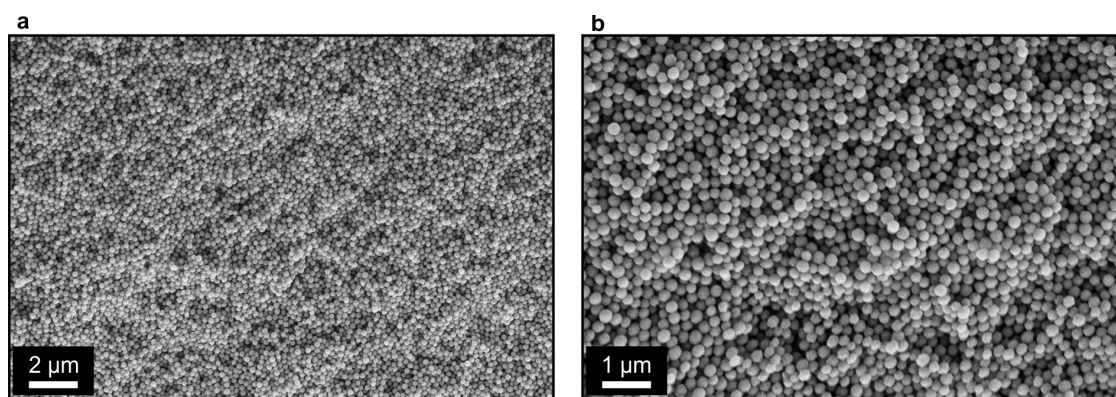


Figure S17: SEM images of the sample prepared via filtration after mixing of all fractions obtained CrEEP synthesis.

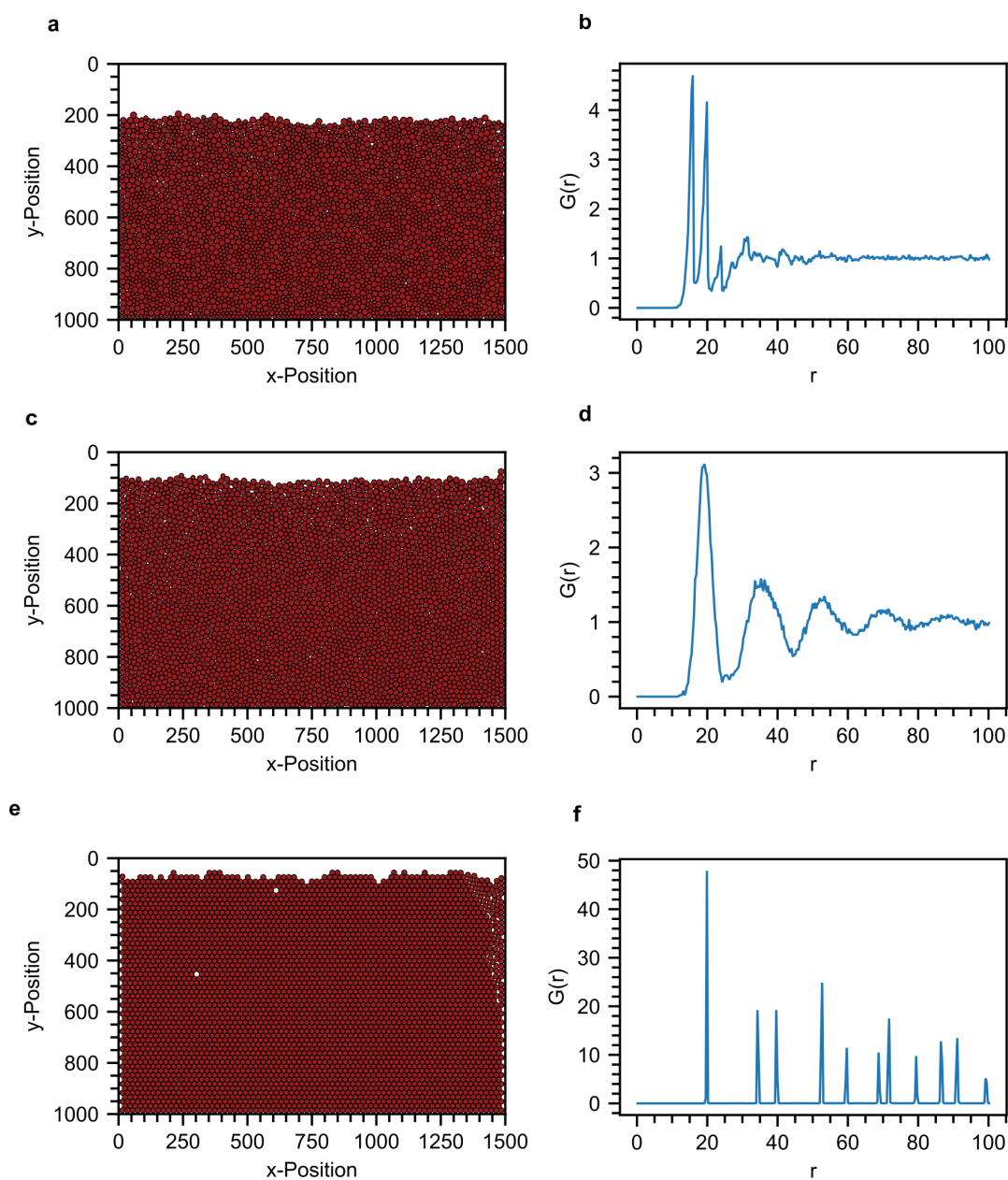


Figure S18: a) 2D rigid body simulation of two types of circles with different diameters falling into a rectangular basin. Diameters are set to exactly 8 or 12 units, respectively, and the total number of each type of circle is the same. b) Radial distribution function ($G(r)$) of the circles after simulation. c) and d) Analogous simulation and $G(r)$ -evaluation of particles with diameters set to arbitrary floating point numbers between 8 and 12 units. e), f) Simulation and $G(r)$ -evaluation of monodisperse circles with a diameter of exactly 10 units resulting in an ordered hexagonal array.

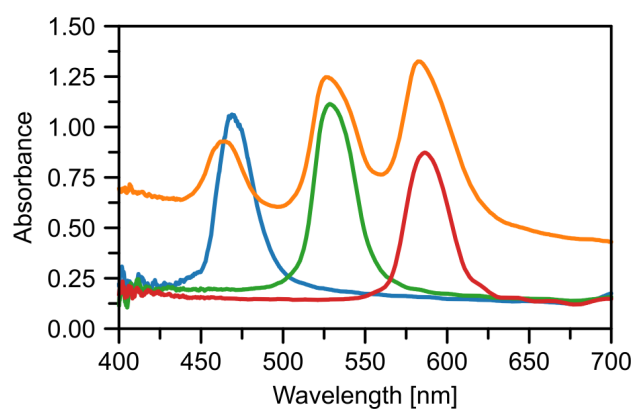


Figure S19: Transmission UV-Vis microspectroscopy of dip-coated colloidal crystals. The blue, green, and red plots correspond to colloidal crystals comprising particles of three different sizes. The orange curve shows the spectrum of a trilayer sample where these three particle types were dip-coated one after the other.

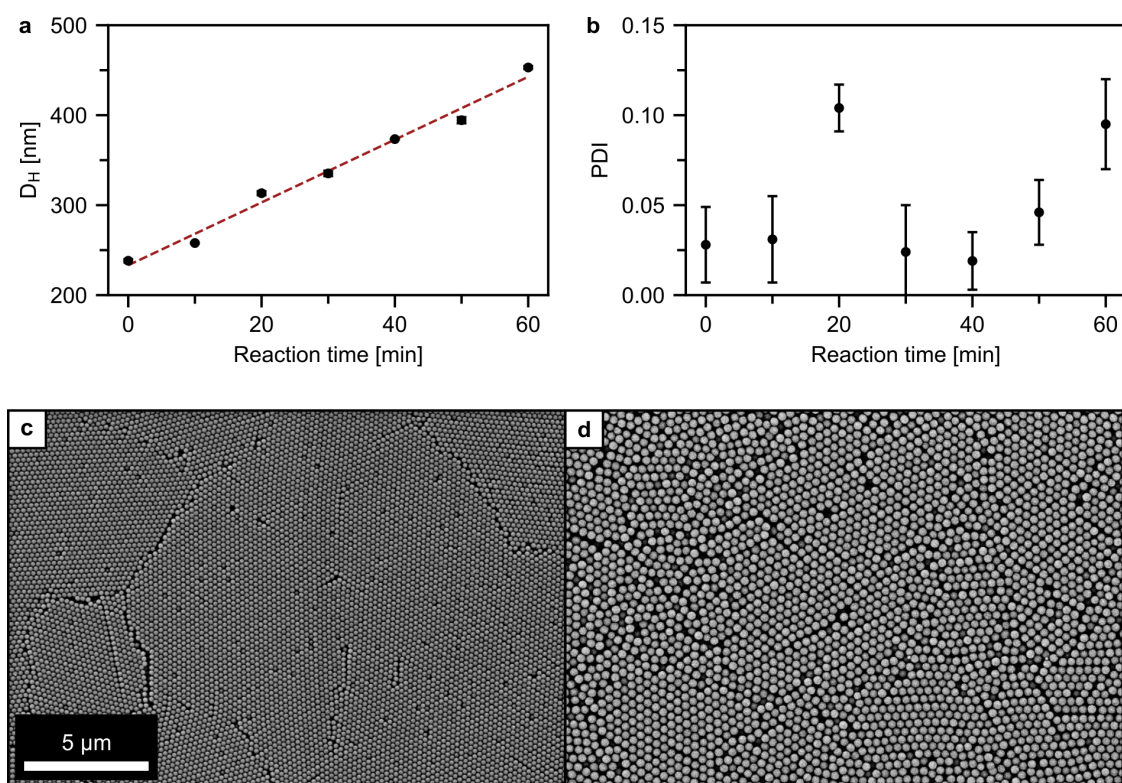


Figure S20: Characterization of a semibatch synthesis with an extended size range. a), b) DLS evaluation of equidistant, monodisperse fractions, showing the linear increase in size and a larger range up to 450 nm. For comparison: the maximum diameter in the synthesis shown in Fig. 1 is 320 nm c), d) SEM images of drop-cast colloidal crystals originating from the first and last fraction, respectively.

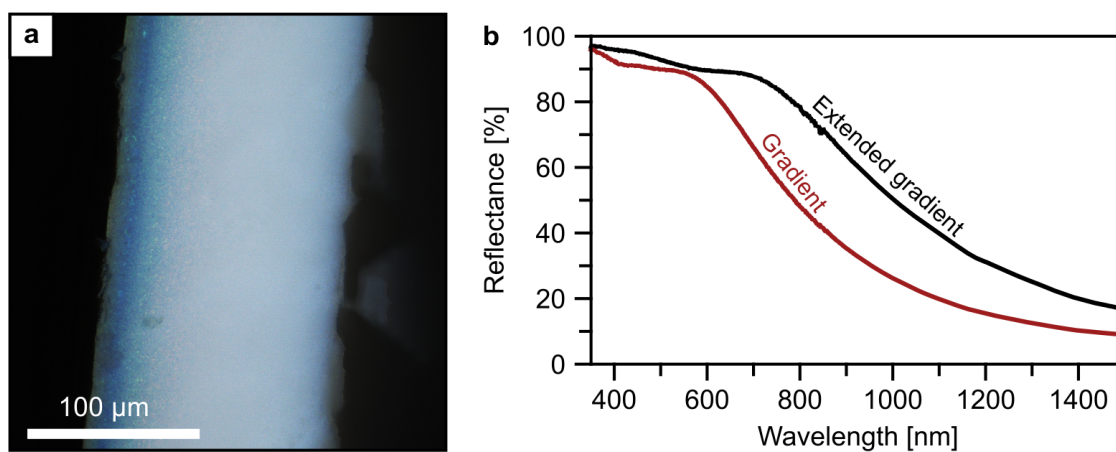


Figure S21: Characterization of the gradient colloidal glass obtained from the synthesis with an extended size range. a) Cross-section image obtained via LSCM of the gradient colloidal glass. The color gradient from blue to red can be observed in the top half of the gradient, whereas the bottom part appears white due to coherent scattering at wavelengths outside the visible region. b) Diffuse reflectance UV-Vis measurements of the extended gradient structure as well as the gradient shown in Fig. 4i. As was targeted, the plateau of the extended gradient covers a greater spectral bandwidth. This result is reminiscent of the red-shift of the step in local UV-Vis spectra obtained with a large spot size shown in Fig. S13c.

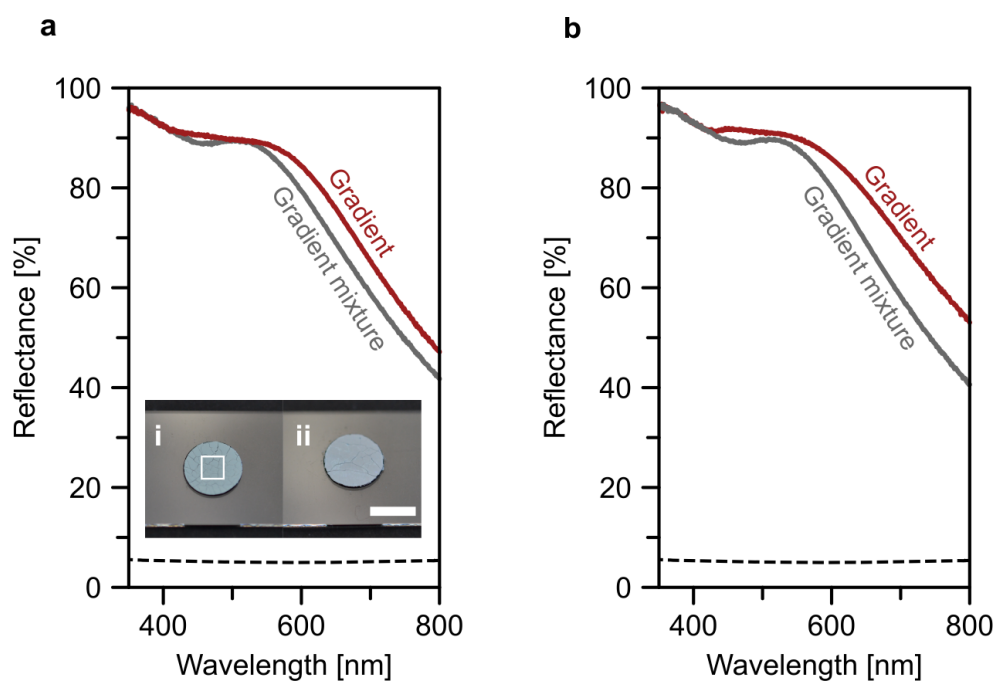


Figure S22: Diffuse reflectance measurements of gradient colloidal glasses as well as the mixed assembly. a) and b) show spectra of colloidal assemblies prepared from a total of 4 different CrEEP syntheses to show the consistent results between samples. The insets in a) show how the samples are prepared for spectroscopy by immobilization on black double-sided tape, i) Mixture and ii) Gradient assembly. The scale bar is 10 mm. The white square shows the spot size of the spectrometer. The black dotted line in the spectra is the reflectance spectrum of the black backing layer.

Eidesstattliche Versicherungen und Erklärungen

§ 8 Satz 2 Nr. 3 PromO Fakultät für Biologie, Chemie und Geowissenschaften

Hiermit versichere ich eidesstattlich, dass ich die Arbeit selbstständig verfasst und keine anderen als die von mir angegebenen Quellen und Hilfsmittel benutzt habe (vgl. Art. 64 Abs. 1 Satz 6 BayHSchG).

§ 8 Satz 2 Nr. 3 PromO Fakultät für Biologie, Chemie und Geowissenschaften

Hiermit erkläre ich, dass ich die Dissertation nicht bereits zur Erlangung eines akademischen Grades eingereicht habe und dass ich nicht bereits diese oder eine gleichartige Doktorprüfung endgültig nicht bestanden habe.

§ 8 Satz 2 Nr. 4 PromO Fakultät für Biologie, Chemie und Geowissenschaften

Hiermit erkläre ich, dass ich Hilfe von gewerblichen Promotionsberatern bzw. –vermittlern oder ähnlichen Dienstleistern weder bisher in Anspruch genommen habe noch künftig in Anspruch nehmen werde.

§ 8 Satz 2 Nr. 7 PromO Fakultät für Biologie, Chemie und Geowissenschaften

Hiermit erkläre ich mein Einverständnis, dass die elektronische Fassung der Dissertation unter Wahrung meiner Urheberrechte und des Datenschutzes einer gesonderten Überprüfung unterzogen werden kann.

§ 8 Satz 2 Nr. 8 PromO Fakultät für Biologie, Chemie und Geowissenschaften

Hiermit erkläre ich mein Einverständnis, dass bei Verdacht wissenschaftlichen Fehlverhaltens Ermittlungen durch universitätsinterne Organe der wissenschaftlichen Selbstkontrolle stattfinden können.

Bayreuth, 22.09.2023

Marius Schöttle
Functional Photonic Gradients
in Colloidal Assemblies
Dissertation, 2023

University of Bayreuth
Physical Chemistry I
Faculty of Biology, Chemistry & Earth Sciences
Universitätsstraße 30
95447 Bayreuth